University of California
Santa Barbara

Rapid infrasound propagation corrections using empirical climatologies: Applications in volcano monitoring and systematic reanalyses of multi-year global datasets

A dissertation submitted in partial satisfaction
of the requirements for the degree

Doctor of Philosophy
in
Earth Science

by

Rodrigo Salvador De Negri Leiva

Committee in charge:

Professor Robin S. Matoza, Chair
Professor Chen Ji
Professor Toshiro Tanimoto

December 2023

The Dissertation of Rodrigo Salvador De Negri Leiva is approved.

Professor Chen Ji

Professor Toshiro Tanimoto

Professor Robin S. Matoza, Committee Chair

September 2023

Rapid infrasound propagation corrections using empirical climatologies: Applications in volcano monitoring and systematic reanalyses of multi-year global datasets

by

Rodrigo Salvador De Negri Leiva

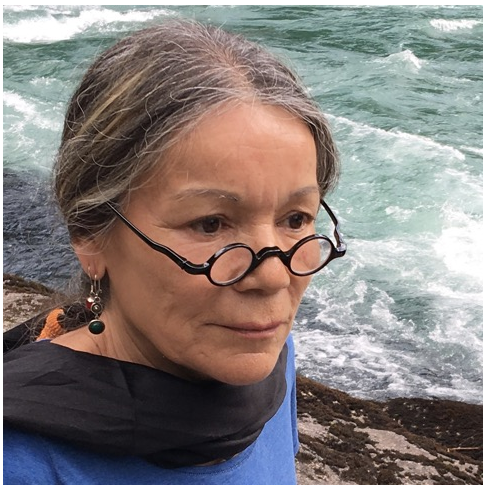

Nadia Oriel Leiva Pasten
I carry you always in my heart
{01/22/1955 - 06/07/2022}

I dedicate this work to my beloved mother, Nadia,

who I am sure would like to see the culmination of my efforts,

which are, essentially, to be like her;

to love books, knowledge, and be curious,

to be aware of who we are on Earth.

This is all thanks to you, dear mom.

Maestra vida,

camara'

te da y te quita

te quita y te da

Rubén Blades.

Acknowledgements

To my advisor, Professor Robin Matoza, and my committee members, Professor Chen Ji and Professor Toshiro Tanimoto, for all the support and dedication to advance my career.

To the National Science Foundation, Grant EAR-1847736, for funding this research.

To the Lewis family, who welcomed me and many other international students to be part of Santa Barbara. Especially Judy and Warren Lewis, who passed during the completion of my degree.

To Catherine Scanlon, who was a pillar during the worst times and has given me uncountable beautiful moments.

To my dear friends, Rafael, Tanya, Melissa, Luna, Ciara, Ale, and Silvia for listening to my story and sharing yours.

To my infrasound group Richard, Sean, Kaelynn, Hugo, and Jeremy, always interested in sounds which cannot be easily heard.

To my geophysics friends, Han, Aaron, Keneni, Cristhian, Brennan, and Scott for making work such an interesting place.

To my geology friends, Justin, Evan, Elisabeth and Judy.

To my international student friends, from who I could better understand my own experience.

Curriculum Vitæ

Rodrigo Salvador De Negri Leiva

Education

2023	Ph.D. in Earth Science (Expected), University of California, Santa Barbara.
2015	M.A. in Earth Science, National Autonomous University of Mexico, Mexico City.
2013	Bachelor in Physics, University of Chile, Santiago.

Publications

1. **R. De Negri**, & R.S. Matoza, *Rapid location of remote volcanic infrasound using 3D ray tracing and empirical climatologies: Application to the 2011 Cordón Caulle and 2015 Calbuco eruptions, Chile*, Journal of Geophysical Research: Solid Earth, 128, e2022JB025735 (2023) [DOI: 10.1029/2022JB025735].
2. **R. De Negri**, K. Rose, R. S. Matoza, P. Hupe, & L. Ceranna, *Long-range multi-year infrasonic detection of eruptive activity at Mount Michael volcano, South Sandwich Islands*, Geophysical Research Letters, 49, e2021GL096061 (2022) [DOI: 10.1029/2021GL096061].
3. R. S. Matoza, D. Fee, J. D. Assink, A. M. Iezzi, D. N. Green, K. Kim, L. Toney, T. Lecocq, S. Krishnamoorthy, J. M. Lalande, K. Nishida, K. L. Gee, M. M. Haney, H. D. Ortiz, Q. Brissaud, L. Martire, L. Rolland, P. Vergados, A. Nippress, J. Park, S. Shani-Kadmiel, A. Witsil, S. Arrowsmith, C. Caudron, S. Watada, A. B. Perttu, B. Taisne, P. Mialle, A. Le Pichon, J. Vergoz, P. Hupe, P. S. Blom, R. Waxler, S. De Angelis, J. B. Snively, A. T. Ringler, R. E. Anthony, A. D. Jolly, G. Kilgour, G. Averbuch, M. Ripepe, M. Ichihara, A. Arciniega-Ceballos, E. Astafyeva, L. Ceranna, S. Cevuard, I. Y. Che, **R. De Negri**, C. W. Ebeling, L. G. Evers, L. E. Franco-Marin, T. B. Gabrielson, K. Hafner, R. G. Harrison, A. Komjathy, G. Lacanna, J. Lyons, K. A. Macpherson, E. Marchetti, K. F. McKee, R. J. Mellors, G. Mendo-Pérez, T. D. Mikesell, E. Munaibari, M. Oyola-Merced, I. Park, C. Pilger, C. Ramos, M. C. Ruiz, R. Sabatini, H. F. Schwaiger, D. Tailpied, C. Talmadge, J. Vidot, J. Webster, and D. C. Wilson, *Atmospheric waves and global seismoacoustic observations of the January 2022 Hunga eruption, Tonga*, Science 377 (July, 2022) 95–100. Publisher: American Association for the Advancement of Science [DOI: 10.1126/science.abo7063].
4. J. Vergoz, P. Hupe, C. Listowski, A. Le Pichon, M. Garcés, E. Marchetti, P. Labazuy, L. Ceranna, C. Pilger, P. Gaebler, S. Näsholm, Q. Brissaud, P. Poli, N. Shapiro, **R. De Negri**, and P. Mialle, *IMS observations of infrasound and acoustic-gravity waves produced by the January 2022 volcanic eruption of Hunga, Tonga: A global analysis*, Earth and Planetary Science Letters 591 (Aug., 2022) 117639 [DOI: 10.1016/j.epsl.2022.117639].

5. K. McKee, C. M. Smith, K. Reath, E. Snee, S. Maher, R. S. Matoza, S. Carn, D. C. Roman, L. Mastin, K. Anderson, D. Damby, I. Itikarai, K. Mulina, S. Saunders, J. D. Assink, **R. De Negri**, and A. Perttu, *Evaluating the state-of-the-art in remote volcanic eruption characterization Part II: Ulawun volcano, Papua New Guinea*, Journal of Volcanology and Geothermal Research 420 (Dec., 2021) 107381 [DOI: 10.1016/j.jvolgeores.2021.107381].

6. K. McKee, C. M. Smith, K. Reath, E. Snee, S. Maher, R. S. Matoza, S. Carn, L. Mastin, K. Anderson, D. Damby, D. C. Roman, A. Degterev, A. Rybin, M. Chibisova, J. D. Assink, **R. De Negri**, and A. Perttu, *Evaluating the state-of-the-art in remote volcanic eruption characterization Part I: Raikoke volcano, Kuril Islands*, Journal of Volcanology and Geothermal Research 419 (Nov., 2021) 107354 [DOI: 10.1016/j.jvolgeores.2021.107354].

Abstract

Rapid infrasound propagation corrections using empirical climatologies: Applications in volcano monitoring and systematic reanalyses of multi-year global datasets

by

Rodrigo Salvador De Negri Leiva

Acoustic waves below the audible frequencies (20 Hz) are called infrasound. Generated by a wide variety of sources, these signals can propagate thousands of kilometers, aided by their low attenuation as well as strong winds and high temperatures in the stratosphere and thermosphere that enable them to return to the ground. Volcanic eruptions are among the most powerful sources of infrasound, and the International Monitoring System (IMS) infrasound network, maintained by the Comprehensive Nuclear-Test-Ban Treaty Organization (CTBTO), is capable of monitoring volcanic eruptions around the globe. However, the spatiotemporal variability of the atmosphere poses a major challenge. In particular, strong horizontal cross-winds affect the observed infrasound arrival back-azimuths, causing source mislocations up to hundreds of kilometers.

This dissertation presents an automatic iterative method combining empirical climatologies (HWM14/NRLMSIS2.0) and 3D ray tracing (infraGA) to obtain rapid, robust first-order estimates of the back-azimuth deviations, producing corrections for location and characterization procedures. The results compare well with a more realistic model of the lower atmosphere using Numerical Weather Prediction (NWP) simulations. Potential applications include near real-time volcano monitoring and large-scale reanalysis of infrasound archives.

To test this method, we first apply it to the eruptions of Puyehue-Cordón Caulle (2011) and Calbuco (2015) in Chile, using data from IMS stations within 5000 km. The

back-azimuth corrections reduce the source mislocation by ∼84% (242 to 38.7 km) and ∼75% (366 to 93.1 km), respectively.

Then, we assess the method's temporal accuracy using data from 2003-2022 from IMS station IS22 (New Caledonia), which has recorded persistent volcanic infrasound from Yasur (∼400 km) and Ambrym (∼700 km) volcanoes (Vanuatu archipelago). We find good agreement with the seasonal variation of the dataset, showing we can provide year-long estimates of the back-azimuth deviation.

Finally, we use the method to identify long-range infrasound signals recorded at the Antarctic IMS station IS27, attributable to episodes of moderate persistent eruptive activity at Mount Michael volcano, 1,670 km away on Saunders island (South Sandwich islands). Examining data from 2004-2020 reveals previously hidden candidate eruptive signals, especially from May 2005 to January 2008 and from May 2016 to April 2018.

Contents

Curriculum Vitae **vi**

Abstract **viii**

1 Introduction **1**
1.1 Sources of infrasound 1
1.2 A brief history of infrasound 2
1.3 Infrasound propagation 6
1.4 Towards infrasound monitoring of volcanic eruptions 10
1.5 Goals and organization of this study 13

2 Rapid location of remote volcanic infrasound using 3D ray tracing and empirical climatologies: Application to the 2011 Cordón Caulle and 2015 Calbuco eruptions, Chile. **14**
2.1 Abstract 14
2.2 Introduction 15
2.3 Data 19
2.4 Methods 22
2.5 Results 27
2.6 Discussion 39
2.7 Conclusions 43

3 Evaluating the temporal capability of empirical climatologies for rapid long-range volcanic infrasound propagation estimates using a multi-decadal dataset of persistent Vanuatu volcanic eruptions **45**
3.1 Abstract 45
3.2 Introduction 46
3.3 The Vanuatu archipelago volcanic arc 50
3.4 Annual back-azimuth deviation estimates comparing climatology and hybrid models 59
3.5 Results 61

3.6 Discussion 74
3.7 Conclusions 80

4 Long-range multi-year infrasonic detection of eruptive activity at Mount Michael volcano, South Sandwich Islands. 84
4.1 Abstract 84
4.2 Introduction 85
4.3 Mount Michael, South Sandwich Islands 86
4.4 Infrasound Observations 88
4.5 Investigating Infrasound Propagation From Mount Michael to IS27 . . . 93
4.6 Comparison With Satellite Detections 99
4.7 Conclusions 102

5 Conclusions 105
5.1 Conclusions 105
5.2 Future work 107

A Supporting information for "Rapid location of remote volcanic infrasound using 3D ray tracing and empirical climatologies: Application to the 2011 Cordón Caulle and 2015 Calbuco eruptions, Chile" 108
A.1 Text S1: calculation time reduction and other possible improvements. . . 108
A.2 Additional Figures 110

B Supporting Information for "Evaluating the temporal capability of empirical climatologies for rapid long-range volcanic infrasound propagation estimates using a multi-decadal dataset of persistent Vanuatu volcanic eruptions" 131
B.1 Additional figures 131

C Supporting Information for "Long-range multi-year infrasonic detection of eruptive activity at Mount Michael volcano, South Sandwich Islands" 145
C.1 Seasonal back-azimuth variation 145
C.2 k-means re-clustering method 146
C.3 Reference amplitudes 146
C.4 In-depth analysis and classification 147
C.5 Additional Figures 149
C.6 Tables 158

Chapter 1

Introduction

Infrasound refers to acoustic waves with frequencies below 20 Hz, typically a non-audible frequency range for the human ear. Unlike for sound waves, the atmosphere imposes a relatively low attenuation for infrasound – on the order of $\sim 10^{-2}$ to 10^{-1} dB/km under 80 km altitude (Sutherland and Bass, 2004). This highlights one of the most useful properties of infrasound: it can travel very long distances, even circumnavigating the Earth several times in a row, provided an energetic enough explosive event (e.g., Matoza et al., 2022b; Judd et al., 1888; Vergoz et al., 2022).

1.1 Sources of infrasound

Contrary to the intuition, infrasound is a common type of acoustic signal, produced by a myriad of natural (e.g., microbaroms, surf, auroras, meteors, lightning, earthquakes, glacier calvings, volcanic eruptions, etc.) and human-made phenomena (e.g., rocket launches, dams, aircraft, chemical explosions, nuclear explosions, etc.) (Campus and Christie, 2010).

1.1.1 Volcanic infrasound

Volcanic eruptions, especially the ones cataloged as explosive, emit intense infrasound signals that are directly related with the disturbances inflicted to the atmosphere by the eruptive process itself (Johnson, 2003; Evers and Haak, 2005; Garcés et al., 2008; Matoza et al., 2007; Fee and Matoza, 2013), which could last from seconds (isolated explosion) (e.g., Ripepe and Marchetti, 2002; Marchetti et al., 2013) to days (sustained ash-column) (e.g., Matoza et al., 2018; Fee et al., 2010). For this reason, infrasound is an outstanding tool to observe and understand volcanic eruptions, and any surface process that could arise from the interaction of an active volcano with the atmosphere.

1.2 A brief history of infrasound

1.2.1 First studies

The origins of infrasound studies of volcanic eruptions trace back to one of the most famous observed eruptions in history, the Krakatoa volcano eruption (Indonesia) in 1883, (Verbeek, 1885; Judd et al., 1888; Self, 1992). In 1888, a careful compilation of 53 barometric records distributed on the globe (Judd et al., 1888) showed that up to seven barometric disturbances were registered after Krakatoa's explosive eruption. These disturbances were indeed infrasound waves circumnavigating the Earth, carrying information not only about the enormous explosive event of Krakatoa, but also about the atmosphere's structure from the ground up to lower thermospheric heights ($\sim<$ 120 km) (Pekeris and Taylor, 1997; Kanamori et al., 1994; Harkrider and Press, 1967). But it was only after a second unparalleled event, this time the Great Siberian Meteor (Russia) in 1908, that the first recorded micobarographs were used to investigate infrasound at long-range distances with an adequate instrumentation for such small pressure fluctuations

(Shaw and Dines, 1905).

1.2.2 Infrasound seismology

With the development of better instrumentation, the use of infrasound was – for most of the first half of the last century – focused on indirect observation of the atmosphere physical properties (e.g., temperature, density, composition, winds, etc.) (Lindemann and Dobson, 1997; Whipple, 1923, 1935; Gutenberg, 1939). The observed signals were in this case, mostly human-made explosions, allowing a better understanding of sound propagation, showing the existence of shadow zones. These implied zones at stratospheric and lower thermospheric heights where sound propagates faster than at the ground ($\sim$340 m/s in a standard atmosphere). In addition, a directional component that implied strong anisotropy at certain heights. The existence of *ducts* at these heights, i.e. layers where sound waves bounce back to the ground, was mainly attributed to the combined effect of global circulation patterns at high altitudes (e.g., the Zonal and Meridional winds at stratosheric heights), which follow seasonal effects driven by the Sun's influence over the atmosphere, and inversions due to compositional changes such as the Ozone layer (e.g., Drob et al., 2003, 2010a; de Groot-Hedlin et al., 2010). The "infrasound seismology" that was developed during the first wave of infrasound research remains a topic of extensive development, especially thanks to a global network of infrasound arrays (e.g., Drob et al., 2010b; Garcés, 2004; Le Pichon et al., 2005b, 2006).

1.2.3 The creation of the International Monitoring System

After the Second World War, the world became acutely aware of the danger that nuclear weapons pose to humankind. By 1996, the world had seen the devastating bombings of Hiroshima and Nagasaki (August 1945), followed by a long chain of 2,046 nuclear

tests (528 on the atmosphere and 1,518 underground) by the United States (1,030), the USSR/Russia (715), France (210), the United Kingdom (45), China (45), and India (1) (Arms Control Association, nd; United Nations, nd). In 1996, the Comprehensive Nuclear-Test-Ban Treaty was put in place by 71 States Signatories from the United Nations to ban all nuclear explosions (CTBTO, ndb). The Comprehensive Nuclear-Test-Ban Treaty Organization (CTBTO) was established to effectively implement the treaty[1], and the creation of the International Monitoring System (IMS) was proposed to monitor for any explosions above 1 kT TNT equivalent anywhere and anytime on Earth. The IMS, with the goal of having 321 monitoring stations, and 16 laboratories on 89 countries around the globe, was designed to detect underground, underwater, and atmospheric traces of nuclear explosions. The technologies involved are seismic (underground), hydroacoustic (underwater), radionuclide (air), and infrasound (air) (Campus and Christie, 2010; Marty, 2019). The infrasound network, currently with 53 certified of 60 planned stations (CTBTO, nda) (see Figure 1.1), has proven effective to detect 1 kT TNT explosions globally (Marty, 2019). The IMS is probably the best example of the benefits of a multi-technology approach to effectively detect, locate, and characterize not only large human-made explosions, but global natural phenomena with a level of detail that has not been possible before. The progressive installation of the IMS infrasound network since 2003 has been the main factor behind a drastic increase in infrasound research in the last two decades.

[1]Called "Preparatory Commission" (or "the Commision") for the Comprehensive Nuclear-Test-Ban Treaty Organization (CTBTO) during the first years of the Treaty establishment, now just called CTBTO.

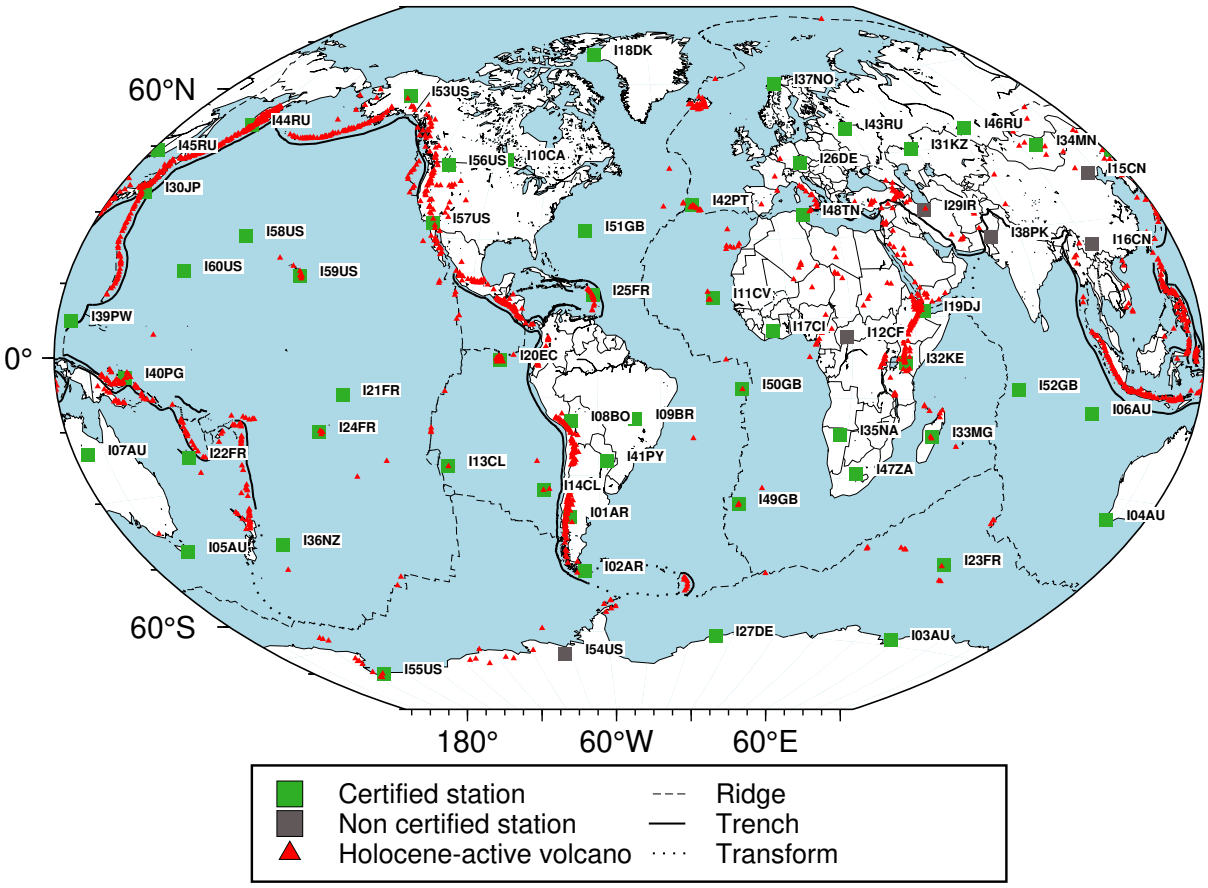

Figure 1.1: IMS infrasound network in 2023, colored by certification status. Green squares: currently certified. Gray squares: currently non certified. In white boxes: the names of each station by type of technology as first character ("I" for infrasound), the number of the station in the next two characters, and a code for the country in charge of the station in the last two characters. The different types of black lines correspond to the geologic features created by the three kinds of plate boundaries (i.e., trench by subducting plates, ridge by divergent plates, and transform faults)

1.3 Infrasound propagation

1.3.1 Local, regional, and global infrasound

The time-dependency scales of atmospheric phenomena (e.g., turbulence, buoyancy waves, thunderstorms, general circulation patterns, etc.) range from minutes to years. Proportionally, the length scales of these phenomena range from meters up to thousands of kilometers (Drob, 2019) (see Figure 1.2). Their effects on infrasound propagation are determined by the temporal and spatial scales of the signal that is to be analyzed as well. Generally, the longer the infrasound propagates, the more important the larger scale phenomena become, and vice-versa. Local (<15 km), regional (15-250 km), and global or remote (>250 km) infrasound describe infrasound propagation in terms of the distance to the source (Drob, 2019; Matoza et al., 2018; Fee and Matoza, 2013). The vertical extent of atmospheric descriptions needed to model acoustic propagation increases with the distance. For example, when considering propagation up to ∼150 km (local/regional), usually no more than 35 km of height is needed; whereas for regional infrasound and above at least ∼70 km should be used, which could be up to ∼140 km if considering the thermospheric duct (Drob, 2019). The temporal and spatial scales involved in atmospheric remote sensing and remote explosion monitoring of volcanoes, will require regional to global infrasound networks and descriptions up to thermospheric altitudes, hence the empirical climatologies.

The separation between local, regional, and global infrasound is, *de facto*, blurred down to local and regional/global (as a synonym) for volcanic infrasound.

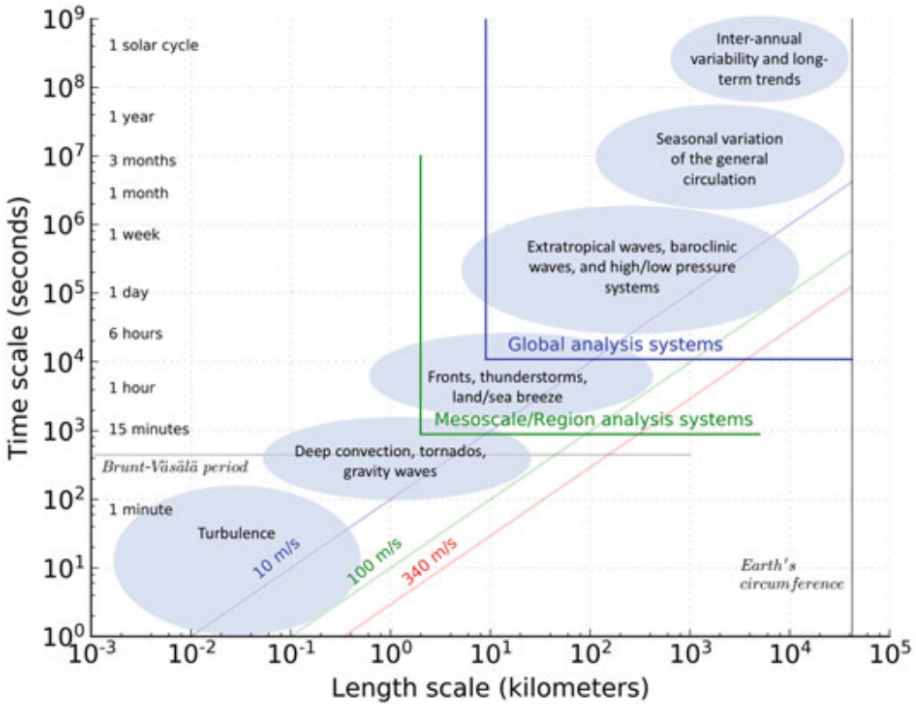

Figure 1.2: From Drob (2019) (*Reproduced with permission of Springer Nature*). Spatiotemporal variability of the most important phenomena that occur in the atmosphere. The green and blue axes depict the reference scales of the Mesoscale/Regional descriptions, and the Global descriptions, respectively.

1.3.2 Local volcanic infrasound

Local volcanic infrasound is generally limited to distances that are up to the order of tens of km, and often refers to observations that are near the active vent of the volcano that is being studied (Johnson, 2019). At these distances, topographic and source effects are very important, and the atmosphere is of somewhat secondary significance for signal propagation, being usually approximated as homogeneous, static medium. Having a very detailed chronology of observations for a sensor that is near the source allows a good estimation of parameters such as the total acoustic energy and spectrum characteristics tailored for the specific volcano being studied

(e.g., Johnson et al., 2003; Johnson and Aster, 2005; Goto and Johnson, 2011; Marchetti et al., 2013; Maher et al., 2022; Matoza et al., 2009). The use of multiple sensors adds the possibility of a precise location that can be used to distinguish between multiple possible active vents, study site effects, and monitor other types of infrasound sources near the volcanic edifice like rockfalls and lahars (e.g., Ripepe and Marchetti, 2002; Jones et al., 2008; Johnson and Palma, 2015; Fee et al., 2021; Sanderson et al., 2021).

At remote, or "long-range", distances (>250 km) the atmosphere becomes the most relevant component to detect, locate, and characterize volcanic signals, imposing its dispersive, attenuating, and ducting effects onto the propagating signals in proportion to the travel path length (e.g., Fee et al., 2010; Dabrowa et al., 2011; Matoza et al., 2011a,b, 2018). At long ranges, this generally means that the acoustic signal loses the higher frequencies it may have had originally, and only the low frequencies survive ($\sim<$ 1 Hz). Additionally, the original waveform duration increases, while the amplitudes reduce to the point it could become impossible to recognize in waveforms alone.

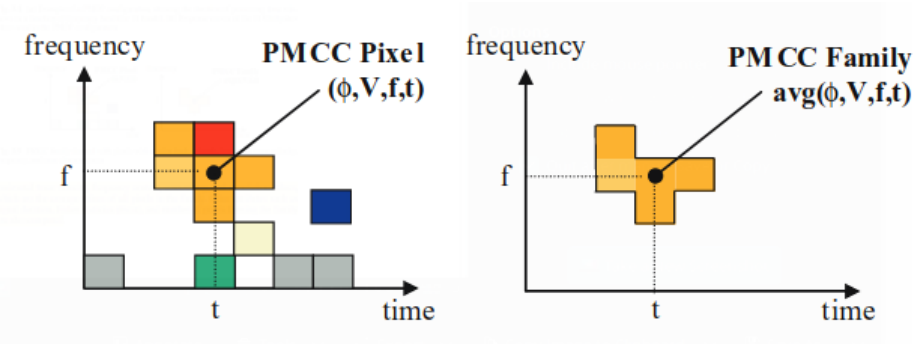

Figure 1.3: From Brachet et al. (2010) (*Reproduced with permission of Springer Nature*). Cartoon depicting the formation of a "family" with several "pixels" that share similar back-azimuths, trace velocities, frequency content, and times. A detection would be the next step, formed by several families with similar average attributes.

1.3.3 Global infrasound and the Progressive Multi-Channel Correlation Method

To be able to recover as much information as possible from the acoustic signals, distinguishing coherent *wanted* infrasound waveforms from other *unwanted* coherent sources – or "clutter" (Matoza et al., 2013), and the abundant ambient noise, the IMS infrasound network stations are designed for performing array processing techniques. Each IMS infrasound station has at least four sensors, separated by ∼1 to ∼3 km, targeting frequencies from 0.01 to 4 Hz. (Green and Bowers, 2010; Mialle et al., 2019; Le Pichon et al., 2009a; Marty, 2019). The main chosen method at the data processing center of the CTBTO, the International Data Centre (IDC) at Vienna, Austria, is the Progressive Multichannel Correlation Method (PMCC) (Cansi, 1995; Cansi and Le Pichon, 2008; Le Pichon and Cansi, 2003; Le Pichon et al., 2010). This method has proven useful to isolate detections parameterized by time, mean frequency, root-mean-square amplitude, and trace velocity, reconstructing the original signal by grouping detections ("pixels") into "families" that share common attributes in a specified time window (Brown et al., 2002; Brachet et al., 2010; Ceranna et al., 2019) (see Figure 1.3).

Overall, this allows the signal to be reconstructed and extract valuable information that can be used for remote detection of energetic explosive events such as volcanic eruptions.

1.4 Towards infrasound monitoring of volcanic eruptions

1.4.1 Infrasound as a component of monitoring and cataloging explosive eruptions

Beyond detecting, locating, and reconstructing the acoustic chronologies of long-range volcanic eruptions (e.g., Fee et al., 2010; Garcés et al., 2008; Matoza et al., 2007, 2018, 2011a,b; De Angelis et al., 2012; Matoza et al., 2019), infrasound volcanic monitoring, early warning, and automatic notification systems have been in constant development (Mialle et al., 2015; Garcés et al., 2008; Caudron et al., 2015; Dabrowa et al., 2011; Kamo et al., 1994; Ripepe et al., 2018; Arrowsmith and Whitaker, 2008; Arrowsmith et al., 2008; Fee et al., 2010; Matoza et al., 2019). Ash-cloud dispersal parameterization is another critical area where infrasound can be of use for automated monitoring of ash-clouds (Taisne et al., 2019; Perttu et al., 2020). Multi-technology approaches combining seismic, satellite, hydroacoustic, and infrasound observations are the most complete way to detect, locate, characterize, and monitor volcanic eruptions on Earth, provided real-time, or near-real-time access to the data (Assink et al., 2019; Green et al., 2013; McKee et al., 2021a,b). Taking advantage of the existence of the IMS network, infrasound temporal arrays, and local permanent stations, is therefore critical for global monitoring (Arrowsmith et al., 2015; Le Pichon et al., 2008; Modrak et al., 2010; Park et al., 2014; Marchetti et al., 2019b).

Attempts to catalog Earth's global volcanism (Engwell et al., 2021; Global Volcanism Program, 2013b), have also been revitalized by the use of historical datasets from the IMS infrasound network (2005-2010) to quanfify the global volcanic explosive record (Matoza et al., 2017).

1.4.2 Challenges

With the current infrasound network infrastructure, the main challenges of long-range global monitoring of explosive sources are the atmospheric temporal and spatial variability (Assink et al., 2019; Drob et al., 2010a; Le Pichon et al., 2009a; Green and Bowers, 2010; Nippress et al., 2014; Waxler et al., 2017), wind noise (Walker and Hedlin, 2010), and clutter discrimination (Matoza et al., 2013, 2019). The mislocation of infrasound volcanic sources, with values that can be hundreds of kilometers from true, is the direct effect of the infrasound propagation path deviation produced by stratospheric and lower thermospheric winds (e.g., Evers and Haak, 2005; Matoza et al., 2018, 2019).

1.4.3 Forward-modeling the atmospheric effects on infrasound

Forward-model approaches have been used to reverse the combined atmospheric effects on the observed waves, with the goal of paralleling the physical complexity of the medium, obtaining accurate simulations, and explaining unexpected arrivals (Arrowsmith et al., 2007; Smets et al., 2015, 2016; Green et al., 2011; Assink et al., 2014; Ceranna et al., 2009; Marcillo et al., 2014). These approaches require realistic models of the atmosphere, physically complete and bounded by as many real observations as available. Atmospheric data assimilation systems (e.g., the Integrated Forecast System (IFS), the Global Forecast System (GFS), the Unified Model (UM), and the Global Spectral Model (GSM), among others) are well suited to provide present and/or past atmosphere esti-

mates based on observations, while Numerical Weather Prediction (NWP) models (e.g., the European Center for Medium-Range Weather Forecasting (ECMWF), the National Centers for Environmental Prediction (NCEP), the United Kingdom Meteorology Office (UKMO), and the Japan Meteorology Agency (JMA), among others), are preferred for forecasts based on theoretical extrapolations of observations (Drob, 2019). However, the complexity of these accurate models imposes constraints for global and historical analyses, rapid calculation of infrasound propagation estimations (perhaps during a natural emergency), and the formulation look-up tables that require large temporal calculations to understand the time-dependent most robust behavior of the atmosphere effects on the long-range infrasound observables (e.g., Drob et al., 2010a; Morton and Arrowsmith, 2014).

Empirical climatologies are robust, whole-atmosphere models, based on observational time-dependent global specifications (∼50 years of satellite and ground observations), that perform data assimilation by means of function fitting. The last iteration of the Naval Research Laboratory Mass Spectrometer Incoherent Scatter Radar Model (NRLMSIS 2.0) (Emmert et al., 2020), and the Horizontal Wind Model (HWM14) (Drob et al., 2015) can provide winds, temperature, density, pressure, and atmospheric composition as a function of the specified latitude, longitude, altitude, day of year, and universal time. Their self-contained programs are also freely available for research purposes (see Suplementary Information of Emmert et al. (2020) and Drob et al. (2015)). Even considering the limitations of these first-order models (e.g., Drob et al., 2003), the combination of empirical climatologies with infrasound propagation methods as 3D ray tracing (e.g., Blom and Waxler, 2012; Virieux et al., 2004) or parabolic equation based methods (e.g., Waxler et al., 2023) could potentially provide *priors* (semi-empirical model-based prior information), for annual and semiannual seasonal variations, and also diurnal, semidiurnal, and terdiurnal migrating tidal variations at regional to global scales.

A third approach, known as hybrid models, matches empirical models of the upper atmosphere with more accurate forecasts or reanalysis of the lower and middle atmosphere (∼75 km) to take advantage of both atmosphere specification types (Drob et al., 2003; Schwaiger et al., 2019). This idea, which is probably the most complete and accurate approach for volcanic infrasound propagation, carries the same problem for large models previously mentioned.

1.5 Goals and organization of this study

In this study, we use historical records of long-range volcanic infrasound ($> 1,000$ km) of explosive eruptions from Chile, South Sandwich Islands, and the Vanuatu archipelago to develop and test a rapid and robust methodology oriented towards the general goal of forward modeling and producing priors for infrasound monitoring of remote eruptions. In particular, we alleviate the mislocation of volcanic sources with the IMS infrasound network.

In Chapter 2, I present the methodology and a test case based on Puyehue, 2011 (Chile), and Calbuco, 2015 (Chile) eruptions considering the nearest eight (∼1000 to 5000 km) available regional infrasound stations. In Chapter 3, I introduce a case that uses the most active volcanoes of the Vanuatu archipelago – Yasur, Lopevi, Ambrym, Gaua, and Ambae – and only one station in New Caledonia at ∼400 to ∼700 km from the possible sources, to perform a year-long model of infrasound modeled arrivals and compare them with ∼20 years of observations. In Chapter 4, I show how, with the help of this methodology, it is possible to uncover infrasound from one of the most remote volcanoes on Earth, with one station at ∼1500 km (Antarctica). In Chapter 5, I summarize this work and present future goals.

Chapter 2

Rapid location of remote volcanic infrasound using 3D ray tracing and empirical climatologies: Application to the 2011 Cordón Caulle and 2015 Calbuco eruptions, Chile.

This chapter appeared in this for in:

De Negri, R., & Matoza, R. S. (2023). Rapid location of remote volcanic infrasound using 3D ray tracing and empirical climatologies: Application to the 2011 Cordón Caulle and 2015 Calbuco eruptions, Chile. Journal of Geophysical Research: Solid Earth, 128, e2022JB025735. https://doi.org/10.1029/2022JB025735

2.1 Abstract

Infrasound (<20 Hz) can propagate thousands of kilometers through the atmosphere, enabling global source location using networks of arrays such as the International Monitoring System (IMS) infrasound network. However, atmospheric spatiotemporal variability poses a major challenge to locating infrasound sources. Strong horizontal cross-winds deviate the observed infrasound arrival azimuths, producing source mislocations that

can be on the order of hundreds of kilometers. We introduce a method that combines empirical climatologies (HWM14/NRLMSIS2.0) and 3D ray tracing (infraGA) to obtain first-order, robust, and rapid estimates of the back-azimuth deviations for source location procedures. For each trial source node and receiver path, day of the year and time, we perform an automatic iterative search for infrasound ground intercepts around the target station and obtain the corresponding back-azimuth deviation. We test the method using IMS infrasound data from stations up to ∼5,000 km range for two similar explosive eruption case studies: 2011 Puyehue-Cordón Caulle and 2015 Calbuco. We obtain a source mislocation reduction up to ∼84% (242 to 38.7 km) and ∼75% (366 to 93.1 km) for Puyehue-Cordón Caulle and Calbuco eruptions, respectively. To evaluate the approach, we repeat the procedure using more realistic hybrid atmospheric descriptions; we obtain comparable results (up to ∼75% mislocation reduction for both eruptions). Potential applications of the approach include long-range volcano monitoring in near-real time by using pre-computed look-up tables or large-scale, multi-year reanalyses of infrasound waveform archives.

2.2 Introduction

Detecting, quantifying, and cataloging the global occurrence of explosive volcanism helps toward several goals in Earth sciences and has direct applications in volcanic hazard mitigation (Matoza et al. (2019), and references therein). Previous work has demonstrated that infrasound arrays can be used to detect, locate, and provide detailed chronologies of remote explosive volcanism, with the potential to provide source parameters for ash transport and dispersal models (e.g., Matoza et al., 2007; Garcés et al., 2008; Fee et al., 2010; Matoza et al., 2011a,b; Dabrowa et al., 2011; Green et al., 2013; Caudron et al., 2015; Ripepe et al., 2018; Matoza et al., 2018; Marchetti et al., 2019b;

Taisne et al., 2019; Perttu et al., 2020). Regional volcano-acoustic monitoring and early warning systems are being investigated and implemented (Kamo et al., 1994; Matoza et al., 2007; Garcés et al., 2008; Fee et al., 2010; De Angelis et al., 2012; Ripepe et al., 2018; Taisne et al., 2019). Recent work has explored the potential of the International Monitoring System (IMS) infrasound network to provide a quantitative catalog of global explosive volcanic activity (Matoza et al., 2017) and automated eruption notifications to Volcanic Ash Advisory Centers (VAACs) (Mialle et al., 2015).

Required elements of a processing workflow to achieve these goals include infrasound signal detection, discrimination, association, and location (e.g., Brown et al., 2002; Evers and Haak, 2005; Le Pichon et al., 2008; Arrowsmith et al., 2008; Arrowsmith and Whitaker, 2008; Brachet et al., 2010; Modrak et al., 2010; Park et al., 2014; Arrowsmith et al., 2015; Sanderson et al., 2020). Challenges to each processing stage result from strong signal variability associated with long-range acoustic propagation through the temporally and spatially varying atmosphere (e.g., Drob et al., 2010a; Le Pichon et al., 2009a; Green and Bowers, 2010; Nippress et al., 2014; Waxler et al., 2017; Assink et al., 2019), and from widely varying incoherent wind noise (e.g., Walker and Hedlin, 2010) and coherent ambient infrasound (clutter) interfering sources (Matoza et al., 2013, 2019).

Here, our emphasis is on developing a method that could be applied rapidly to produce near-real-time analysis products to aid volcano monitoring, or that could be applied automatically and systematically to large data archives. Thus, we seek to provide rapid, first-order location solution estimates using automated procedures that do not require downloading and manipulating large realistic atmospheric specification products, emphasizing rapid and efficient computation speed over atmospheric and infrasound propagation realism (Smets et al., 2015, 2016; Schwaiger et al., 2019).

Stratospheric and lower mesospheric zonal winds have a strong influence on the observed wave parameters of infrasound detections (e.g., Garcés, 2004; Le Pichon et al.,

2005a,b; Evers and Haak, 2005; Le Pichon et al., 2006; Drob et al., 2010b). At mid-to-high latitudes especially, the cross-winds at stratospheric heights become a primary factor controlling global infrasound source mislocation (e.g., Evers and Haak, 2005; Matoza et al., 2011a; Mialle et al., 2019), which has been up to hundreds of kilometers from true for IMS case studies (e.g., Evers and Haak, 2005; Matoza et al., 2017, 2019). A common approach for assessing the expected source mislocation is to forward-model the atmospheric effects on the infrasound detections (e.g., Arrowsmith et al., 2007; Le Pichon et al., 2009a; Green et al., 2011; Assink et al., 2014; Marcillo et al., 2014; Matoza et al., 2018).

Atmospheric infrasound propagation modeling requires specifications of temperature, wind velocity, density, and molecular composition from the ground surface up to ∼140 km altitude. To model infrasound propagation, these specifications are typically obtained in three main ways: (1) using data assimilation analyses such as the European Center for Medium-Range Weather Forecasting (ECMWF), which gathers ground-based and meteorological data as constraints to physically model the atmosphere from the ground to ∼80 km in altitude every 6-hours; (2) empirical climatologies, which use multidecadal historical archives of the atmospheric data to statistically represent the atmosphere from the ground to the exobase (∼750 km) with 12-hour intervals (e.g., the Horizontal Wind Model (HWM) (Drob et al., 2015) and the NRLMSIS2.0 model (Emmert et al., 2020); or (3) hybrid models that seamlessly integrate both approaches (e.g., the Naval Research Laboratory Ground to space (G2S) (Drob et al., 2003), or AVO-G2S (Schwaiger et al., 2019). The most recent trend in infrasound studies is toward increasing propagation realism and accuracy (more accurate characterization of atmospheric state and finer spatio-temporal scales), implementing either data assimilation analyses or hybrid models (Ceranna et al., 2009; Smets et al., 2015; Fee et al., 2020). However, this comes with the cost of a greatly increased computational burden that can quickly escalate for

global models and/or multi-decadal studies. Empirical climatologies, on the other hand, are succinct self-contained programs that reduce computational needs to a minimum, but generally underrepresent smaller scale atmospheric variations (e.g., stratospheric zonal jets) (Drob et al., 2003). Here we explore the potential of using empirical climatologies for a first-order "good enough" estimate of stratospheric cross-wind corrections for rapid infrasound signal association and source location, with the goal of real-time application or retrospective systematic reanalyses of large multi-decadal data archives. Our approach builds on that of pre-computed look-up tables, generally based also on empirical climatologies (e.g., Drob et al., 2010a; Morton and Arrowsmith, 2014).

Matoza et al. (2017) introduced a signal association and location method algorithm (IMS_vASC), which uses array processing results from the global IMS infrasound network to automatically detect and catalog global multiyear (2005 to 2010) explosive volcanic signals. In this paper, we aim to incorporate first-order rapid corrections of the cross-winds effects on this trial source location process. Thus, we explore the use of empirical climatologies combined with infraGA 3D ray tracing (Blom and Waxler, 2012) to estimate the back-azimuth deviation produced by the cross-winds for a large grid of trial source locations on the Earth's surface. Since infrasound propagation strongly depends on ducting conditions, we also investigate the use of a simplified Gaussian wind jet parameterization (Jones, 1986, user manual) to perturb the climatology profiles and force a stratospheric or thermospheric return within reasonable bounds for the wind strength.

In Section 2.3, we present two similar explosive eruption event case studies that we use to assess the method. In Section 2.4, we introduce the methodology to model the back-azimuth deviations, as well as possible improvements to deal with the oversimplification of the lower atmospheric descriptions. In Section 2.5, we summarize our findings in reducing the source mislocation with IMS_vASC and compare the effects of choosing different atmospheric descriptions and modeling parameters. In Section 2.6, we discuss

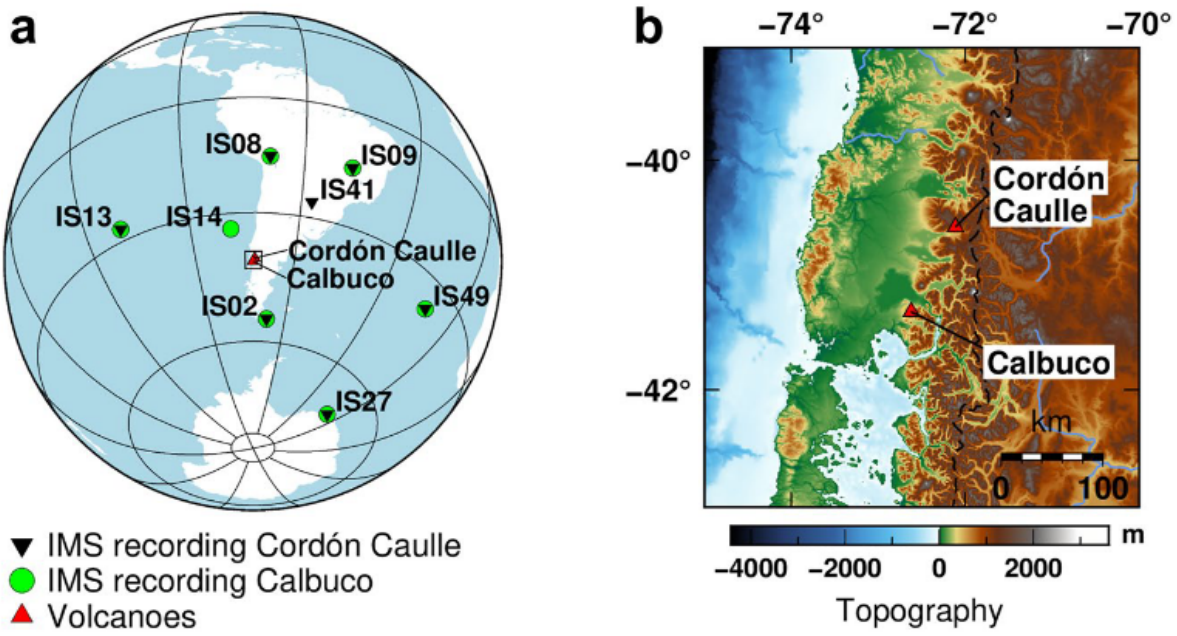

Figure 2.1: Location of IMS stations and volcanoes. (a) Black inverted triangles: IMS stations that were recording during 2011 Puyehue-Cordón Caulle volcanic complex (Cordón Caulle) eruption. Green circles: IMS stations that were recording during the 2015 Calbuco eruption. Red triangles: PCCVC and Calbuco locations. Black rectangle indicates the zoomed area in (b). (b) Topographic map of the zoomed area of volcanoes (red triangles). Black-dashed line: border between Chile and Argentina.

the feasibility of the method to obtain first-order approximations for global infrasound back-azimuth deviations.

2.3 Data

2.3.1 Volcanic setting

Puyehue-Cordón Caulle volcanic complex is a Pleistocene-Holocene active area composed of three volcanoes: Cordillera Nevada caldera (∼1000 m a.s.l), Cordón Caulle fissure system (∼1500 m a.s.l.), and Puyehue stratovolcano (∼2000 m a.s.l). It is located in the southern Andes volcanic zone, inside Puyehue National Park, Los Lagos Region,

Chile (-40.5828°, -72.1122°). Since the Late Pleistocene, Cordón Caulle has been the only active volcano, with at least three eruptions in the last century (1921, 1960 and 2011) (Elissondo et al., 2016). On June 4 at 18:45 UTC, 2011, after two months of increasing seismicity, the eruption started with an explosive event that generated a plume of ∼9-12 km high (Elissondo et al., 2016; Collini et al., 2013). This paroxysmal plinian/subplinian phase lasted about two days, followed by a period of about two months with a fluctuating activity that resulted in sustained column heights between 4 and 12 km.

Calbuco volcano, Chile (-41.3300°, -72.6183°) is a ∼2000 m a.s.l. stratovolcano located at about 100 km SW from Cordón Caulle (Global Volcanism Program, 2013a). On April 22, 2015, at 21:05 UTC, Calbuco started a subplinian/plinian explosive phase after a relatively short period of shallow seismic precursor activity, sending ash to an altitude of 15 km. The maximum intensity of the eruption was reached on April 23, with a phase of 6 hours in which column height reached 17 km (Castruccio et al., 2016; Van Eaton et al., 2016; Matoza et al., 2018). The intensity decreased rapidly after this phase, falling back into a pre-eruptive activity regime in about a month.

Cordón Caulle and Calbuco eruptions occurred at similar altitudes (∼2000 and ∼1500 meters, respectively) and locations, under strong zonal mid-latitude eastward winds (See Figure 2.1; see also Figures A.6 and A.7). Both eruptions were cataloged as VEI 4 (volcanic explosivity index, Newhall and Self (1982)), with sustained plume heights of more than 10 km that lasted several days (Elissondo et al., 2016; Collini et al., 2013; Castruccio et al., 2016; Van Eaton et al., 2016), and occurred during atmospheric stratospheric winds prevailing towards the East.

2.3.2 IMS data

The IMS network is the main monitoring infrastructure of the Comprehensive Nuclear-Test-Ban Treaty Organization, integrating seismic, hydroacoustic, infrasonic, and radio nucleoid detection technologies. The IMS infrasound network currently has 53 (of 60 planned) stations detecting coherent acoustic waves that could be generated by explosions down to 1 kt of TNT anywhere on Earth (Christie and Campus, 2010). Each IMS station is composed of at least four microphone sensors with a flat response from 0.02 to 4 Hz within 3 dB. At the International Data Center of the CTBTO (Vienna, Austria) the raw waveforms from all IMS stations are processed with the Progressive Multichannel Cross-Correlation method algorithm (PMCC) (Cansi, 1995; Cansi and Klinger, 1997) in real-time, generating detection lists.

For this study, we considered the nearest eight IMS infrasound stations to both volcanoes (see Figure 2.1), which range from ∼1,600 (IS02, Argentina) to ∼5,100 km (IS49, United Kingdom). We downloaded the available IMS waveforms in a time window of 20 days, centered at each eruption time. We use PMCC to extract coherent detections for further analysis (see Figure 2.2 for a glance at the most interesting sequences). We implemented PMCC with 15 log-spaced frequency bands between 0.01 and 5 Hz, following Matoza et al. (2013).

We note that during the Cordón Caulle eruption (2011), the station IS14 was not operational after the destructive effects of the tsunami generated by the Chilean M8.8 Maule earthquake on February 27, 2010. Similarly, during Calbuco eruption (2015), station IS41 could not provide detections due to a reduced number of detecting channels (see Figure 2.1). We discuss the effects of the consequent station distribution difference in Section 2.6.

2.4 Methods

IMS_vASC is a brute-force, grid-search, cross-bearings method (Matoza et al., 2017) to localize sustained explosive volcanic infrasound signals with the IMS infrasound network of arrays. It enhances sources that have a sustained but limited time span (i.e., volcanic eruptions) by cleaning unwanted background detections (clutter) from the data. It localizes the source by performing cross-bearings for the nearest detecting stations with the back-azimuth information of the cleaned detections. Although this approach takes advantage of the IMS infrasound network capabilities, atmospheric winds in the propagating path of the signals can considerably alter their apparent back-azimuths and detectability (see Figure 2.3), causing source mislocations up to hundreds of kilometers (e.g., Garcés, 2004; Le Pichon et al., 2005a,b; Evers and Haak, 2005; Le Pichon et al., 2006; Drob et al., 2010b). IMS_vASC allows the use of back-azimuth correction values in the source location process, but lacks a robust process to implement it. Thus, we aim to estimate the expected back-azimuth deviations by modeling infrasound propagation under reasonable atmospheric conditions, providing IMS_vASC with a set of corrections to reduce the source mislocation. Once some basic parameters are defined (e.g., source and station locations, time, etc.), our approach automatically performs an iterative calculation of expected back-azimuths (if any) by modeling infrasound propagation with 3D ray tracing (infraGA) (Blom and Waxler, 2012), and an empirical set of atmospheric descriptions obtained from a combination of the Horizontal Wind Model (HWM14) (Drob et al., 2015) and the Mass Spectrometer Incoherent Radar Model (NRLMSIS2.0) (Emmert et al., 2020).

2.4.1 Modeling the atmosphere

2.4.1.1 Raw climatologies

The "raw" climatological descriptions refer to the default atmospheric model obtained by combining HWM14 and NMRLSIS2.0. For each source-station direction and time, we obtain the horizontal winds (i.e., zonal and meridional), temperature, density, and pressure values every 50 km. For heights from 0 to 170 km in steps of 0.5 km, we average each parameter along the source-station direction, thus obtaining one set of estimations per height. The resulting model will be a layered range-independent atmosphere representative of each ray propagation direction, which is saved in tables (1D profiles) that will be used by the ray tracing algorithm to model infrasound ray propagation on a 3D spherical layered atmosphere. For the next atmospheric model types, the discretization follows the same procedure.

The strong assumption of a range-independent atmosphere is a reasonable first-order approximation that allows a reduced computational cost for 3D ray tracing propagation (see the infraGA/geoAC manual). As we use real observations to evaluate the validity of our approach, the comparison with more realistic but computationally demanding models (e.g., range-dependent ray propagation) should be considered in future developments (e.g., Figure A.19).

For this study, the eruption times are 2011-06-04 at 19:00 UTC for Cordón Caulle, and 2015-04-22 at 21:00 UTC for Calbuco.

In addition to the raw empirical climatologies used by default, we explore perturbing the wind values obtained with HWM14 to enhance along-path stratospheric winds in a simplified manner.

2.4.1.2 Perturbed climatologies

Numerous case studies (e.g., Arrowsmith et al., 2007; Evers and Haak, 2007; Ceranna et al., 2009; Assink et al., 2014; Green et al., 2011; Le Pichon et al., 2015; Smets et al., 2016; Lalande and Waxler, 2016) have shown that long-range infrasound detection is often dependent on marginal ducts. Smoothed atmospheric profiles available in both weather reanalysis products and climatologies fail to capture small-scale fluctuations on which infrasound propagation depends, thus controlling detection vs. non detection for a source-receiver pair (e.g., Matoza et al., 2011a). A fundamental limit of the climatologies used in this study is that they tend to underestimate the atmospheric propagation ducts. In prior studies, this issue has been tackled by using gravity-wave perturbations of the profiles to obtain more realistic infrasound arrivals (ground intercepts) (e.g., Green et al., 2011; Norris et al., 2009; Gibson et al., 2006; Kulichkov et al., 2010; Smets et al., 2016). However, this type of approach tends to be computationally expensive, departing from our rapid first-order main goal. Instead, we investigate the use of a simplified parametric Gaussian wind jet (Jones, 1986) perturbation to enhance the stratospheric winds that could cause ducting (see Figure 2.4). The perturbation is centered at 40 km of altitude, with a standard deviation of 10 km, and amplitude equivalent to 30% of the maximum effective speed (see Equation 2.1) in this altitude range (∼20 to 60 km; see Figure 2.4c,d). Additionally, the perturbation is applied only when positive along-path winds are present at these altitudes to avoid creating unrealistic zonal ducts [1].

$$c_{eff} = c_T + \hat{n} \cdot \vec{c}. \tag{2.1}$$

Where $\vec{c} = (u, v)$ is the wind speed in height, with u and v the zonal and meridional

[1] This perturbation only affects the propagation speed of the infrasound waves, but indirectly affects the ray paths (e.g., propagation length) as the horizontal winds in height used by the 3D ray-tracing algorithm are changed.

winds, respectively; $\hat{n}$ is the propagation direction from the source to the station; and c_T is the adiabatic sound speed in height.

We note that this simplified wind perturbation approach is justifiable given the method application in a grid-search source location procedure (Matoza et al., 2017). In this procedure, a trial source node is only illuminated if there are corresponding observed detections at multiple stations. Thus, the Gaussian wind jet is simply a tool to help assess if a given trial source node is feasible for a given set of infrasound observations given reasonable deviations of the atmospheric profiles.

We assess how the raw and perturbed climatologies results compare to more realistic atmospheric descriptions corresponding to a hybrid model based on the European Centre for Medium-Range Weather Forecasts (ECMWF) descriptions.

2.4.1.3 Hybrid model

We build a hybrid set of descriptions by merging the European Centre for Medium-Range Weather Forecasts (ECMWF) reanalysis v5 (ERA5) data for the model reference levels (137 levels from ∼0 to ∼80 km altitude) with empirical climatologies (>80 km altitude) in height (see Figure 2.4). We download ERA5 descriptions of horizontal winds and temperature for the area and time of interest, and complete the descriptions in height with the empirical climatologies using a simple linear interpolation of the averaged in values per height. This results in more realistic wind and temperature descriptions under ∼80 km altitude for the infrasound raypaths (i.e., small tropospheric or stratospheric ducts), completed above ∼80 km with the robust but coarser climatological descriptions (See Figures A.2, A.3, A.4, and A.5).

2.4.1.4 Perturbed hybrid model

We also calculate a set of perturbed hybrid profiles following the same procedure as in Section 2.4.1.2. In this case, the resulting descriptions will not match the realistic model, but could account for other type of phenomena that are still not present in the ERA5 profiles (i.e., gravity waves types of perturbations).

Once the atmosphere model is defined, we continue with an iterative approach to determine the back-azimuth deviation for each source-station pair.

2.4.2 Iterative back-azimuth deviation estimation

For a given trial source node and receiver (station) pair, we begin by using infraGA 3D ray tracing to launch two sets of rays, with azimuths ϕ_1 and ϕ_2, that azimuthally enclose the station location (see Figure 2.5, left panel). The launch azimuths are modified iteratively to converge to a value where it is possible to obtain ground intercepts or to otherwise declare the case as "ill-conditioned" (no ground arrivals near the station). Both sets of rays, with corresponding back-azimuths φ_1 and φ_2, are launched with inclinations from 0.5° to 40.0° in steps of 0.5°. If the ground intercepts (depicted as white circles in 2.5 , left panel) have a great-circle annular distance smaller than the threshold value, d_r (0.5° for this study), their back-azimuths are averaged and used as a starting value to launch the next iteration. The next launching azimuths, ϕ_1' and ϕ_2', are modified to reduce the great-circle radial distance from the average location of ground intercepts to the receiver, d_ϕ (Figure 2.5, right panel). This process continues until d_ϕ is reduced below a threshold value (0.05° for this study). Once the ground intercepts are near enough to the receiver, their average properties are calculated and used to determine the modeled back-azimuth, φ_{app}. If a maximum number of attempts is exceeded during the search process (40 in this study), the case is also declared to be "ill-conditioned", reflecting

atmospheric conditions that in practice will impede infrasound detections at the station (e.g., strong stratospheric winds that oppose the propagation direction). Finally, the back-azimuth deviation, $\Delta\varphi$, is calculated as the difference between the geographical back-azimuth, φ_{true}, and the modeled back-azimuth, φ_{mod} (i.e., $\Delta\varphi = \varphi_{true} - \varphi_{mod}$).

We note that infraGA includes a powerful ray search method that could be used for determining ray parameters as we did in this study. However, at the propagation ranges we consider (∼700 to ∼5000 km), the infraGA search method will be unable to find arrivals at the target stations, which is essentially due to the increasing launch angle sensitivity with range. Different approaches could also be used to deal with this issue (e.g., Blom, 2020).

2.5 Results

2.5.1 Waveforms and PMCC detections

We display the waveforms and PMCC detections from the IMS stations considered in this study in Figure 2.2 from one day before each eruption onset to five days after for Cordón Caulle and two days after for Calbuco. We note IS41, the station with the longest PMCC detection sequence during Cordón Caulle eruption (2.2b, left), was not recording during Calbuco eruption (2.2b, right). Additionally, the lack of IS13 and IS14 records from Figure 2.2 was a choice to emphasize the most relevant stations detections, despite their datasets being still considered in our analysis (see Figure A.1). The prevalence of strong eastern stratospheric winds during both eruptions (see Figures A.6 and A.7) made these stations unable to detect long-range infrasound coming from the east i.e., upwind sound propagation).

The expected arrival times of the observed explosive eruption phases (Elissondo et al.,

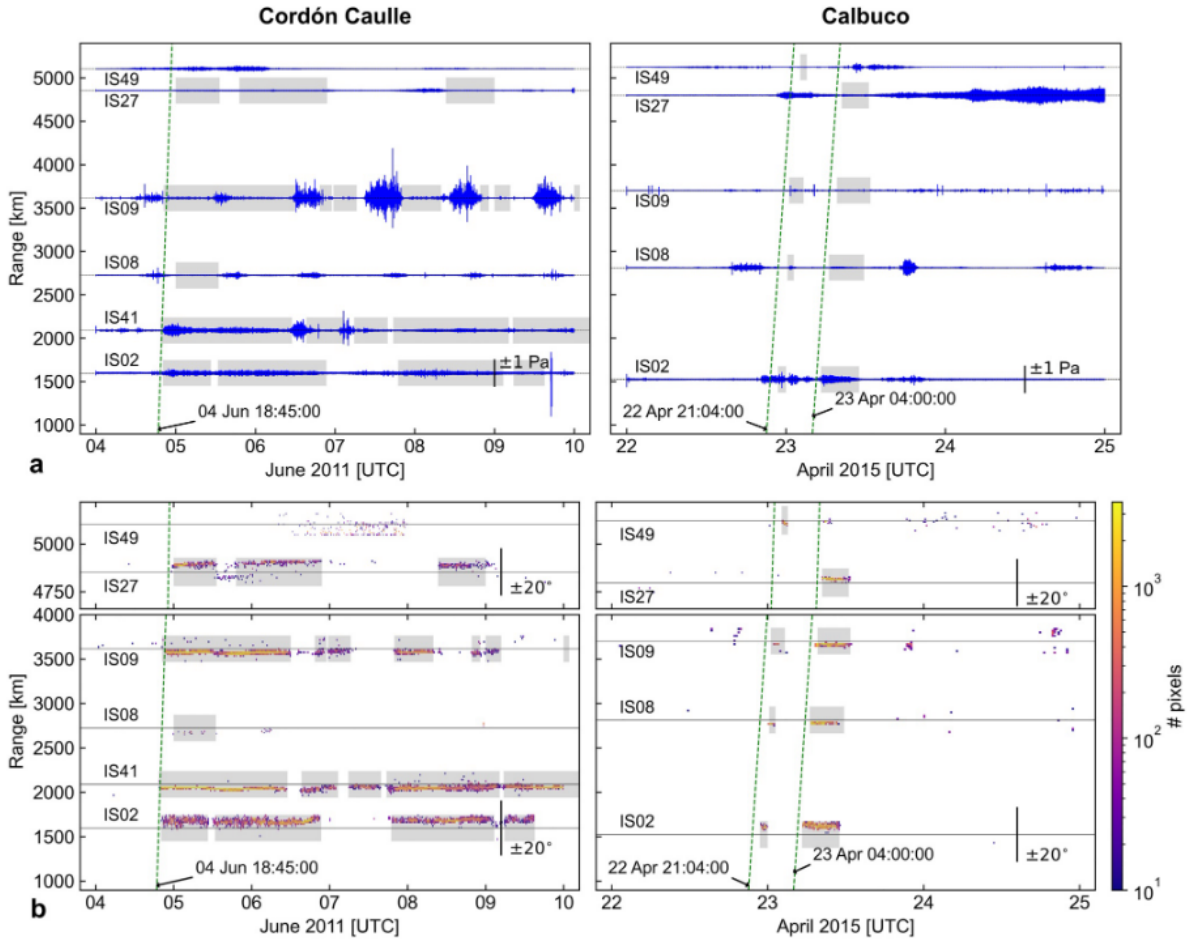

Figure 2.2: (a) Beamformed waveforms ($0.5 < f < 5$ Hz) for each station array, except upwind and non-recording stations (IS13, IS14, and IS41 for Calbuco only). In a gray background, we depict the associated detections attributable to the source in (b). In green slanted dashed lines, we show the estimated arrival time ($c = 300\,\mathrm{m/s}$) of the acoustic wave with origin time on each eruption's onset. (b) PMCC detections from all available stations for Cordón Caulle (left) and Calbuco (right) volcanoes. For each station, we display a 2-D histogram that shows the number of pixels of parsed ($0.5 < f < 5$ Hz) PMCC detections in time (x-axis) by azimuth relative to the geographical station-to-source value (y-axis). Only values in the range $\pm 20°$ for each station have been considered.

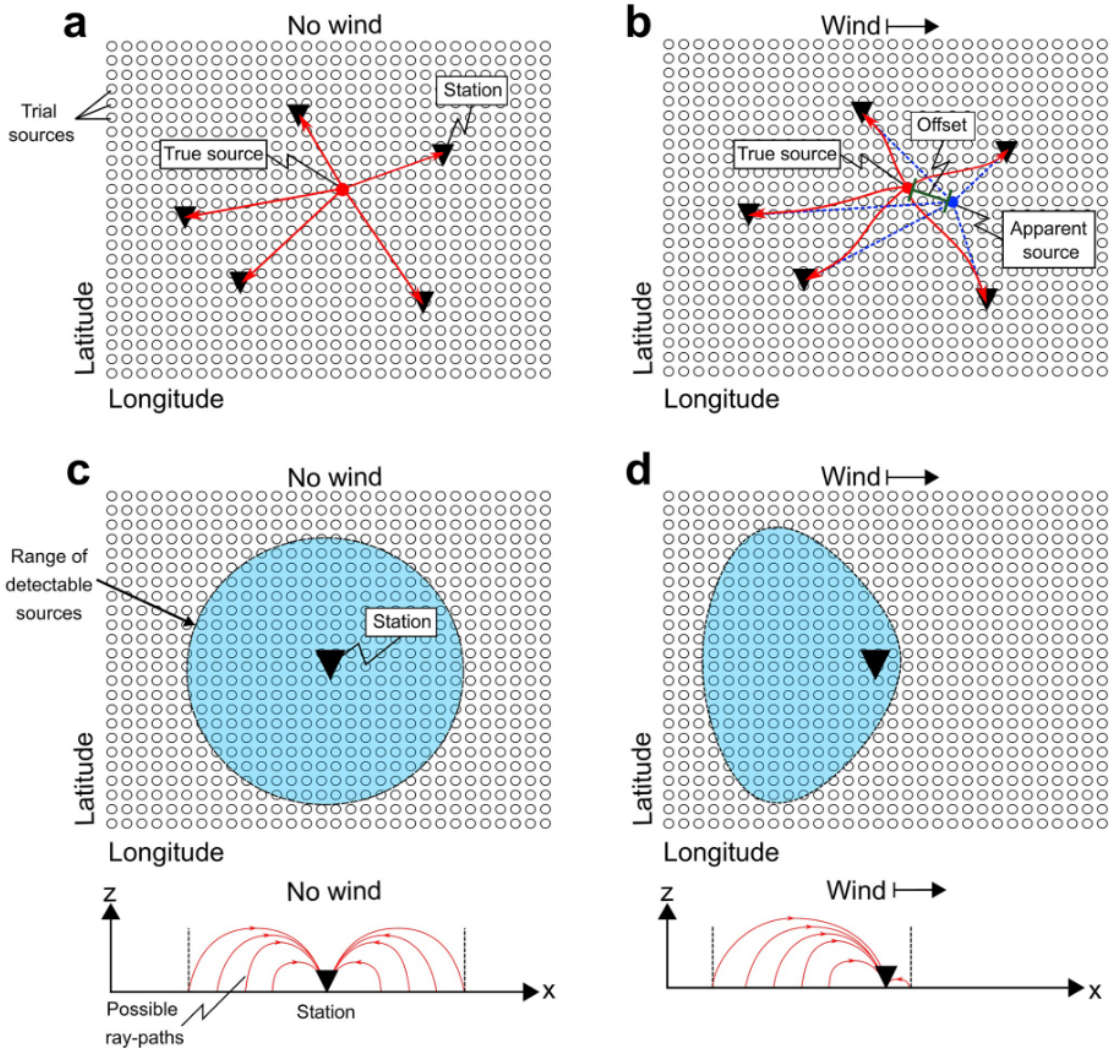

Figure 2.3: Effect of stratospheric winds on the source offset (top) and the source detectability (bottom). The stations are depicted as black inverted triangles, while the possible trial sources as a grid of white circles surrounding them. (a) A source (red circle) produces signals that travel undisturbed to each station (no wind present). (b) The moving medium (i.e., winds) bends the ray paths (red). Under winds blowing from west to east, the source seems to be shifted eastwards when performing cross-bearing locations with the apparent back-azimuths (blue dashed line), producing an offset. (c) Without winds, the detectable sources should be inside the light-blue circle around the station (black triangle). (d) With wind blowing from west to east as shown in this figure, the detectable range is now enhanced in the downwind direction from the trial sources or similarly the upwind direction from the station (i.e., here more trial sources to the West of the station are possible candidates for signals detected by the station). Conversely, the detectable range is reduced in the downwind direction (East) from the station (corresponding to the upwind direction from these trial sources East of the station toward this station). Cartoons of example ray paths in 2D show how the wind affects detectability at the bottom of (c) and (d).

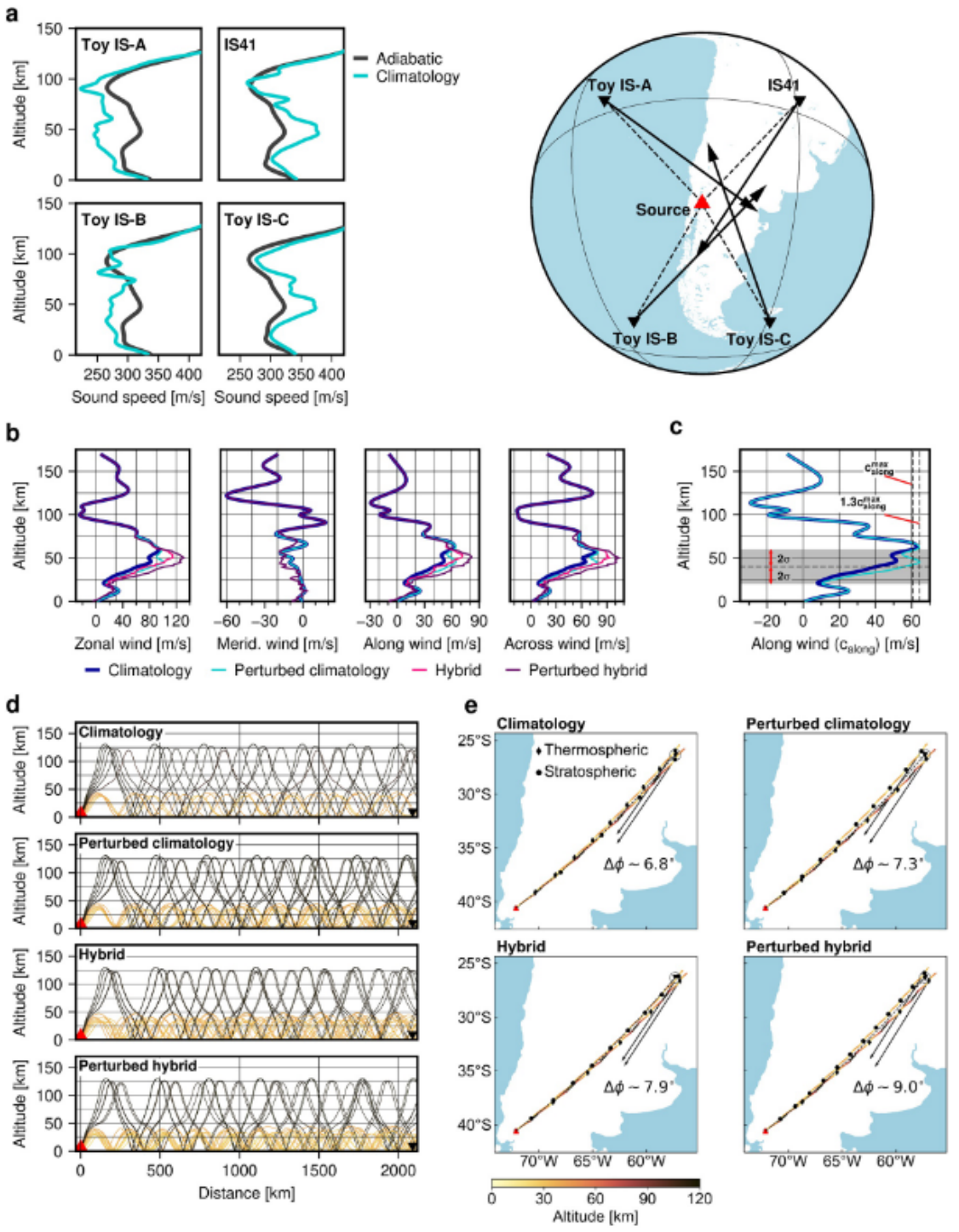

Figure 2.4: (a) Right: example case of cross-bearings for Cordón Caulle location (red triangle) during predominant Winter-like eastward zonal winds (the only real infrasound station is IS41). Here the source appears to be East of the true source location. (Continues on next page)

Figure 2.4: (From previous page) In black arrows: modeled back-azimuth from each station. In black-dashed lines: geographical azimuths from Cordón Caulle to each station (black inverted triangles). Left: reference average sound speed profiles in altitude calculated with empirical climatologies for each station. (b) Reference zonal, meridional, along-path, and across-path atmospheric winds in altitude for Cordón Caulle to IS41 direction, from empirical climatologies (blue line), perturbed climatologies (cyan line), hybrid (purple), and perturbed hybrid descriptions (pink). (c) Close-up comparison between empirical climatologies and perturbed climatologies, showing the heights where the empirical climatologies are perturbed to match $1.3 \times c_{along}^{max}$ ($\sim$20 to 60 km). (d) Comparison of ray tracing results for IS41 using the atmospheric descriptions in (b). The selected rays are colored by turning altitude (see color bar at bottom right). (e) Overhead maps with a stratospheric and a thermospheric ray from (d). The rays are colored by altitude. The back-azimuth deviations of each ray at IS41 ($\Delta\phi$) are depicted by black arrows, while the average azimuth deviation is indicated numerically in the map as well. The black dots and diamonts represent the stratospheric and thermospheric ray ground intercepts, respectively.

2016; Collini et al., 2013; Castruccio et al., 2016; Van Eaton et al., 2016) for celerities of 300 m/s across the stations (green dashed lines) help visualize the difference between the background PMCC detections before and after volcanic activity. For both volcanoes, the eruptive onset can be observed in at least four stations. These are IS02, IS41, IS09, and IS49 for Cordón Caulle; and IS02, IS08, IS09, and IS49 (first explosion) or IS27 (second explosion). On the other hand, it is clear that much of the observable waveforms do not match the coherent volcanic detections (gray boxes in 2.2a).

The general back-azimuth deviation of the detections is similar for both eruptions, with stronger effects due to higher regional zonal winds for Cordón Caulle (June 2011) than Calbuco eruption (April 2015) (see Figures A.2, A.3, A.4, and A.5 for effective sound speed profiles; also Figures A.6 and A.7 for average zonal winds in area of study). The station coverage is affected by the zonal wind conditions, generating an azimuthal gap of detecting stations of ($\sim$200°) on the western quadrant (IS02 to IS08). The eastern quadrant stations (i.e., downwind signal propagation) have an azimuthal gap of $\sim$107° instead (from IS09 to IS27), and carry the bulk of the detection information that will be

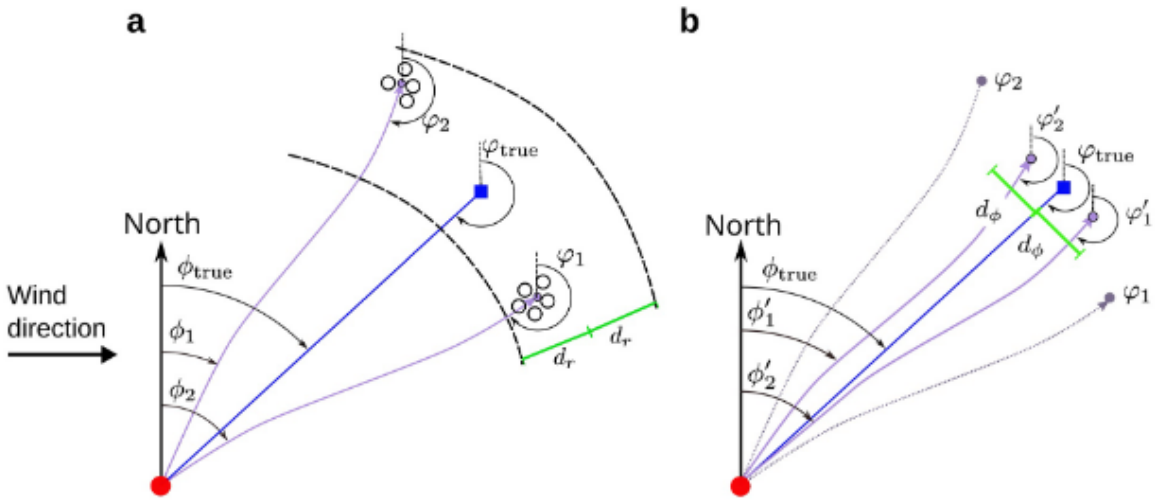

Figure 2.5: Iterative back-azimuth deviation estimation for an *a priori* known source location (red dot). (a) The source has a geographical azimuth (blue line), or "true azimuth", towards the receiver (blue square). First, we launch two sets of rays (purple curved lines) with azimuths, ϕ_1 and ϕ_2, containing the true azimuth, ϕ_{true}. The curvature of the launched rays represents the effect of eastward winds (black arrow on each subplot), introducing an back-azimuth deviation. If the ground intercepts (white circles) are inside an annular area of width $2d_r$ (green intervals), their average (purple dot) is used to obtain their respective back-azimuths, φ_1 and φ_2. (b) Next, we reduce the angular distance and recalculate the back-azimuths as in (a). The new launch azimuths (ϕ'_1 and ϕ'_2) still contain the true azimuth (ϕ_{true}), and should be inside the annular area in (a). We repeat this process iteratively until the desired threshold, d_ϕ, is reached. The final back-azimuths, φ'_1 and φ'_2, are averaged to determine the back-azimuth deviation, $\Delta\varphi$, for the source-receiver pair.

used to find the most probable source location.

An evident difference between Cordón Caulle and Calbuco eruptions (Figure 2.2b) is that the PMCC infrasound detections last for at least five days for the former, while only some hours for the latter. The apparent source locations for both eruptions should be then determined by similar wind effects, but with a better station coverage (IS41) and a considerably higher number of detections for Cordón Caulle than Calbuco.

2.5.2 Predicted back-azimuth deviations

For each atmosphere model defined in Section 2.4, we run a simulation to estimate the back-azimuth deviation at each station for signals coming from both eruptions (Figure 2.6). Additionally, we classify our results by the turning height of the ground intercepts, labeling them as "only strato." when only using rays with stratospheric turning heights (<60 km), or "strato. and thermo." when also including ground intercepts with thermospheric turning heights (usually ∼120 km).

The modeled back-azimuth deviations are positive (i.e., observed azimuth is smaller than the true azimuth) when the source-station direction has a north component, and negative (i.e., observed azimuth is bigger than true) on the opposite case, matching the observed deviations in Figure 2.2. The back-azimuth deviation magnitudes range from ∼1° (IS49) to ∼12° (IS02), with higher values for Puyehue-Cordón Caulle (∼2 to ∼12°) than for Calbuco (∼1 to ∼10°), in concordance with stronger eastward zonal winds for June than April in the area of study (See Figures A.6 and A.7).

Near all "strato. and thermo." cases successfully provided deviation values, although IS13 and IS14 have associated deviations with extreme arrival transmission looses (see Figures A.8 and A.9) that render their predictions invalid for data correction purposes.

When "only stato." and "strato. and thermo." models give deviation estimates,

we see the values are comparable, with generally smaller magnitudes for "only strato." results (e.g., IS90, IS27, IS41, or IS49). The exception to this rule is IS02 for Calbuco when using a hybrid model, where a strong tropospheric jet, invisible for the climatologies, allows arrivals with a much smaller back-azimuth deviation (see Figures A.4 and A.5).

For cases with enough detections and clear bell-like distributions (see Figures A.11 and A.12) we included estimations of the observed back-azimuth deviation mean, median, and standard deviation in Figure 2.6 (IS02, IS08, IS09, and IS27 for both volcanoes, while IS41 only for Cordón Caulle). We see a general agreement of the observed mean and medians with the predicted values across all models, but especially the perturbed cases, as they produce higher back-azimuth deviations. The climatologies compare well with the hybrid models, with back-azimuth deviations that differ by $\sim$1 to 2°.

2.5.3 Source locations

We first calculated the uncorrected (straight ray great-circle path assumption) source location with IMS_vASC, finding a mislocation of $\sim$242 km for Puyehue-Cordón Caulle eruption that increased to $\sim$366.4 km for Calbuco eruption (Figures 2.7 and 2.8). These values represent the baseline mislocation due to atmospheric conditions during each eruption.

After using the modeled back-azimuth deviations (Figure 2.6) as correction values for IMS_vASC, we observe that regardless of the atmospheric model used, the mislocations reduce for all the "strato. and thermo." results (Figure 2.7), but almost always increase for the "only strato." results (only the Hybrid model reduces the mislocation).

For the Puyehue-Cordón-Caulle case, the $\sim$242 km original offset reduces from $\sim$24% ($\sim$184.3 km, "Hybrid pert. strato. and thermo.") to $\sim$84% ($\sim$38.7 km, "Perturbed clim. strato. and thermo."). For Calbuco case ($\sim$366.4 km), the reduction ranges from $\sim$65%

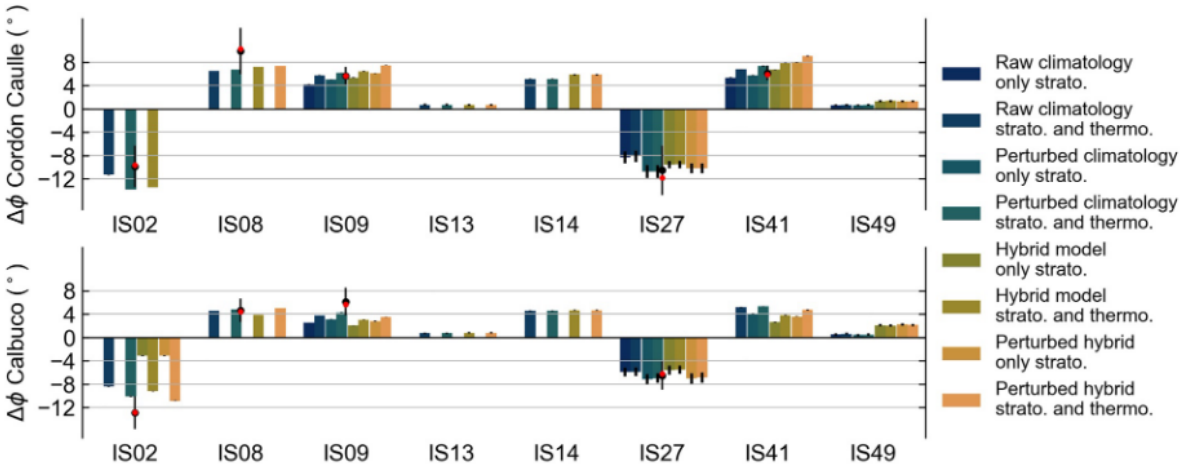

Figure 2.6: Comparison of back-azimuth deviation results modeled for all considered stations for both eruptions. Each result is a combination of the model choices described in Section 2.4.1 using only arrivals that turned at stratospheric heights ("only strato."), or using arrivals that have both stratospheric and thermospheric turning heights ("strato. and thermo."). Each bar represents the back-azimuth deviation value (see Section 2.4.2). Some of the stations do not have an associated back-azimuth deviation, indicating the method does not converge. Each bar has a standard deviation size range indicated on a black vertical line. For the stations IS02, IS08, IS09, IS27 for both volcanoes, and IS41 for Cordón Caulle only, we show the real back-azimuth deviation mean (black dot), median (red dot), and standard deviation (vertical black line) for the first two days since each eruption (Figure 2.2; Figures A.11 and A.12).

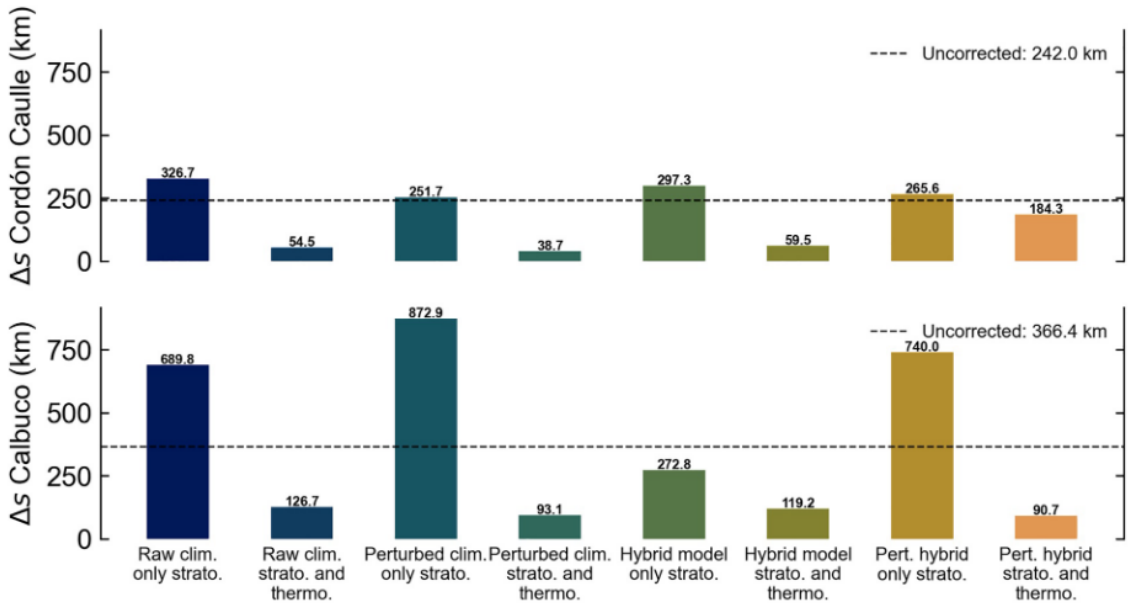

Figure 2.7: Summary of modeled source location offsets (km) using IMS_vASC for each combination of choices (see Figure 2.6). In a black-dashed line, we depict the offset when no corrections are used (i.e., "uncorrected").

(∼126.7 km, "Raw clim. strato. and thermo.") to ∼75% (90.7 km, "Pert. hybrid strato. and thermo.").

The association and location method, IMS_vASC, also finds the nearest Holocene potentially active volcano (Global Volcanism Program, 2013a) after calculating the apparent location of the source. In Table 2.1, we summarize the apparent source and nearest active volcano mislocations to the actual targets. The climatological corrections have comparable mislocation reduction results with the hybrid corrections, with better results than the hybrid model when using perturbed climatologies with stratospheric and thermospheric arrivals.

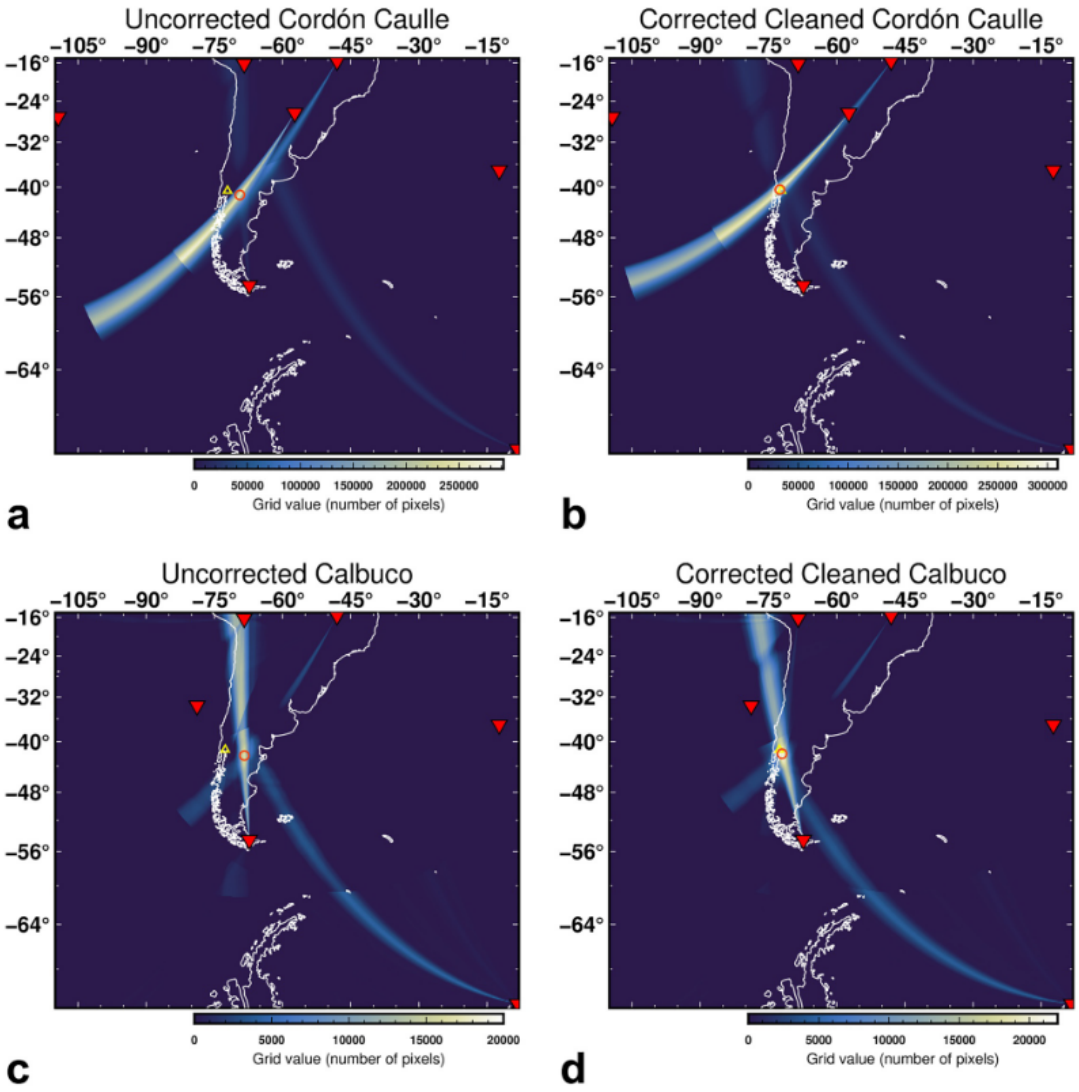

Figure 2.8: Left (a,c): uncorrected source locations with IMS_vASC for PCCVC and Calbuco volcanoes, with offsets of 242 km and 366.4 km, respectively. Right (b,d): best source location results by absolute source location with IMS_vASC for Cordón Caulle and Calbuco volcanoes, with offsets of 38.7 km and 90.7 km for the models "Perturbed clim. only strato." and "Perturbed hybrid strato. and thermo.", respectively (Figure 2.7). All source location plots correspond to the cleaned grid, $\mathbf{G}^c$, results (Matoza et al., 2017).

Table 2.1: Summary of IMS_vASC results. "Abs. Δs (km)" refers to the distance between the obtained apparent source location to the true source location for each case. "Near. Δs (km)" refers to the distance between the nearest holocene-active volcano from the apparent location to the true location of the source.

Volcano	Model	Abs. Δs (km)	Near. Δs (km)	Nearest volcano
Cordón Caulle	Uncorrected	242.0	226.3	Crater Basalt Field
	Raw clim., only strato.	326.7	228.8	Laguna Blanca
	Raw clim., strato. and thermo.	54.5	65.8	Osorno
	Pert. clim., only strato.	251.7	228.8	Laguna Blanca
	Pert. clim., strato. and thermo.	38.7	26.1	Carrán-Los Venados
	Hybrid model, only strato.	297.3	228.8	Laguna Blanca
	Hybrid model, strato. and thermo.	59.5	73.2	Mocho-Choshuenco
	Hybrid pert., only strato.	265.6	251.6	Tralihue
	Hybrid pert., strato. and thermo.	184.3	186.1	Sollipulli
Calbuco	Uncorrected	366.4	215.7	Crater Basalt Field
	Raw clim., only strato.	689.8	537.8	Río Murta
	Raw clim., strato. and thermo.	126.7	52.5	Cuernos del Diablo
	Pert. clim., only strato.	872.9	983.7	Viedma
	Pert. clim., strato. and thermo.	93.1	50.8	Yate
	Hybrid model, only strato.	272.8	215.7	Crater Basalt Volcanic Field
	Hybrid model, strato. and thermo.	119.2	62.4	Hornopirén
	Hybrid pert., only strato.	740.0	537.8	Río Murta
	Hybrid pert., strato. and thermo.	90.7	62.4	Hornopirén

2.6 Discussion

2.6.1 Crosswinds and observed detections

During the eruptions of Cordón-Caulle (June 2011) and Calbuco (April 2015) strong eastward seasonal winds occurred at stratospheric altitudes, producing similar effects on the infrasound propagation ray paths. West of both volcanoes, the upwind propagation direction of the signals left stations IS13 and IS14 unable to detect the eruptions. On the east side, the downwind propagation direction favored long-range propagation that resulted in clear volcanic infrasound at most of the stations. With volcanic infrasound detection frequencies usually lower than 2 Hz, this is an expected effect of the yearly global stratospheric wind circulation patterns (Le Pichon et al., 2009a). The observed back-azimuth deviations (see Figure 2.2) follow the patterns of a source that seems to be "pushed" downwind (east, as illustrated in Figure 2.3b), producing azimuths that are smaller than true (i.e., positive deviation) for stations to the north of both sources (e.g., IS08, IS09, and IS41), and larger than true (i.e., negative deviation) for stations to the south (e.g., IS02 and IS27) of the sources (e.g., Evers and Haak, 2005; Matoza et al., 2011a, 2018).

2.6.2 Predicted back-azimuth deviations

We see a general agreement between the predicted back-azimuth deviations (Figure 2.6) and the observed back-azimuth deviations (Figure 2.2b). The deviation magnitudes correlate with the crosswind strength along the propagation path of each profile. Stations south from both volcanoes show generally higher deviations than stations at the north, as the zonal winds were stronger at mid-to-high latitudes (see Figures A.6 and A.7). High deviations from arrivals that are only thermospheric are associated with near-north

or near-south profiles (IS08 and IS02, respectively). High deviations where arrivals are mostly stratospheric are the product of strong crosswinds with an along-path component that increase the effective sound propagation of the signals (e.g., IS27, IS41, and IS09). Low deviations with stratospheric and thermospheric arrivals are present only for IS49, located almost downwind from both volcanos with a strong favorable stratospheric wind jet (see Figures A.2, A.3, A.4, and A.5). Except for IS49, the farthest station considered (∼5,000 km) with a subsequent high attenuation propagation, all detecting stations had observations with similar back-azimuth deviations than our predictions (see Figure 2.6).

2.6.2.1 Thermospheric arrivals

In cases when both "strato." and "strato. and thermo." models have associated back-azimuth deviations, their values are similar (e.g., IS09, IS27, IS41, and IS49). The slightly higher average back-azimuth deviation estimation for the "strato. and thermo." cases (∼1°) is produced by the higher deviations thermospheric arrivals have in our models. The agreement between "strato." and "strato. and thermo." values, suggests that in cases where no stratospheric arrivals were found (e.g., stations IS02 and IS08 in Figure 2.6), thermospheric arrivals aid with modeling crosswind effects. This is also reinforced by the significant mislocation reduction obtained when applying corrections derived from "strato. and thermo." models (see Figure 2.7). Despite thermospheric infrasound observations being less feasible and usually not considered in most studies due to their high upper atmosphere absorption (Sutherland and Bass, 2004), our models indicate thermospheric arrivals could explain observations at stations with high crosswinds effects (e.g., IS02 and IS08). Thermospheric paths have been interpreted before for infrasound recorded at IS22, New Caledonia for signals from Lopevi volcano in Vanuatu at a range of ∼650 km (Le Pichon et al., 2005b), at IS19 for signals from Nabro volcano at a range of 264 km (Fee et al., 2013), at the LITE array for signals from Tungurahua at a range of

∼251 km (Assink et al., 2012), and discussed as a possibility for Calbuco (2015) (Matoza et al., 2018). The long-range propagation for the considered stations (>1,500 km) and possible thermospheric path for 2015 Calbuco and 2011 Cordon Caulle warrants further investigation.

2.6.2.2 Tropospheric arrivals

The existence of tropospheric turning heights (∼< 25 km) in the hybrid model case from Calbuco to IS02 (Figure A.10) suggests considering a third category of arrivals in the search process. However, the modeled back-azimuth deviations for tropospheric arrivals are much smaller than the "strato. and thermo." cases (∼3° vs. ∼10°) and we did not find many observations with such deviations values (see Figure A.12). Additionally, tropospheric wind jets tend to have shorter time spans and cover smaller regions (Drob et al., 2003), which are features that will be smoothed out by the empirical climatologies (e.g., Le Pichon et al., 2005a).

2.6.2.3 Perturbed cases

The climatological perturbed models have higher deviation values, generally better matching the observed mean and median observed of the detections. For some of the hybrid results (e.g., IS09 and IS41 for Cordón Caulle), it seems that the Gaussian perturbation introduces an overcorrection that results in an increased overall mislocation (see Figure 2.7 for Cordón Caulle hybrid "strato. and thermo." cases). When perturbing the empirical climatologies, on the other hand, the source mislocations always reduce for "strato. and thermo." cases, supporting the idea of using a simple Gaussian perturbation to enhance the stratospheric duct effects.

2.6.3 Source locations

The completeness of the IMS network is critical for source location purposes (Le Pichon et al., 2009a) and this manifests when comparing the Cordón Caulle and Calbuco results. The lack of IS41 detections on April 2015 produces a basal (uncorrected) source mislocation increment of ∼120 km for Calbuco when compared to Cordón Caulle, setting a limit on the location accuracy for Calbuco eruption that is clear across our source location results (Figures 2.7 and 2.8). Another major factor in the increase or reduction of the source mislocation was the existence of correction values for the most relevant detecting stations. From Figure 2.8 it is clear that the mislocation increases when applying corrections to a very limited number of stations. For example, the case of perturbed climatologies with only stratospheric arrivals does not find deviations for IS02 and IS08, which are determinant to constrain the source longitude, resulting in a cross-bearing maximum that is actually much farther from the uncorrected location (see Figure 2.7; also see Figures A.13 to A.18). The low number of predictions for "only strato." cases shows that the iterative search of arrivals is less effective in converging towards the target station location when using only rays with stratospheric turning heights. We think this could be partially tackled by fine-tuning the iteration launch parameters case by case (e.g., changing the launch azimuths for IS02 or IS08), but in this study we kept the same modeling parameters across all cases for consistency (see A.1) for more insights of possible improvements in the search algorithm). Nevertheless, the "strato. and thermo." cases are very effective in reducing the source mislocation as they provide robust deviation estimations for nearly all stations. This suggests that when using a cross-bearings approach such as IMS_vASC, the corrections should only be applied if a minimum number of detecting stations is involved. In this study, whenever the stations IS02, IS08, IS09, IS27, and IS41 had associated correction values we obtained a significant source

mislocation reduction (Figure 2.7 and Table 2.1).

Our results indicate that our automatic climatology-based methodology could provide rapid and robust predictions of the back-azimuth deviation for similar source location cases. Applications of this methodology extend to the case of using yearly predictions of back-azimuth deviation behavior to discriminate volcanic infrasound from clutter (De Negri et al., 2022). Upon further testing and performance tuning (see A.1) we think the method has good potential to be used for studies that involve large temporal and spatial data sets, and also near real-time infrasound location systems.

2.6.4 Blind search

We expect that our approach should generally limit the contribution of clutter (Matoza et al., 2013) and reduce the rate of false associations and detections by limiting the number and spatial distribution of trial source nodes that can be linked for each station (Figure 2.3). In this sense, *a priori* trial source nodes could be mapped to specific back-azimuth deviation values, or rejected as implausible trial source locations, depending on the time of the year and receiver location, generally improving source location and association capabilities. The present study investigates the degree of mislocation reduction for known sources and the overall feasibility of the method (Figure 2.3). Further implementation and integration into a blind search algorithm (Matoza et al., 2017) could be explored in future work.

2.7 Conclusions

We introduce a method for rapid first-order estimates of infrasonic back-azimuth deviation to improve source-location procedures for a grid of trial source-receiver pairs based on empirical climatologies (HWM14/NRLMSIS2.0) and 3-D ray tracing (GeoAc/infraGA).

The use of empirical climatologies enables the estimates to be pre-computed a priori, rendering the method suitable for real-time applications or systematic analyses of large infrasound data archives. Our approach prioritizes rapid and efficient computation speed over atmospheric and infrasound propagation realism. We employ a simple Gaussian wind jet profile perturbation parameterization to enhance marginal ducting conditions within reasonable bounds and thus compensate for the missing information on fine-scale atmospheric structure in the empirical climatologies. We evaluate our approach based on infrasound source location case studies for two volcanic eruptions in Chile recorded by the IMS: the 2011 eruption of Puyehue-Cordón Caulle volcanic complex and the 2015 eruption of Calbuco. Overall, we find that our approach using perturbed empirical climatologies provides an improvement in source location compared to having no back-azimuth deviation correction. For the two case studies considered, the results using climatological models compare well with results based on realistic hybrid atmospheric specifications (ECMWF ERA 5 reanalysis below $\sim$ 80 km combined with climatologies for higher altitudes). Thus, a practical workflow for real-time monitoring applications can combine empirical climatologies for rapid first-order source-location estimates, followed later by refined source-location estimates using hybrid atmospheric specifications once available. We emphasize that in this study we used the known volcanic source locations *a priori* to compute the back-azimuth deviations at the stations, with the goal of evaluating the overall approach with climatologies. Extension of the method to a blind search process with a grid of trial source nodes represents future work.

Chapter 3

Evaluating the temporal capability of empirical climatologies for rapid long-range volcanic infrasound propagation estimates using a multi-decadal dataset of persistent Vanuatu volcanic eruptions

This chapter appeared in this for in:

Rodrigo De Negri, Robin S. Matoza, Patrick Hupe, Alexis Le Pichon, Kaelynn M. Rose, S. Cevuard, and J. J. Niroa (2023). Evaluating the temporal capability of empirical climatologies for rapid long-range volcanic infrasound propagation estimates using a multi-decadal dataset of persistent Vanuatu volcanic eruptions Geophysical Journal International. [In submission September 2023]

3.1 Abstract

Aided by atmospheric ducts primarily in the stratosphere and thermosphere, infrasound can propagate thousands of kilometers, allowing detection of activity even from remote (>250 km) volcanoes. The International Monitoring System (IMS) infrasound

network is capable of detecting and monitoring volcanic eruptions around the globe. However, near-real-time monitoring is challenging due to the computationally-heavy processing needed to detect, associate, discriminate, and locate the sources of infrasound. For infrasound source location procedures using triangulation of back-azimuths, crosswinds can result in back-azimuth deviations of over 10°, corresponding to source mislocations of hundreds of kilometers. Here we assess a first-order methodology for the correction of the crosswind induced azimuth deviations that is based on empirical climatologies and 3D ray-tracing and is designed for rapid computation. A multi-decadal 2003–2022 dataset from IMS infrasound station IS22, New Caledonia has recorded persistent volcanic eruption infrasound from Vanuatu volcanoes and provides a test case to evaluate the temporal capability of the methodology at long-range (>400 km) and over a multi-year scale. We show that our rapid methodology based on empirical climatologies provides year-long estimates of the back-azimuth deviation, in first-order agreement with more accurate hybrid atmospheric specification products. Our results indicate that empirical climatologies and 3D ray-tracing are sufficient for first-order estimates of infrasound arrival parameters and should help improve near-real time source-location applications.

3.2 Introduction

Explosive volcanic eruptions are powerful sources of infrasound (acoustic waves <20 Hz), including the most powerful infrasound recorded on Earth (Matoza et al., 2022b; Vergoz et al., 2022). Infrasound from a typical VEI 4 eruption (Matoza et al., 2011a, 2018) can propagate hundreds to thousands of kilometers due to low intrinsic attenuation (Sutherland and Bass, 2004) and the formation of atmospheric ducts. These atmospheric waveguides result from the combination of vertical gradients in horizontal winds and temperature, primarily at stratospheric and thermospheric altitudes (Dabrowa et al.,

2011; Matoza et al., 2019, 2011a, 2018, 2022b; Vergoz et al., 2022; Waxler and Assink, 2019; Le Pichon et al., 2009b).

The International Monitoring System (IMS) of the Comprehensive Nuclear-Test-Ban Treaty Organization (CTBTO) includes a global infrasound network that currently has 53 certified of 60 planned infrasound arrays (Christie and Campus, 2010; Marty, 2019). The IMS, designed to detect explosions with a yield greater than 1 kT TNT equivalent anywhere on Earth (Green and Bowers, 2010; Le Pichon et al., 2009a; Marty, 2019), has recorded numerous eruptions (Campus and Christie, 2010; Matoza et al., 2019; Dabrowa et al., 2011). For example, 68 of 110 volcanic events worldwide (61%) were detected by least one infrasound station from 2002 to 2009 (Dabrowa et al., 2011), when only up to 41 IMS stations were certified (sending data to the IDC), respectively (Headlin et al., 2002; Christie and Campus, 2010; Hupe et al., 2022).

Previous studies have shown that we can use several infrasound arrays to detect, locate, and track the chronology of distant volcanic eruptions, and provide eruption source parameters for ash transport and dispersal models (Caudron et al., 2015; Dabrowa et al., 2011; Fee et al., 2010; Garcés et al., 2008; Green et al., 2013; Marchetti et al., 2013; Matoza et al., 2007, 2018, 2011a,b, 2017; Perttu et al., 2020; Taisne et al., 2019). Although most practical algorithms require detection by at least two or three infrasound arrays (called here a "station") to locate the source (Arrowsmith et al., 2008; Evers and Haak, 2005; Matoza et al., 2017, 2011a; Modrak et al., 2010; Morton and Arrowsmith, 2014), single-station detection (i.e., detection by one array) of volcanic infrasound signals can still provide valuable information on eruption occurrence (De Angelis et al., 2012; De Negri et al., 2022; Fee et al., 2010; Gheri et al., 2023; Marchetti et al., 2019a; Matoza et al., 2019; Morelli et al., 2022; Ortiz et al., 2020). For example, multi-year infrasound observations for a single IMS array (IS27, Antarctica) were attributed to a South Sandwich volcano (most likely Mount Michael) at ∼1,600 km range (De Negri et al., 2022).

The dynamic nature of the atmosphere presents a major challenge for infrasound monitoring. Spatiotemporal variability at all temporal scales, including hourly, daily, and annual seasonal, and at all spatial scales from the microscale to synoptic scale, are variously captured by different atmospheric specification products (Drob et al., 2010a; Schwaiger et al., 2019; Garcés et al., 1998; Smets et al., 2016; Blom et al., 2023; Nippress and Green, 2023). The vector wind fields contain contributions to infrasound waveguides (i.e., along-path winds) but also include cross-path components (cross-winds) leading to observed back-azimuth deviations from the great-circle path connecting the true source and receiver locations (Evers and Haak, 2005; Matoza et al., 2011a; Green et al., 2012; De Negri and Matoza, 2023). These back-azimuth deviations are typically on the order of 5° but can be up to ∼10° (Le Pichon et al., 2005b; Antier et al., 2007; Assink et al., 2014; Morelli et al., 2022), which in turn can result in source mislocations of up to hundreds of kilometers for eruption infrasound recorded at remote distances (>250 km) and located using back-azimuth cross-bearing (i.e., triangulation) methods (De Negri and Matoza, 2023; Matoza et al., 2017, 2018, 2011b).

Morton and Arrowsmith (2014) showed that by combining 3D ray-tracing techniques with realistic atmospheric profiles, look-up tables for celerity (ratio of range over total travel-time) and back-azimuth priors can be produced to describe global seasonal effects that could improve infrasound detection, location and association. A similar approach was used by Drob et al. (2010a), who proposed combining the τp equations (Garcés et al., 1998) and hybrid ground-to-space (G2S) atmospheric descriptions of Drob et al. (2003), to account for hourly, daily, and seasonal changes for real time detection, location, and characterization automated algorithms at the International Data Center (IDC) of the CTBTO.

Building on the previous ideas, Matoza et al. (2018) and De Negri and Matoza (2023) showed that the mislocation of known volcanic sources could be reduced by an order of

magnitude by applying corrections to observed back-azimuths before locating the source with a brute-force, grid-search, cross-bearings method (Matoza et al., 2017). De Negri and Matoza (2023) compared the results of using different atmospheric models in this approach, and found that stochastic models, also known as empirical climatologies (specifically in their study, the Horizontal Wind Model HWM14 (Drob et al., 2015) and the MSIS2.0 model (Emmert et al., 2020)), can perform reasonably well for first-order back-azimuth estimates compared to the more advanced and accurate hybrid models (specifically in their study, the European Centre for Medium-Range Weather Forecasts (ECMWF) reanalysis v5 (ERA5) for the first ∼80 km of the atmosphere merged with the empirical climatologies for higher altitudes). However, the study by De Negri and Matoza (2023) was limited to considering two eruption case studies with data windows lasting on the order of days, representing specific time snapshots of the atmospheric states.

Recently, Blom et al. (2023) introduced a framework to quantify spatial and seasonal trends in atmospheric structure with empirical orthogonal function analysis for each season and location, reducing the atmospheric data into a smaller representative set that can be analysed using numerical tools more efficiently. With that, they could use infrasonic ray tracing and finite frequency modal propagation analyses to construct propagation path geometry and transmission loss statistics for localization and yield estimation of infrasonic sources. Based on a global ground truth event database, Nippress and Green (2023) developed an updated global celerity-range model and introduced a global back-azimuth deviation model, showing that while the variations in celerity are range-dependent, the variations in back-azimuth deviations are not.

Here we further evaluate the utility of empirical climatologies for rapid infrasound calculations. We use a multi-decadal single-station (IMS infrasound array) dataset to investigate the match between ray-tracing predictions and observations of back-azimuth deviations for persistent volcanic signals originating at ranges of about 400 km. Our goal

is to compare the accuracy and limitations of results from rapid calculations based on empirical climatologies with those from more advanced and accurate (and thus computationally expensive) calculations using hybrid specifications over a continuous multi-year time frame. We use a dataset from IMS infrasound array IS22, New Caledonia, which is well-known to record persistent infrasound from volcanoes in the Vanuatu volcanic archipelago (∼400 to 800 km); this well-studied dataset now spans ∼20 years (Antier et al., 2007; Assink et al., 2014; Le Pichon et al., 2005a; Le Pichon et al., 2006; Morelli et al., 2022).

This study is organized as follows. In Section 3.3, we introduce the area of study, highlight the most infrasonically active volcanoes in the region, and present the datasets we use to compare with our models. In Section 3.4, we introduce the methodology and explain the different model types and parameters we use. In Section 3.5 , we summarize the annual back-azimuth prediction results, and compare them with the multi-year dataset. In Section 3.6 we discuss the results. Finally, in section 3.7 we review our findings and establish our conclusions.

3.3 The Vanuatu archipelago volcanic arc

The Vanuatu archipelago (South Pacific Ocean), a product of subduction of the Australian Plate beneath the Pacific plate (Eissen et al., 1991; Simkin and Siebert, 1994), is composed of more than 80 islands oriented northeastward along the South Vanuatu Trench. This active volcanic arc has a rare diversity of eruptive styles, from effusive to highly explosive eruptions, which makes it a valuable laboratory for volcanologists to better understand eruption dynamics (Beaumais et al., 2016; Coppola et al., 2016; Meier et al., 2016; Vergniolle and Métrich, 2016).

Multi-year (2000-2015) remote sensing observations of the Vanuatu archipelago vol-

canoes indicate that Yasur (Tanna island), Lopevi (Lopevi island), Ambrym (Ambrym island), Lombenben (Ambae island, herein referred as Ambae) and Mont Garet (Gaua island, herein referred as Gaua) volcanoes are the most active (Coppola et al., 2016). Dedicated local multi-parameter studies have been performed at several of these volcanoes but with relatively short-duration datasets compared to the long data record from the IMS IS22 station (Maher et al., 2022; Marchetti et al., 2013; Matoza et al., 2022a; Meier et al., 2016; Park et al., 2021; Spina et al., 2016).

3.3.1 An outstanding multi-decadal long-range volcanic infrasound dataset

At ∼400 km southwest of the Vanuatu archipelago, the IMS infrasound station IS22 (Grande Terre island, New Caledonia) has been recording infrasound signals from Vanuatu volcanoes since 2003 (Figure 3.1). The station IS22 (or I22FR) is composed of four microbarometers MB2000 separated by ∼1 km (Figure 3.1, bottom right panel). Each microbarometer has a flat frequency response (within 3dB) between 0.01 and 8 Hz, with noise levels less than 2 mPa between 0.02 to 4 Hz, and a sampling frequency of 20 Hz (Marcillo et al., 2012).

The Progressive Multi-Channel Correlation (PMCC) Method (Cansi, 1995) is used by the International Data Centre (IDC) of the International Monitoring System (IMS) to process the globally collected infrasound waveforms in real time. This time-domain method has proven effective to extract the mean frequency, trace velocity, amplitude, and azimuth of coherent waveforms from signals with a low signal-to-noise ratio. The PMCC method groups similar chronological coherent waveforms across sensors, building detections that allow the reconstruction of single events in time (e.g., eruptions) that have an infrasonic signature that has been affected by atmospheric propagation effects

(e.g., dispersion, attenuation, and scattering).

Among other natural and human-made sources of infrasound (e.g., microbaroms, surf, mining explosions, etc.), the persistent eruptive activity of Yasur volcano (19.532°S, 169.447°E; 361 m summit altitude), Ambrym volcano (16.25°S, 168.12°E; 1334 m summit altitude), and Lopevi volcano (16.507°S, 168.346°E; 1413 m summit altitude) (see Figure 3.1) stand out as near-continuous infrasound waves, with clear PMCC detections at IS22 (∼400 to 700 km) during most of the last ∼20 years (see Figure 3.2). These incessant detections have provided a test-bed for infrasound studies that have compared and evaluated the accuracy of the available stochastic atmospheric models (HWM/MSISE) against novel Numerical Weather Prediction based models (NRL-G2S and ECMWF) (Le Pichon et al., 2005a,b; Drob et al., 2003; Le Pichon et al., 2006; Antier et al., 2007; Assink et al., 2014), used passive atmospheric inversion techniques targeting high-altitude winds (Le Pichon et al., 2005a,b), assessed and proposed optimizations and improvements for the IMS infrasound network with emphasis on remote detection capabilities, and testing new techniques for remote detection of volcanic eruptions (Le Pichon et al., 2010; Le Pichon et al., 2009b; Tailpied et al., 2017; Morelli et al., 2022).

3.3.2 Infrasound detections

3.3.2.0.1 Considered data The first comprehensive systematic broadband (0.01-5 Hz) analysis of historical IMS infrasound data using PMCC with 15 logarithmically-spaced frequency bands was conducted by Matoza et al. (2013). Recently, Hupe et al. (2022) used a 26-band PMCC configuration to reprocess the available dataset (2003-2020), and introduced four open-access data products that are updated regularly (currently covering 2003-2022). These novel data products represent a summarized version of all the IMS infrasound PMCC detections in different frequency bands with additional

data quality parameters. As previously shown (Antier et al., 2007; Assink et al., 2014; Le Pichon et al., 2005a; Morelli et al., 2022), we expect most of the infrasound at IS22 from Lopevi/Ambrym and Yasur volcanoes to be centered at ∼1 Hz and ∼2 Hz, respectively. Therefore, in this study, we select the "high-frequency" (1-3 Hz) products (Hupe et al., 2021b) (Figure 3.2).

Additionally, we consider 26-band PMCC bulletin files covering 2003 to 2022 (Hupe et al., 2022), and 15-band PMCC bulletin files from 2003 to 2017 (Ceranna et al., 2019; Matoza et al., 2013) in the the Supplementary Information of this paper (Figures B.1,B.2,B.3)

3.3.2.0.2 Regional winds and detectability The regional stratospheric winds oscillate from prevalent west to east directions in intervals of about six months per year, with eastward winds from April to September and westward winds from October to March, (e.g., Figures 3.3a,b,c). This oscillatory behavior has a stronger, more stable component during westward zonal winds, whereas the eastward ducts tend to be interrupted by short time scale wind reversals such as Sudden Stratospheric Warmings (SSW) (Figure 3.3d on July; see Assink et al. (2014)), and show generally weaker stratospheric winds. Transition periods (seasonal equinoxes) between both wind regimes usually do not sustain ducts, and occur between the two wind regimes (e.g., April and November in Figures 3.3d,e,f).

The westward zonal winds, produce an increased detectability of sources at the east of IS22 (i.e., Vanuatu volcanoes), as ducts at ∼50 km altitude appear (e.g., mid-November to March in Figures 3.3d,e,f for 2019). The contrary is expected during predominant eastward winds, with low to almost no detectability from the Vanuatu volcanoes at IS22. For volcanoes predominantly at North/South azimuths from IS22 (i.e., Ambrym/Lopevi/Gaua/Ambae), the stratospheric ducts should be practically non-existent,

but the zonal winds should cause the highest azimuth deviations. During seasonal equinox transition wind regime periods (e.g., April and November in Figures 3.3d,e,f), the thermosphere provides the primary duct (Figures 3.3d,e,f, near 120 km altitude).

3.3.2.0.3 Observations From 2003 to 2022, the bulk of the infrasound detections oscillate around Yasur (∼43°) and Ambrym/Lopevi (∼13°) volcano azimuths (Figures 3.2a,b,c). Other sources of infrasound in this frequency range are mainly surf (April to October each year, from ∼225 to ∼270°), and human-made infrasound, possibly from mining activity (e.g., narrow azimuth band at ∼135° across most years in Figure 3.2a). The distribution of Yasur detections by azimuth over time appears to have a "bottom-half sinusoid" shape with a minimum centered at the transition between the end of each year and start of the next (Figure 3.2b). Ambrym/Lopevi detections seem to be sparser through the years, indicating less continuous explosive volcanic activity than Yasur (Figures 3.2a,c). During years with higher concentrations of detections at Ambrym/Lopevi azimuths (e.g., 2004-2008; Figure 3.2c), their distribution resembles a sinusoidal curve with azimuth values reaching a minimum in apparent phase with Yasur detections (in between years). This is in agreement with the expected effects of the seasonal regional wind patterns, with stratospheric zonal winds that sustain a westward duct centered in summer months (December-February) and a reversed eastward duct centered in winter months (June-August) (e.g., see Figure 3.3).

The observed periods of activity by the Vanuatu Meteorology and Geo-hazards Department (VMGD) (Figures 3.2b,c in gray vertical lines and shaded areas; also by relative Real-time Seismic Amplitude Measurement (RSMA) from a couple of available stations near the volcano in 3.2c) indicate partial agreement with the persistent infrasound detections. This mismatch is expected from different detection technologies (seismic sensors vs. infrasound arrays) and rather enhances the infrasonic observations (De Negri et al.,

2022). Interestingly, in the case of the Lopevi, Ambrym, Ambae and Gaua volcanoes (Figure 3.2c), grouped at azimuths between 4.7° and 14.3° and distances from ∼877 and ∼647 km, there is a clear superposition of potential periods of activity that skews the overall expected observed sinusoidal behavior from Ambrym/Lopevi directions. In particular, during 2010, a numerous group of detections appears near Gaua volcano azimuth, which can be linked with a long eruptive period that occurred from September 2009 to July 2010 (Bani et al., 2016, also observed by the VMGD). This group, in addition to smaller numbers of infrasound detections from the Gaua and Ambae azimuth through the years, forms a cumulative effect that marks a secondary azimuthal direction (see Figure 3.2d,f).

The seasonal effects and yearly behavior of this dataset become apparent when the detections are viewed by the day of year. This trivial reordering of the displayed detections, should ensure that yearly repetitive detections occurring at the same location (e.g., a continuous volcanic source) stack into larger numbers at their respective back-azimuths, compared with transient groups (e.g., sporadic volcanic eruptive periods separated by several years). Hence, the effect of the seasonal, first-order atmospheric variability on the back-azimuth of these repetitive signals should be present in our models. (Figures 3.2d,e,f). The bulk of the detections arriving from the approximate back-azimuth of Yasur occur between October and March (days ∼280 to 365, and 1 to ∼100). Relatively large groups of detections also appear sporadically between May and August with azimuth deviations ranging from ∼-4 to +6° (Figure 3.2d; zoom in Figure 3.2e). These detections are likely produced by transient stratospheric ducts which are not seasonal and have been linked with Sudden Stratospheric Warming (SSW) events in the region (Assink et al., 2014). Overall, this creates a "capped arc" shape of detections around Yasur's back-azimuth, with minimum values by the end of December and start of January; transition periods from below-zero to near-zero and vice-versa back-azimuths from March

to April and from October to November, respectively; low detection periods centered on May and September; and sporadic maximums and below-zero groups through June to August (Figure 3.2e).

The detections around the back-azimuths of Ambrym/Lopevi sorted by day of year (Figure 3.2f), range from ∼-10° to ∼8°, a clear increase from Yasur's case (∼-4 to +6°). This is likely related to the North-to-South direction from Ambrym/Lopevi to IS22, intensifying the crosswind effects of the zonal winds on the propagating signals. Most of the detections are now present during transition wind regimes (March-April; August-October) indicating that is a thermospheric duct which likely allows infrasound waves to travel from the direction of Ambrym/Lopevi during periods of weakened stratospheric winds (e.g., see Figure 3.3d,e,f). The primary cause of the observed deviation in azimuth can be attributed to the crosswinds caused by the zonal wind (E-W) component at stratospheric heights (e.g., see Figures 3.3d,e,f), with similar effects to the case of Yasur, but impeding the formation of ducts during the strongest periods of westward winds (November to February). From January to the first week of May, and July to November, the detections resemble the sides of the "arc" of detections with steeper slopes than previously seen around Yasur's azimuth. Some groups of detections also appear from June to August, with back-azimuths that decouple from the variations (slopes) seen on the transition months, and almost random azimuth variations. A "secondary arc" underneath the Ambrym/Lopevi back-azimuths appears mainly in April, and August to September. These detections have a similar back-azimuth variation to the ones attributed to Ambrym/Lopevi, and could represent eruptions from Gaua/Ambae from 2003 to 2022. This group of detections consistently arrives ∼3 to 5° under the Ambrym/Lopevi detections (Figure 3.2f).

At the start of 2018, we observe two groups of detections spanning ∼10 to 45° that appear to be artifacts (Figure 3.2a; also Figure 3.2b at the end of January, February,

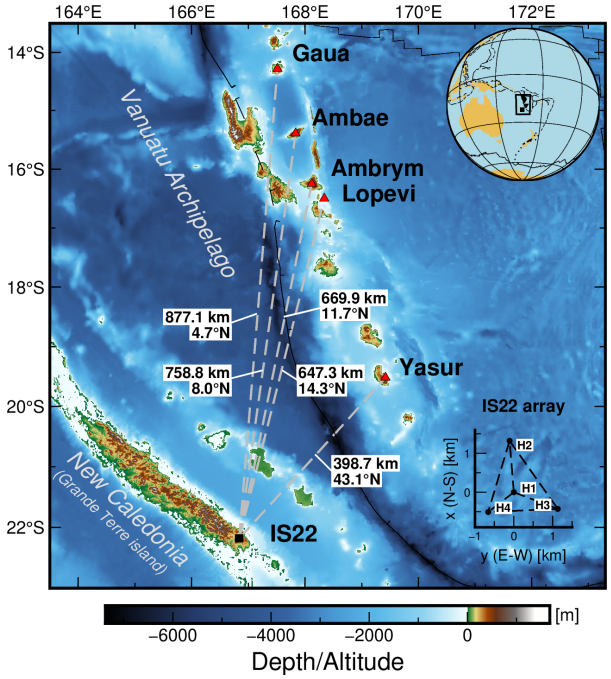

Figure 3.1: Study region (see box in upper right inset), comprising the Vanuatu archipelago and the main island of New Caledonia (Grande Terre). Black square: location of IS22, New Caledonia. Red triangles: location of the most active volcanoes; names on right. Gray dashed lines: great-circle distances and azimuths from IS22 to each volcano (annotated). Lower-right: IS22 array geometry in Cartesian coordinates [km].

and the start of March). These groups of detections are also present in the 26-band PMCC dataset during the same time window (Figure B.2), and were likely produced by temporary station issues, possibly due to a malfunction of one of the sensors. The dataset also shows the formation of azimuthal bands of detections at ∼1.25 Hz steps around Yasur's back-azimuth (Figures 3.2b and 3.2e) that appear to be artifacts. They are present in the 26-band PMCC data (Figures B.2b,e) but not the 15-band PMCC data (Figures B.3b,e) and are likely a processing artifact effect of the 26-band configuration.

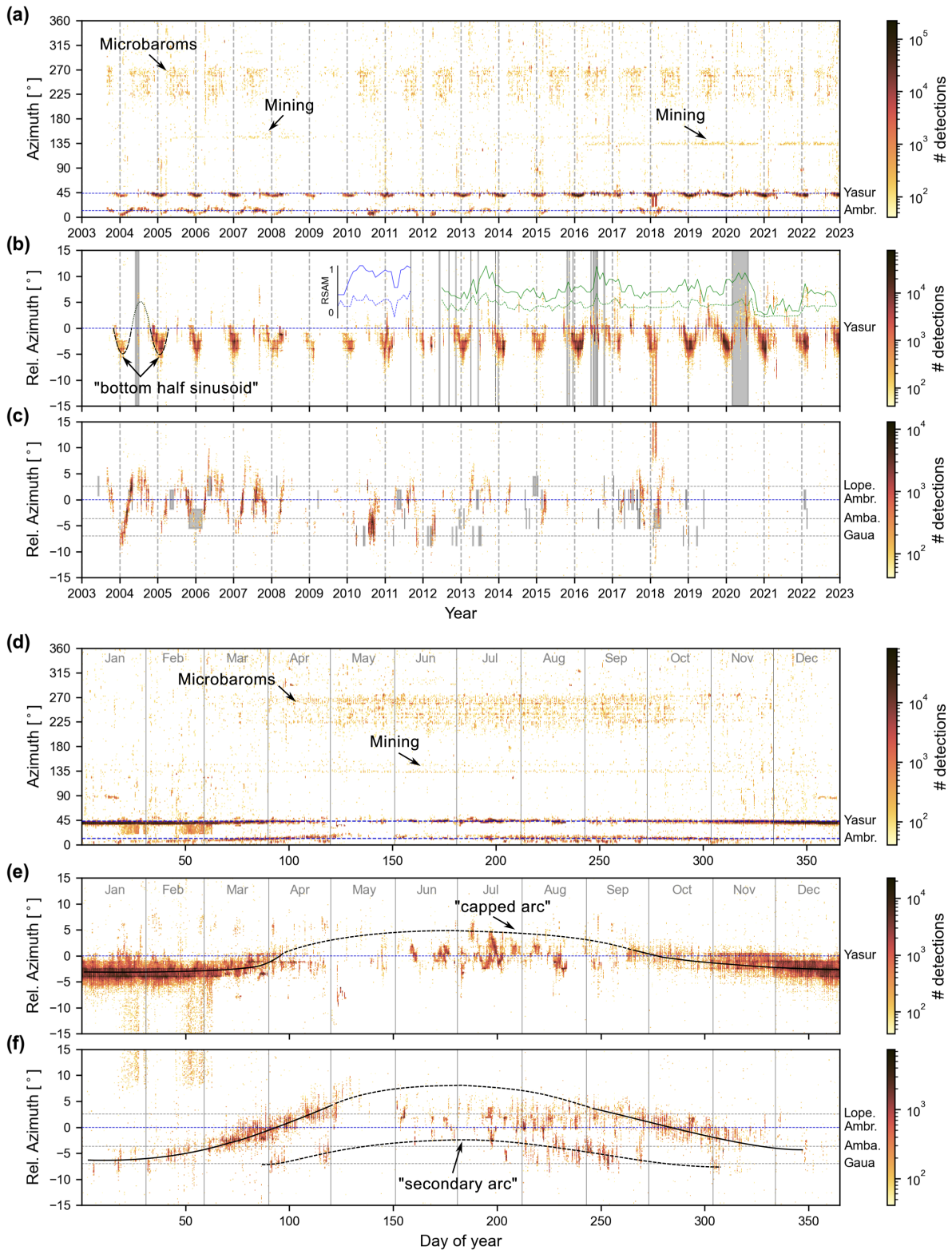

Figure 3.2: Infrasound detections at IS22 from mid-2003 through 2022 (Hupe et al., 2022). (Caption continues on next page) 58

Figure 3.2: (From previous page) (a) 2D color-shaded histogram of detections by year (x-axis) vs. azimuth (y-axis), colored by the number of detections in each bin. Each 2D bin is 277.4 hours (∼12 days) wide and 1.8° high. Horizontal dashed blue lines and annotations indicate the back-azimuths from IS22 to Yasur and Ambrym volcanoes. (b) and (c) Zooms around Yasur (43.1°), and Ambrym (11.7°) azimuths, respectively; an insert in (b) shows the minimum (dashed) and maximum (continuous line) relative values of the Real-time Seismic Amplitude Measurement (RSAM) from the Vanuatu Meteorology and Geo-hazards Deparment stations, YAS (blue) and YASH (green); dashed gray lines in (c) depict relative azimuths of Lopevi, Ambae, and Gaua volcanoes with respect to Ambrym. In (c) and (d), the active periods of each volcano (Vanuatu Meteorology and Geo-hazards Department observations) are shown as solid gray vertical lines (single day event) and solid gray shaded areas (multi-day event). (d) similar to (a), but the data for all years are collapsed and folded into a single year and plotted by day-of-year. In (d), the bin size is 14.6 hours wide by 1.8° high. (e) and (f) are zooms around the average azimuths of Yasur and Ambrym, respectively; bin size is 14.6 hours wide by 0.3° high. For a version without the interpretative labels, see Figure B.13

3.4 Annual back-azimuth deviation estimates comparing climatology and hybrid models

3.4.1 Methodology

We use the methodology introduced by De Negri and Matoza (2023) (see the "ARCADE" open-source repository link in Acknowledgments), to simulate the observed detections at IS22 from the two main sources of infrasound in the Vanuatu archipelago (i.e., from the locations of Yasur and Ambrym volcanoes).

This procedure automatically searches iteratively for arrivals at predefined receiver locations (stations) coming from an arbitrary number of source locations (volcanoes), at previously specified dates and times. By default, it couples empirical climatologies (HWM/MSIS) (Drob et al., 2015; Emmert et al., 2020) and models infrasound propagation with 3D ray tracing (infraGA) (Blom, 2020; Blom and Waxler, 2012, 2017). The empirical climatologies are stochastic models based on interpolations of historical data

collections, which are improved over time as new global datasets are gathered. In this sense, they are robust atmospheric descriptions, but smooth out smaller scale changes in time and space which are especially important in the lower parts of the atmosphere (troposphere and stratosphere) (Drob et al., 2003, 2010a; Drob, 2019). This methodology of De Negri and Matoza (2023) also allows the use of more accurate atmospheric specifications, employing a hybrid model that merges the European Centre for Medium-Range Weather Forecasts reanalysis v5 (ECMWF ERA 5, or ERA 5 for simplicity) descriptions (horizontal winds, pressure, and temperature) below ∼78 km altitude, with pure (raw) empirical climatologies at higher altitudes. The ERA 5 reanalysis models, available from 1959 to the latest processed forecast model, describe the lower atmosphere in greater detail than the climatologies, with forecasts that are dependent on the year and date-time, with a minimum time step of one hour and a minimum spatial step of 31 km (Bell et al., 2021).

Additionally, the atmospheric models can be discretized as range-independent (layered spherical) or range-dependent (specifications by height on a 3D grid for the area). Instead of requiring multiple statistical realizations to account for arrivals produced by fine-scale structure or gravity wave effects (Assink et al., 2014; Smets et al., 2016), the range-independent atmospheric models can be perturbed to favor stratospheric ducts by adding a Gaussian wind jet (Jones, 1986) around 40 km altitude (see Figure 3.4), with an amplitude of 30% of the wind component in the along-path direction from the source to the receiver, for altitudes from 20 to 50 km (De Negri and Matoza, 2023).

3.4.2 Propagation models

We produce year-long infrasound propagation models corresponding to the year 2004 for Ambrym volcano and 2019 for Yasur volcano. These years are particularly complete in

the dataset for each volcano (Figure 3.2; also B.2), which helps provide a good reference to assess the accuracy of the models.

We calculate five different models per volcano and year: range-independent with raw climatologies, range-independent with perturbed climatologies, range-independent with hybrid model, range-dependent with raw climatologies, and range-dependent with hybrid model. For each case, we search for ground intercepts inside an area around ∼5 km distance from IS22 for rays launched at 00:00:00 UTC, 00:06:00 UTC, 00:12:00 UTC, and 00:18:00 UTC every day of 2004 (Ambrym) or 2019 (Yasur). We include arrivals with stratospheric (∼40 km) and/or thermospheric (∼120 km) turning heights in the search process. Finally, we use the resulting back-azimuth deviation estimates to calculate year-long interpolations and compare them with the observations (Figures 3.5 and 3.6).

3.5 Results

3.5.1 Year-long back-azimuth estimates

We summarize the six-hour interval, year-long back-azimuth deviation estimation results for Ambrym (2004) and Yasur (2019) in Figures 3.5 and 3.6, respectively. We use the daily average of the obtained azimuth deviations (up to four), to calculate a B-spline 1-D interpolated curve with a smoothing factor of 10 for the climatology-based models, and 50 for the hybrid-based models (blue line in Figures 3.5 and 3.6). We also we also calculate the daily standard deviation to observe the spread of the difference values by time of day throughout the year (right panels of Figures 3.5 and 3.6).

3.5.1.0.1 Missing predictions The range-dependent, raw climatology model for Ambrym volcano was the only model that completely failed to predict ground intercepts

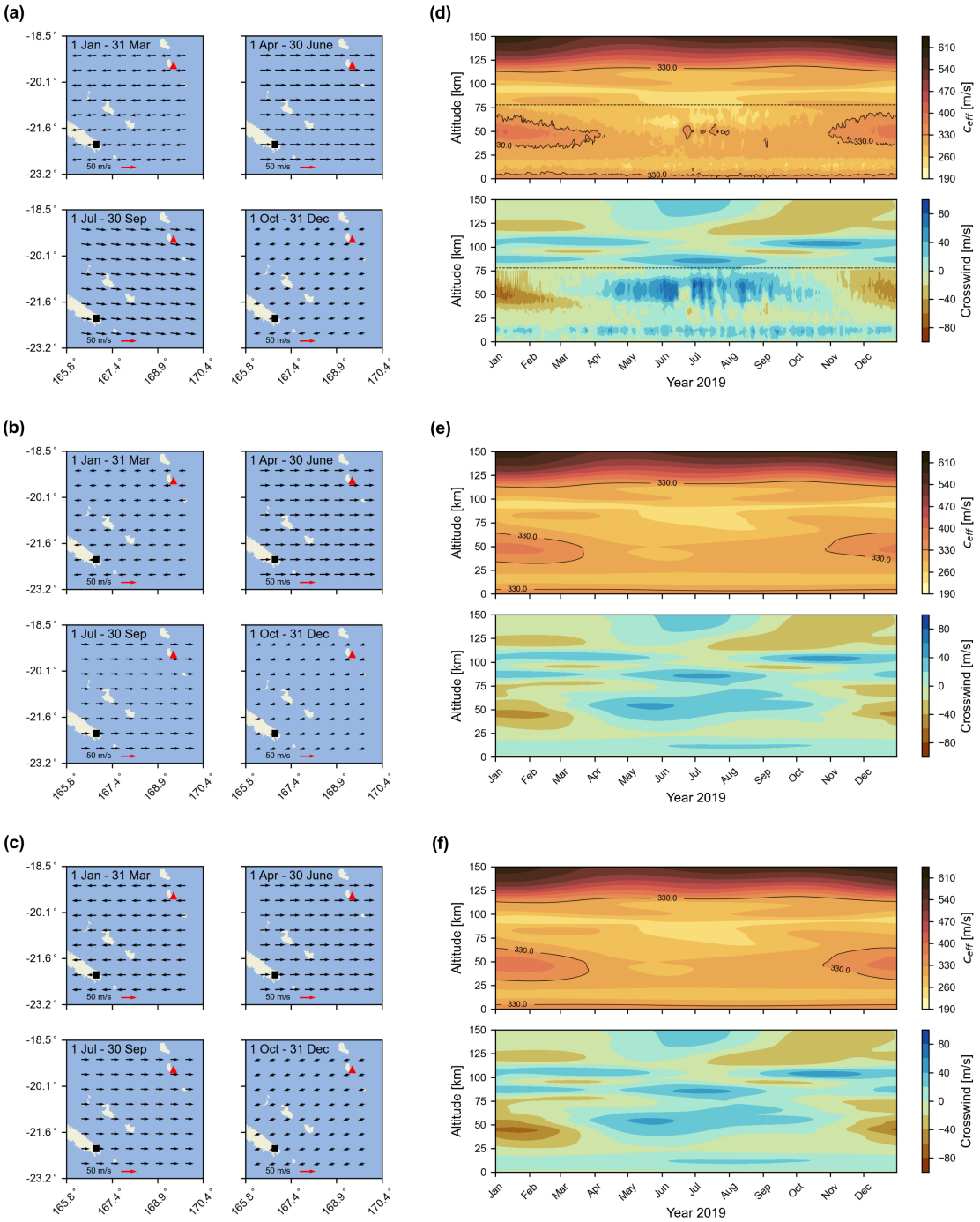

Figure 3.3: Seasonal atmospheric conditions at 00:00:00 UTC from 1 January 2019 to 31 December 2019. (a) and (d) Captured by a hybrid model combining ECMWF ERA 5 atmospheric specifications below ∼80 km with HMW14/MSIS2.0 from ∼ 80 to 140 km. (Continues on next page)

Figure 3.3: (From previous page) (b) and (e) Captured only by the empirical climatologies (HWM14/MSIS2.0). (c) and (f) Captured by the empirical climatologies with a Gaussian enhancement of 30% (i.e, "perturbed") in the along-path winds centered at 40 km. (a), (b), and (c) Average horizontal wind vectors for each set of atmospheric descriptions from 40 to 70 km for four characteristic times of year: 1 January to 31 March (upper left), 1 April to 30 June (upper right), 1 July to 30 September (lower left), and 1 October to 31 December (lower right). In each case, a red arrow indicates a scale of 50 m/s (all panels have same scale for vector lengths). Black square: IS22; red triangle: Yasur. (d), (e), and (f) Average along-path effective sound speed (top) and crosswinds (bottom) for each set of atmospheric descriptions as a function of altitude (0 to 150 km) from Yasur to IS22 during 2019.

(arrivals) near IS22. This could indicate an unstable propagation model, where the ray propagation becomes too sensitive to small changes in the launching parameters, and should be clarified in the future.

During days ∼120 to ∼180, the range-independent, perturbed climatologies model for Yasur, and part of the Ambrym analogous model (only at 12:00:00 UTC), failed to predict arrivals to calculate the back-azimuth deviation estimates. This seems to be a consequence of the enhancement of the stratospheric winds at ∼40 km, which produce unstable atmospheric condition for infrasound to reach the thermospheric duct (∼110 km altitude). Despite this issue, the interpolated curve alleviates the lack of predictions during this time window, giving comparable estimates to the rest of the models (Figures 3.5,3.6).

3.5.1.0.2 Diurnal variation All models present a similar semi-diurnal oscillatory back-azimuth peak behavior. From October to April (day of year ∼300 to end of year, and 1 to ∼100), the biggest negative deviations are at 12 h UTC and 0 h UTC; the smallest negative deviations at 6 h UTC and 18 h UTC. This behavior is less clear for positive deviations (day ∼100 to 300), but has a similar pattern. The biggest positive deviations are at 0 h and 12 h UTC, while the smallest positive deviations are at 6 h and 18 h UTC. The semi-diurnal effect is generally less prevalent for the hybrid model,

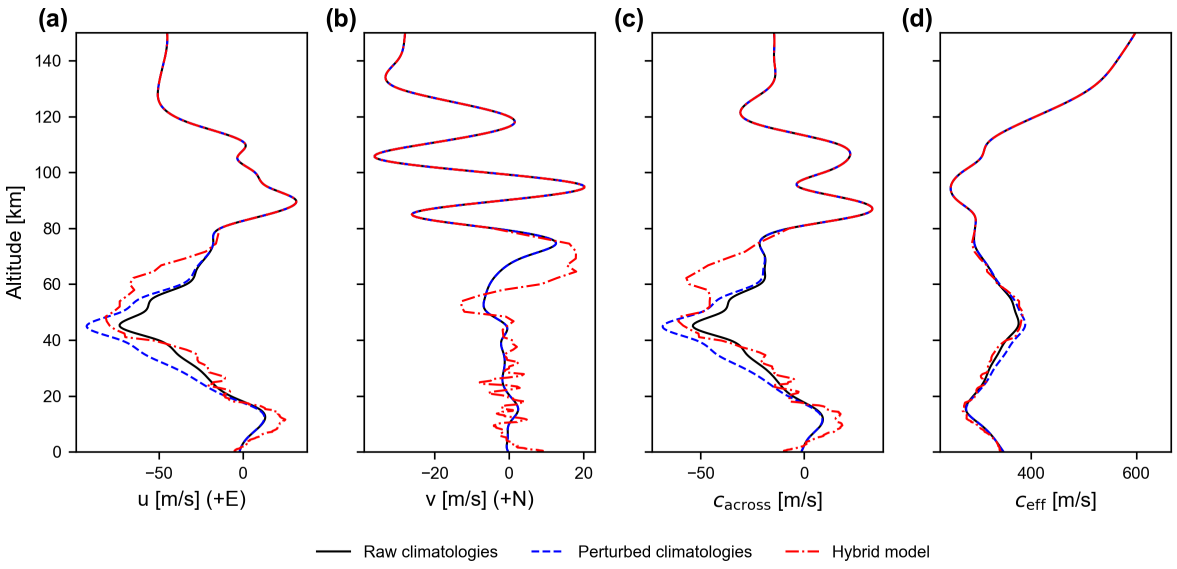

Figure 3.4: Example of horizontal winds in altitude for 15 January 2019 at 00:00:00 UTC as curves with average values from Yasur to IS22 (x-axis) in steps of 0.5 km altitude (y-axis), calculated with climatologies (black line), perturbed climatologies (blue dashed line), and the hybrid model (red point-dashed line) descriptions. (a) Zonal winds (positive towards the east). (b) Meridional winds (positive towards the north). (c) Crosswinds (positive towards north-east). (d) Effective sound speed considering the along-path winds and temperature in altitude.

which adds considerable variability to the seemingly continuous (first-order) effect of the empirical climatologies.

The back-azimuth estimations can have differences from less than a degree up to ∼5° per day. To assess the general diurnal variability of each model, we calculate the standard deviation per day, when four estimates are present (right side panel of each subplot in Figures 3.5,3.6). The climatology-based models show arrivals with diurnal standard deviations above 1° during the strongest zonal winds (westwards; day ∼300 to 365, and 1 to ∼80; Figure 3.5,3.6), down to less than 0.5° during weaker zonal wind conditions. The spreads follow a pattern that is seasonal. The hybrid-based results have a less smooth pattern, but still show variations above 1° concentrated at the first and last months of the year. The range-dependent, hybrid models resemble the range-independent ones, but with slightly less variability per day.

Using the daily standard deviation for each model, we calculate the corresponding average standard deviation per year and the standard deviation of this average. For the Ambrym case, the average standard deviations per year are ∼0.8±0.3° for all but the range-dependent, hybrid model, which is ∼0.6±0.3°. For Yasur volcano, on the other hand, the average standard deviation is ∼0.6±0.3° for all models except for the range-dependent, perturbed climatologies with ∼0.5±0.3° (Figure 3.7).

3.5.1.0.3 Seasonal variation Both models reflect the regional wind patterns previously described (Section 3.3.2.0.2). From October to the first week of April (from day of year ∼300 to 365, and 1 to ∼100) predominant westward zonal winds produce negative back-azimuth deviations that peak by the December and January. From May to August (day of year ∼120 to ∼240), eastward zonal winds tend to produce positive back-azimuth deviations that peak between May and July (days ∼150 to ∼200) (Figures 3.5,3.6). The empirical climatologies appear almost continuous throughout the year,

with smooth changes over time that resemble sinusoidal (seasonal) changes. The hybrid models present a complex behavior that contrasts the raw climatologies, with local peaks that fall on the previously described time windows, but seemingly random variations that do not follow seasonal trends. These second-order effects are dominant during summer months, including complete inversions of the general tendency of increasing positive back-azimuth deviations. Interestingly, for both the years 2004 and 2019, similar reversals in azimuth deviation occur around day ∼170.

The back-azimuth deviation values vary depending on the propagation direction of the infrasound signals. For Yasur volcano (southwest propagation), the empirical climatologies show deviations that have maximum values of ∼-5/+2.5°, while the hybrid models have maximum values of ∼-5/+5° (reversals; Figure 3.5). For Ambrym volcano (south propagation), a similar asymmetry is present for the empirical climatologies, but the maximum deviation values are ∼-7/+4°, while the hybrid models predict extremes of ∼-5/+6° (Figure 3.6).

3.5.2 Comparison with year-long and multi-year datasets

3.5.2.0.1 Data reduction We compare observations (infrasound array detections) and modeled ray arrivals at IS22 based on overall average behavior of the volcanic-related detections. To do so, we first select the high-frequency products (Hupe et al., 2021b) that have a quality parameter $Q > 0.4$ (Hupe et al., 2022), and a mean family size above 10. Next, we consider only the detections inside the back-azimuth range of ±10° around the true direction of each volcano. Later, we average the detections inside a 90% confidence interval around the mean in 7-day correlative time windows. We then compare the 7-day 90% confidence averaged detections with the model interpolations previously presented (Figures 3.5 and 3.6) and calculate summary statistics. To ensure

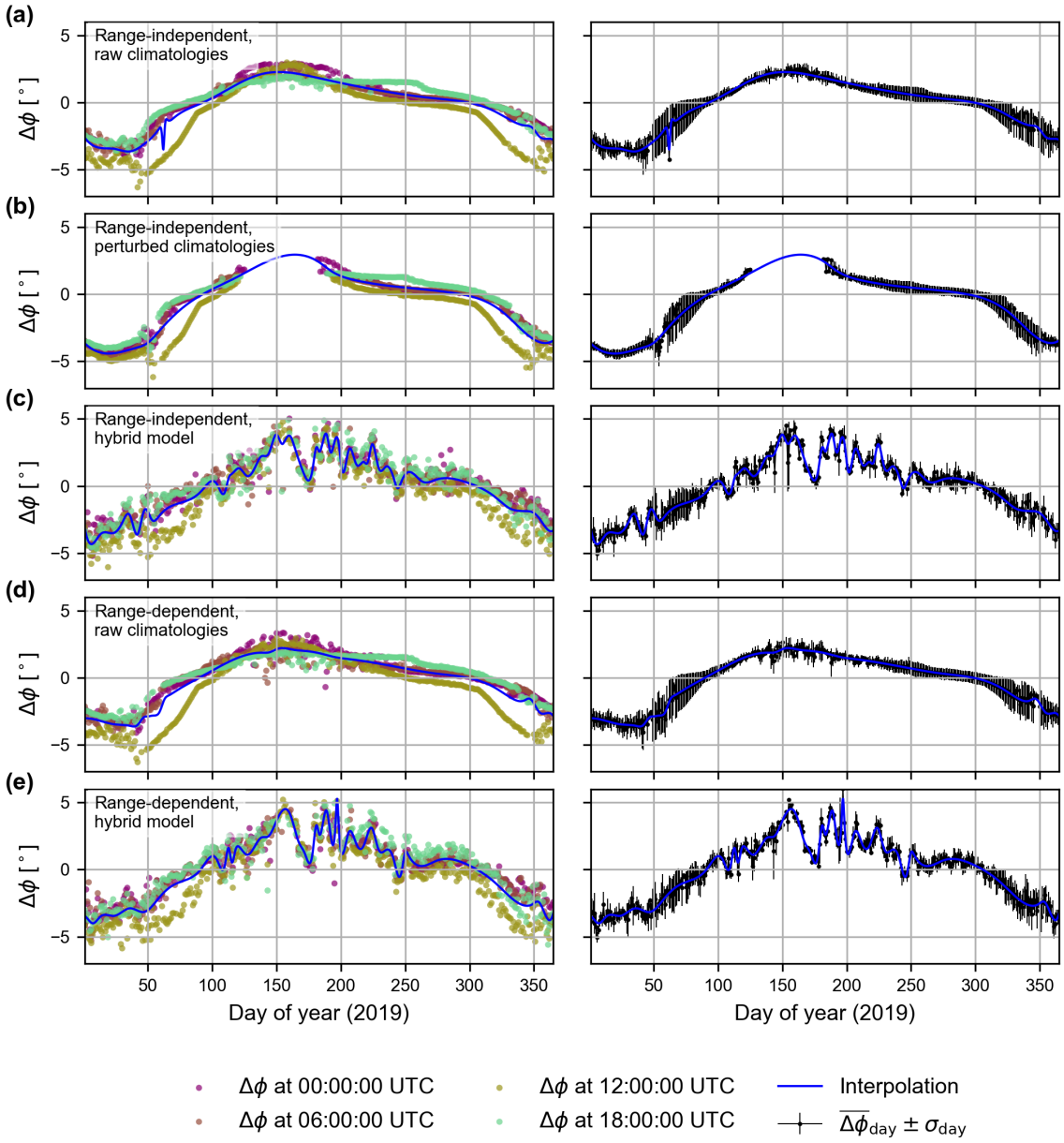

Figure 3.5: Comparison of 3D ray-tracing (Blom and Waxler, 2012) results for infrasound propagation from Yasur to IS22 during year 2019. For each 6-hour time snapshot, we plot the average azimuth deviation of predicted arrivals falling within a distance of 5.5 km from IS22 relative to Yasur's azimuth (∼43.1°). (a) to (e) Results calculated for five different model types indicated in the annotations. The calculations are performed at six-hour time-snapshots (colored points in left panels); an interpolated average of these results is indicated by a blue line. In the right-hand panels, the interpolated average (blue line) is plotted again along with the averaged daily values $\overline{\Delta\phi}_{\text{day}}$ displayed as black dots with their daily standard deviation σ_{day} indicated by a vertical thin black bar.

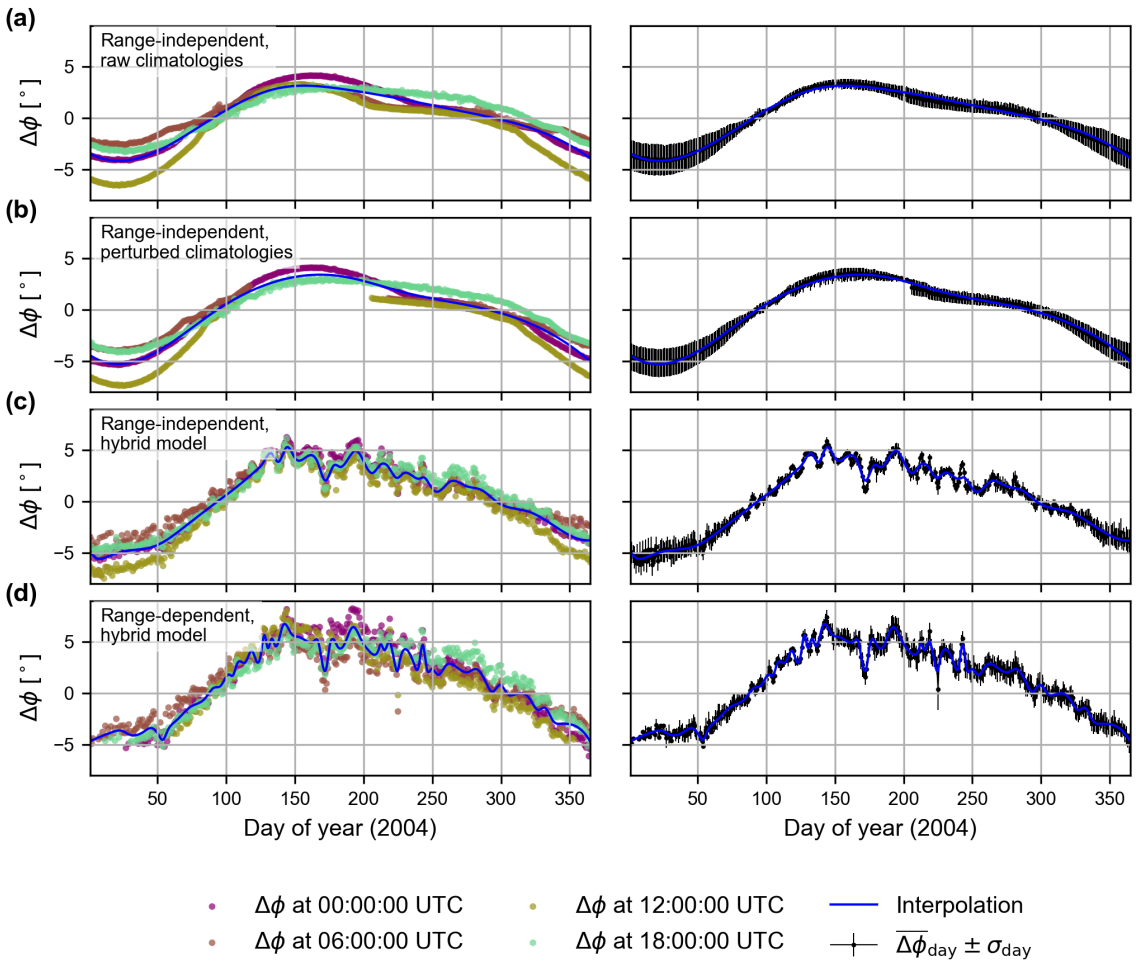

Figure 3.6: Similar to Figure 3.5, but results for 3D ray-tracing from Ambrym volcano to IS22 during 2004. In this case, the range-dependent raw-climatologies do not predict arrivals within our criteria (within 5.5 km from IS22) and we do not show these results.

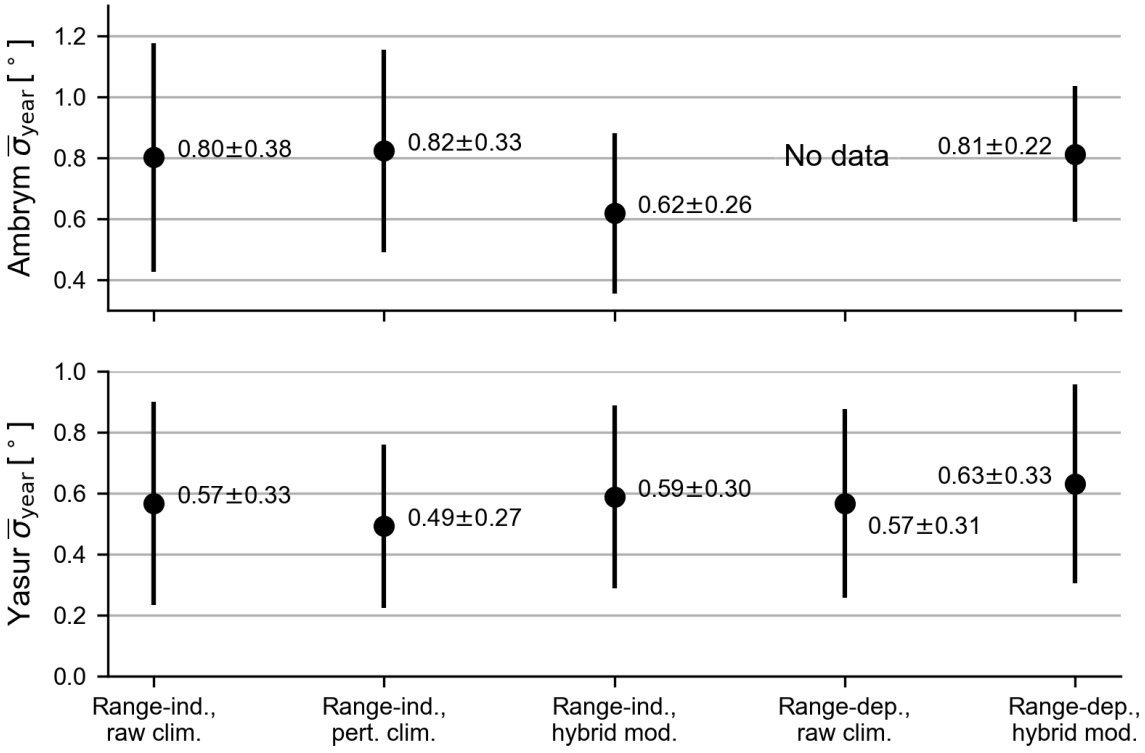

Figure 3.7: Mean yearly standard deviations $\overline{\sigma}_{\text{year}}$ based on 2004 for Ambrym (top) and 2019 for Yasur (bottom) (Figures 3.5 and 3.6). Vertical bars show the standard deviation. Only days with predicted arrivals at all four time snapshots of the day (i.e., at 00:00:00, 06:00:00, 12:00:00, and 18:00:00 UTC) were used to estimate the means.

our results are representative across datasets, we apply the same reduction techniques to the additional 15-band and 26-band PMCC detections as well (see Figures B.7,B.8,B.9)

3.5.2.0.2 Ambrym/Lopevi 2004 and Yasur 2019 We compare the back-azimuth interpolated model results for Ambrym (2004) and Yasur (2019) (blue lines in Figures 3.5 and 3.6) with their reduced detections (see 3.5.2.0.1) as 2D histograms (Figure 3.8, left panels), and the 7-day 90% confidence averaged detections (Figure 3.8, right panels).

Ambrym's detections (Figure 3.8a, left) have an azimuth deviation tendency with high negative deviations ($\sim$-7.5°) at the start of the year, increasing up to $\sim$5° towards the middle (day $\sim$150), an effect that is present in all models from days $\sim$40 to 120. Detections that do not follow the model predictions, possibly produced by Gaua/Ambae volcanoes (see 3.3.2.0.3), are present mostly after this period, until day $\sim$250. Some numerous but transient detections which fall into the modeled back-azimuths of the empirical climatologies ($\sim$0.8$\pm$0.4°), are predicted by the hybrid models with much better accuracy (e.g., day $\sim$180. The 7-day averages (Figure 3.8a, right) give us a clearer picture of the weekly tendencies of the reduced detections. The outlier 7-day averages have a higher frequency content. The high variability of the detection groups better matches the hybrid predictions, falling outside the models that use empirical climatologies, but following their patterns through the year. The match between the observations and the modeled results is again especially good from days $\sim$40 to 120 for all models, both following a similar rate of back-azimuth change in time. The actual azimuth deviation values are underestimated in the beginning and end of the $\sim$40-120 day of year period, but are better represented by the hybrid models in the latter.

Yasur's 2019 case shows considerably more detections in the first 100 days (January-March) and last $\sim$70 days (November-December) (Figure 3.8b, left), when a strong westward stratospheric duct is present (Figure 3.3). The 7-day averaged detections have

higher frequencies (∼1-2 Hz), especially during the periods of time where the westward stratospheric duct appears. The models predict the 7-day averaged detections with good agreement in the same period (January-March; November-December), with the exception of the range-independent, perturbed climatologies, which overestimates them. This is an expected effect which is also present during the eastward duct (days ∼120-200), as the ducts are enhanced to compensate for assumed under-predicted climatologic descriptions. Several 7-day averaged detections that are clearly outliers for the empirical models are predicted by the hybrid models (e.g., day of year ∼180, with ∼1.8 Hz, and azimuth deviation of ∼0°). Most of these outliers appear during weaker duct conditions (days 120 to 250). For the days ∼250 to 320, the 7-day averaged detections are under-predicted by all the models, but well described in terms of the rate of change of the deviations. The hybrid models generally perform better during periods of time when weaker ducts are present.

3.5.2.0.3 Ambrym/Lopevi and Yasur multi-year (2003-2022) comparison When plotting the whole datasets by day of year (i.e., stacking) (Figures 3.9; also Figures B.8,B.9), we observe that the 7-day averaged detections now clearly contain frequencies near ∼1 Hz for Ambrym/Lopevi, and frequencies near ∼2 Hz for Yasur.

The artifact linear-like clusters of detections (see 3.3.2.0.3) appear in steps of ∼1.25° around Yasur's back-azimuth, which could skew the overall statistics for this group (Figure 3.9b). Nevertheless, the general distribution of the stacked detections remains well represented when compared with the 15-band dataset, which does not contain this apparent artifact (Figure B.9).

In this multiyear dataset, the second-order variations in the results of the hybrid models will not be representative due to their temporal dependency on their specific year. However, these results should keep the expected first-order seasonal behavior that

is captured by the empirical climatologies. Generally, the periods from day of year 1 to ∼100, and ∼250 to 365 have most of the detections that resemble the predicted arrivals at IS22.

The models for Ambrym tend to under-predict the high deviations at the start of the year. The hybrid models better represent the positive deviations near day 100-120, which the climatologies predicted to be declining. Between day ∼120 and ∼250, the possible Gaua/Ambae group of 7-day averaged detections (see 3.3.2.0.3) appears under Ambrym's modeled deviations (Figure 3.9a) from ∼2.5° to -5.0°, and contains higher frequencies than the rest (∼1.6-2.2 Hz). These detections are the effect of superimposing transient events from 2003 to 2022 as previously observed (Figure 3.9a, left).

For the Yasur case, most of the detections are grouped during the observed days of favorable ducts that occur during 2019 (∼300 to 365, 1 to 120; Figure 3.8b). The artifacts affect the 7-day average values by "flattening" the azimuth deviation changes, although still preserving the overall variation (see Figure B.9). The unfavorable duct periods observed in 2019 (days ∼120 to ∼300) coincide with the occurrence of sporadic outlier detections for the multi-year dataset. Several of these events show negative deviations, from 0 to -2.5°, and occur near days 180-220. During days ∼280 to ∼320 and days ∼80 to ∼100, groups of less numerous, lower frequency detections (∼1.4-1.8 Hz) transition towards more numerous, higher-frequency groups.

3.5.2.0.4 Error estimation The models are qualitatively comparable with the reduced data (Figures 3.8,3.9). For a more quantitative comparison on a per month, and per year basis, we start by averaging the modeled back-azimuth deviations in 7-day time intervals. We use these values to calculate the differences between the predicted 7-day azimuths and the data as 7-day 90% confidence interval from the mean. Next, we calculate the Euclidean distances between the two sets of 7-day values and obtain 28-day

averages that better represent the variation of the monthly differences (Figure 3.10). Finally, we calculate the year-long Euclidean distances by averaging the 28-day values for each model (Figures B.10,B.11,B.12)

For 2004, Ambrym maximum 28-day averaged differences shows peaks near the beginning, middle, and end of the year at ∼3-4° (Figure 3.10a). The lowest differences occur most consistently during days ∼50 to 180 (<1°), with other similar 28-day low values occurring from days ∼250 to 330 for most of the models. The range-dependent, hybrid model is the most affected by the apparent outliers in the middle of the year, accumulating the largest differences overall, with a yearly average difference of 1.59±1° (Figure B.10). The best-performing model is the range-independent, perturbed climatologies model, with a 0.94±0.89° year average difference from the data. Most of the models have similar average differences for 2004, around ∼1° with a ∼1° standard deviation, except for the hybrid model, which sits at 1.59°.

For 2019, Yasur 28-day averaged differences are more consistent throughout the year (Figure 3.10b). In all models, there is a peak centered at day ∼150 that is both preceded and followed by an under ∼1° plateau. All models have relatively similar averaged differences, from 0.6 to 0.74°, and spreads of ∼0.4 to 0.7°. The best performing model in this case is again the range-independent, perturbed climatologies model, with a yearly average difference of 0.59±0.54°, while the worst is the range-independent, hybrid model (0.74±0.64°).

The comparison with the 2003–2022 stacked dataset shows an increased yearly average difference that is especially notable at Yasur (Figure 3.10c,d; Figures B.11,B.12 for more details), with values that start at 0.91±0.74° (range-independent, raw climatologies) up to 1.22±0.89° (range-dependent, hybrid). This is due to a widening of the highest difference peak observed at day ∼150, with more outliers present in the time window from day ∼100 to ∼250. This effect is also seen in the Ambrym case, with a

stark difference in the yearly average that begins around day ∼150 and ends around day ∼250. The previously observed peak ∼3° differences at the beginning and end of the year for Ambrym are not present here, with values below 1.5° for all models. The observed plateau below ∼1° for Yasur only spans days 1 to ∼50, and ∼250 to 365. For Yasur, the influence of the linear clusters near ∼-3° shows up in the 7-day 90% confidence average data, which in the 15-band PMCC 2003–2017 dataset has more spread and sits around ∼2° (Figure B.12). The same comparison applied to the 15-band PMCC dataset shows smaller year average differences, which range from 0.86±0.85° (range-independent, perturbed climatologies) to 1.9±1.39° (range-dependent, hybrid) for Ambrym, and from 0.88±0.56° (range-independent, raw climatologies) to 1.24±0.71° (range-dependent, hybrid) for Yasur (Figure B.12).

3.6 Discussion

Higher diurnal variability for Ambrym can be attributed to modeled ground intercepts that refract from thermospheric altitudes (Figure 3.6). This is in agreement with previous observations that most of the detected infrasound arriving from the Lopevi azimuth (and therefore the Ambrym direction as well) had thermospheric height characteristics (Assink et al., 2014; Le Pichon et al., 2005a). The Sun's effect on the thermospheric ducts is likely the predominant cause of this semi-diurnal behavior, as it has an oscillatory effect that peaks every 12 hours (∼11 am and 11 pm local time). This effect is also present for Yasur but is less distinct, as the ground intercepts are mostly arriving from stratospheric heights, which are not as influenced as thermospheric ones by semi-diurnal changes in the atmosphere (Figure 3.5).

The average daily variability is comparable across climatology-based and hybrid models (Figure 3.7). The behavior of the climatology-based model daily variability is

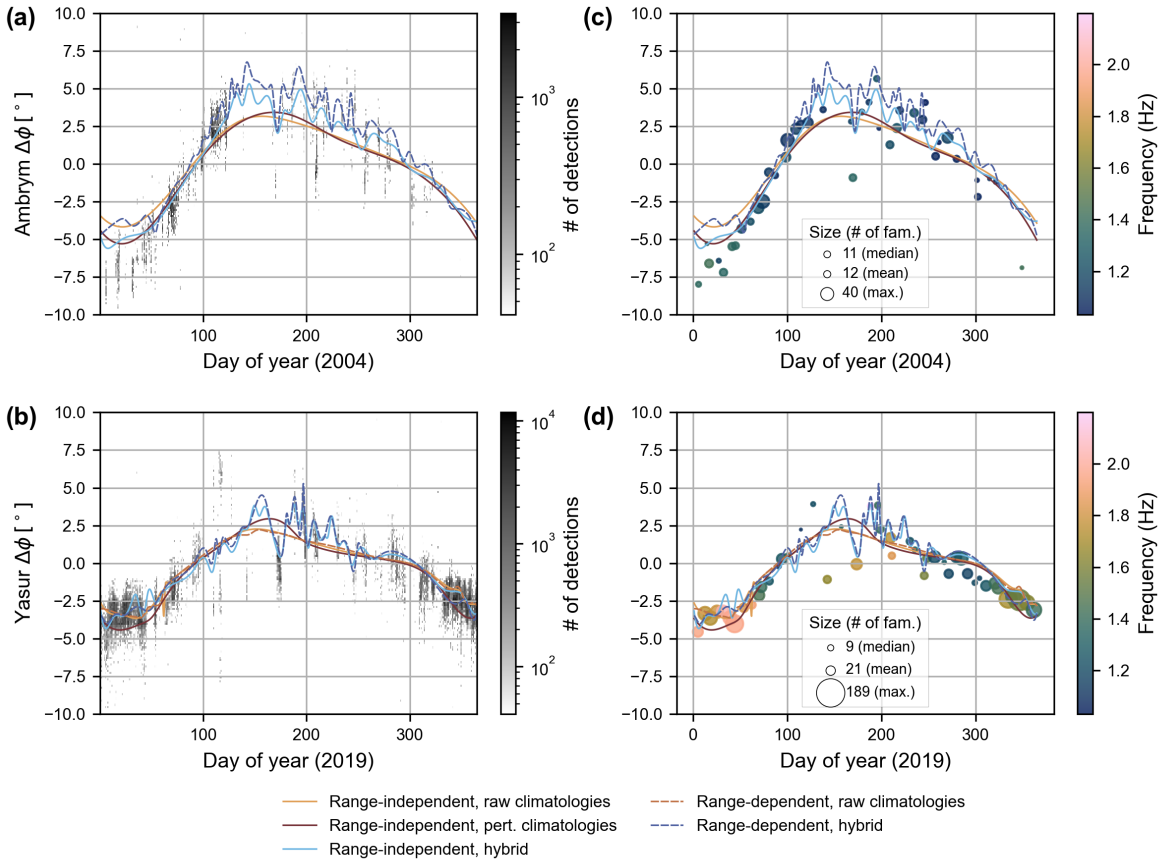

Figure 3.8: Modeled predicted back-azimuth deviations compared to IS22 observations (high-frequency 1–3 Hz products of Hupe et al. (2021b)). (a) 2004 Ambrym and (b) 2019 Yasur. In each plot (a, b, c, d) we display the final interpolated ray-tracing predictions for the different model runs (lines with color indicated by the legend), as shown in Figures 4 and 5. We compare these to (a, b) array detection observations as a 2D histogram (see Figure 3.2) and (c, d) 7-day averages of these detections that are within the 90% confidence interval from the mean, colored by their mean frequency content. In (c, d), the size corresponds to the number of "families" in the detection (a measure of time-frequency span of the signals).

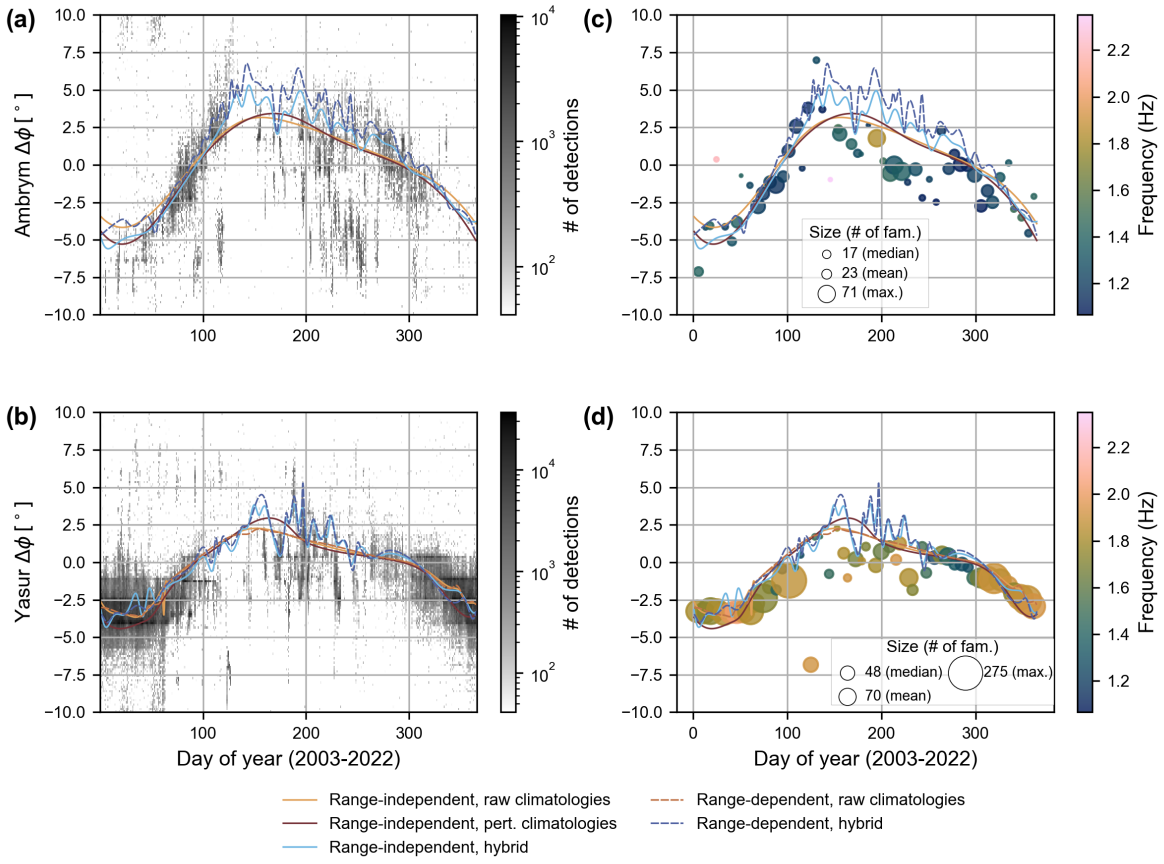

Figure 3.9: Same as Figure 3.8, but showing all of the multi-year observations from 2003 to 2022 (1–3 Hz products (Hupe et al., 2021b)).

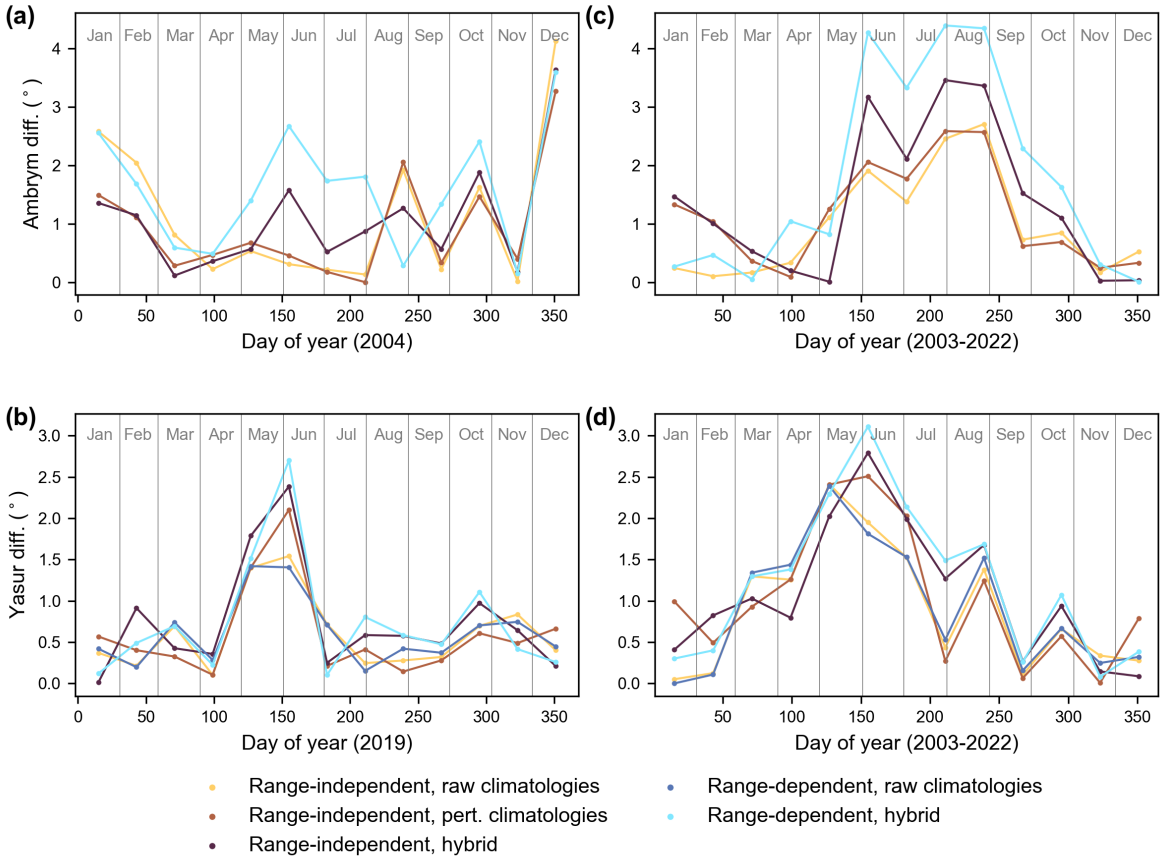

Figure 3.10: Euclidean distance between reduced high-frequency PMCC products (Hupe et al., 2021b) (Figure 3.8, 3.9) and interpolated modeled back-azimuths in 28-day intervals. (a) 2004 Ambrym. (b) 2019 Yasur. (c) 2003-2022 Ambrym. (d) 2003-2022 Yasur. The gray labels on top, separated by vertical gray lines mark each month (see Figures B.10,B.11,B.12).

Volcano	Year(s)	Model type	Average difference [°]
Ambrym	2004	Range-ind., raw clim.	1.13 ± 1.20
		Range-ind., pert. clim.	0.94 ± 0.89
		Range-ind., hybrid	1.08 ± 0.91
		Range-dep., raw clim.	No data
		Range-dep., hybrid	1.59 ± 1.00
Yasur	2019	Range-ind., raw clim.	0.60 ± 0.43
		Range-ind., pert. clim.	0.59 ± 0.54
		Range-ind., hybrid	0.74 ± 0.64
		Range-dep., raw clim.	0.62 ± 0.39
		Range-dep., hybrid	0.73 ± 0.69
Ambrym	2003–2022	Range-ind., raw clim.	0.97 ± 0.86
		Range-ind., pert. clim.	1.15 ± 0.83
		Range-ind., hybrid	1.38 ± 1.24
		Range-dep., raw clim.	No data
		Range-dep., hybrid	1.79 ± 1.66
Yasur	2003–2022	Range-ind., raw clim.	0.91 ± 0.74
		Range-ind., pert. clim.	1.04 ± 0.80
		Range-ind., hybrid	1.10 ± 0.79
		Range-dep., raw clim.	0.93 ± 0.75
		Range-dep., hybrid	1.22 ± 0.89

Table 3.1: Summary of average differences in the considered time-window between the models and high-frequency (1-3 Hz) PMCC datasets (Hupe et al., 2021b).

smoother than that of the hybrid model, which is an expected effect of the first-order nature of the climatologies.

The general deviation effects follow the stratospheric seasonal wind directions, but the second-order effects in the hybrid models, previously attributed to SSW events (Antier et al., 2007; Assink et al., 2014), manifest chiefly during the summer months. These effects are not present in the empirical climatologies, as they only portray first-order changes and are stochastic, averaging out smaller scale changes that are very relevant for infrasound propagation. This is a good example of the limits of the predictions we can obtain with the stochastic atmospheric descriptions, as it shows that during periods of weaker ducting conditions, the azimuth deviation predictions should be used as a general reference, but not a hard boundary condition to assess the real directions of a long-range source.

Despite the ability of the hybrid models to predict arrivals from transient favorable ducts, Ambrym 2004 maximum 28-day averaged differences ($\sim$2-4°) are higher for the hybrid models than the climatologies during periods of wind reversals and eastward zonal winds (Figure 3.10a; days $\sim$100 to 250).

For both years, there seems to be no significant difference between range-independent and range-dependent models, which indicates that the smaller and second-order spatial effects are less relevant for infrasound propagation for the ranges we consider in this study ($\sim$400 to 700 km).

The increased averaged differences between the 2003–2022 dataset (Figure 3.10c,d) can be attributed to the stack of sources that provide numerous detections during relatively short time windows. To eliminate this effect, further data processing is required. Possible approaches would be to consider only sources that repeat a minimum number of times per year, or a minimum number of years at each 2D bin.

The greatest alignment between the models and observations is generally the begin-

ning (days 1 to ∼120) and end (days ∼250 to 365) of the year. The least alignment occurs between those two time periods, marked by either weaker winds or transition periods which produce detections that have azimuth deviations contrary to the average tendency of the climatologies. Nevertheless, the hybrid models can recreate only some of the several outlier detections, presenting a similar average deviation as the climatology-based models. This could be due to other infrasound sources, not necessarily a lack of detail in the atmospheric models.

The range-independent models provide better or comparable results than the range-dependent models, which is likely due to the atmospheric descriptions in the area of study not changing significantly between altitude steps. This supports the usage of range-independent models for year-long cases with long-range propagation. For the Ambrym 2004 case, the minimum year average difference between the models and the data was 0.94±0.89° (range-independent, perturbed climatology), and the maximum was 1.59±1.00° (range-dependent, hybrid) The Yasur 2019 case had a minimum year average difference of 0.59±0.54° (range-independent, perturbed climatology) and a maximum of 0.74±0.64° (range-independent, hybrid) (Figure B.10).

The Ambrym 2003–2023 differences are from 0.97±0.86° (range-independent, raw climatologies) to 1.79±1.66° (range-dependent, hybrid) In comparison, the Yasur 2003-2024 differences are from 0.91±0.74° (range-independent, raw climatologies) to 1.22±0.89° (range-dependent, hybrid) (Figure B.11).

3.7 Conclusions

We test a methodology that aims to calculate robust, first-order estimates of long-range infrasound arrival characteristics, particularly the back-azimuth, using empirical climatologies. We produce year-long models of infrasound propagation for arrivals at

IMS station IS22 (Grande Terre, New Caledonia) from the Vanuatu archipelago region, including from Yasur (Tanna island, at ∼400 km and ∼43°N azimuth) and Ambrym (Ambrym island, at ∼670 km and ∼12°N azimuth) volcanoes.

Our goal was to investigate if the empirical climatologies were sufficient, and to what extent, to model the atmospheric variability effects present every year for a case where the sources are well localized, and can be assumed as nearly-continuous. To do so, we modeled the atmospheric conditions for infrasound propagation from the ground to 150 km (horizontal winds, temperature, pressure, and densities) with empirical climatologies (HWM14/MSIS2.0), and also considered a manually perturbed set of descriptions that enhance along-path winds.

To evaluate the accuracy and limitations of the above approach using simplified perturbations to empirical climatologies, we also repeat the calculations using more accurate hybrid models that merge the the European Centre for Medium-Range Weather Forecasts reanalysis v5 (ERA 5) descriptions (winds and temperatures) from the ground to ∼80 km with the climatologies for higher altitudes. To investigate the degree of model complexity required to match observations, we performed both range-independent and range-dependent 3D ray-tracing modeling (infraGA/geoAC), resulting in five different model types that we compared with observations. We compare our results with multi-decadal (2003–2022) high-frequency (1-3 Hz) PMCC products (Hupe et al., 2021b), their 26-band PMCC provenance (Hupe et al., 2022), and a 15-band PMCC multi-year dataset as well (2003-2017) (Matoza et al., 2013).

We found that the range-dependent propagation models provide comparable results to the range-independent cases, supporting the use of a simplified, layered model of the atmosphere for regional and global calculations. From July to April, all the models depict seasonal back-azimuth changes that are generally aligned with the year-long, and stacked multi-year observations From May to June, the reversal of the zonal winds from prevalent

westward winds to eastward winds shows scarcer observations, higher differences with the models, and only transient groups of detections likely produced by regional scale wind perturbances and transient favorable ducts (e.g., Sudden Stratospheric Warmings). The average difference per year between the models and the high-frequency PMCC products shows that the empirical climatologies can provide comparable results with the hybrid models. The match is generally better for Yasur volcano than Ambrym, which is likely the combined effect of increased crosswinds and propagation path length, plus other possible eruptive sources from similar locations such as Gaua and Ambae volcanoes. For specific years, the hybrid model was the only one capable of reproducing detections from transient ducts during the worst matching period (April-June). The hybrid models also better characterize the back-azimuth changes during the transition periods towards the stratospheric seasonal wind reversal (around April and October).

Our results indicate that the range-independent, raw climatologies models are reasonably well-suited to obtain robust first-order estimates of arrivals for large-scale, year-long infrasound propagation in this region. The diurnal back-azimuth variability is comparable across models, showing a higher spread ($\sim 0.8 \pm 0.3^{\circ}$) for Ambrym than Yasur ($\sim 0.6 \pm 0.3^{\circ}$) sources (Figure 3.7). The year-long average model differences with the observations (see Table 3.1) show that the range-independent, raw and perturbed climatologies cases are also comparable with their hybrid counterparts, ($\sim 1 \pm 1^{\circ}$). However, the monthly discrepancy variations (from October to May vs. June to September; see Figure 3.10), should be always considered when applying corrections to the observed back-azimuths. Global studies with other well known volcanic sources could complete the picture to better understand the applicability of sets of priors to source location in near-real time. The range-dependent, hybrid models better depict second-order propagation effects of the atmospheric variability, especially during periods of unfavorable wind propagation conditions, but require computation resources that impose constraints on

the scale of the models that could be studied.

Chapter 4

Long-range multi-year infrasonic detection of eruptive activity at Mount Michael volcano, South Sandwich Islands.

This chapter appeared in this form in:

De Negri, R. S., Rose, K. M., Matoza, R. S., Hupe, P., & Ceranna, L. (2022). Long-range multi-year infrasonic detection of eruptive activity at Mount Michael volcano, South Sandwich Islands. Geophysical Research Letters, 49, e2021GL096061. https://doi.org/10.1029/2021GL096061

4.1 Abstract

Mount Michael stratovolcano, South Sandwich Islands is extremely remote and challenging to observe, but eruptive activity has been sporadically observed since 1820 and captured by satellite methods since 1989. We identify long-range infrasound signals recorded by the International Monitoring System attributable to episodes of persistent eruptive activity at Mount Michael. Analysis of multi-year (2004-2020) infrasound array

data at station IS27, Antarctica (range 1,672 km) reveals candidate signals especially from May 2005 to January 2008 and from May 2016 to April 2018. By combining ray-tracing with empirical climatologies and atmospheric specifications, we show that systematic variations in the observed back-azimuth of the signals (at IS27) are broadly consistent with annual variability in stratospheric propagation conditions for a source at Mount Michael. Observed signal amplitudes combined with transmission loss estimates are consistent with moderate explosive eruption. We highlight selected events of infrasound signals that match with satellite observation of eruptions.

4.2 Introduction

Attempts to catalog Earth's global volcanism compile a variety of data sources (e.g., Engwell et al., 2021; Global Volcanism Program, 2013b), but activity at remote volcanoes lacking ground-based instrumentation and observers remains likely underreported (e.g., Webley and Mastin, 2009). Infrasound (atmospheric acoustic waves $\sim$0.0120 Hz) from explosive volcanism can propagate hundreds to thousands of kilometers in atmospheric waveguides under favorable conditions (e.g., Dabrowa et al., 2011; Matoza et al., 2011a,b, 2018). Accordingly, recent work has explored the potential of the Comprehensive Nuclear-Test-Ban Treaty Organization (CTBTO) International Monitoring System (IMS) infrasound network to provide a quantitative catalog of global explosive volcanic activity (Matoza et al., 2017).

Mount Michael (57.800°S, 26.482° W), a basaltic to andesitic stratovolcano on Saunders Island, South Sandwich Islands, southern Atlantic Ocean (Global Volcanism Program, 2013b) is an unusually remote volcano that has been particularly challenging to observe with current space-borne systems (Patrick and Smellie, 2013; Gray et al., 2019). Here we investigate remote infrasonic detection of Mount Michael using the nearest three

IMS infrasound stations IS27 (1,672 km), IS02 (2,520 km), and IS49 (2,526 km; 4.2), finding long-range infrasound signals attributable to Mount Michael at IS27, but not at IS02 or IS49.

4.3 Mount Michael, South Sandwich Islands

The 11 South Sandwich Islands and related seamounts comprise a volcanic arc resulting from active subduction, where the South Sandwich Plate subducts under the South American Plate (Leat et al., 2016). Saunders Island is composed of a central volcanic edifice which includes 843-m-high Mount Michael, and sits at the intersection of two submarine seamount chains (Leat et al., 2016). The South Sandwich Islands are a breeding ground for significant populations of seabirds, especially penguins, with an estimated half of the global Chinstrap penguin population (Hart and Convey, 2018; Liu et al., 2021; Lynch et al., 2016, and references therein). Thus, an eruption in the South Sandwich Islands could have a global impact on these terrestrial and marine ecosystems.

Volcanic activity has been sporadically observed at the mostly glacier-covered Mount Michael since at least 1820 and includes occasional observations of vapor emissions, volcanic plumes, thermal anomalies, and Strombolian eruptions (Patrick and Smellie, 2013; Gray et al., 2019). Lava fields observed by Baker (1990) indicate recent activity covering large parts of the island. The 500-m diameter summit crater of Mount Michael has a frequently active lava lake, identified by thermal satellite imagery (Gray et al., 2019). The current eruptive period began on 12 November 2014, and continues to the time of writing, January 2023 (Global Volcanism Program, 2013b). Due to the extreme remoteness of Saunders Island, direct observations of eruptive activity at Mount Michael are rare, but have become more frequent in recent years with the availability of satellite imagery such as from Sentinel-2, ASTER, and Landsat 8. Evidence of eruptions, volcanic

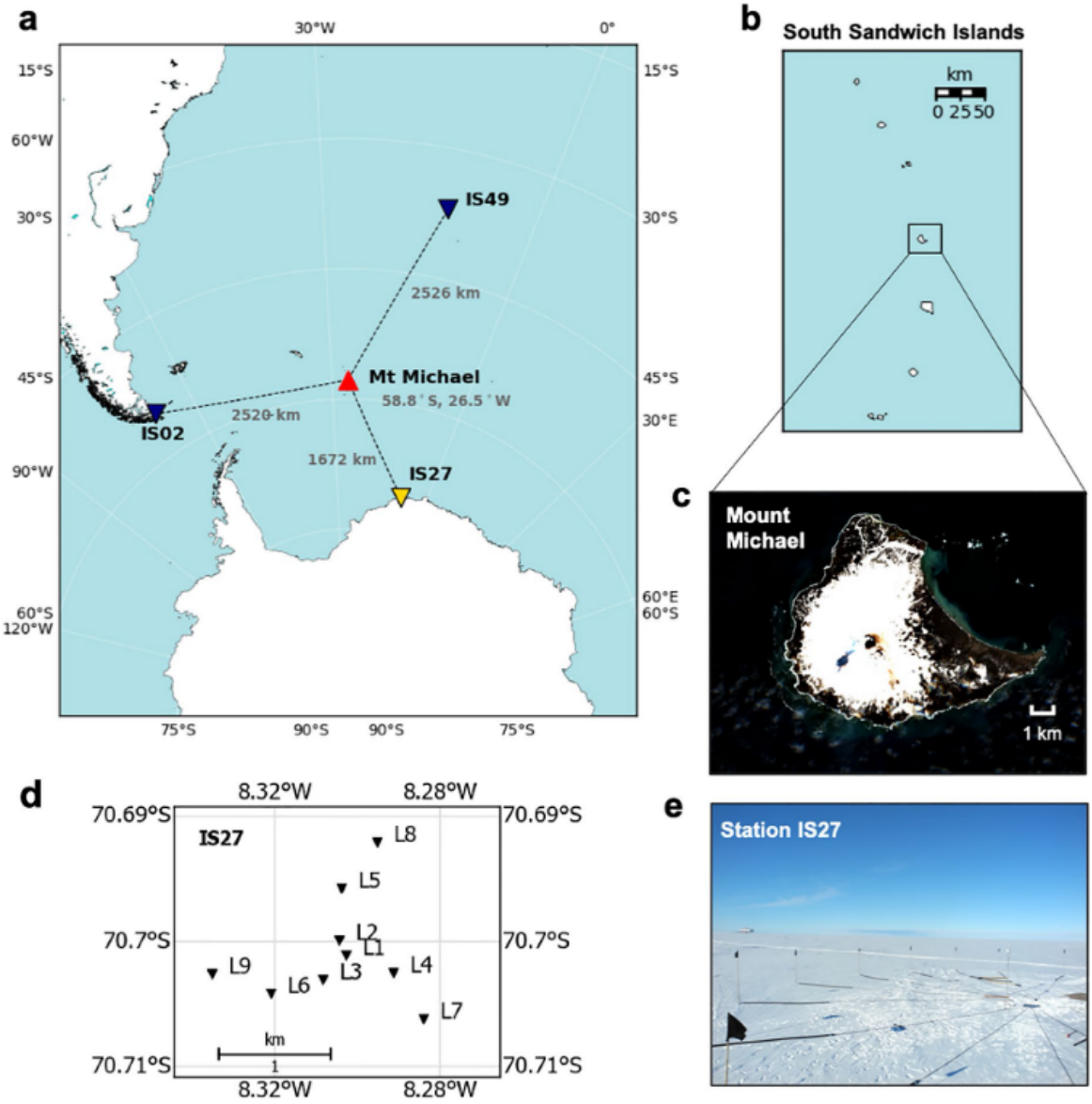

Figure 4.1: (a) Location of Mount Michael volcano and infrasound stations considered in this study (IS27, IS02, and IS49). IS27 (yellow inverted triangle) intermittently detects infrasound that we attribute to Mount Michael; IS02 and IS49 (dark blue inverted triangles) are non-detecting stations. (b) Location of Mount Michael on Saunders Island within the South Sandwich Islands chain. (c) Visual-band satellite image from 10 February 2018, of Saunders Island with Mount Michael volcano visible with a crater in the center of the island, showing a small plume rising from the crater (Modified Copernicus Sentinel Data, 2018). (d) Infrasound array element configuration of station IS27, Neumayer, Antarctica. (e) Photograph of one array element of IS27, with spatial wind filter pipe inlets indicated by flags.

clouds, plumes, possible lava lakes, and thermal hotspots has been observed by satellite since 1989 (Gray et al., 2019), including an increase in observations of eruption activity in 2016-2021 (Global Volcanism Program, 2013b; Gray et al., 2019). However, satellite observations are often limited by persistent meteorological cloud cover; weeks or months may pass without a clear view of the volcano (Gray et al., 2019).

4.4 Infrasound Observations

4.4.1 Systematic Infrasound Array Analysis 2004-2020

The global IMS infrasound network is nearing completion; there are currently 53 certified infrasound stations of a planned total 60 (Marty, 2019). Each infrasound station is an array of at minimum four infrasound sensors with a flat response between ±5% in amplitudes from 0.02 to 4 Hz (Marty, 2019). The average inter-station spacing for the complete network will be about 2,000 km and numerical studies indicate that the complete network can detect explosions with a yield of at least 1 kT TNT equivalent anywhere on Earth (Green and Bowers, 2010; Le Pichon et al., 2009a).

We consider the nearest three IMS infrasound stations to Mount Michael: IS27 (1,672 km), IS02 (2,520 km), and IS49 (2,526 km). We process the multi-year (2004-2020) infrasound array data using the Progressive Multi-Channel Correlation method (PMCC) to isolate correlated infrasound signals from uncorrelated wind noise and estimate plane-wavefront parameters (e.g., back-azimuth, apparent velocity, frequency) for the correlated signals (Cansi, 1995; Le Pichon et al., 2010) We implement PMCC with both a 15-band log-spaced frequency configuration (Matoza et al., 2013) and a new 26-band log-spaced configuration from 0.01 to 4 Hz, which are products of systematic processing of IMS infrasound data (Ceranna et al., 2019; Hupe et al., 2021a, 2022; Matoza et al., 2013) We

choose to use the 26-band (one-third octave band) configuration for improved accuracy of signal parameter estimation (e.g., frequency and azimuth) as it has the longest temporal coverage and uses the latest PMCC implementation (Hupe et al., 2021a, 2022). The 26-band multi-year (2004-2020) array processing results for IS27 are shown in Figure 2. In this configuration, we use time window lengths of 600 to 30 s duration that advance in time steps of 10% of the window length; the window lengths are proportional to the inverse of the minimum frequency of the band (Hupe et al., 2021a, 2022). With both PMCC implementations, there are minor artifacts at the lowest frequencies (Figure 4.4c) as discussed by Hupe et al. (2021a, 2022) which do not affect any of the results presented here.

Signals arriving from the back-azimuth of Mount Michael are intermittently observed at the closest station IS27 (Figure 4.4). The more distant stations IS02 and IS49 have no signals clearly attributable to Mount Michael based on manual inspection of the array processing detection list. This is likely due to unfavorable propagating conditions for IS02 (Le Pichon et al., 2019) and frequently low signal-to-noise ratios[1] for IS49 (Matoza et al., 2013). Therefore, we subsequently focus on IS27.

4.4.2 Signal Identification and Source (Clutter) Discrimination

As with all IMS infrasound arrays (Matoza et al., 2013), IS27 records persistent ambient infrasound (sometimes termed "clutter") from a variety of sources, including microbaroms (∼0.1-0.5 Hz), probable surf infrasound at ∼1-4 Hz (Garcés et al., 2003), and possible iceberg and glacier calving also at ∼1-4 Hz (Figure 4.4a; Appendix Section C.4). The microbarom detectability is clearly linked with the prevailing seasonal stratospheric winds (Ceranna et al., 2019; Le Pichon et al., 2009a). During austral winter, strong eastward stratospheric winds at mid-latitudes enhance detection for signals orig-

[1]Constant surf and wind noise on both locations.

inating from the west, and the situation reverses in the summer (Ceranna et al., 2019; Le Pichon et al., 2009a). The number of detections diminishes twice a year around the time of the equinox, when the reversal of the stratospheric wind direction (from east to west) weakens the stratospheric wind jet[2] ; this reduces the long-range propagation ducts for microbaroms and other signals. Additionally, IS27 shows a decrease in the amplitude of the detections from ∼20 to ∼10 mPa from October to December, which we attribute to the increase of snow cover[3] during winter (Figure C.19).

4.4.3 Candidate Mount Michael Infrasound Detection Characteristics

Near the true (great circle) back-azimuth of Mount Michael (320° as viewed from IS27), we observe two distinct time periods with candidate (possible Mount Michael) infrasound: from 2005 to 2007, and 2016 to 2018 (Figures 4.4a and 4.4b). The IS27 infrasound data are frequently obscured by high-amplitude wind noise at frequencies above 1 Hz. However, on days with low wind noise, candidate infrasound signals arrive as indicated by increases in frequency content in the 1-4 Hz range corresponding to consistent PMCC detections from the back-azimuth of Mount Michael. Cleaned (parsed) array processing results with mean frequencies between 0.7 and 4 Hz and back-azimuths between 250° and 350° (Figure 4.4b) show more clearly the inferred Mount Michael signals by reducing the clutter (primarily microbarom) as viewed for the full results shown in Figure 4.4a. The May 2005 detection sequence (Figures 4.4 and C.10) starts with near-continuous ∼1-1.5 Hz infrasound signals that show positive azimuth deviations following

[2]This is clear in Figure C.1, which shows how from days 1 to ∼80 (January to March) and ∼300 to 365 (November to December) the expected arrivals are only thermospheric (no stratospheric duct). This effect is also present in the dataset yearly (e.g., Figures C.10 to C.18), with periods of low vs. high detectability in the mentioned months.

[3]Snow cover likely acts as a buffer as it partially blocks the pressure inlets of the station wind-noise filtering pipes (see Figure 4.2e).

seasonal stratospheric winds trends through time (i.e., maxima in winter and minima in summer). This behavior continues in subsequent years, but the detections become more intermittent and scarcer until almost disappearing at the beginning of 2008. The May 2016 detection sequence (Figures 4.4 and C.14) is composed of a large group of ∼1 Hz infrasound signals that end in July 2016. Later, from February to April 2017 and January to April 2018 (Figures 4.4, C.15 and C.16), higher frequency (∼1.5-2.5 Hz) detections appear in numbers that indicate a possible mixture of background sources (e.g., surf and glacier) and possible volcanic activity (see Section 4.4.4). From May to July 2013, February 2020, and April 2020, we detect occasional sporadic candidate signals from Mount Michael. These detections have frequencies of ∼1-1.5 Hz and azimuths from ∼320° to ∼328° (Figures 4.4, C.17 and C.18). In the stacked 2004-2020 frequency versus azimuth space (Figures 4.4c and 4.4d), two main clusters or groups of detections, one centered at ∼1 Hz at ∼328°, and the other at ∼2 Hz at ∼323°, show up as candidate infrasound associated with transient volcanic activity. With further analysis (Appendix Section C.1), we conclude that these two clusters are composed mainly of detections from 2005 to 2007 and from 2016 to 2018, which correspond to the time periods visible in Figures 4.4a and 4.4b previously analyzed. From 2005 to 2007, we observe two groups of detections with centroids of frequencies ∼1.4 and ∼2.7 Hz, located at ∼326° and ∼323°, respectively. During May 2016, we see one candidate detection group with a centroid of ∼1 Hz at ∼328°. From February to April 2017 and January to April 2018, both candidate groups have a centroid of ∼2 Hz at ∼323°. The azimuth deviation values from true agree with the expected seasonal stratospheric wind effects on the propagating signals, with a maximum modeled deviation of ∼12° in June and a minimum ∼0° in late December or early January (Figure C.1), while the centroid frequency of the candidate detections increases with decreasing azimuth deviation. Therefore, we interpret that the two groups represent winter and summer characteristic values of frequency and azimuth

for detections from Mount Michael volcano. Given the limitations of single-station remote detection (Matoza et al., 2019), it remains possible that some candidate eruptive signals may be sourced by other volcanoes from the South Sandwich Islands (e.g., Bristol Island). However, the satellite evidence of strong explosive eruptions (see Figure 4.4a) with visible volcanic clouds through the last 30 years, the probable presence of a stable lava lake (Gray et al., 2019), and the concurrent persistent gas emissions (Liu et al., 2021), render Mount Michael the most plausible source of most (if not all) of the candidate volcanic infrasound signals detected at IS27.

4.4.4 Discriminating Remote Volcanic Signal From Local Glacial Infrasound

In some cases, we can attribute signals to volcanic activity with relatively low ambiguity from interfering signals (e.g., June 2016; Appendix Section C.4). For example, relatively high-amplitude PMCC detections on 10 June 2016 reflect an increase in signal power at frequencies from ∼1 to 3 Hz (Section 4.6). In other cases, however, volcanic signal arrivals are apparently complicated by the superposition (interference) by local glacier calving events with overlapping back-azimuth and frequency characteristics (e.g., February to April of years 2017 and 2018; Appendix Section C.4). These presumed glacial signals generally have a wider frequency range of 1-4 Hz, and concentrate at higher frequencies. The distinguishing feature of these interpreted glacier calving signals is that they simultaneously emerge and disappear in small detection clusters concentrated at an azimuth that is stable in time (Figures C.15 and C.16). On the other hand, candidate Mount Michael infrasound appears as a more populous detection cluster that exhibits systematic seasonal variations in azimuth deviation (with broader spread in azimuth), which we investigate in Section 4.5. We further discuss the discrimination of Mount

Michael signals from local glacial infrasound and other clutter sources in the following sections as well as in Appendix Section C.4.

4.5 Investigating Infrasound Propagation From Mount Michael to IS27

Although the inferred Mount Michael signals are only intermittently observed at IS27 (1,672 km range), systematic seasonal variations in the received signal back-azimuth are typical of long-range infrasound propagation effects (back-azimuth deviation from cross-winds) that have been observed for more sustained and continuously active volcanic sources (e.g., Antier et al., 2007; Assink et al., 2014; Le Pichon et al., 2005b). Seasonal variations in observed back-azimuth values are related to the seasonal infrasound propagation (ducting) conditions, particularly seasonal reversal of the stratospheric winds (Drob et al., 2003, 2010a; Garcés et al., 1998) For example, Le Pichon et al. (2005b) observed systematic annual variability in azimuth deviation for multiple volcanoes from Vanuatu recorded at IS22 (New Caledonia) and related these to seasonal variation in north to southward stratospheric and thermospheric propagation paths.

4.5.1 Observed Annual Variability in back-azimuth

Accordingly, if the observed signals are indeed sourced from Mount Michael, the observed annual variability in back-azimuth values at IS27 should relate to the relevant atmospheric ducts from source-to-receiver, which should be largely captured by ray-tracing and empirical climatologies (e.g., Drob et al., 2003; Le Pichon et al., 2005b). Thus, to further investigate if the observed IS27 signals characteristics are consistent with a source at Mount Michael, we compare the observed annual variation in back-azimuth values for

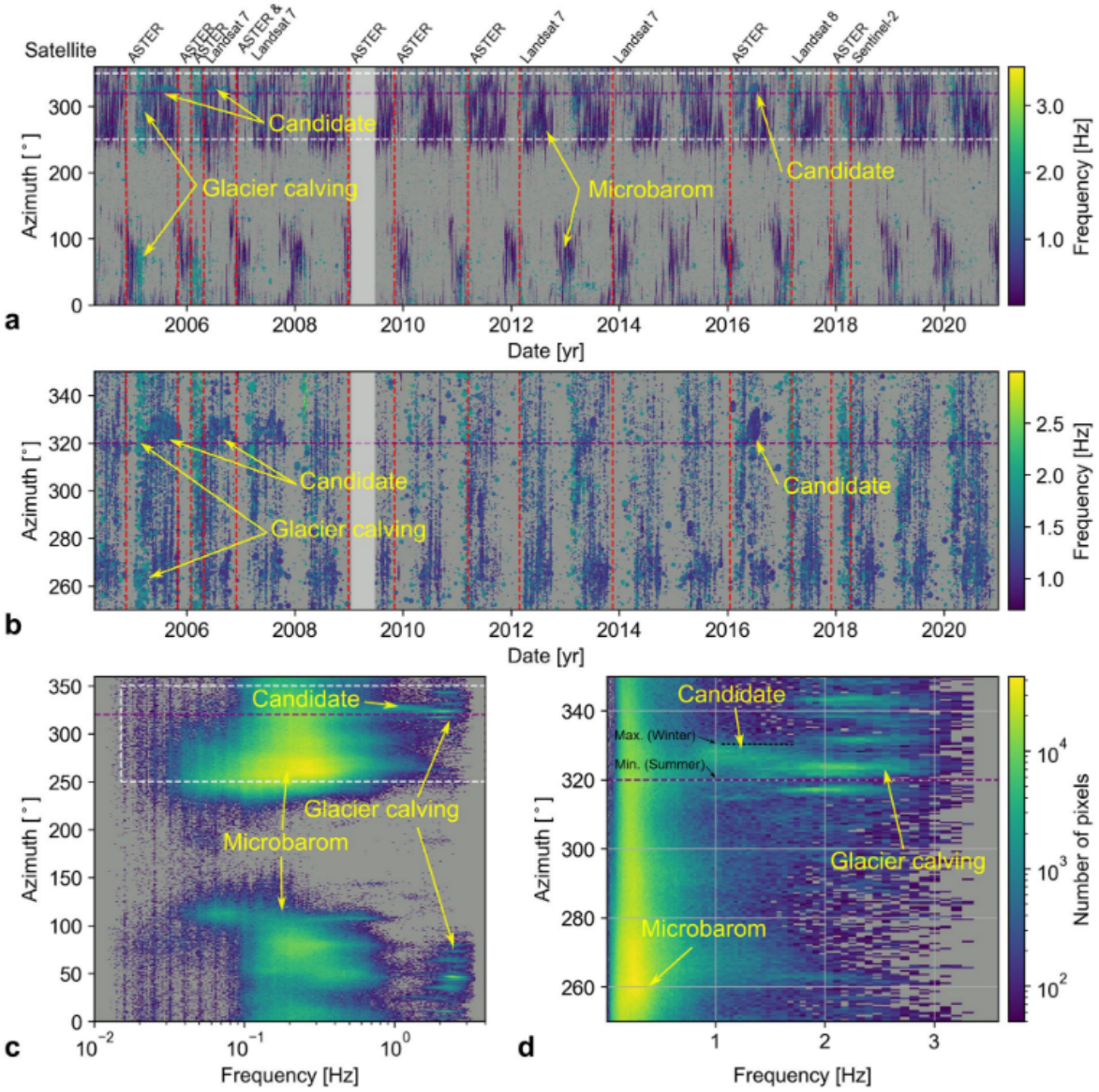

Figure 4.2: Progressive multi-channel correlation (PMCC) array processing results at IS27 from 2004 to 2020. Yellow labels and arrows: microbarom, glacier calving, and candidate Mount Michael infrasound detections at IS27. Note that during the first half of 2009, there is a data gap (light gray box) resulting from the physical relocation of IS27 to a nearby site (∼5 km). (a) PMCC azimuth versus time, with symbol color indicating frequency. Dashed white lines indicate the range of panel (b). (b) As for (a), but for azimuth windowed around the back-azimuth of Mount Michael (∼320°, purple dashed line), selected detections corresponding to mean frequencies >0.7 Hz, and scaled up size of circles for detections between 1 and 2 Hz (i.e., main candidate infrasound frequencies). Red vertical dashed lines indicate eruption detections based on satellite data (Gray et al., 2019). (Continues on next page)

Figure 4.2: (From previous page) (c) 2D histogram of 2004-2020 PMCC results in azimuth-frequency space. Color-scale indicates the number of pixels (detections); bin sizes are 0.01 Hz in frequency and 0.5° in azimuth. White box indicates the range of panel (d). In (c), the narrowband vertical lines across all azimuths at frequencies below 0.1 Hz are minor processing artifacts resulting from the PMCC algorithm implementation. (d) As for (c) but windowed around the Mount Michael back-azimuth (∼320°); visible peaks (clusters of detections) occur from ∼0.7 to 3.0 Hz and in two distinct back-azimuth values (∼1 Hz at ∼328° and ∼2 Hz at ∼323°); maximum (∼330°) and minimum (∼320°) azimuths corresponding to modeled winter and summer values are in black labels.

the signals with predictions from ray-tracing through empirical climatologies (Drob et al., 2015; Picone et al., 2002). Since the Mount Michael signals are not continuously but only intermittently observed, we perform the comparison on the detection time-series folded or collapsed by day of year (Figure 4.5). This also facilitates a more natural comparison with the empirical climatologies, which are specified by day of year and are not related to an absolute date. Figure 4.5 shows the resultant multi-year (2004-2020) infrasound array processing results collapsed to day of year for detections >0.7 Hz mean frequency. To emphasize the dominant signal characteristics, the array processing results are also summarized into clusters of similar array detections using a simple implementation of a k-means clustering algorithm based on the PMCC method implementation (Cansi and Le Pichon, 2008, also Appendix Section C.2).

4.5.2 Comparison With Annual back-azimuth Deviation Predicted by Ray-Tracing and Empirical Climatologies

We predict azimuth deviations for signals sourced at Mount Michael arriving at IS27 by combining empirical climatologies HWM14 and NRLMSISE-00 (Drob et al., 2015; Picone et al., 2002) and 3D ray-tracing (infraGA/GeoAc; Blom and Waxler, 2012).

We model the seasonal effects of stratospheric and thermospheric winds on infrasound

propagation from Mount Michael toward IS27 by launching a set of rays from 0.5° to 45° in steps of 0.5° for each day of the year at 00:00 UTC.

Ground intercepts at ∼5.5 km from IS27 are used to determine a modeled apparent azimuth as reference for an expected azimuth deviation as the difference between the geographical azimuth and the modeled azimuth of the ground intercepts (arrivals). We note that the choice for the threshold distance (∼5.5 km) is arbitrary, but small enough to calculate a reference azimuth deviation that is representative of the theoretical ground intercept at the station. In Figure 4.5a, a continuous fuchsia line depicts the interpolated modeled azimuth deviation values. It follows the azimuth deviation tendency of the observations from austral mid-fall to the first half of austral spring, generally overestimating the deviation by ∼2.5° with a standard deviation of ∼3.3° (fuchsia line, Figure 4.5b). This group of detections is the one that contains most of the candidate infrasound (Figures C.10, C.11, C.14). The frequency range of this group of detections is ∼0.75-2.8 Hz, which agrees with our observations in Figure 4.4.

In years 2017 to 2018 we observe simultaneously occurring azimuthal bands of detections pointing northwest and northeast with frequencies between ∼2-3 Hz likely reflecting contamination by local glacier infrasound (Section 4.4.4), which increases the apparent centroid frequency of the candidate signals at this time (Appendix Section C.4). Nevertheless, the candidate Mount Michael infrasound appears as a populous detection cluster that exhibits systematic seasonal variations in azimuth deviation, which is modeled by favorable zonal winds (eastern direction) from April to August, especially June to July.

Considering signal amplitude loss over the path from Mount Michael to IS27, Figure 4.5c depicts the estimated transmission loss (TL) values of ray paths that arrive at IS27 for a source at Mount Michael modeled with ray-tracing and empirical climatologies for a 1-year time interval, accounting for spherical geometric spreading and thermo-viscous absorption losses (Blom and Waxler, 2012; Sutherland and Bass, 2004). We separate the

estimated values by the turning height of each ray path, obtaining average TL values of 74.87 and 82.63 dB for stratospheric and thermospheric paths, respectively. All of the modeled TL values fall between the theoretical cylindrical, and spherical geometric spreading values to IS27 (Figure 4.5c), as expected. The travel-time calculations for the modeled stratospheric and thermospheric ray-paths are 1 hr 32 min (corresponding to a celerity of 0.303 km/s) and 1 hr 46 min (0.263 km/s), respectively.

Assuming that the observed signals are from Mount Michael, Figure 4.5 indicates that the empirical climatologies underpredict wind speed during austral spring and overpredict wind speed during austral winter. To further investigate this, Figure 4.5d compares the effective sound speed as a function of altitude at 14:00 UTC on 10 June 2016, for both the empirical climatologies and more realistic descriptions obtained from the European Centre for Medium-Range Weather Forecasts (ECMWF) ERA5 reanalysis for the lower ∼80 km altitude, plus empirical climatologies for the upper atmosphere (black line). Below ∼50 km (Figure 4.5d), the effective sound speed values for ECMWF are lower in the stratosphere than for empirical climatologies, but still produce theoretical arrivals near IS27 with TL values ranging from ∼50 to ∼90 dB for turning heights from ∼40 to ∼120 km. Figure 4.5e shows the ray paths using only empirical climatologies (upper panel), and also as a combination of the ECMWF realistic atmospheric description and climatologies (lower panel). For this time of the year (austral winter), we obtained stratospheric arrivals (∼40-50 km height) with an average TL value of ∼78.4 dB at IS27 from the combined descriptions (i.e., "ECMWF+Climatologies").

4.5.3 Transmission Loss Estimates and Plausibility of Volcanic Source Signal Amplitude

The TL values are calculated in decibels [dB] for the acoustic pressure normalized to a reference distance of 1 km:

$$\mathrm{TL} = 20 \log_{10}(P/P_{\mathrm{ref}}) \tag{4.1}$$

Considering the average stratospheric TL value at IS27 derived from ray-tracing, we estimate the adjusted pressure amplitude at a reference distance of 1 km (Dabrowa et al., 2011) from Mount Michael using the observed amplitudes of detected signals.

The observed signals at IS27 that we attribute to Mount Michael have amplitudes at IS27 from $\sim 1.8 \times 10^{-3}$ to $\sim 4.8 \times 10^{-3}$ Pa (See Appendix Section C.3). The TL predictions from ray-tracing for a source at Mount Michael to station IS27[4] (Figure 4.5c) have a typical value of ∼74.9 dB assuming a stratospheric path (which has the lowest TL, thus likely represents the dominant amplitude). Using this stratospheric TL and the observed amplitude at IS27, these signals would have a corresponding amplitude of approximately ∼10.1-26.7 Pa[5] at a reference distance of 1 km ($r = 1$ km) from the source if they had indeed originated from Mount Michael.

For comparison, Matoza et al. (2007) recorded the acoustic signature of a small phreatic (steam-driven) explosion at Mount St. Helens, WA, USA on 8 March 2005. This signal was also recorded ∼250 km (SCJW) and ∼445 km (IS56) to the east and northeast due to long-range stratospheric ducting (Matoza, 2009). For this Mount St.

[4]The source frequency is 1 Hz. The atmosphere is considered range-independent (spherically stratified) and described with the hybrid model (ECMWF+Climatologies). The geometric spreading and absorption (Sutherland and Bass, 2004) are used to obtain the final TL value.

[5]These pressure ranges correspond to the equivalent values at 1 km from the source, based on the selected events mentioned in the Appendix Section C.3. The equivalent pressures are calculated with Eq. 4.1. The pressures are also summarized in Table C.1.

Helens phreatic explosion, the acoustic pressure at 13.4 km from the source (CDWR station) was ∼1 Pa maximum amplitude (Matoza et al., 2007). Correcting back to a 1 km reference distance assuming spherical spreading gives ∼13.4 Pa at $r = 1$ km. Thus, the observed Mount Michael signals together with the TL predictions from ray-tracing place the acoustic signals of Mount Michael (corrected to a common reference distance of 1 km from the source) at about the same acoustic amplitude or greater than the phreatic explosion event at Mount St. Helens documented by Matoza et al. (2007). This lends further plausibility to the attribution of the observed IS27 signals to a moderate explosivity volcanic eruption source at Mount Michael, which is ducted to the long range (1,672 km) under favorable propagation conditions and recorded successfully when signal-to-noise levels at IS27 are no lower than 0.5 (Cansi et al., 2005; Matoza et al., 2013) as presented on Figure 4.6d.

4.6 Comparison With Satellite Detections

Gray et al. (2019) provide a list of satellite observations of eruptive activity at Mount Michael from January 1989 through April 2018, including observations of eruptions, volcanic clouds, plumes, possible lava lakes, and thermal infrared (TIR) hotspots. We compare these observations as well as our observations from satellite imagery from Sentinel-2 and Landsat 8 satellites with a selection of candidate Mount Michael infrasound from May 2016 to April 2018. Observations from Landsat-8 are visual-band, and observations from Sentinel-2 are visual-band or short-wave infrared spectral range (SWIR) band imagery, and were obtained from Sentinel Hub Playground (Modified Copernicus Sentinel Data, 2018). Sentinel satellite imagery is not available for the area of Mount Michael during 2017 and partially useful through 2018 due to cloud cover. Cloud cover also limits the utility of Landsat-8 satellite imagery for the area at times of candidate Mount

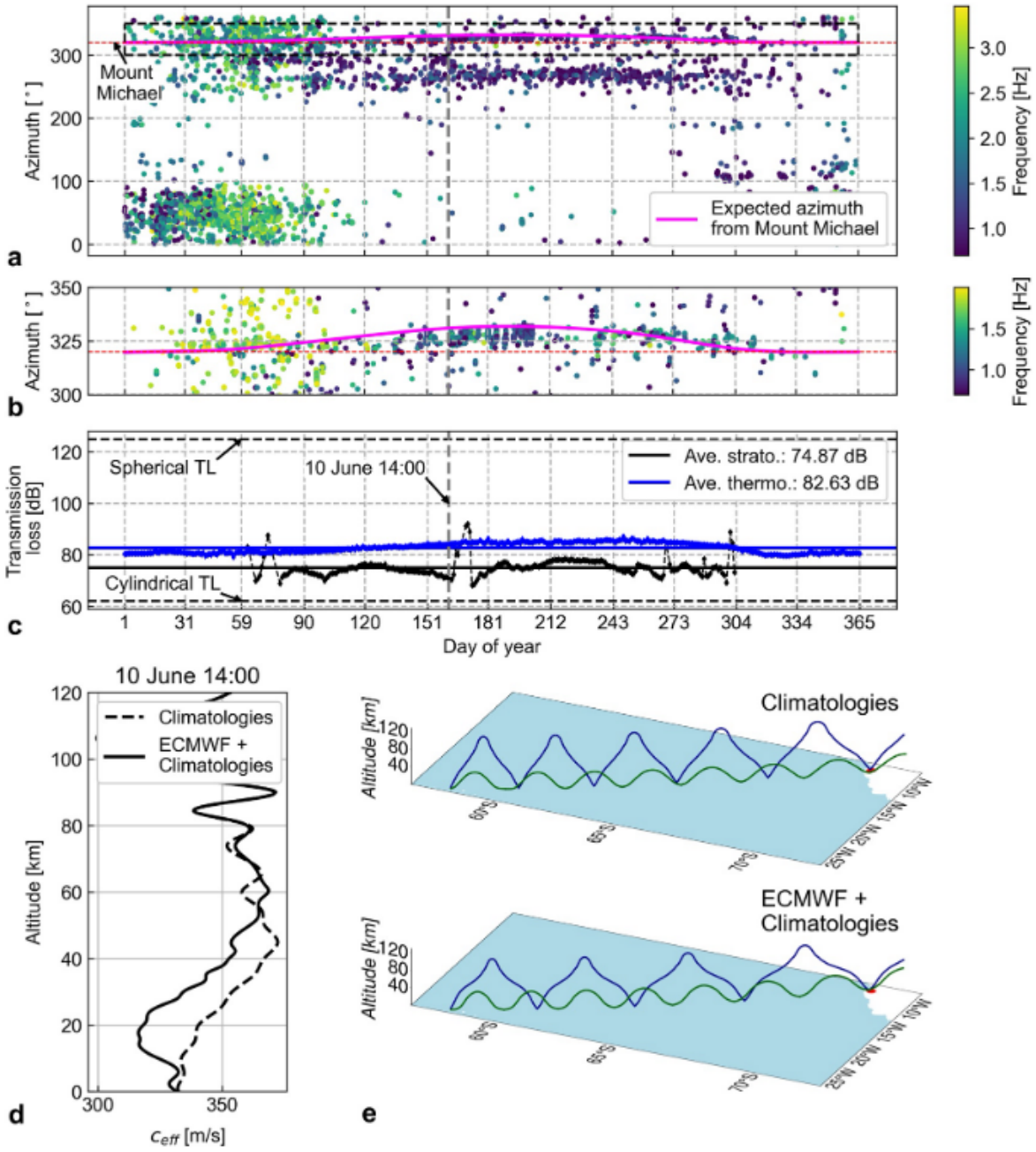

Figure 4.3: (a) IS27 multi-year-average progressive multi-channel correlation (PMCC) results (2004-2020 results collapsed by day-of-year, DOY) compared with predicted azimuth arrivals for a source at Mount Michael based on ray-tracing and empirical climatologies. Each circle (with color indicating frequency) represents a cluster of PMCC detections with similar wavefront properties. Red dashed line is the true great-circle back-azimuth to Mount Michael (∼320°). A fuchsia line indicates modeled azimuths from Mount Michael as a function of DOY. A vertical gray dashed line depicts the date of example profiles in panel (d). (Continues on next page)

Figure 4.3: (From previous page.) (b) Zoom over plot area depicted by a black dashed box in panel (a) with frequencies from 0.7 to 2.5 Hz only. (c) Modeled transmission loss values for each day of year separated by stratospheric and thermospheric turning heights. The reference theoretical spherical and cylindrical geometric spreading values are depicted in dashed horizontal lines, with values of 125 and 62 dB, respectively. Horizontal black and blue lines indicate the average TL stratospheric and thermospheric values, respectively. (d) Example effective sound-speed profile (as a function of altitude above sea level) from Mount Michael to IS27 on 10 June 2016 at 14:00 UTC for both (dashed line) climatology-only and (solid line) ECMWF-ERA5 (0-∼80 km altitude) fused with climatology (∼80-170 km altitude). (e) 3D ray-tracing (infraGA/ GeoAc) for the atmospheric specifications in panel (d) for two selected rays that arrive near the station (<50 km). IS27 location is depicted by a red circle. The green ray has a stratospheric turning height (∼40-60 km altitude); the blue ray has a thermospheric turning height (∼110 km altitude).

Michael infrasound. These limitations prevent further comparisons using this data set than exemplified in the following.

Figure 4.6 shows a selection of candidate infrasound signals at IS27 compared to the satellite data where available. Figure 4.6a shows an example of relatively high-amplitude PMCC detections on 10 June 2016 reflecting an increase in signal power at frequencies from ∼1 to 3 Hz (Section 4.4.4). Although no satellite data were available for this event, based on the signal characteristics alone (Figure 4.6a), we interpret these detections as resulting from an eruption at Mount Michael that produces detections from May to July in significant numbers with no other prominent background sources at this frequency range (see Figure C.14).

Evidence for volcanic activity at Mount Michael in 2017 was reported by Gray et al. (2019), who list 8 March 2017 as a day with observed volcanic eruption at Mount Michael. Figure 4.6e presents Landsat-8 visual satellite imagery from 8 March 2017, showing eruption plumes above the extensive cloud cover. Similarly, based on Sentinel-2 satellite imagery, Gray et al. (2019) reports 11 April 2018 as a day with a possible eruption (Figure C.14) and a possible lava lake on 10 February 2018 (Figure 4.6f). These observations support our interpretation that the consistent higher-frequency PMCC detections during

February to March 2017 and 2018 (Figure 4.6; Appendix Section C.4) result from explosive volcanic eruption activity at Mount Michael, in some cases (e.g., 3 February 2018, Figure 4.6c) contaminated by local clutter (i.e., glacier calving).

4.7 Conclusions

We report long-range infrasound detections attributable to eruptive activity at Mount Michael, South Sandwich Islands within a multi-decadal 2004-2020 record at IMS infrasound station IS27, Antarctica (range 1,672 km). Suspected Mount Michael signals occur particularly during two general times: (a) from May 2005 to the start of 2008, and (b) from May 2016 to April 2018. The latter (b) is composed of three broad detection sequences May to July 2016, February to April 2017, and late January to April 2018. The inferred Mount Michael signals are only intermittently observed at IS27 and their detection and unique attribution to a source is further complicated by local glacial infrasound clutter with overlapping signal characteristics. Nevertheless, systematic seasonal variations in the received signal back-azimuth are typical of longrange infrasound propagation effects (back-azimuth deviation from cross-winds) that have been observed for more sustained and continuously active volcanic sources and are inconsistent with local glacier infrasound. Infrasound ray-tracing with empirical climatologies shows that the observed IS27 annual evolution in signal characteristics are broadly consistent with a source originating at Mount Michael subject to seasonal stratospheric crosswind effects. The observed signal amplitudes at IS27 combined with the predicted TL values of the modeled stratospheric ray paths ($\sim$74.9 dB), imply an acoustic pressure amplitude of $\sim$10.1-26.7 Pa at a reference distance of 1 km from the source. These values are comparable to and slightly exceed those of a small Mount St. Helens phreatic explosion on 8 March 2005 ($\sim$13.4 Pa corrected to a reference distance of 1 km), supporting the plausi-

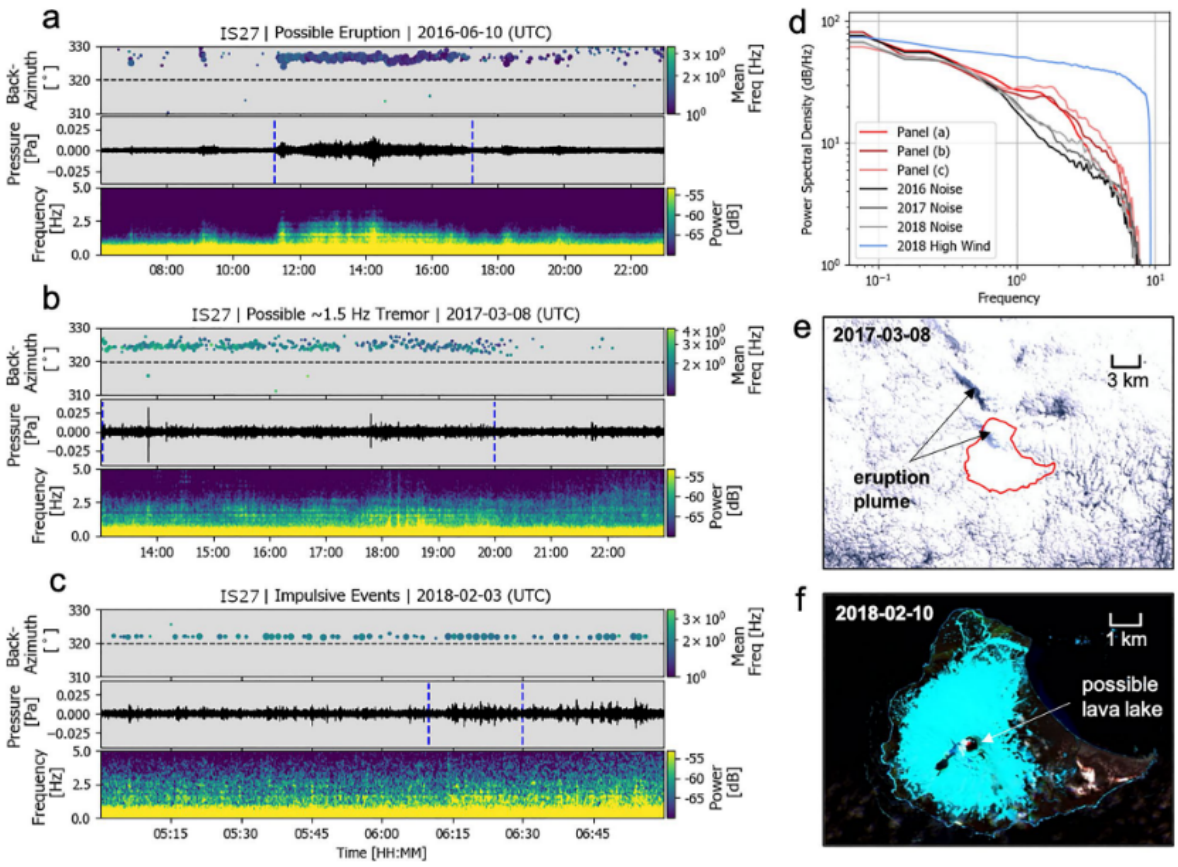

Figure 4.4: (a, b and c) Progressive multi-channel correlation (PMCC) detections, waveforms, and spectrograms for three selected time intervals of possible volcanic activity based on signals detected with back-azimuth close to that of Mount Michael. Waveforms are time-domain beams based on the true back-azimuth to Mount Michael using all array elements filtered from 1 to 4 Hz to reduce noise while spectrograms are based on unfiltered beams. Blue vertical dashed lines indicate possible volcanic signals windowed to calculate power spectral density in panel (d). (a) A sequence of PMCC detections corresponding to an increase in signal power at frequencies from 1 to 3 Hz, which we interpret as a possible eruption at Mount Michael. (b) Sustained PMCC detections 1-3.5 Hz with a strong frequency component at ~1.5 Hz, which we interpret as possible eruption tremor. (c) Sporadic PMCC detections corresponding to intermittent impulsive signals, which we interpret as dominantly a sequence of iceberg calving events northwest of IS27. (d) Power spectral density of selected signals shown compared to a noise sample from 2018 during a time of high wind. (e) Landsat-8 visual-band satellite imagery for 8 March 2017, corresponding to the date of panel (b), showing an eruption plume above meteorological cloud cover, with Saunders Island outlined in red to show its position. The presence of the plume supports the attribution of the infrasound signals to eruptive activity at Mount Michael. (f) Sentinel-2 thermal-band satellite imagery for 10 February 2018 showing Mount Michael with its summit crater unobscured by cloud cover and a small steam plume rising from the crater (Modified Copernicus Sentinel Data, 2018).

bility of these signals as originating from Mount Michael moderate eruptive activity and being detectable at IS27 under favorable propagation and noise conditions. We highlight a selection of times of remote infrasound observations at IS27 that also correspond to independent confirmation of eruptive activity by satellite observations. Satellite observations are not always available for the times of candidate infrasound signals at IS27 and similarly infrasound appears marginally detectable, as a function of atmospheric propagation conditions and station noise variations. Despite these limitations, the long-range infrasound data further indicate long-lived sustained eruptive activity at Mount Michael.

Chapter 5

Conclusions

5.1 Conclusions

We developed a rapid, automated, first-order methodology based on empirical climatologies and 3D ray tracing to forward-model infrasound propagation for long-range cases, producing estimates of infrasound back-azimuth deviation, among other arrival parameters (e.g., time travel, TL, etc.). This methodology also allows the utilization of a simple Gaussian wind jet profile perturbation to the atmospheric descriptions at stratospheric heights, to account for fine-scale changes that are not present in the climatologies. It additionally can employ a more accurate set of descriptions by replacing the empirical climatologies with a hybrid model, which results from merging the ECMWF ERA5 reanalysis descriptions from the ground to ∼80 km altitude with the empirical climatologies from ∼80 km and above.

Using historical datasets from the nearest eight stations (∼1,500 km to ∼5,000 km) to the eruptions of Puyehue-Cordón Caulle volcano, 2011 (Chile), and Calbuco volcano, 2015 (Chile), we obtained considerable reductions of the source mislocation, ranging from ∼24% to ∼84%, and ∼65% to ∼75%, respectively.

We analyzed the available multi-decadal (2003-2022) infrasound detections from IS22, New Caledonia, and compared year-long modeled estimations of the azimuth devia-

tions with volcanic infrasound coming from the most active volcanoes of the Vanuatu archipelago: Yasur, Ambrym, Lopevi, Gaua, and Ambae. We found that the models using the empirical climatologies compare well at first-order with the hybrid cases, and that the range-independent models are as well comparable with the range-dependent models. However, the best match with the observations generally happens during winter (days 1 to ∼120 and ∼250 to end of year). During transition periods of stratospheric duct reversals (winter to summer and vice-versa) and weak atmospheric ducting (summer), the predictions will likely fail to represent chaotic, short-lived atmospheric phenomena like Sudden Stratospheric Warming events, which could be only partially emulated by the hybrid atmospheric models. The stochastic, seasonal behavior of the atmospheric effects of long-range infrasound propagation in the region are well represented, with statistical variations of the difference between models and data generally below the azimuth deviation effects (up to $\sim \pm 5^{\circ}$). Our results indicate that it is possible to build year-long estimates of infrasound back-azimuths that could help in the process of discriminating the sources of infrasound in near-real-time, but expanding our tests to other regions on Earth is still a necessary (and feasible) step before calculating global look-up tables.

We also studied the multi-decadal (2004-2020) infrasound records of IS27, Antarctica, and used our methodology to constrain and discriminate "candidate" infrasound previously unreported coming from Mount Michael, South Sandwich Islands (range 1,672 km) during two main periods (2005 to 2008 and 2016 to 2018), which indicates long-lived sustained eruptive activity at Mount Michael. We inferred that this remote island volcano – one of the few with a stable lava lake, and the main habitat of Chinstrap penguins in the world, among other important endemic species – presents eruptions comparable to and possibly more energetic than the 8 March 2005 phreatic explosions of Mount St. Helens (Washington, USA). To our knowledge, this is the first analysis of the acoustic signals of Mount Michael, adding only to previously scarce remote observations with satellite

imagery.

5.2 Future work

Future work should continue to assess the source location improvements achieved for 2011 Cordón Caulle and 2015 Calbuco (Chile), by comparing them with recent explosive eruptions with associated high-altitude (∼10 km) sustained ash-plumes at different locations (e.g., 2021 La Soufrière (Saint Vincent and the Grenadines); 2014 Kelud (Indonesia)). Additionally, multi-year analysis similar to the Vanuatu archipelago area should be considered in the northern hemisphere to assess the method's year-long results of back-azimuth deviations (e.g., Etna volcano, Italy from IS48, Turkey). Among the several methodological improvements that could be done in the implementation of the iterative search method (ARCADE), better understanding and insights of the atmosphere model differences could be investigated by adding other ensemble-type, or hybrid, models (e.g., AVO-G2S (Schwaiger et al., 2019), and WACCM-X (NCAR High Altitude Observatory, nd). For the climatology-based models, the evaluation of different effective speed perturbation amounts (30%) and the altitudes at which it is applied (40 km) should be also considered in order to obtain arrivals that are comparable with the induced by second order effects. Propagation at short distances (under ∼250 km) could be achieved, but has not been considered in this study, and would require the adjustment of the atmospheric and ray-tracing parameters, and perhaps the use of a different propagation scheme/algorithm. Finally, the implementation of this methodology into multi-technology approaches for remote detection and characterization of syn-eruptive changes in volcanic activity is an achievable goal, and should be considered in the future.

Appendix A

Supporting information for "Rapid location of remote volcanic infrasound using 3D ray tracing and empirical climatologies: Application to the 2011 Cordón Caulle and 2015 Calbuco eruptions, Chile"

A.1 Text S1: calculation time reduction and other possible improvements.

All the calculations done in this study have taken less than an hour (∼55 mins.) per model type in a machine with eight available threads with a clock speed of 2.4 GHz. Obviously, the total calculation time of each scenario will depend on the number of trial source-receivers to simulate (e.g., eight pairs in this work per volcano and model type). The total time of calculation, though, will depend on several other factors. We identify as the main one the distance range to be covered in each calculation, which for this study ranges from ∼1500∼5000 km. Another important factor is the maximum number of tries each pair trial source-receiver has set as threshold during the iterative process (40 in this

study).

Finding a more suitable maximum number of tries that reduces the search time, but allows a fair search process, could dramatically reduce the total calculation time. Changing the distance threshold criteria to consider ground intercepts as near enough to the receiver ($d_r = 0.5^\circ$ and $d_\phi = 0.1^\circ$ in this study; see Figure 2 in main paper) could also reduce the total calculation time, at the expense of having a more strict search that finds no ground intercepts, or not accurate enough azimuth deviation predictions. Finally, the attenuation threshold also has a clear impact on the calculation time of each case. In this study, we have allowed a very "relaxed" search by not imposing a threshold to associate ground intercepts to a particular receiver to allow a set of predictions as complete as possible, but this has generally increased the total calculation time by establishing unrealistic arrival searches in some cases (e.g., IS13 and IS14 that could have been declared as "ill-conditioned" from the beginning).

The method considers a range-independent atmosphere, with layered averages in height that vary per profile (trial source to receiver direction and time). This approach helps to simplify the process, reducing the discretization and ray tracing calculation times considerably. However, the model also allows range-dependent calculations that could be used for more in-detail studies where it is less relevant to process combinations of trial-sources, receiver networks, and times. As a suggestion for these types of studies, we recommend using a range-independent model first to narrow down the model parameter set, and then launching a full range-dependent calculation.

The case of iteratively searching for raypaths that connect a trial source and a receiver is linked mathematically with finding eigenrays. We note that infraGA, as with similar 3D ray tracing algorithms, includes an eigenray searching method that we do not use in our method. Instead, we implement the iterative search to maximize flexibility and control over the search parameters when looking for reasonable ground intercept predictions.

It is likely that implementing infraGA's own eigenray method would allow obtaining estimates in a shorter calculation time than in this study, but we will leave this idea for future work.

Another advantage of infraGA, present on the latest implementation, is parallel calculation capabilities. As we developed the base method when the ray tracing algorithm did not have this option, we developed a rudimentary approach that sends each trial source-receiver ray tracing calculation to a different CPU. This is also an interesting space for more time calculation improvements that should be considered in future versions of the method.

A.2 Additional Figures

- Figure A.1 is an extended version of Figure 2.2 in the main text, showing that IS13 and IS14 do not play a relevant role in detecting the eruptions of Puyehue-Cordón Caulle (2011) and Calbuco (2015).

- Figures A.2 and A.3 are useful to understand and compare the differences between effective sound speed profiles in height from Cordón Caulle to each one of the IMS stations considered at the eruption start time. Figure A.2 shows profiles calculated with empirical climatologies only, while Figure A.3 has profiles calculated with hybrid profiles.

- Figures A.4 and A.5 are analogous to A.3 and A.4, but for Calbuco location and eruption start time.

- Figures A.6 and A.7 illustrate the average horizontal winds from 40 to 60 km for Cordón Caulle and Calbuco eruption start times, respectively. They also serve to compare the climatological and hybrid descriptions for the area.

- Figures A.8, A.9, A.10 are snapshots of the iterative search process for cases considered to be unrealistic (Figures A.8 and A.9) or anomalous (Figure A.10).

- Figures A.11 and A.12 show the histograms that helped determine the mean and median of the PMCC detections for several stations. The characteristic values are used in Figure 6 to show how the azimuth deviation predictions fit the observations.

- Figures A.13 to A.18 show the IMS_vASC association and location results for each one of the eight different modeling schemes (see Figures 2.6 and 2.7 in main text) for Cordón Caulle and Calbuco volcanoes.

- Figure A.19 shows preliminary results of range-dependent calculations for both volcanoes in comparison with range-independent raytracing. As the range-dependent modeling is much more computationally expensive to calculate, it has not been considered an option for rapid estimations. Nevertheless, it is still possible to use range-dependent raytracing for other applications. As an example, the calculations for raw climatologies with range-dependent propagation took about 21 hours, while the same machine spent only one hour using range-independent modeling. We deemed the results as comparable, but future work should better constrain the differences for more general cases.

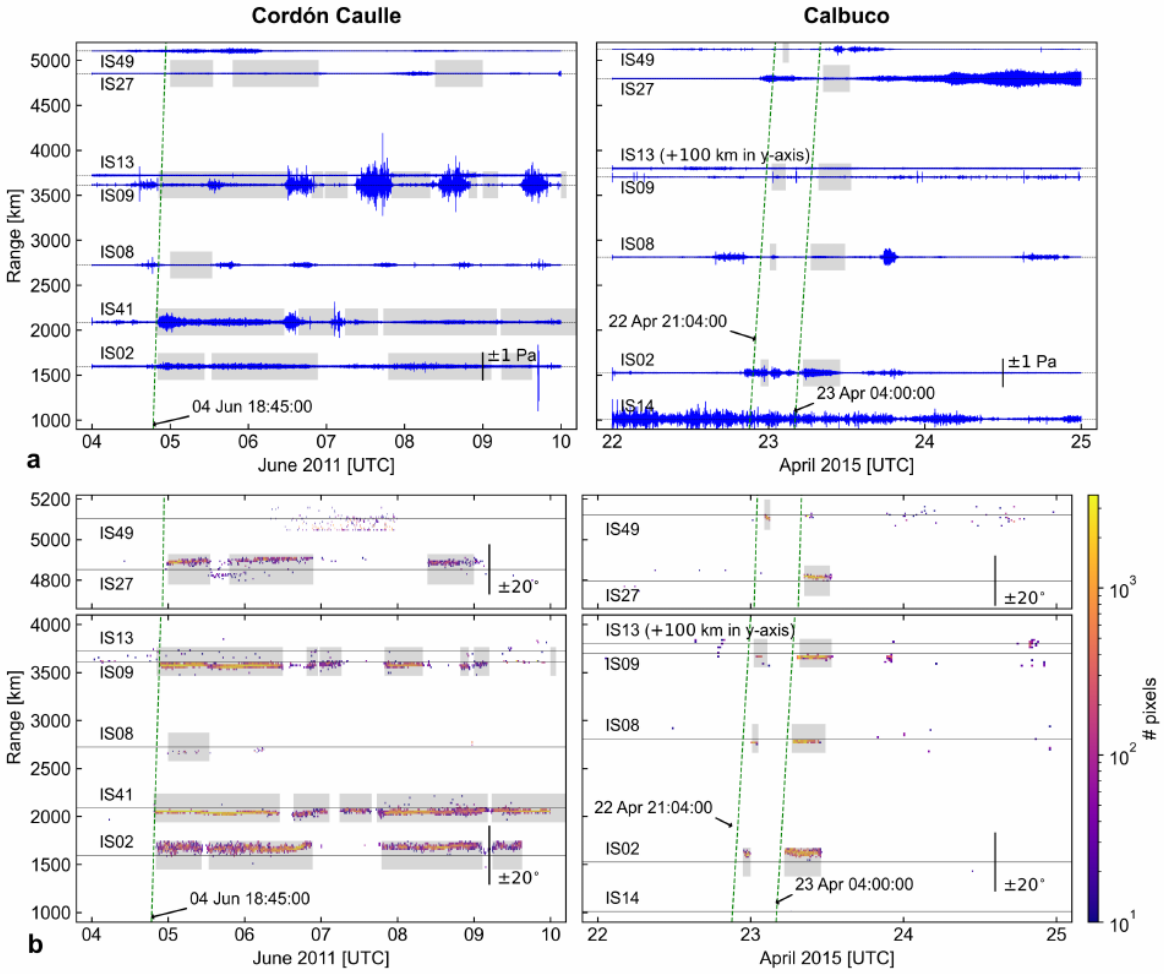

Figure A.1: Extended version of Figure 5 in main paper. For Cordón Caulle volcano, the station IS13 has been added to the plot. For Calbuco volcano, the stations IS13 and IS14 are included. Both IS13 and IS14 do not contribute to the PMCC detections available to associate and locate the volcanoes (no visible detections in b).

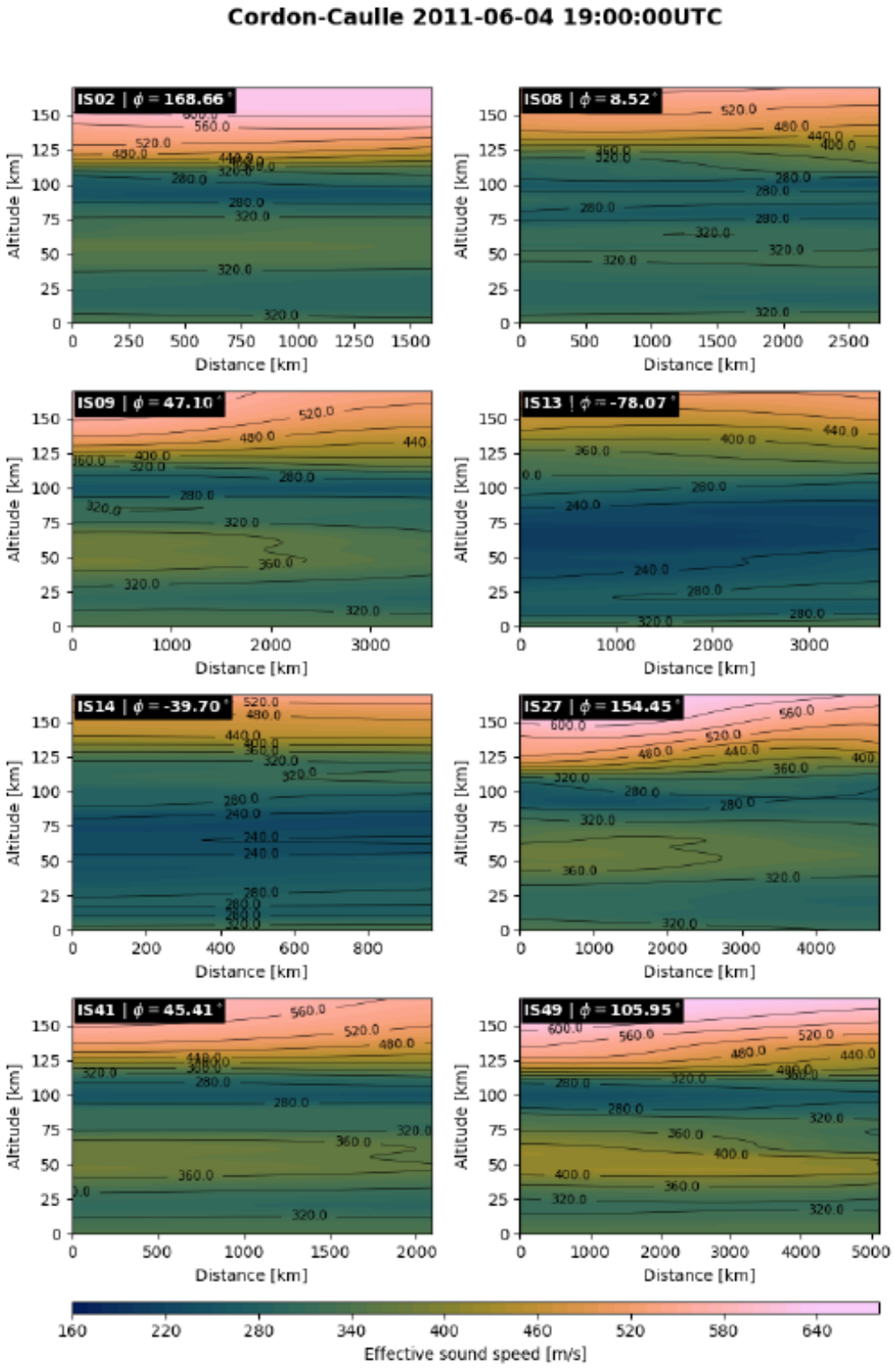

Figure A.2: Effective sound speed profiles for Cordón-Caulle using only climatologies.

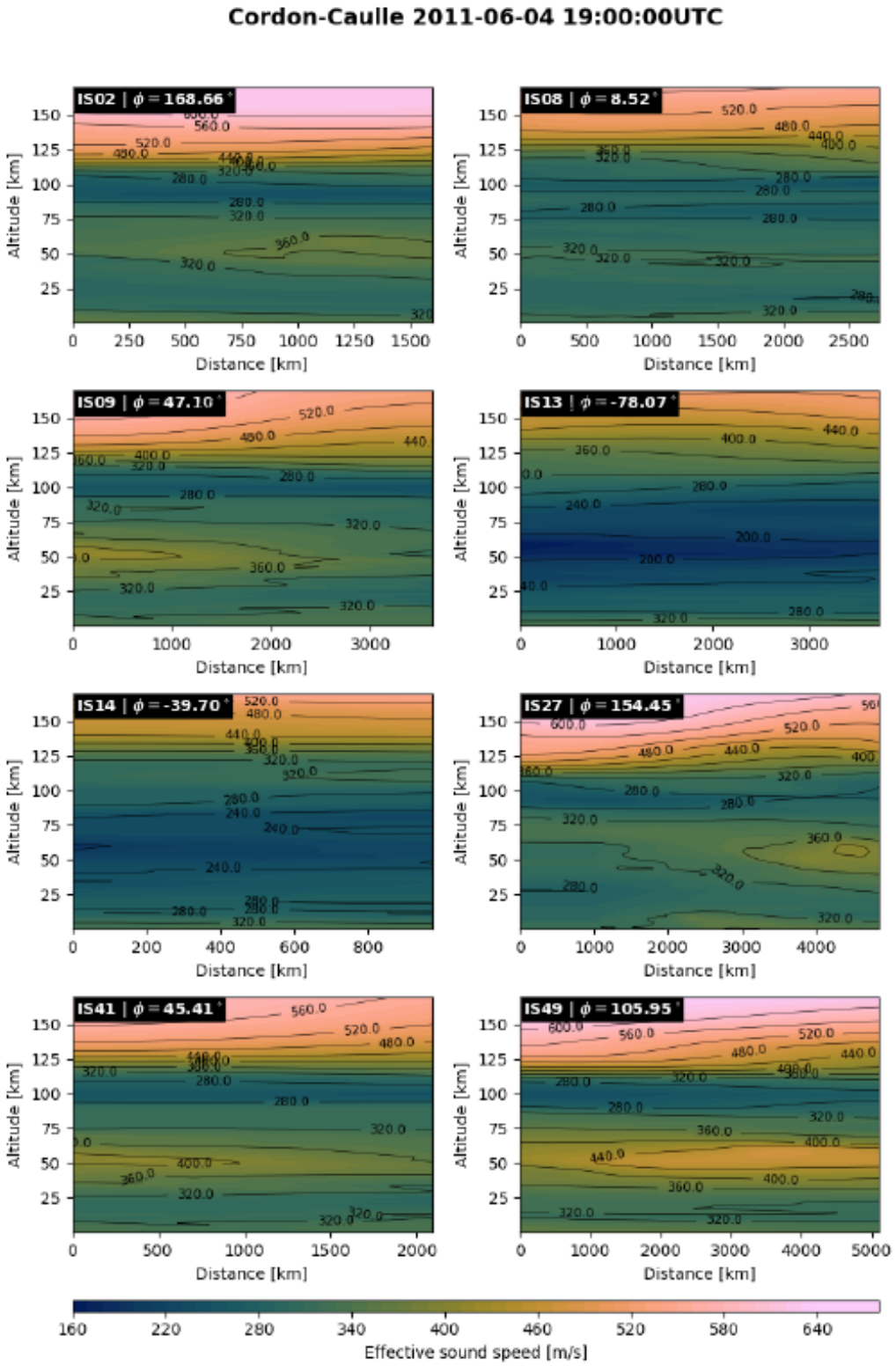

Figure A.3: Effective hybrid sound speed profiles for Cordón-Caulle.

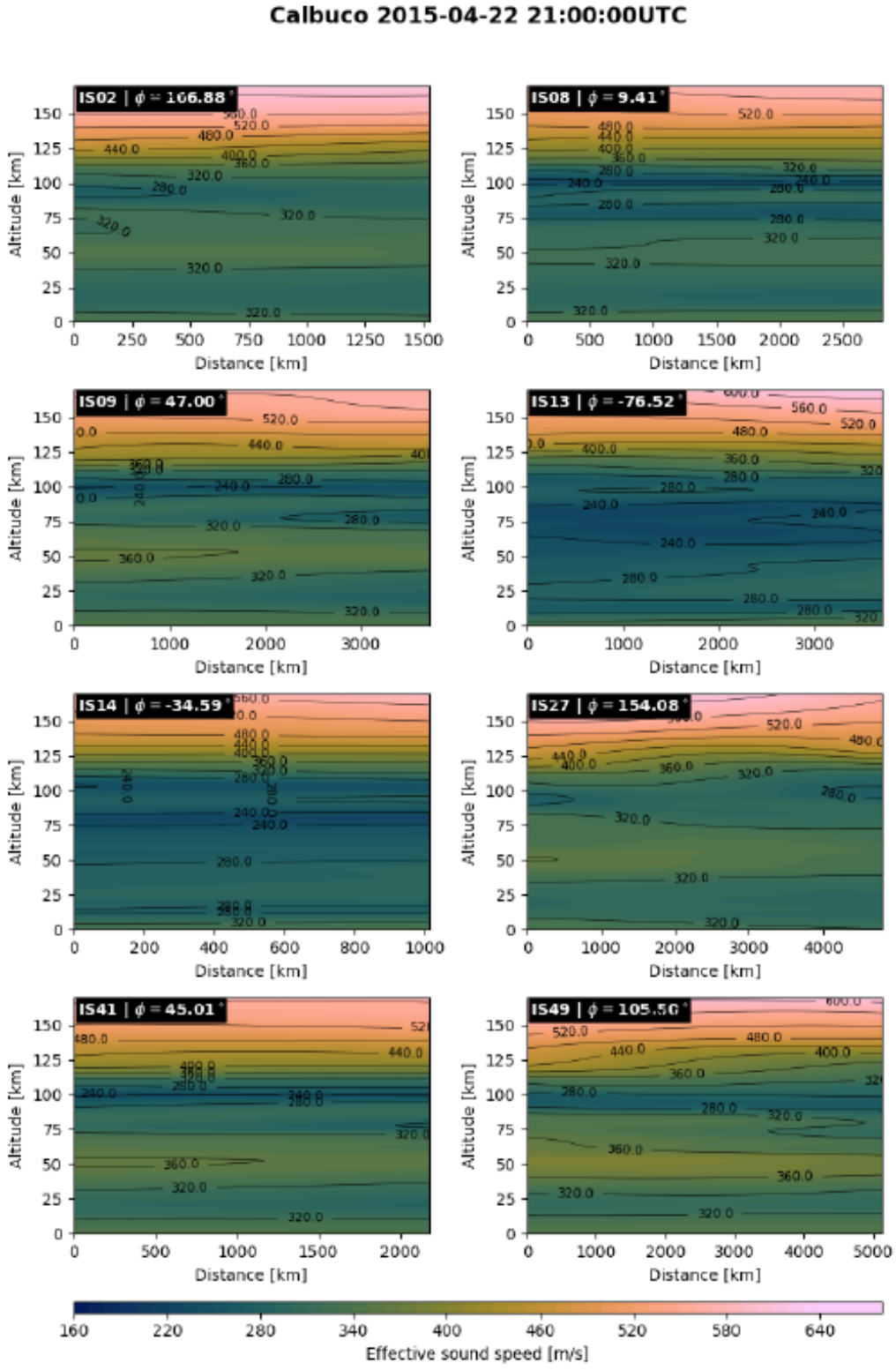

Figure A.4: Effective sound speed profiles for Calbuco using only climatologies.

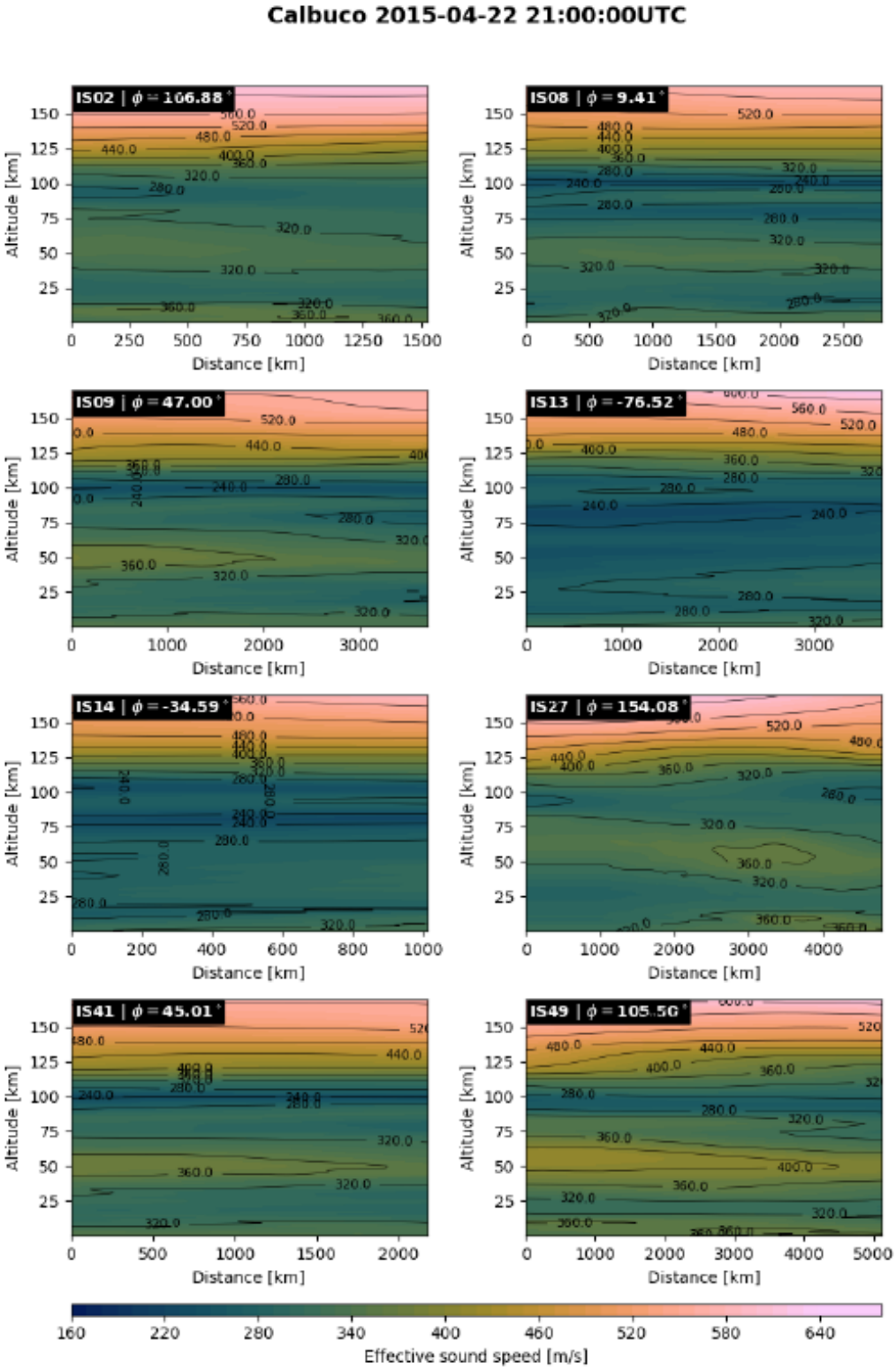

Figure A.5: Effective hybrid sound speed profiles for Calbuco.

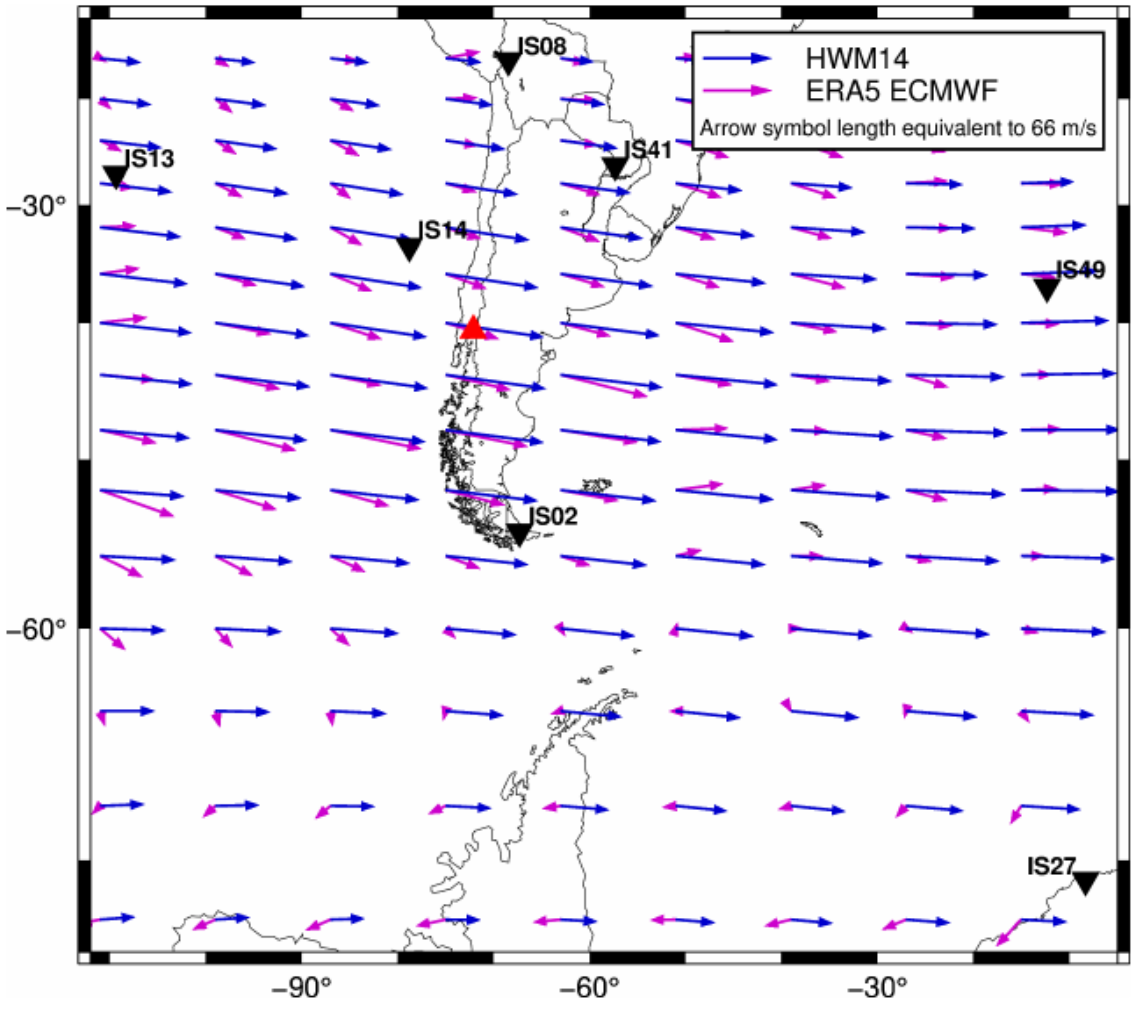

Figure A.6: Average of horizontal winds from 40 to 60 km altitude for Cordón-Caulle approximated eruption time (2011-06-04 19:00 UTC).

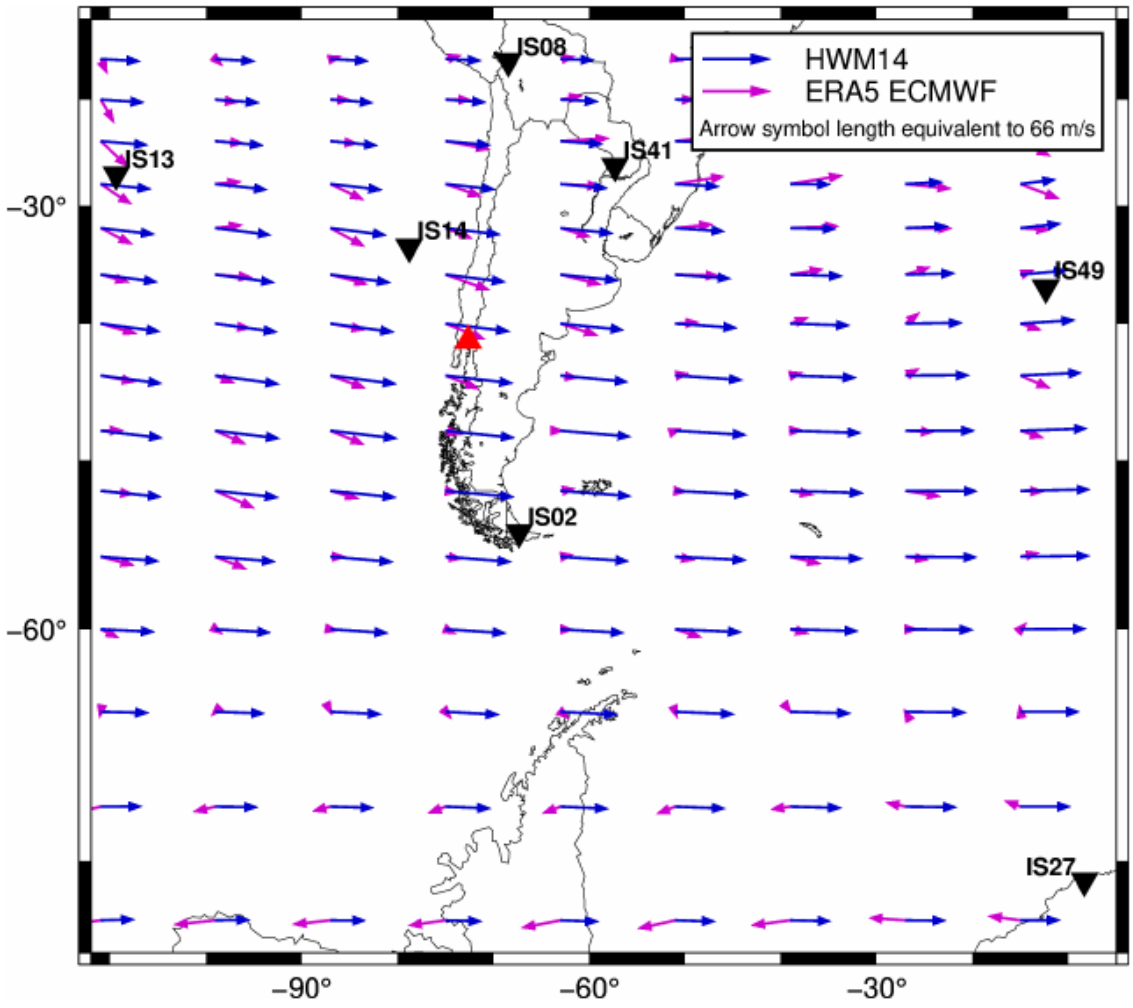

Figure A.7: Average of horizontal winds from 40 to 60 km altitude for Calbuco approximated eruption time (2015-04-22 21:00 UTC).

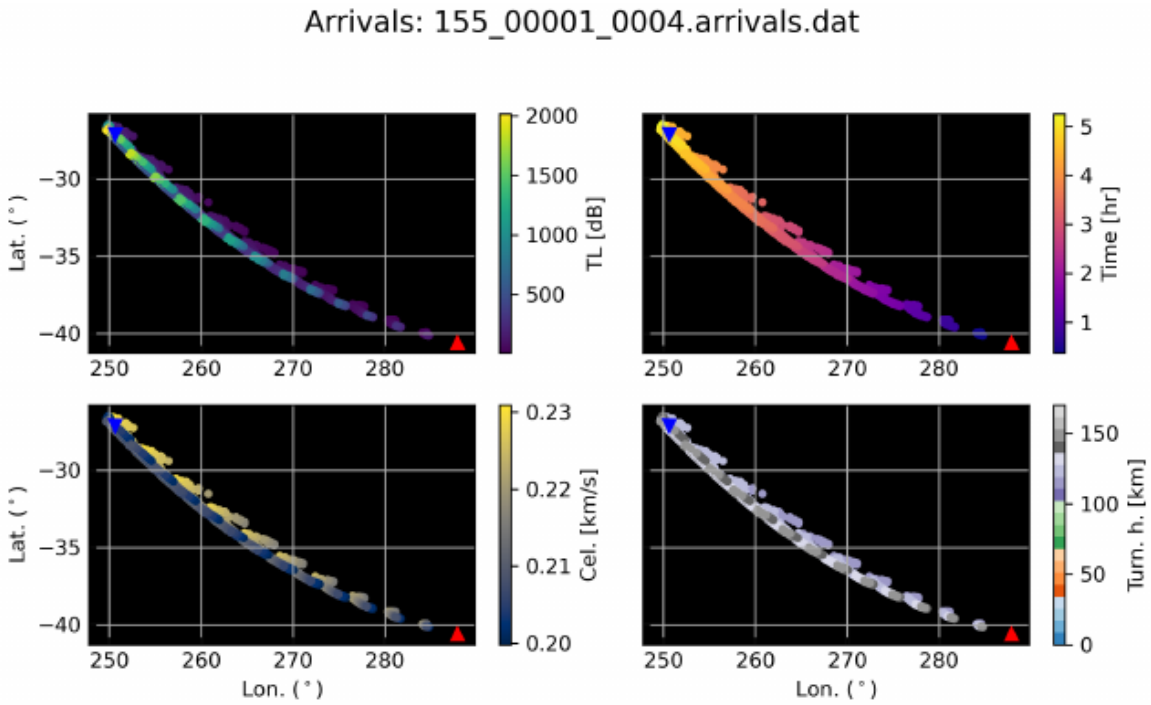

Figure A.8: Ground intercept information for rays modeled from Cordón Caulle to IS13 station for approximate eruption time (2011-06-04 at 19:00 UTC). The model corresponds to a raw climatology, considering stratospheric and thermospheric arrivals ("strato. and thermo."). Red triangle: position of Cordón Caulle. Blue inverted triangle: position of station. Each panel colors the ground intercept by a different property. Top left: transmission loss (dB). Top right: travel time (hrs.). Bottom left: celerity (km/s). Bottom right: turning height (km).

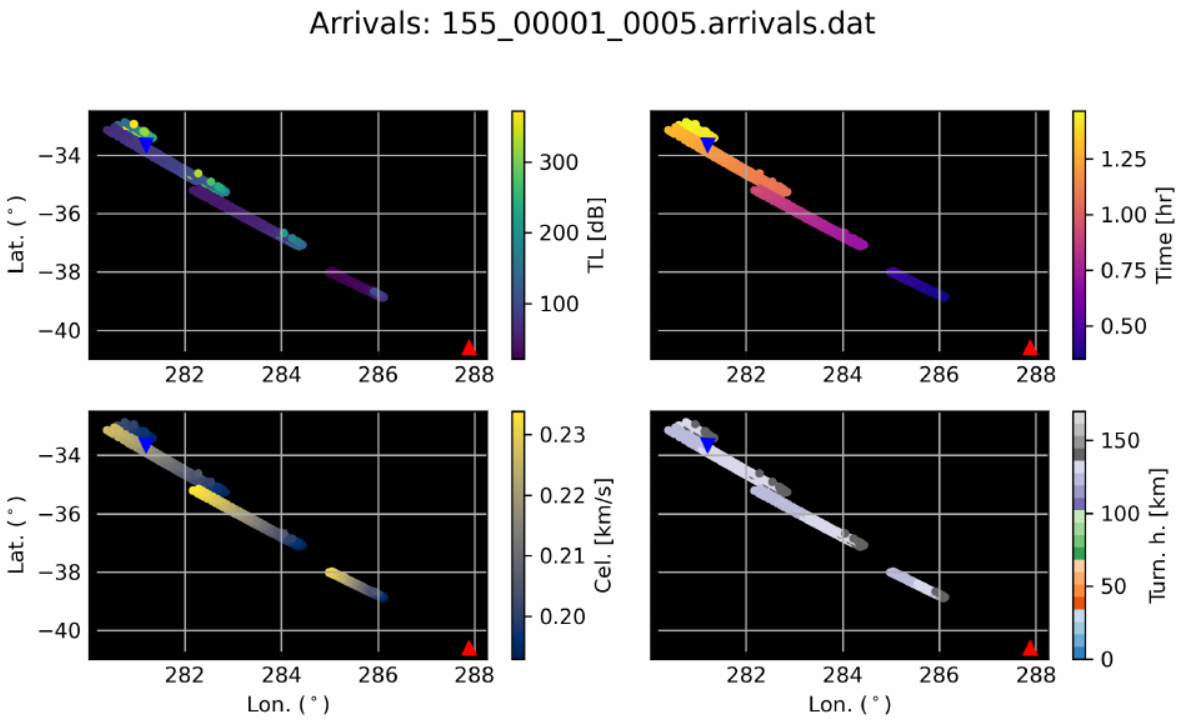

Figure A.9: Ground intercept information for rays modeled from Cordón Caulle to IS14 station for approximate eruption time (2011-06-04 at 19:00 UTC). Model and plot characteristics are analogous to Figure A.8.

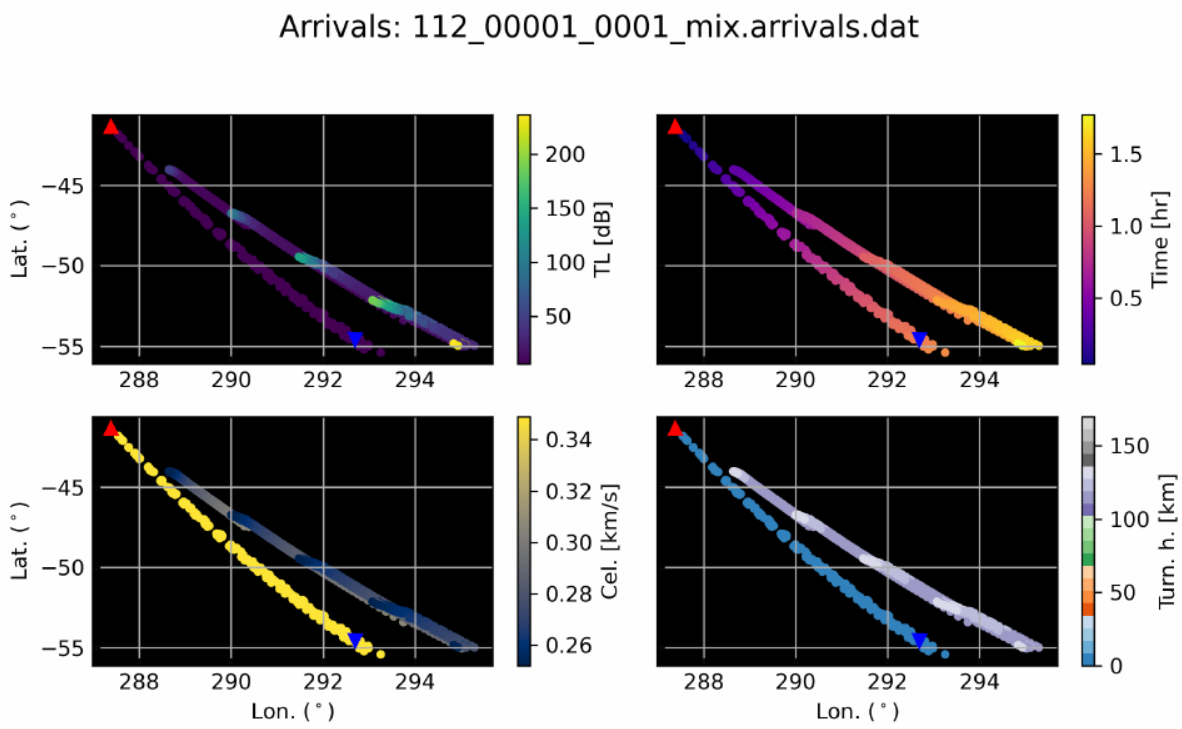

Figure A.10: Ground intercept information for rays modeled from Calbuco to IS02 station for approximate eruption time (2015-04-22 at 21:00 UTC). In this case, the model is hybrid, considering stratospheric and thermospheric arrivals ("strato. and thermo"). Same plot types as A.8.

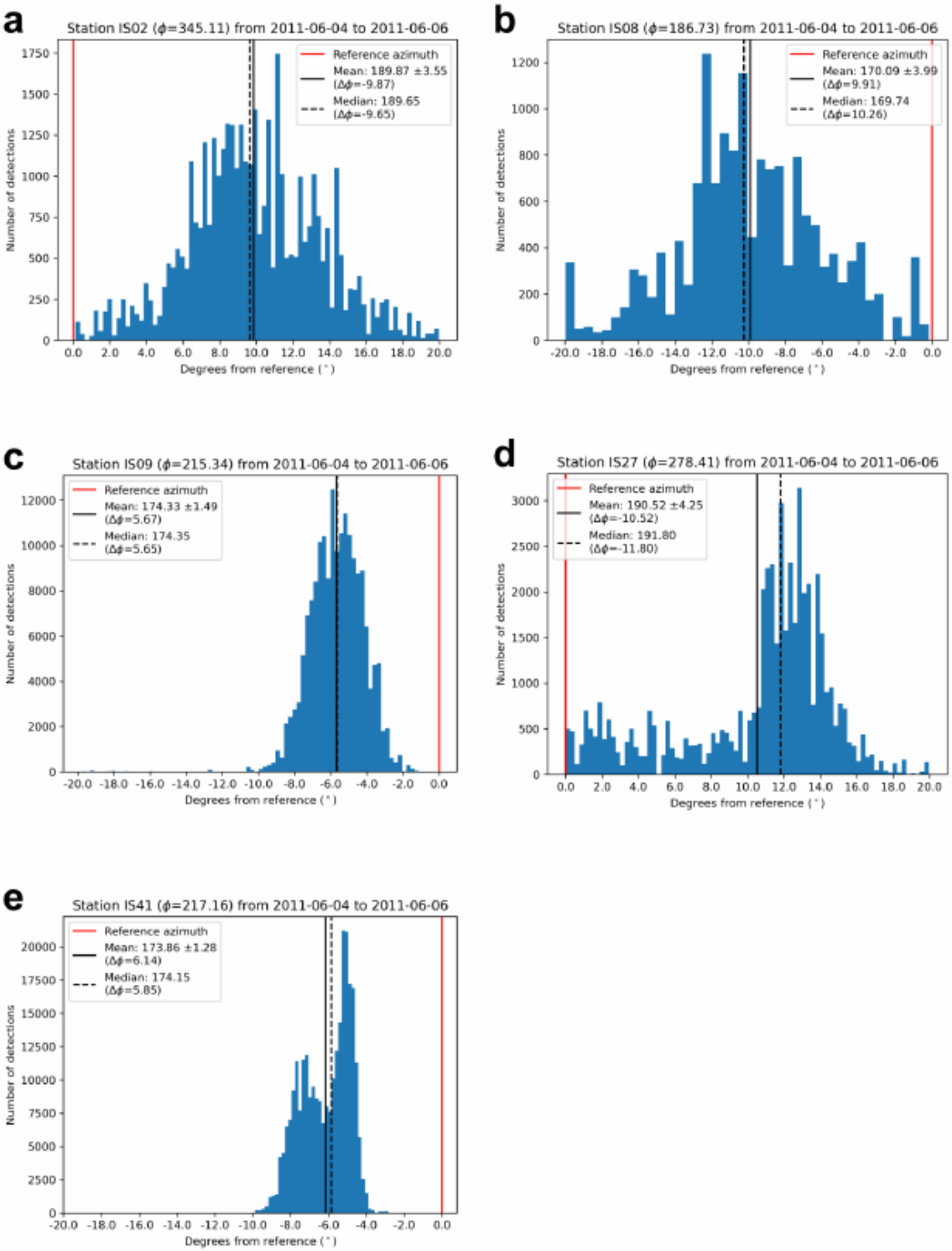

Figure A.11: Histograms for PMCC detections in 2-day window from eruption onset of Puyehue-Cordón Caulle (2011-06-10). Bins of 0.25° are used for an azimuth range that starts at reference azimuth from each station to ±20°, depending on the expected deviation of the modeled detections.

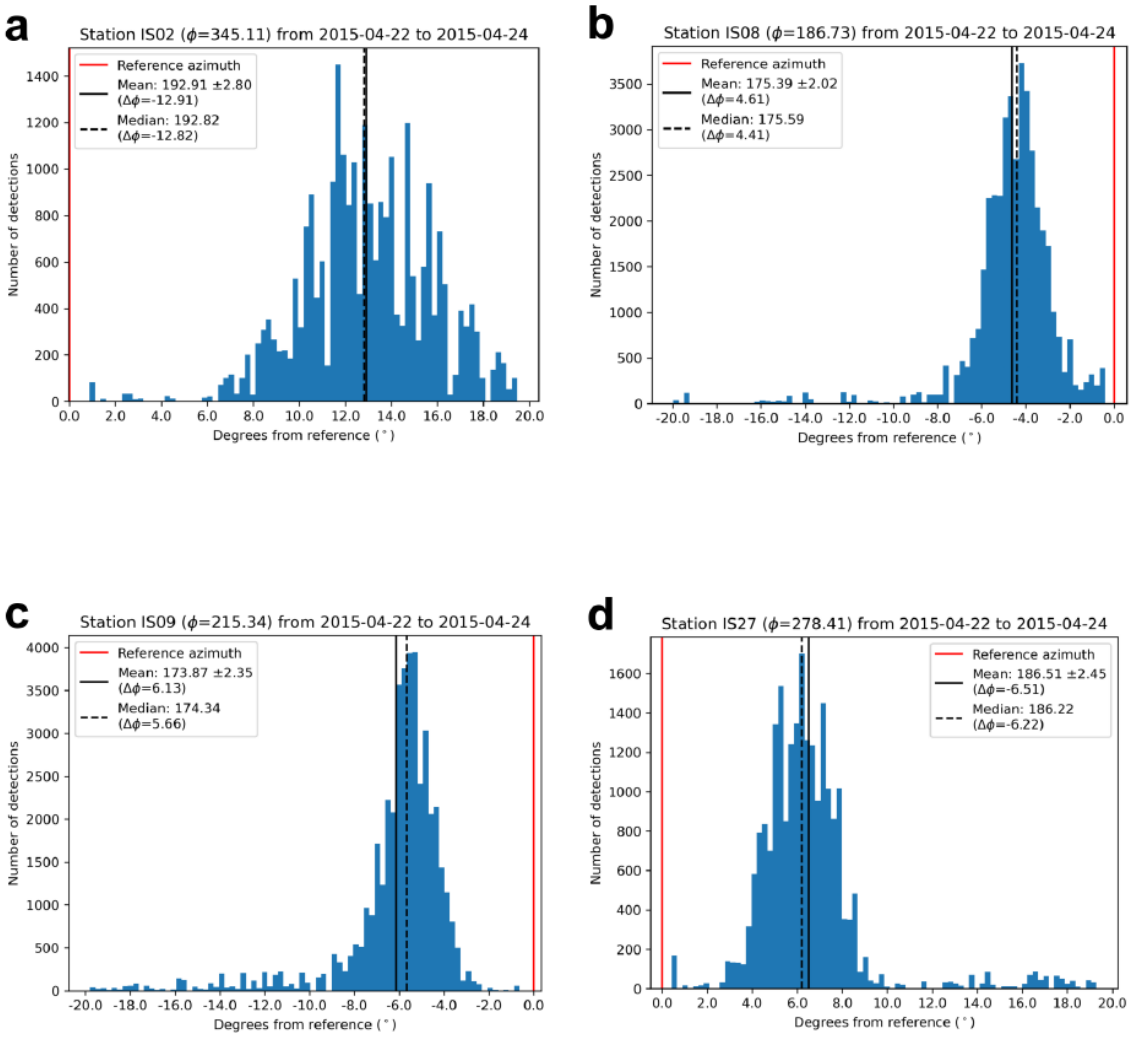

Figure A.12: Histograms for PMCC detections in 2-day window from eruption onset of Puyehue-Cordón Caulle (2011-06-10). Same discretization as Figure A.11.

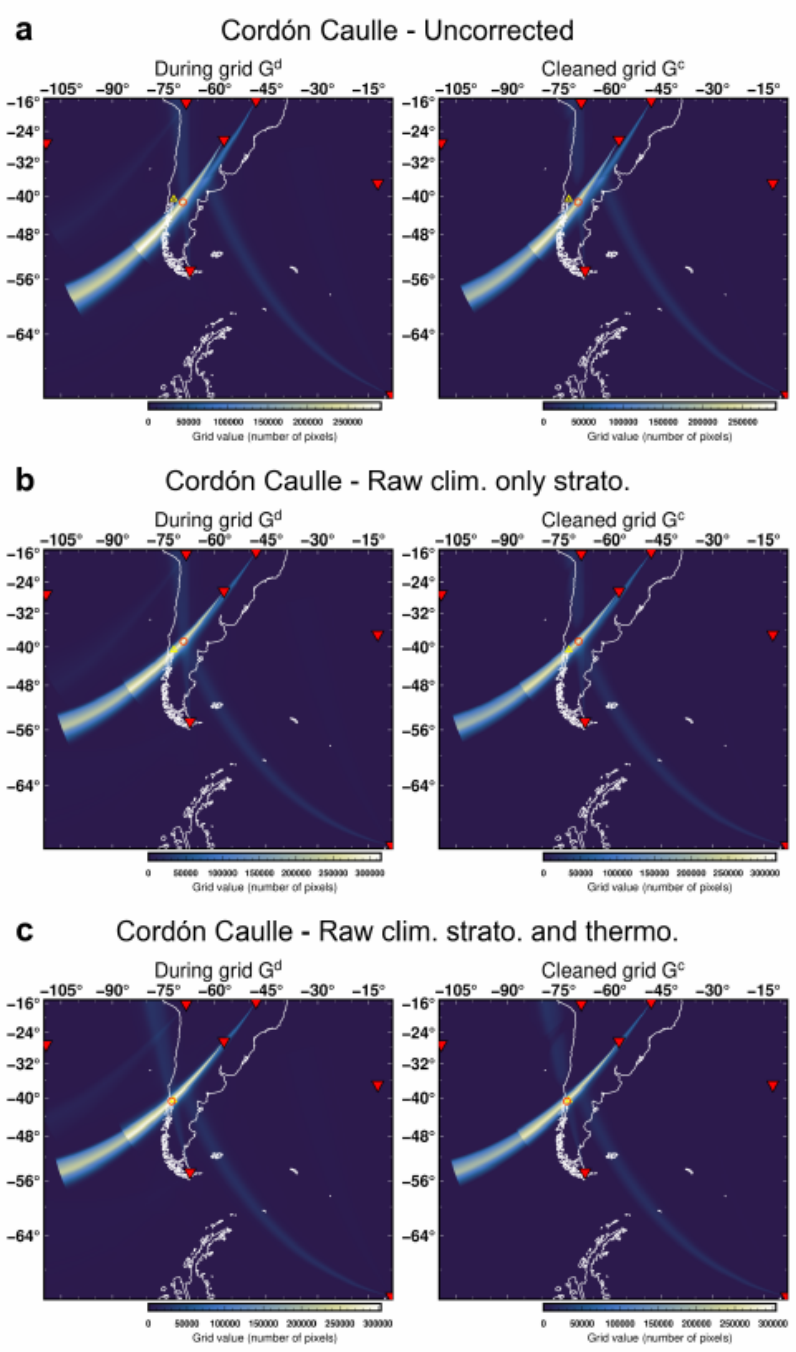

Figure A.13: IMS_vASC results for Puyehue-Cordón Caulle eruption with data from the available stations up to ∼5,000 km distance. Yellow triangles: position of volcano. Red inverted triangles: positions of recording stations. Yellow circle: apparent source location after cross-bearings.

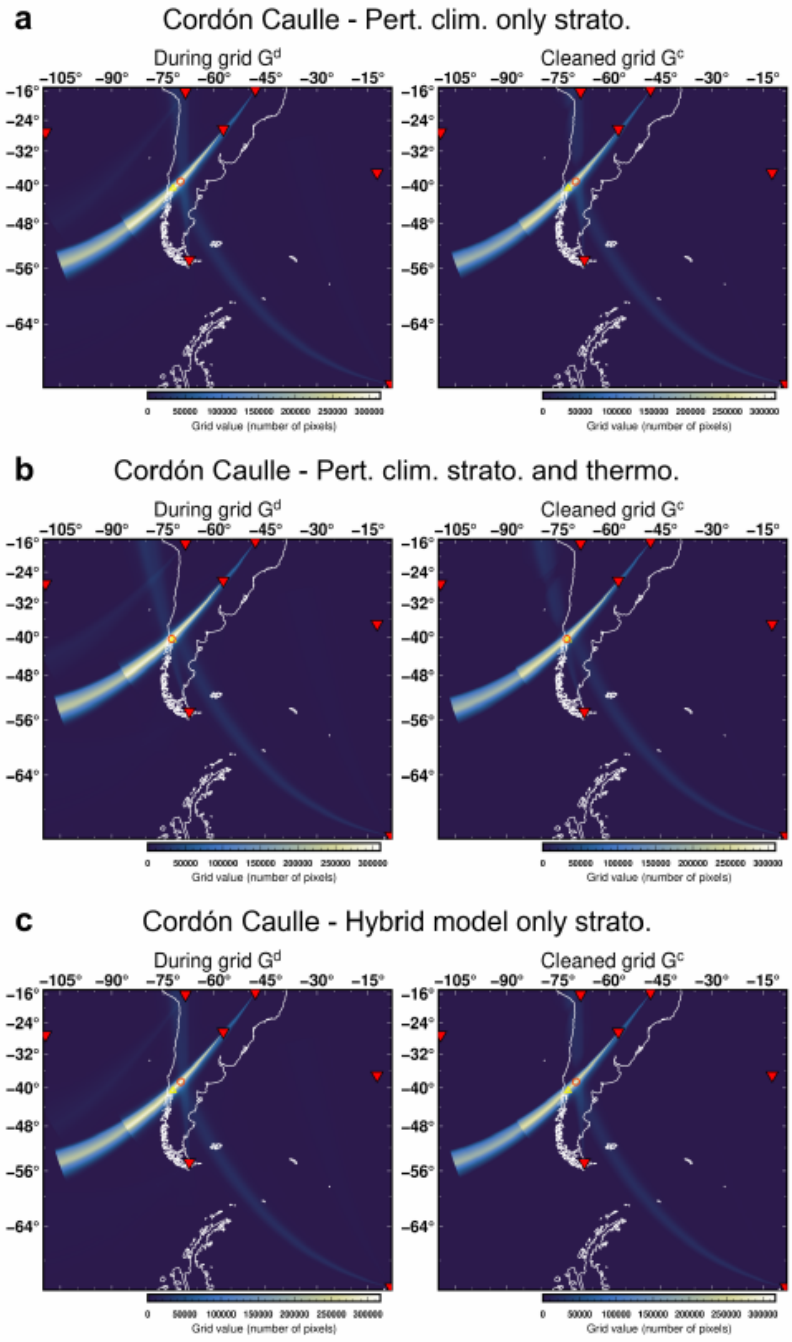

Figure A.14: IMS_vASC results for Puyehue-Cordón Caulle eruption with data from the available stations up to ∼5,000 km distance (continuation of Figure A.13).

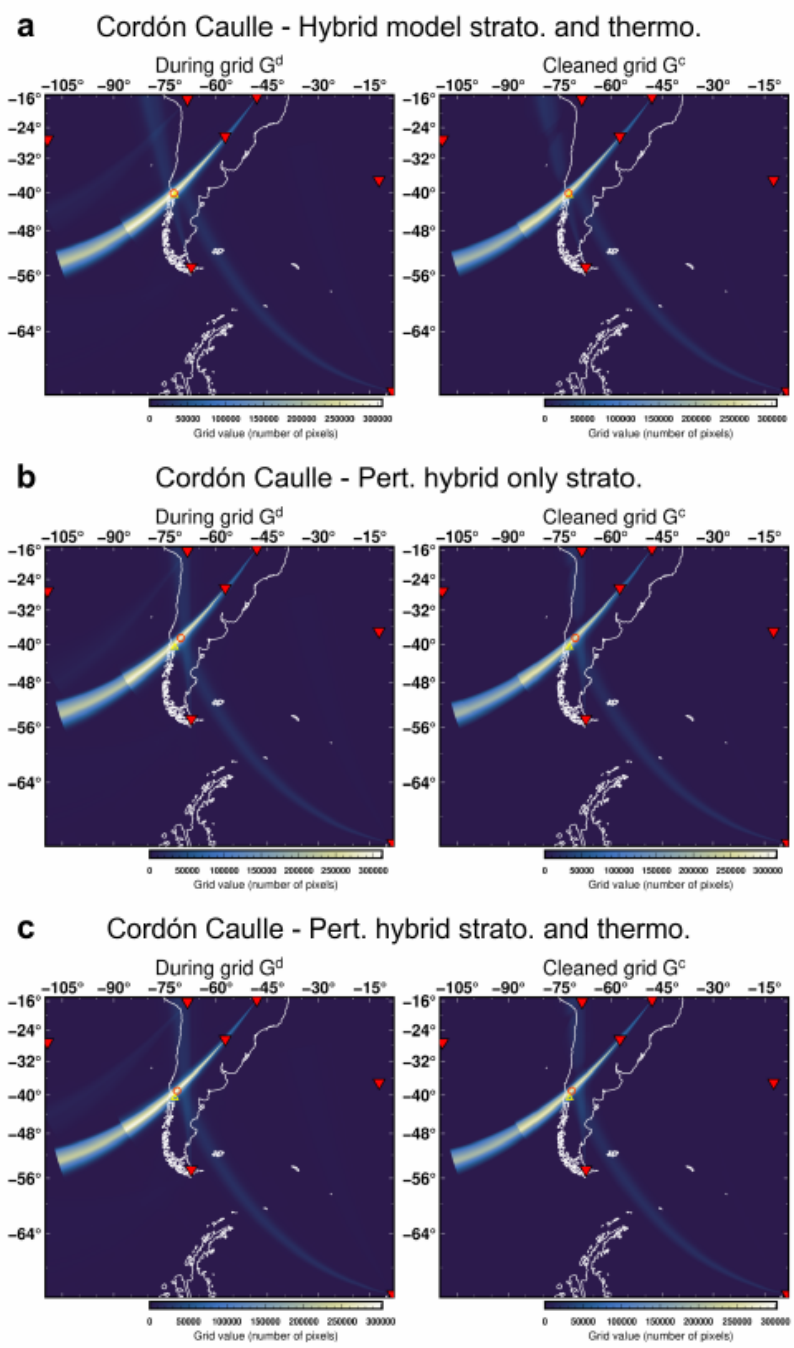

Figure A.15: IMS_vASC results for Puyehue-Cordón Caulle eruption with data from the available stations up to ∼5,000 km distance (continuation of Figure A.13).

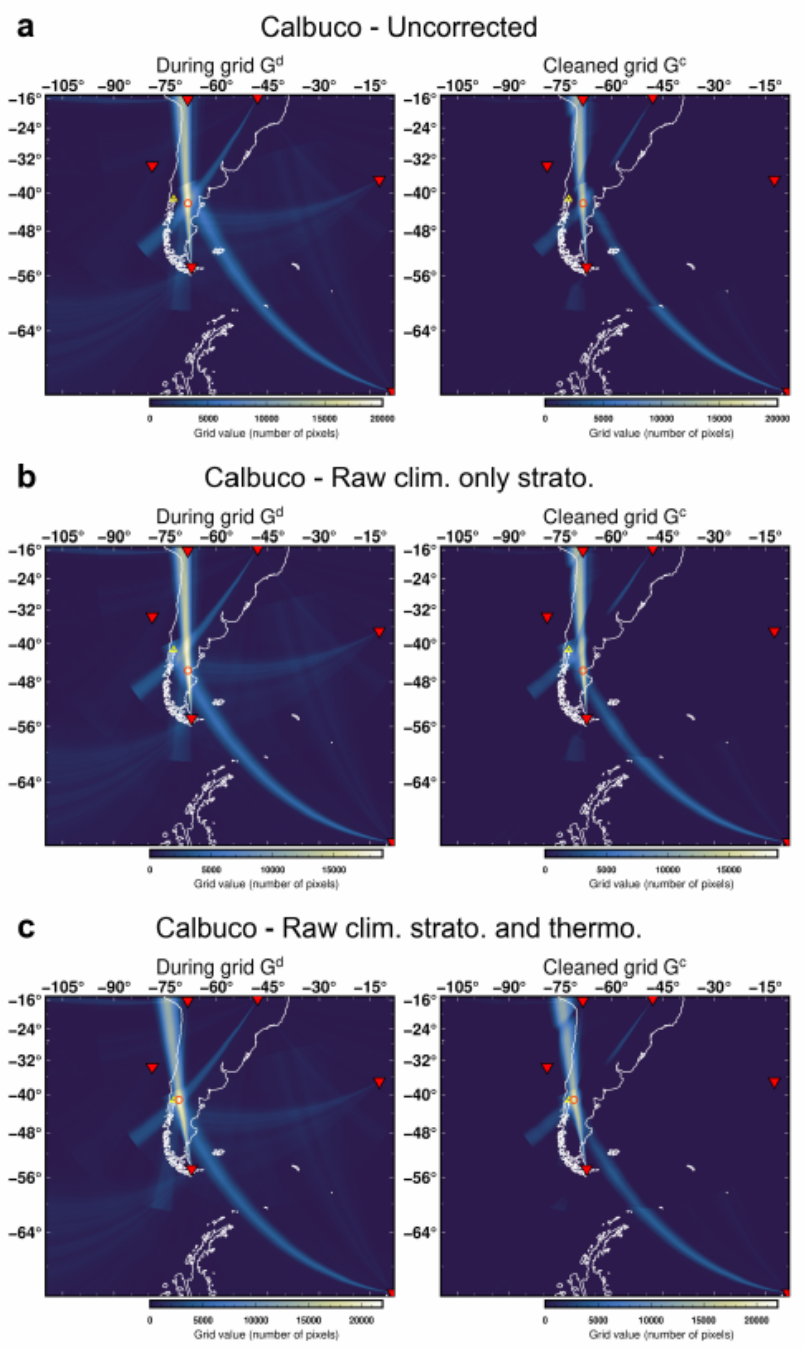

Figure A.16: IMS_vASC results for Calbuco eruption with data from the available stations up to ∼5,000 km distance. Yellow triangles: position of volcano. Red inverted triangles: positions of recording stations. Yellow circle: apparent source location after cross-bearings.

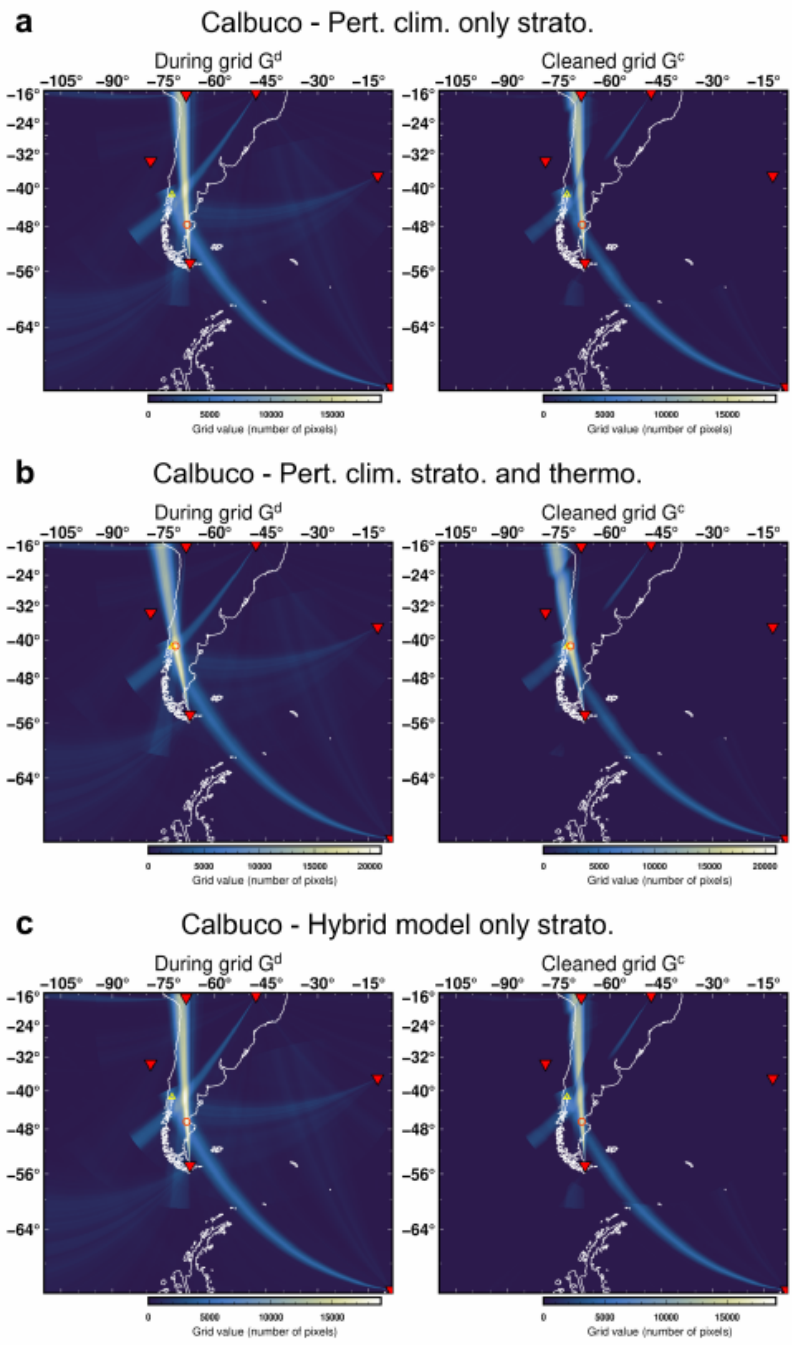

Figure A.17: IMS_vASC results for Calbuco eruption with data from the available stations up to ∼5,000 km distance (continuation of Figure A.16).

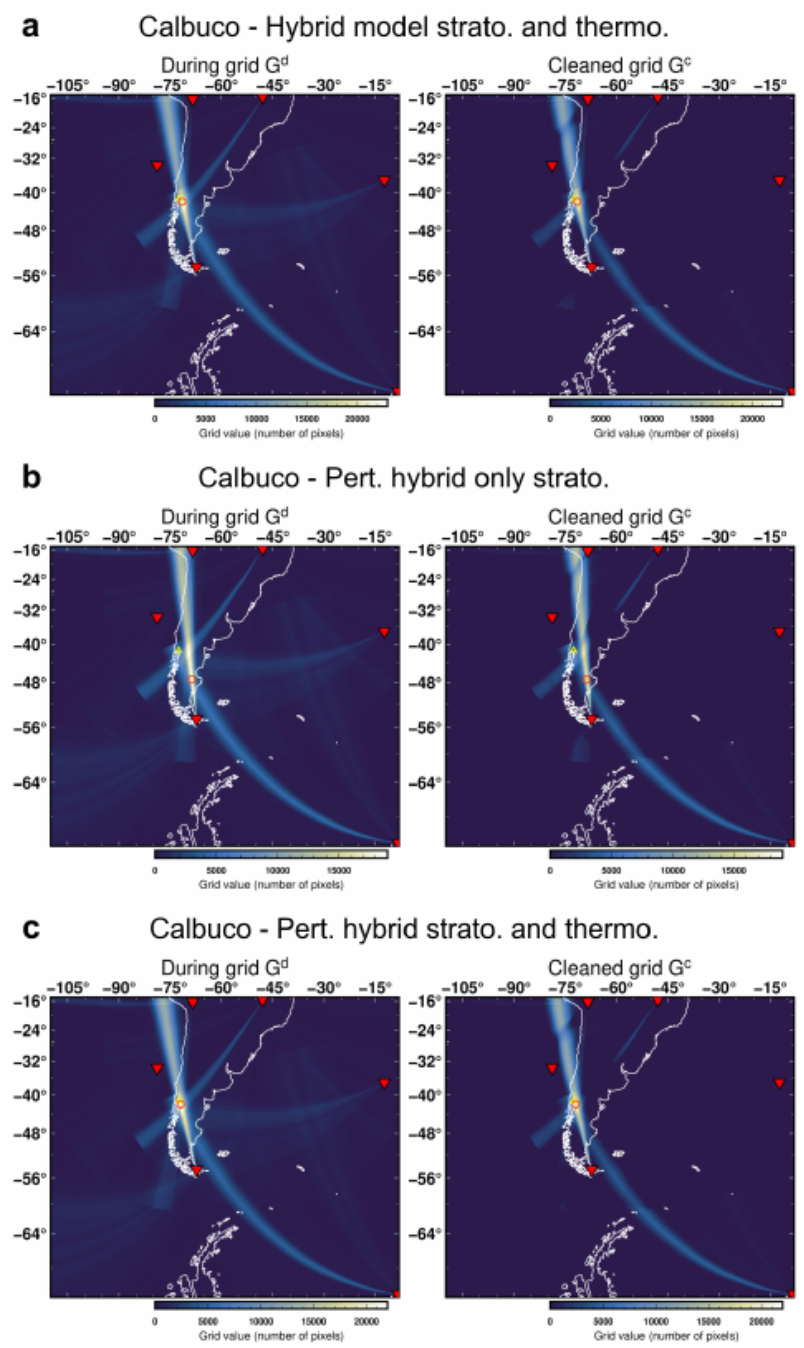

Figure A.18: IMS_vASC results for Calbuco eruption with data from the available stations up to ∼5,000 km distance (continuation of Figure A.16).

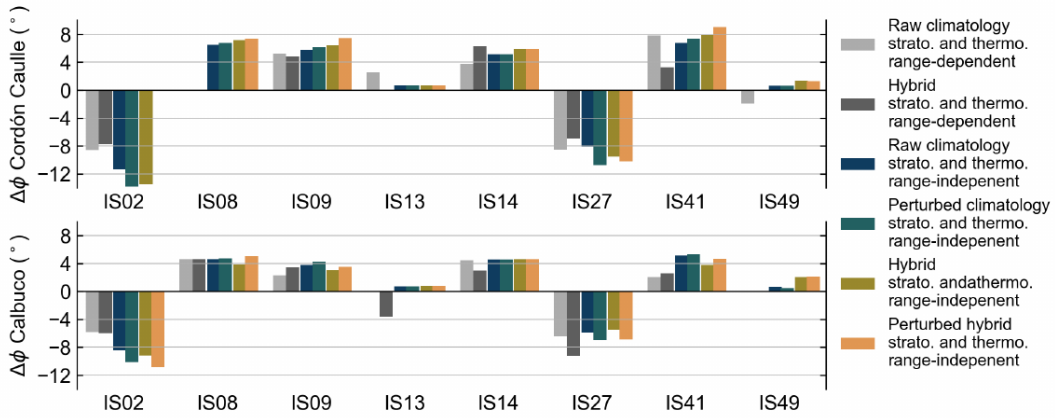

Figure A.19: Comparison of "strato. and thermo." back-azimuth deviation results for both volcanoes. In gray bars, range-dependent calculations performed using climatologies and hybrid descriptions.

Appendix B

Supporting Information for "Evaluating the temporal capability of empirical climatologies for rapid long-range volcanic infrasound propagation estimates using a multi-decadal dataset of persistent Vanuatu volcanic eruptions"

B.1 Additional figures

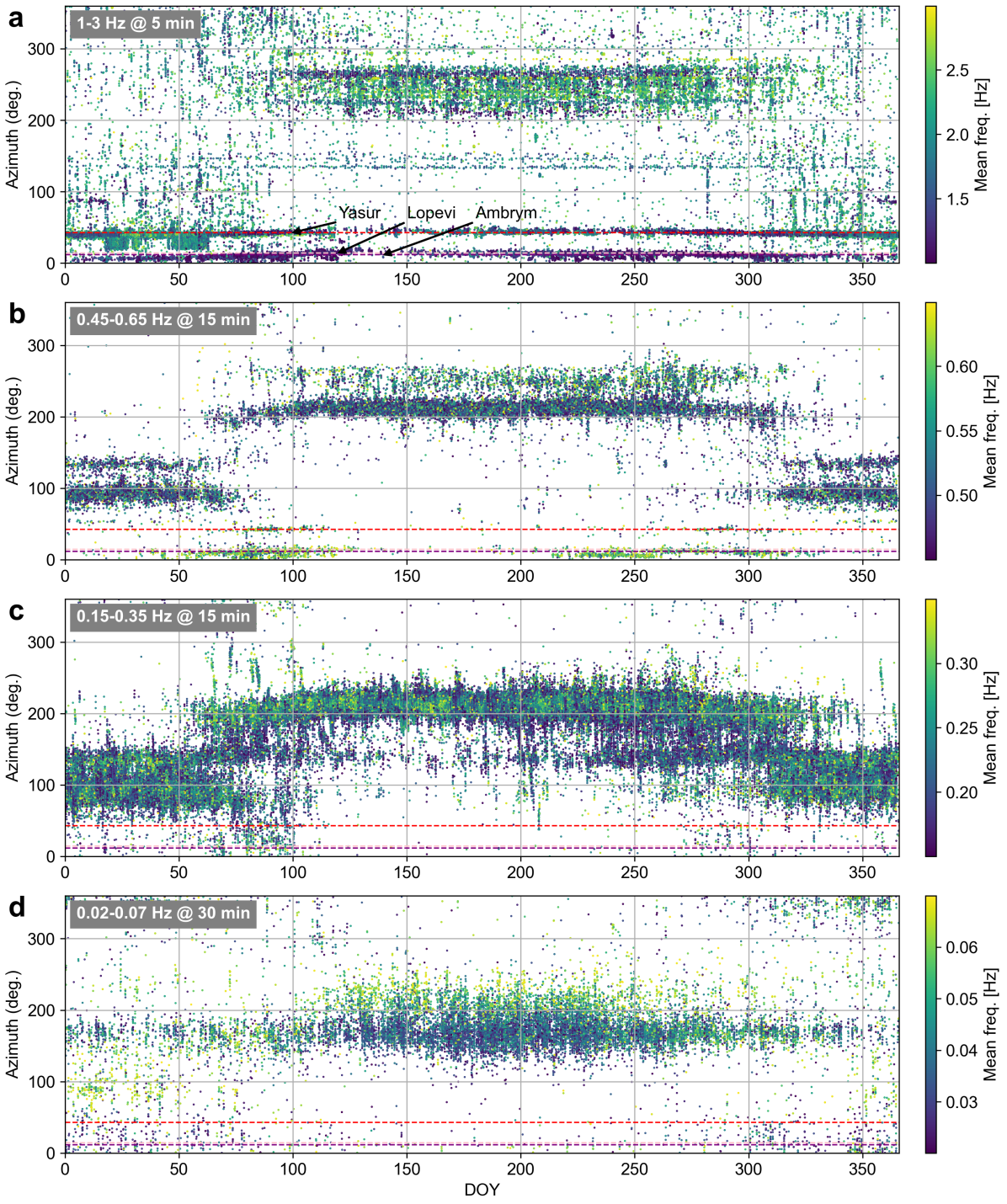

Figure B.1: All detections from 2003 to 2022 for the four PMCC products considered in this study. (a) "High-frequency" products (1-3 Hz), which are used in this study. (b) "Microbarom high-frequency" (0.45-0.65 Hz) products, that also have detections (less numerous than the high-frequency) at Ambrym/Lopevi azimuths. (c) "Microbarom low-frequency" (0.15-0.35 Hz) products. (d) "Mountain-associated waves" (0.02-0.07 Hz) products.

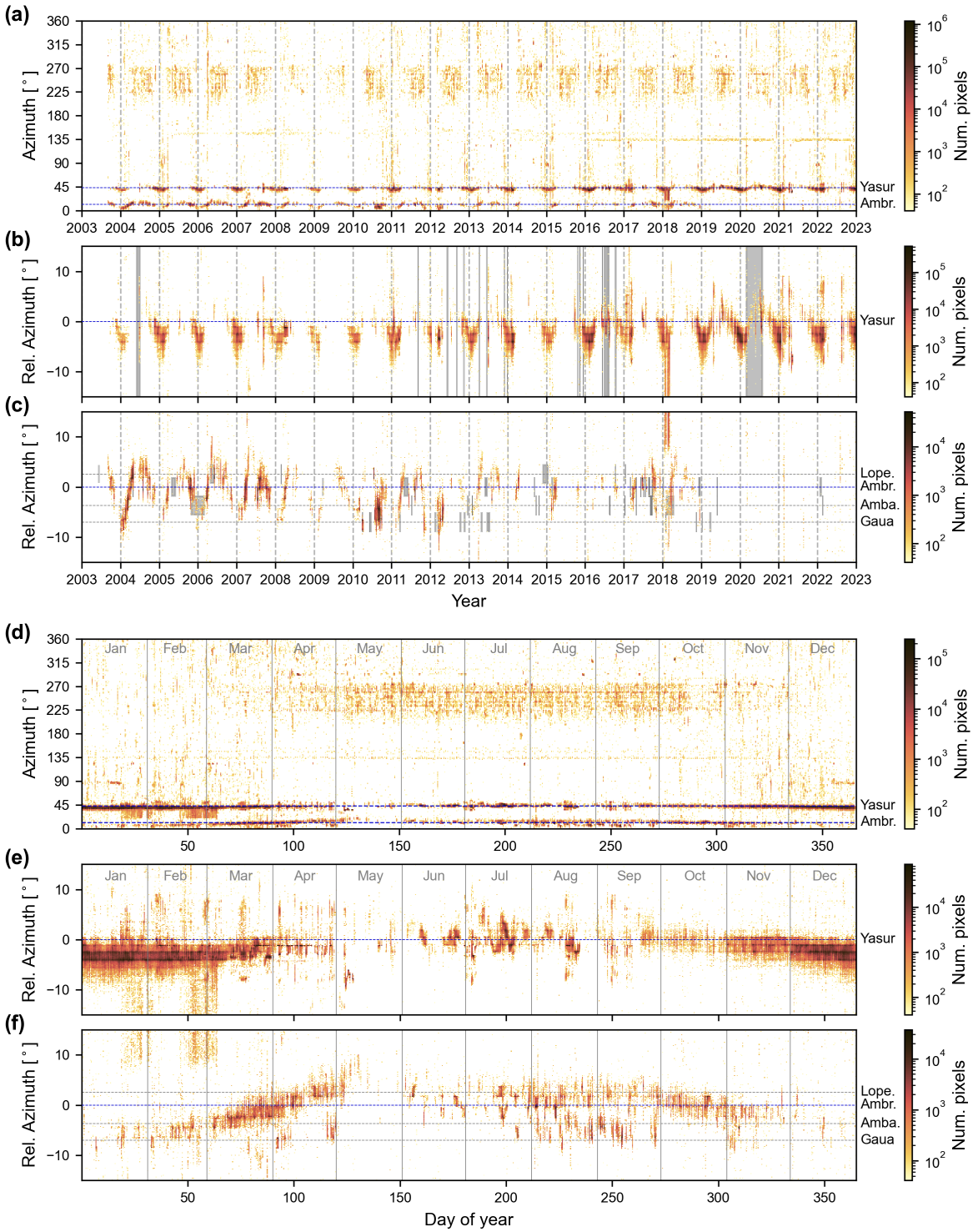

Figure B.2: Similar to 2 in main paper, but using 27-band PMCC detections (2003 to 2022) instead.

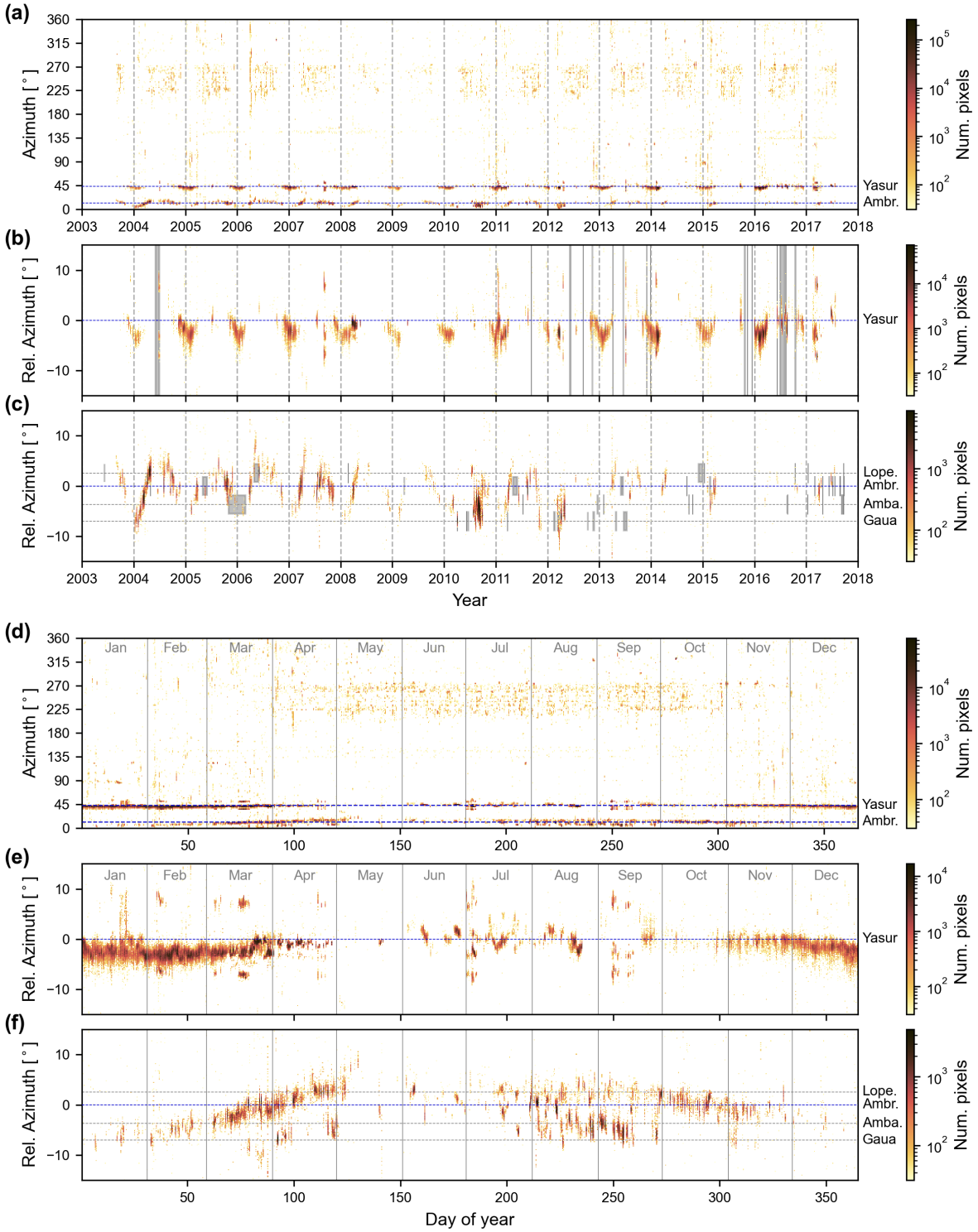

Figure B.3: Similar to 2 in main paper, but using 15-band PMCC detections from 2003 to 2017 (inclusive) instead.

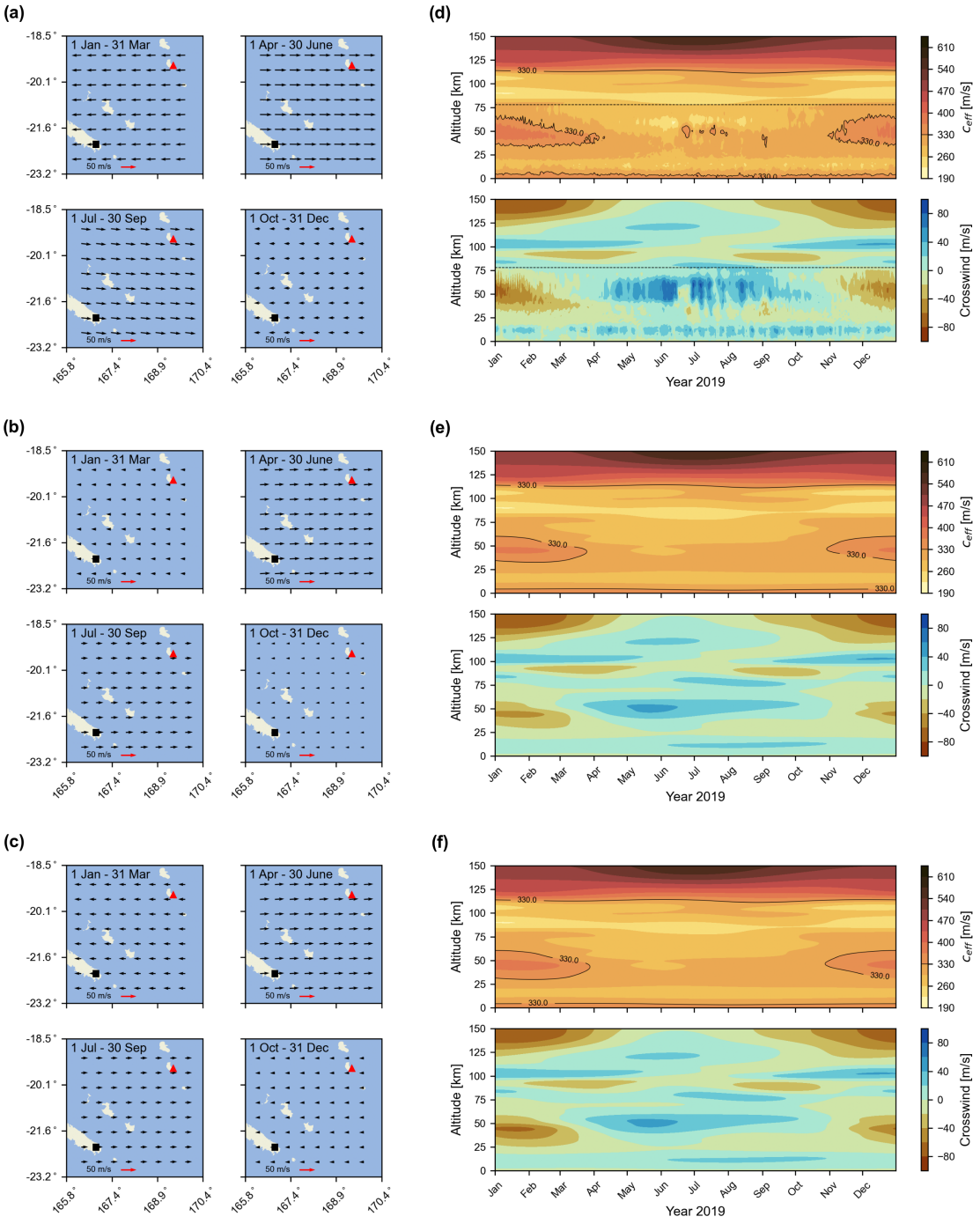

Figure B.4: Similar to 3 in main paper, but at 06:00:00 UTC

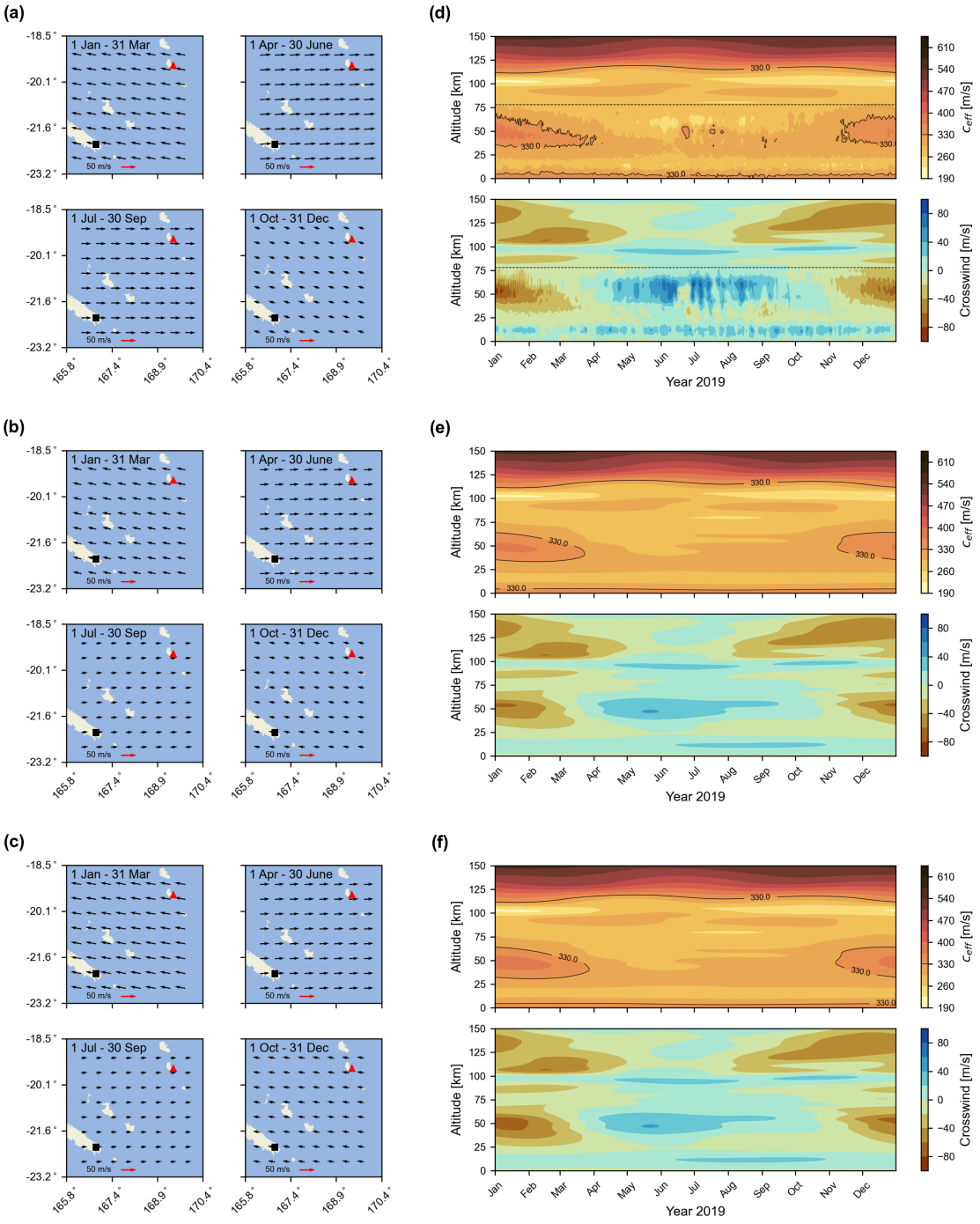

Figure B.5: Similar to 3 in main paper, but at 12:00:00 UTC

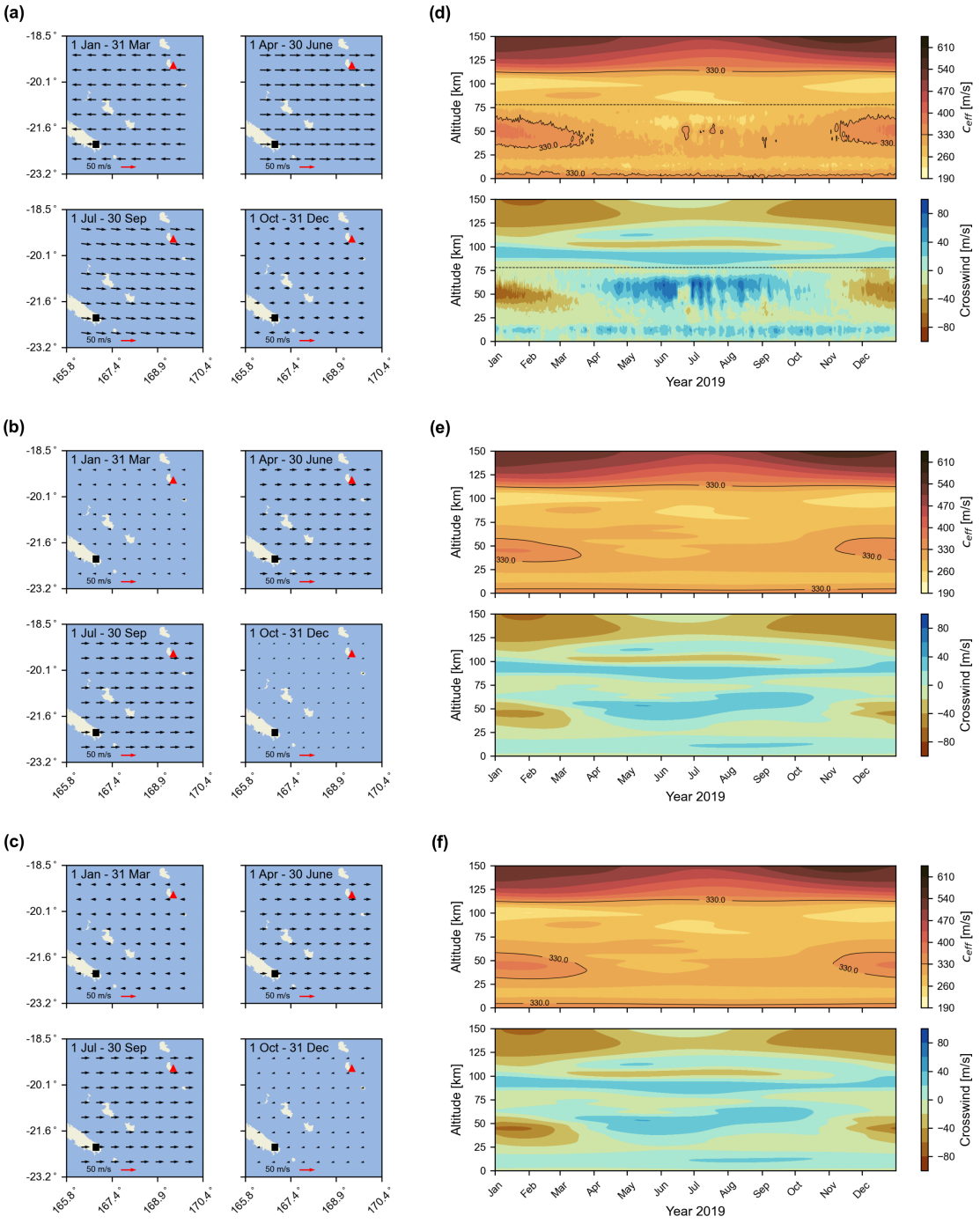

Figure B.6: Similar to 3 in main paper, but at 18:00:00 UTC

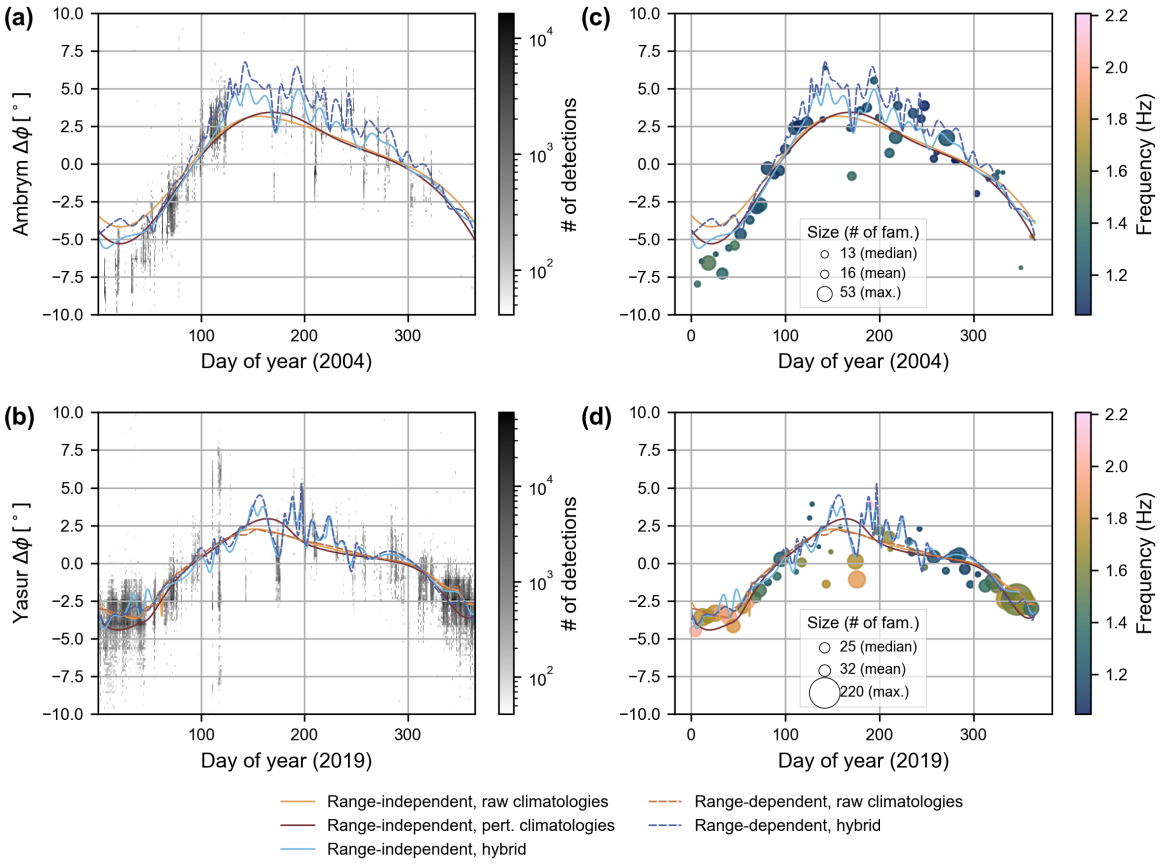

Figure B.7: Similar to Figure 7 in main paper, but using 26-band PMCC detections for Ambrym (2004) and Yasur (2019) (SI Figure B.2)

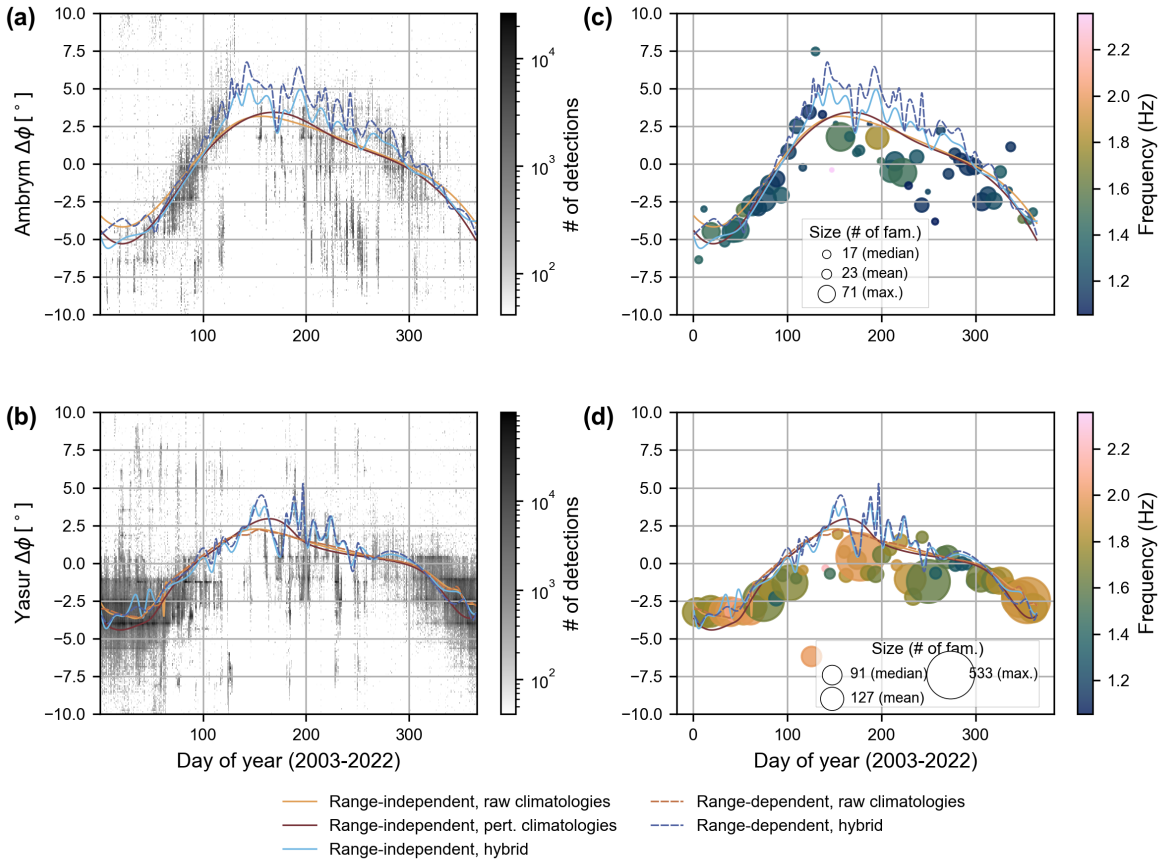

Figure B.8: Similar to Figure 8 in main paper, but using 26-band PMCC detections from 2003 to 2022 (SI Figure B.2)

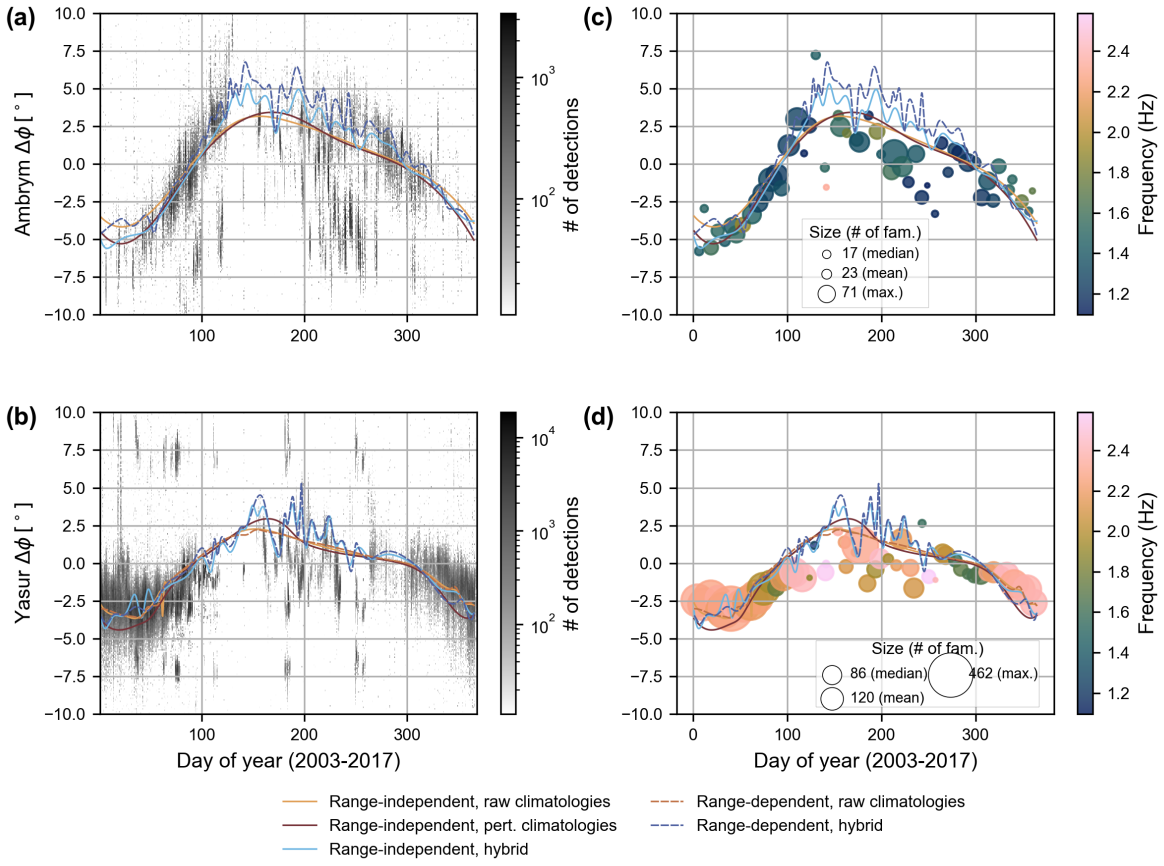

Figure B.9: Similar to Figure 8 in main paper, but using 15-band PMCC detections from 2003 to 2017 (SI Figure B.3)

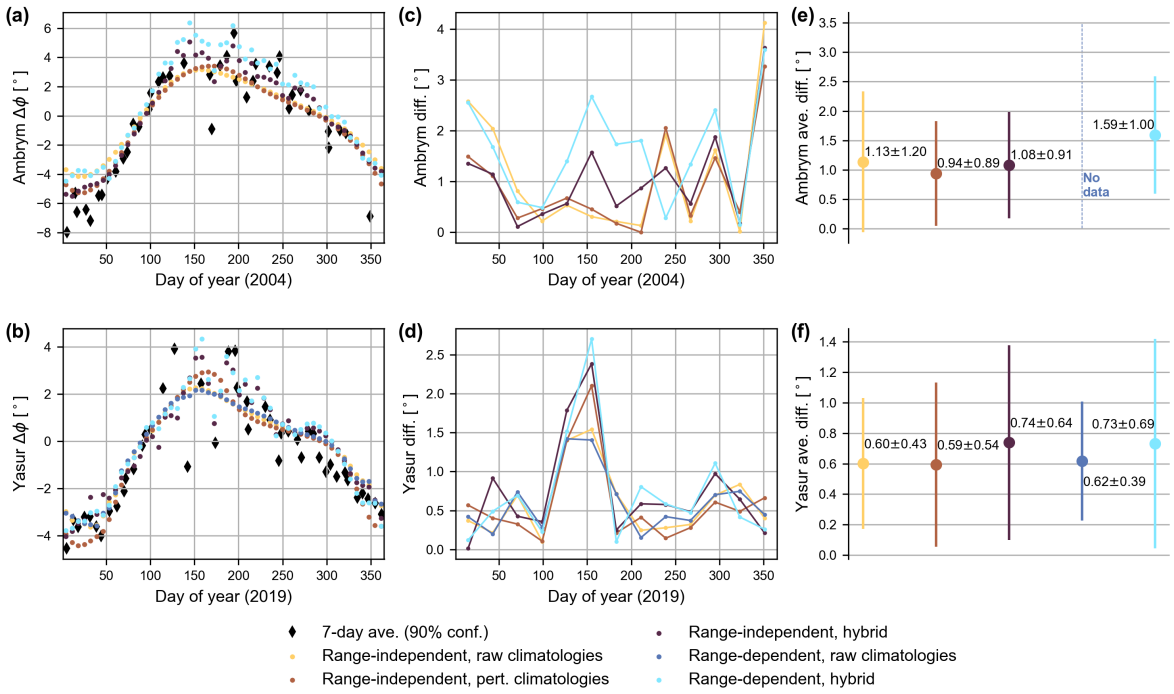

Figure B.10: Comparison of 7-day average of detections with 90% confidence interval and model results. Subplot (a), left: scatter plot of the high-frequency (1-3 Hz) PMCC detection products (Hupe et al., 2021b), for 2004 (black diamonds) and all the models calculated for Ambrym (colored dots, see legend on bottom). Subplot (a), middle: Euclidean distance between the detections and the models for intervals of 28 days through the year, colored by the model case. Subplot (a), right: averaged difference for the whole years based on the information displayed in the middle plot, following the same color meanings. We include the standard deviations of each model in vertical thin bars. Subplot (b) is analogous to (a), but for Yasur in 2019.

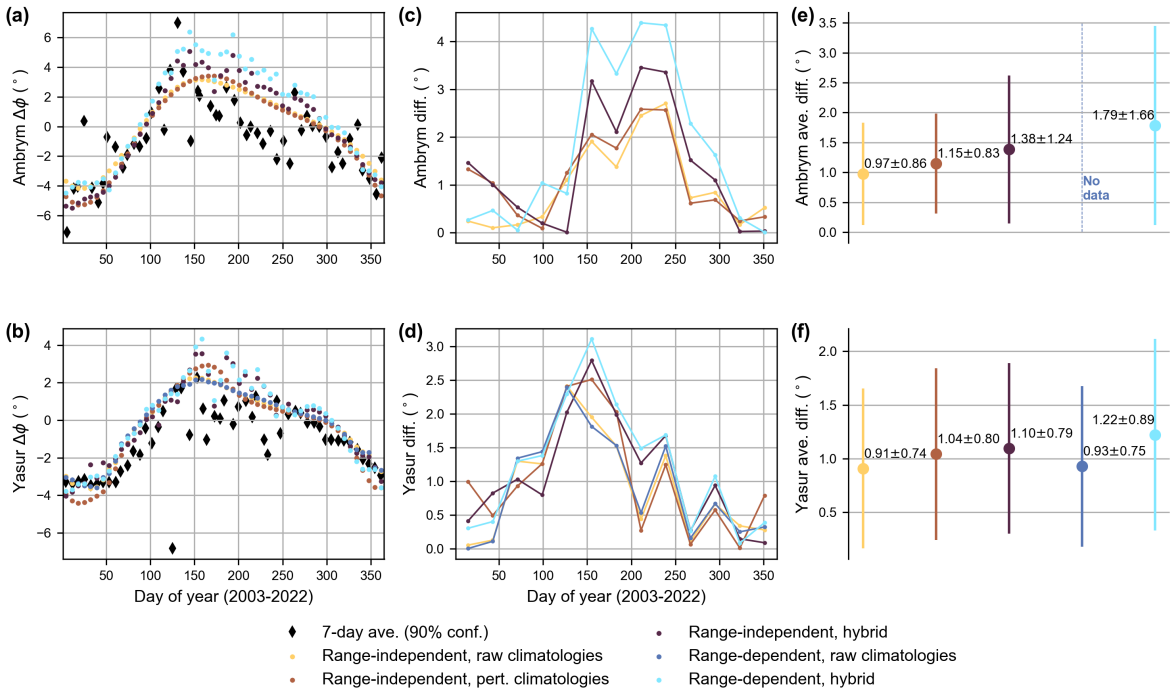

Figure B.11: Similar to Figure B.10, high-frequency (1-3 Hz) PMCC detection products from 2003 to 2022 (Hupe et al., 2021b).

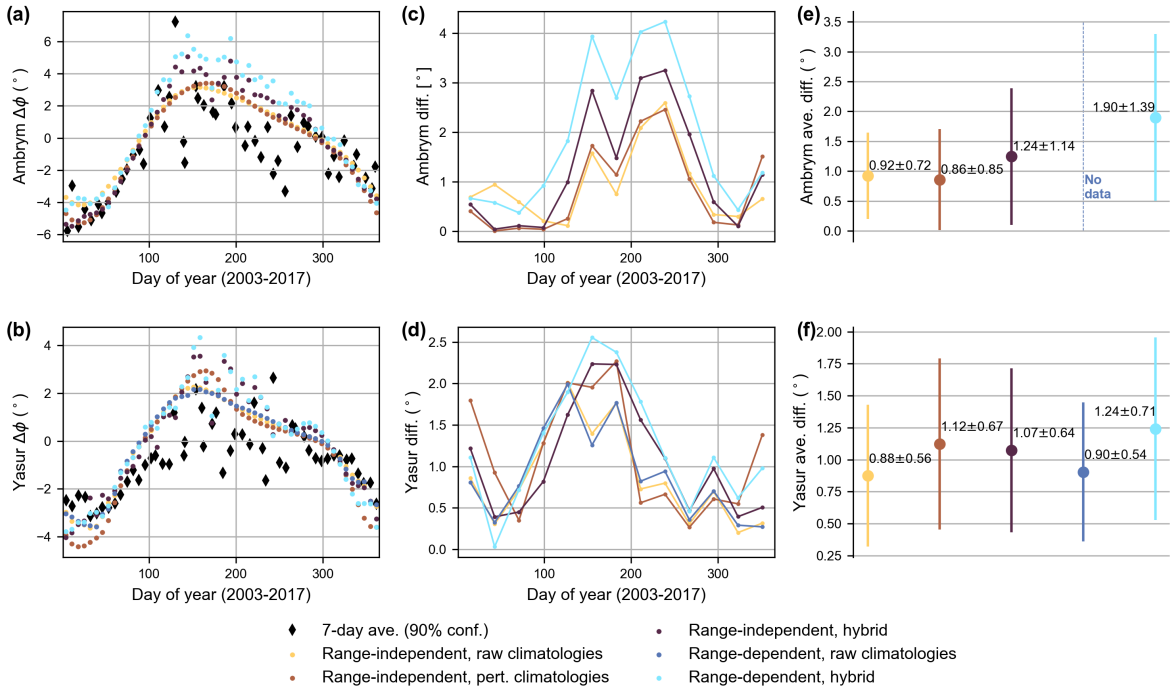

Figure B.12: Similar to Figure 11 in main paper, but using 15-band PMCC detection products from 2003 to 2017 (Matoza et al., 2013)

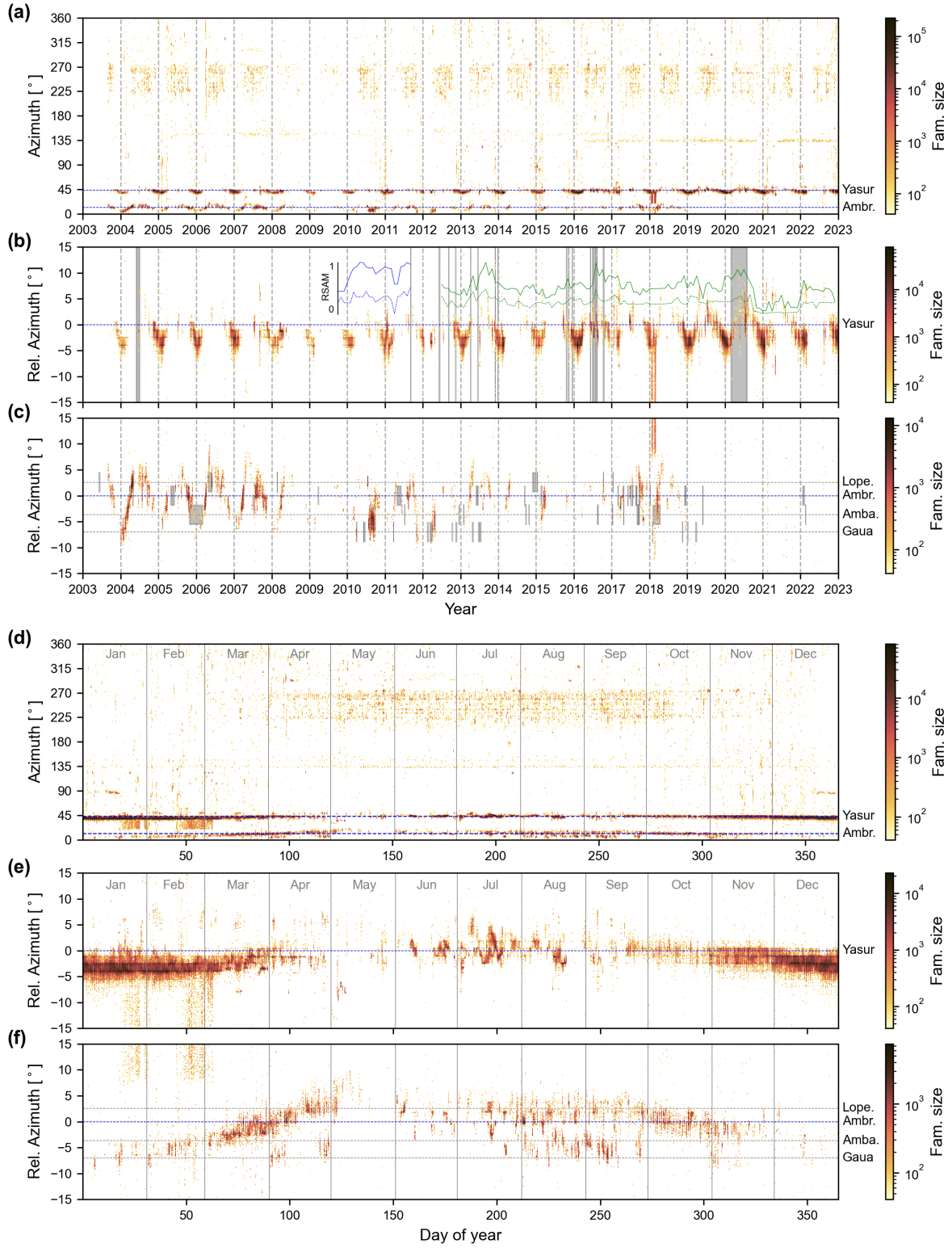

Figure B.13: Unlabeled version of Figure 2 in main paper.

Appendix C

Supporting Information for "Long-range multi-year infrasonic detection of eruptive activity at Mount Michael volcano, South Sandwich Islands"

C.1 Seasonal back-azimuth variation

We expect (candidate) detections at IS27 from Mount Michael with azimuths from ∼320 to 330 (see Figure C.1) degrees and frequencies from ∼0.7 to 3.0 Hz. By manual inspection of frequency vs. azimuth 2D histogram plots, we found candidate infrasound mainly from 2005 to 2006 and 2016 to 2018. To show this, we depict four consecutive 2D histograms of PMCC detections in the frequency-azimuth domain from 1 January 2005 to 1 January 2021 (see Figure C.2). It is clear that from 2007 to 2015 (Figure C.2b) and 2019 to 2021 (Figure C.2d), small numbers of detections in the candidate range appear, while from 2005 to 2006 (Figure C.2a) and 2016 to 2018 (Figure C.2c), two distinctive groups of detections are present. We isolated each of the two groups for each time interval with clear candidate infrasound and calculated the centroid considering the number of pixels of each 2D bin. We note the resulting frequency-azimuth coordinates for

the centroids in boxes in Figure C.2a,c. These centroids serve as reference characteristic detection parameters for candidate infrasound from Mount Michael. Figure C.3 shows the same time intervals but zoomed over 300 to 360 degrees.

C.2 k-means re-clustering method

The simplified resulting azimuth deviation curve from Figure C.1 is not straightforward to compare with the multi-year PMCC IS27 dataset. Therefore, following Cansi and Le Pichon (2008), we re-cluster the dataset to reduce the number of detections with a higher scatter in the time-trace velocity-azimuth-frequency domain using a k-means algorithm (see Eq. C.1). First, we test if the 4-D distance, d_{ij}, for each pair of pixels in the dataset is less than 1. Then, we re-cluster the pixels by the resulting average of each parameter. Figure 4.5a (main paper) is composed by re-clustered PMCC pixels where we calculate the 4-D distance using $\sigma_t = 100$ s, $\sigma_v = 0.01$ km/s, $\sigma_a = 1.0$ degrees, and $\sigma_f = 0.5$ Hz. Figures C.4 and C.5 show the original and the resulting re-clustered PMCC dataset in absolute time and day of year, respectively.

$$d_{ij} = \sqrt{\frac{(t_i - t_j)^2}{\sigma_t^2} + \frac{(v_i - v_j)^2}{\sigma_v^2} + \frac{(a_i - a_j)^2}{\sigma_a^2} + \frac{(f_i - f_j)^2}{\sigma_f^2}} \tag{C.1}$$

C.3 Reference amplitudes

We estimate the pressure amplitude at IS27 from detections that occur during time intervals where we see more probable volcanic activity from Mount Michael. Following Section 3.3 (main paper), we selected four times, considering azimuths from 320 to 330 degrees, and frequencies from 0.6 to 2.5 Hz:

1. From 1 May 2005 to 1 January 2008 (see Figure C.6).

2. From 1 May 2016 to 4 July 2016 (see Figure C.7).

3. From 1 February 2017 to 2 April 2017 (see Figure C.8).

4. From 1 January 2018 to 2 April 2018 (see Figure C.9).

We use the number of pixels of each detection as weights to average the observed pressure at IS27 (1,672 km). To estimate the pressure at 1 km from Mount Michael, we use Eq. 4.1 from the main paper with a reference stratospheric transmission loss of ∼74.9 dB, obtained from our 3D ray-tracing modeling. We display the resulting values for each time window in Table C.1.

C.4 In-depth analysis and classification

We determine the different types of infrasound at IS27 (i.e., microbarom, glacier calving, volcanic, etc.) by analyzing the PMCC dataset (2004-2020) through year-long (time vs. azimuth) and month-long (frequency vs. azimuth) plots (Figures C.10 to C.18). We refer to "candidate" infrasound as PMCC detections that explosive eruptive events at Mount Michael may produce. We use the azimuth deviation curve (Figure C.1) in each plot to distinguish detections that are within the expected azimuth in time. As examples of such plots, in this supplementary document we include:

1. Three years with "candidate" infrasound: 2005 (Figure C.10), 2006 (Figure C.11), and 2016 (Figure C.14).

2. A year with the only extensive data gap, caused by the relocation of IS27: 2009 (Figure C.12).

3. A year without "glacier calving" or "candidate" infrasound: 2014 (Figure C.13).

4. Two years with "mixed" infrasound (i.e. both glacier calving and candidate infrasound signatures): 2017 (Figure C.15) and 2018 (Figure C.16).

5. Two years with smaller candidate event sequences: 2013 (Figure C.17), 2020 (Figure C.18).

We summarize the main characteristics of candidate vs. glacier calving infrasound in Table C.2.

C.5 Additional Figures

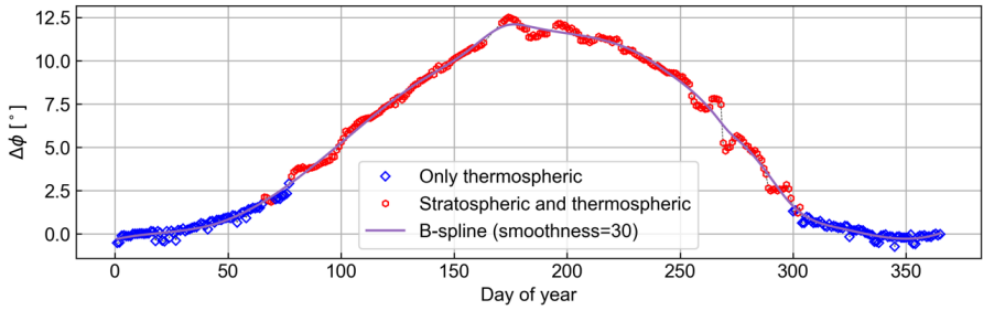

Figure C.1: 1-year model results for the azimuth deviation values at IS27 from Mount Michael. In the vertical axis: azimuth deviation in degrees as the difference between the geographical azimuth to Mount Michael from IS27 and the modeled azimuth of the infrasound rays that arrive at IS27. In the horizontal axis: day of year (DOY) of 2020 (note that the year is not relevant as we use empirical climatologies). In blue diamonds: azimuth deviation values calculated with rays that have thermospheric turning heights ∼120 km) only. In red hexagons: azimuth deviation values calculated with rays what have both stratospheric (∼40 km) and thermospheric turning heights.

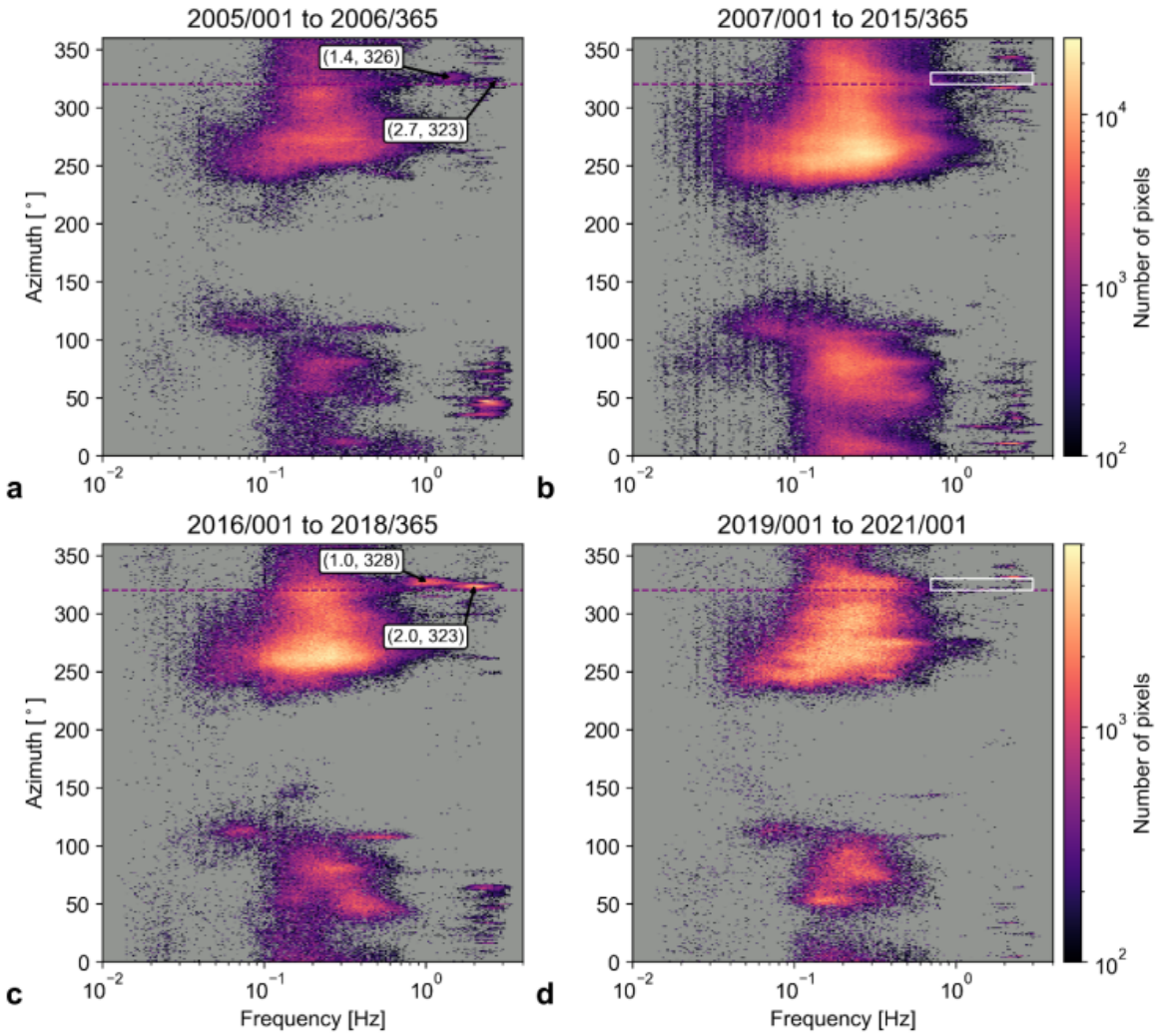

Figure C.2: Overview of IS27 PMCC detections in frequency vs. azimuth 2D histograms for four consecutive time periods. In a dashed purple line: Mount Michael azimuth from IS27. In white boxes with arrows for panels a and c: coordinates of centroids of the two characteristic groups of candidate detections in frequency (Hz) and azimuth (degrees). In a white rectangle for panels b and d: depiction of frequency-azimuth range of possible detections from Mount Michael. (a) From 1 January 2005 to 31 December 2006. (b) From 1 January 2007 to 31 December 2015. (c) From 1 January 2016 to 31 December 2018. (d) From 1 January 2019 to 1 January 2021.

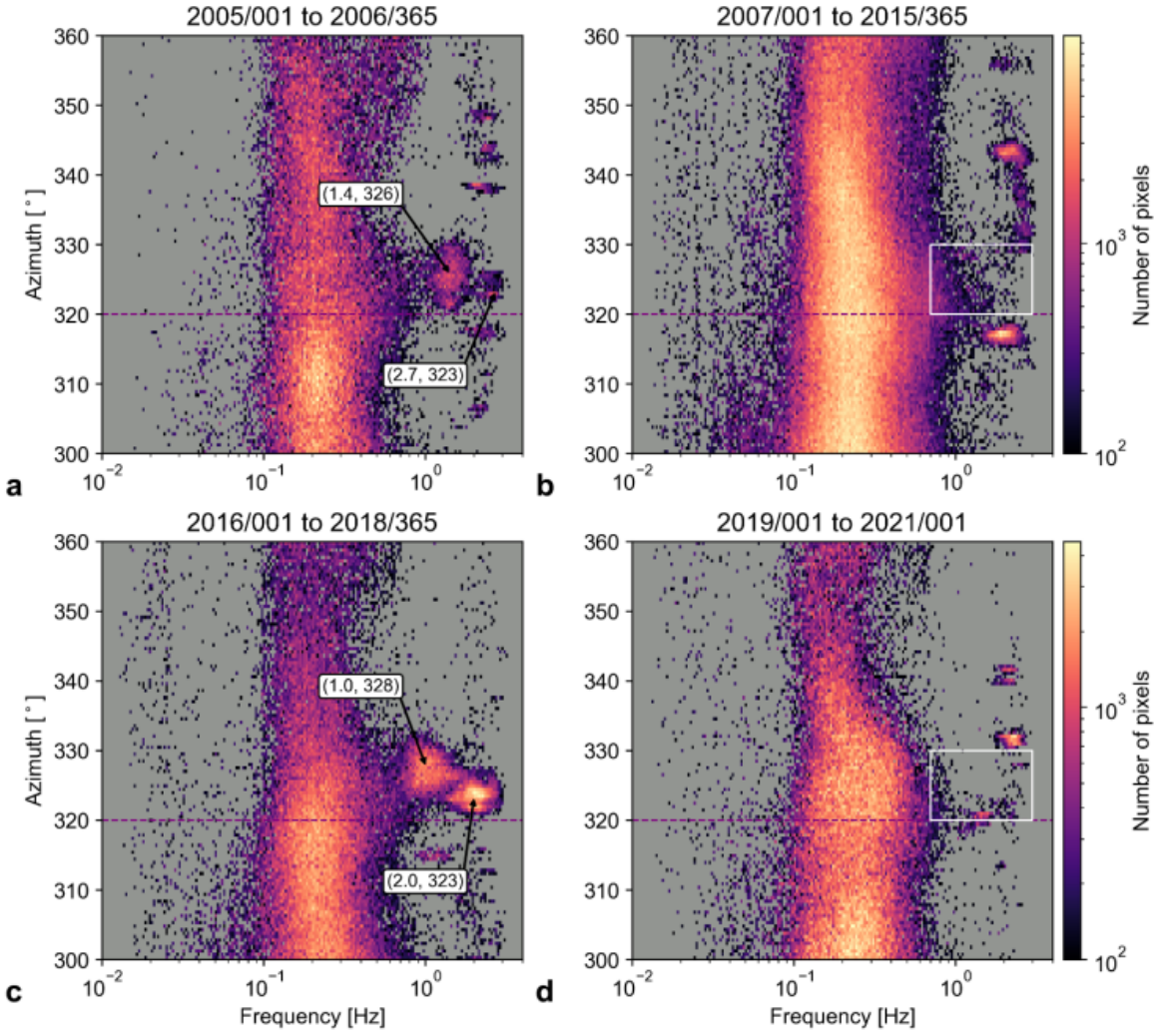

Figure C.3: Zoom of Figure C.2 from 300 to 360 degrees.

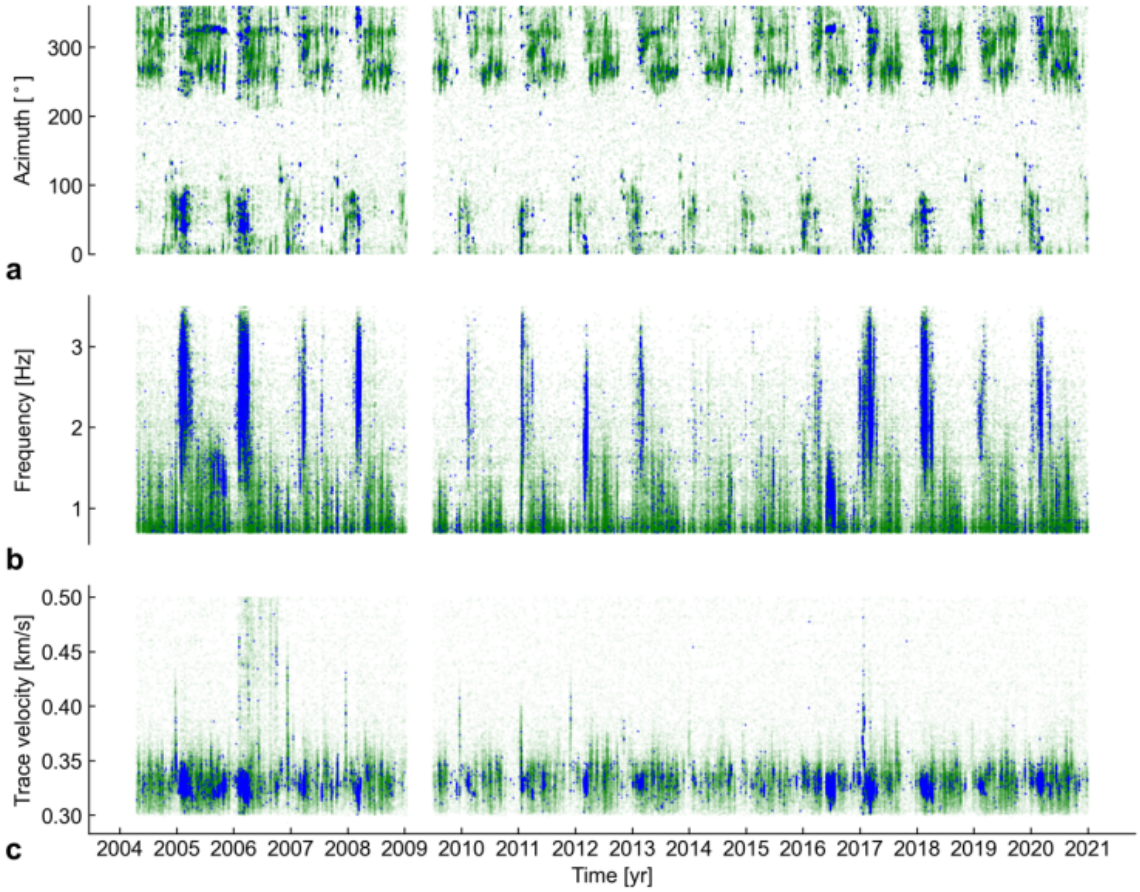

Figure C.4: Progressive Multichannel Correlation (PMCC) algorithm results (green dots) and re-clustered values (blue dots) by absolute time in years. (a) Time vs. azimuth (degrees). (b) Time vs. frequency (Hz). (c) Time vs. trace velocity (km/s).

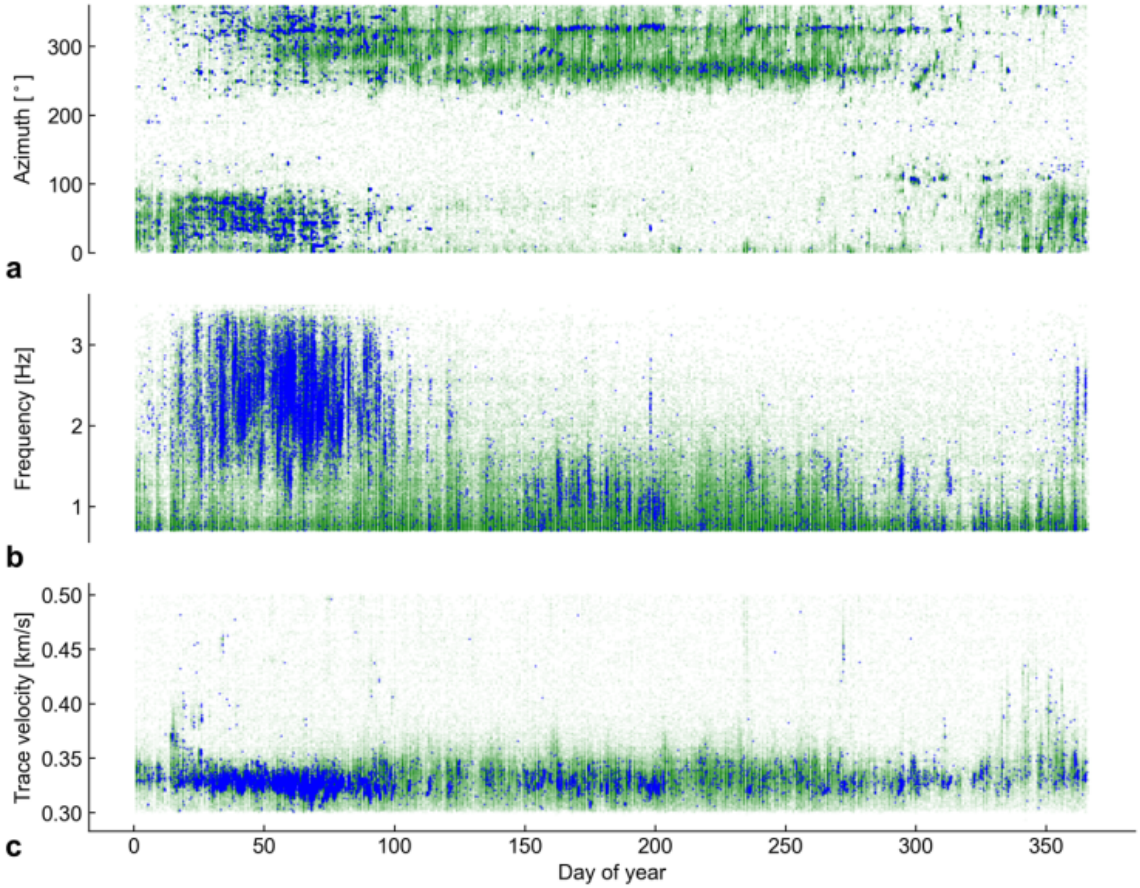

Figure C.5: Progressive Multichannel Correlation (PMCC) algorithm results (green dots) and re-clustered values (blue dots) in time by day of the year (DOY). (a) DOY vs. azimuth (degrees). (b) DOY vs. frequency (Hz). (c) DOY vs. trace velocity (km/s).

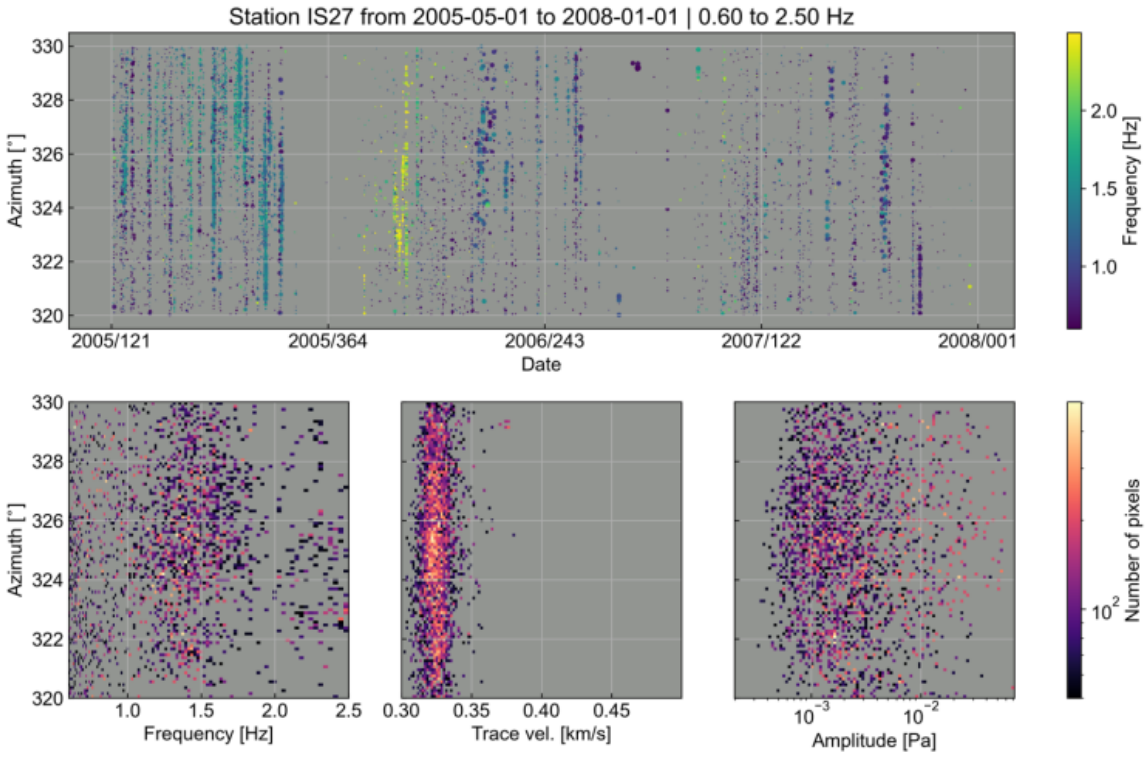

Figure C.6: Progressive multichannel correlation algorithm (PMCC) dataset from 1 May 2005 to 1 January 2008, filtered from 320 to 330 degrees in azimuth, and 0.6 to 2.5 Hz in frequency. Upper panel: time in year and day of year vs. azimuth of detections. Lower three panels: 2D histograms with azimuth in vertical axis, and (from left to right) frequency (Hz), trace velocity (km/s), and amplitude (Pa) in horizontal axis.

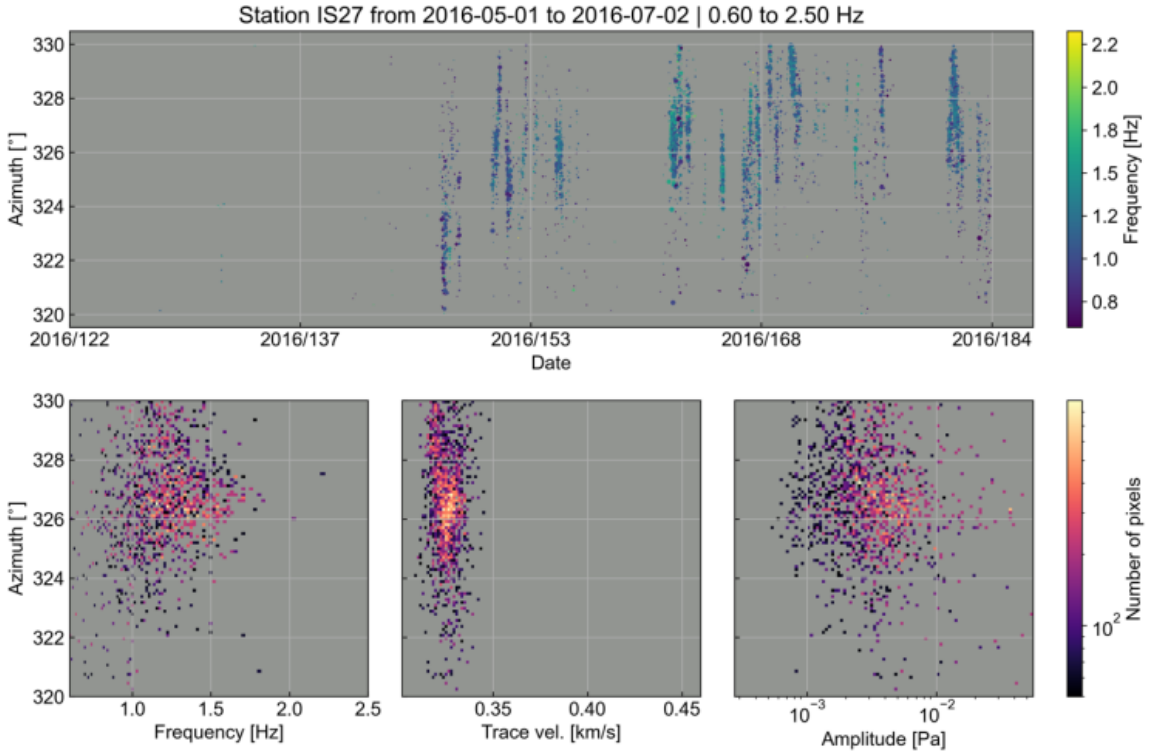

Figure C.7: Progressive multichannel correlation algorithm (PMCC) dataset from 1 May 2016 to 2 July 2016. See Figure C.6.

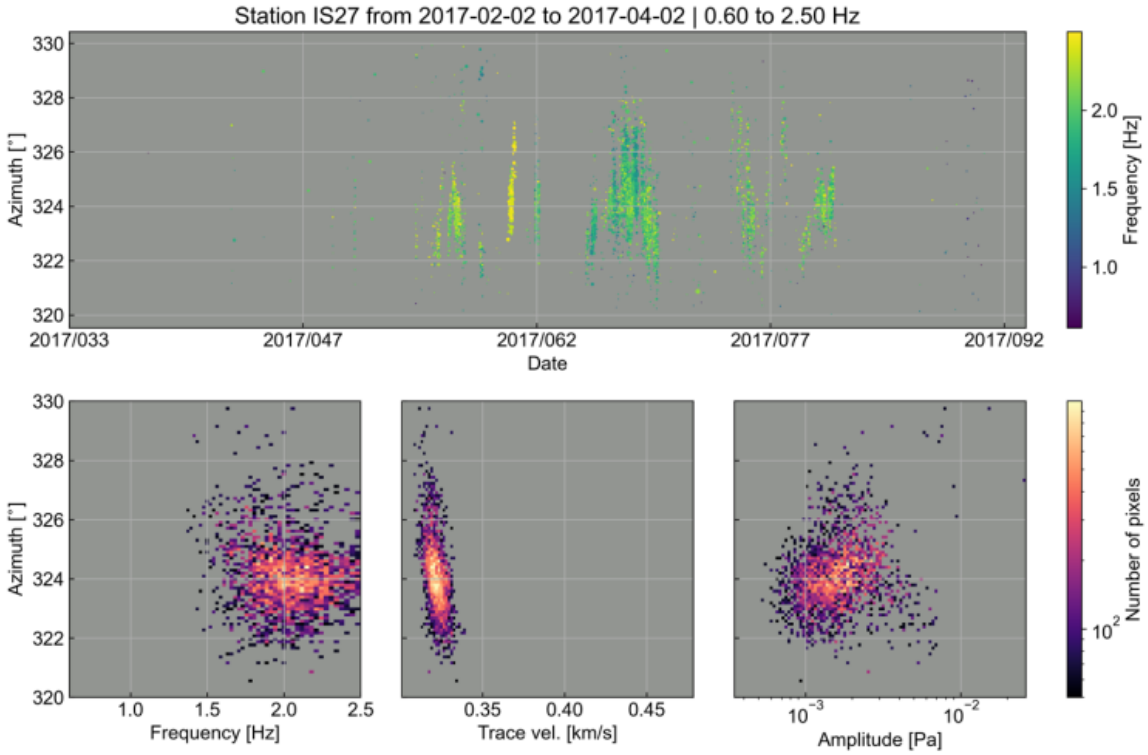

Figure C.8: Progressive multichannel correlation algorithm (PMCC) dataset from 2 February 2017 to 2 April 2017. See Figure C.6.

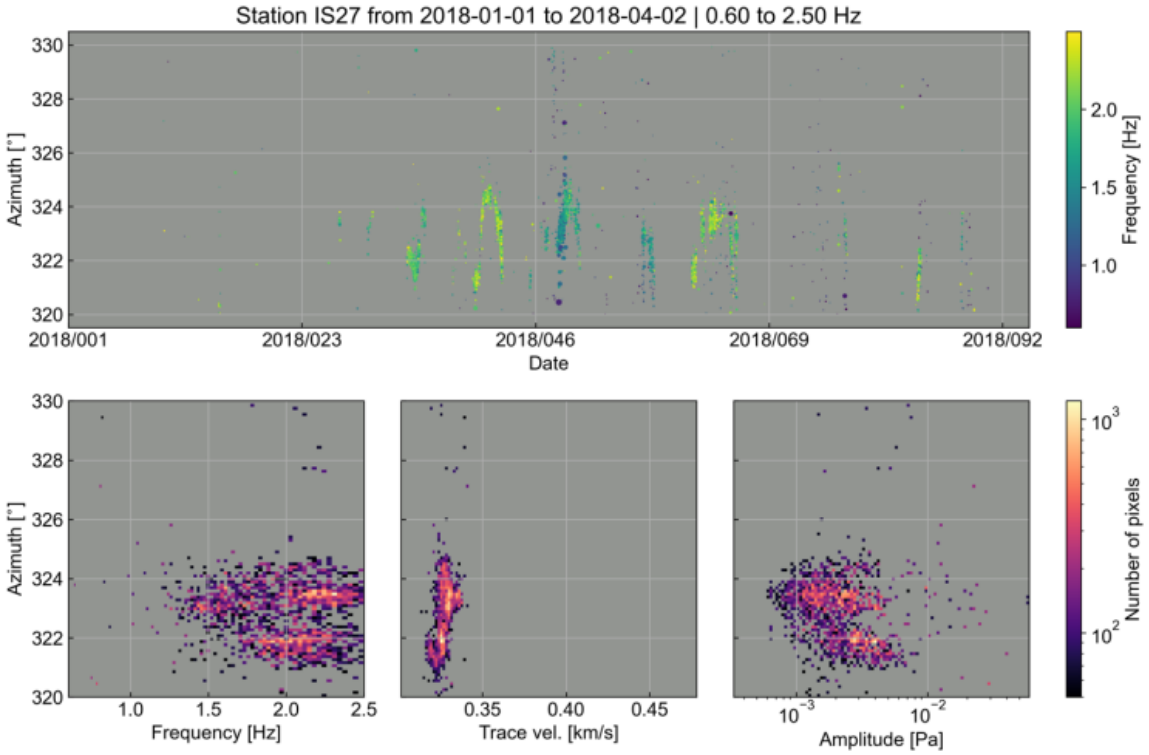

Figure C.9: Progressive multichannel correlation algorithm (PMCC) dataset from 1 January 2018 to 2 April 2018. See Figure C.6.

C.6 Tables

Time window	Pressure at IS27 (1672 km) [Pa]	Pressure at 1 km (with TL = 74.87) [Pa]
1 May 2005 to 1 January 2008	4.81×10^{-3}	2.67×10^{1}
1 May 2016 to 4 July 2016	4.49×10^{-3}	2.49×10^{1}
1 February 2017 to 2 April 2017	1.82×10^{-3}	1.01×10^{1}
1 January 2018 to 2 April 2018	2.95×10^{-3}	1.63×10^{1}

Table C.1: Reference amplitude results for selected time windows, calculated using Eq. 4.1 in main paper with a transmission loss (TL) of ∼74.9 dB (stratospheric ray paths).

Characteristics, observations	Candidate infrasound	Glacier calving
Time of the year	April - September (particularly June - August)	January - April (i.e. the warmest months, end of the Antarctic summer)
Dominant frequencies	1-2 Hz	2-4 Hz
back-azimuths from IS27	320-330 degrees (see Section 3.3)	0-90 degrees (Atka Bay) and 270-360 degrees (north-eastern Weddell Sea)
Seasonal effects, peculiarities	Stratospheric zonal winds, azimuth deviation up to 10° (Fig. C.1) due to crosswind effects	Hardly affected by stratospheric winds (Figs. C.10-C.18), indicating local sources (e.g. Atka Bay)

Table C.2: Characteristics of candidate infrasound and glacier calving events detected at IS27.

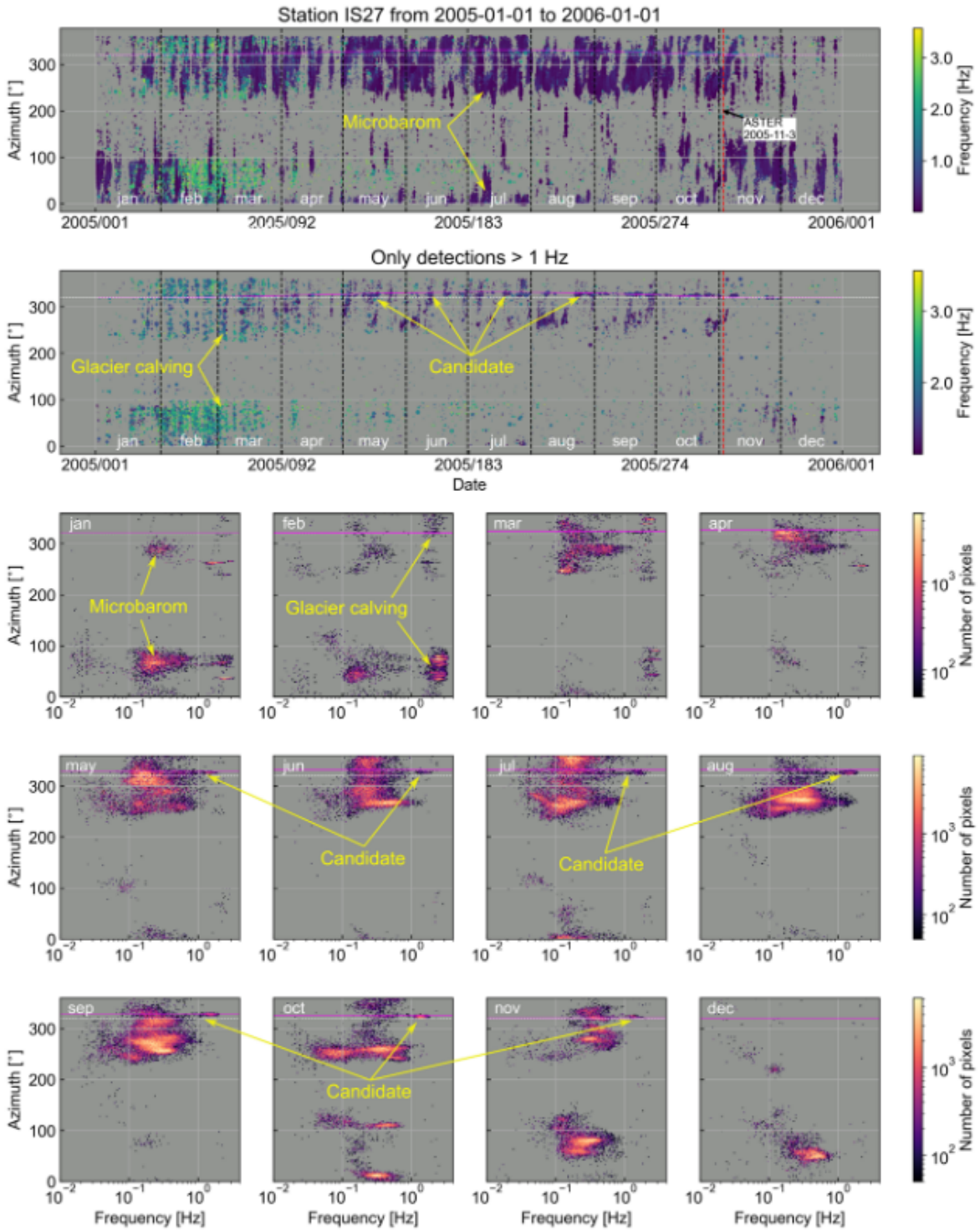

Figure C.10: 1-year PMCC dataset for 2005. In yellow labels with arrows: example types of infrasound. Top panel: date by day of year vs. azimuth, colored by frequency. (Continues on next page)

Figure C.10: (From previous page.) Labels on the bottom indicate each month, with vertical black dashed lines in between. A fuchsia horizontal curve near Mount Michael's azimuth ∼320 degrees) depicts the modeled azimuth deviation for rays traveling from Mount Michael to IS27 in an atmosphere described by climatologies. Second horizontal panel: same as top panel, but only detections above 1 Hz (different color scaling). Next 12 panels in a 4x3 arrangement: frequency vs. azimuth plots per month, colored by number of pixels. Each plot has a label in the upper-left corner that indicates the month, and a fuchsia horizontal line representing the maximum modeled azimuth per month. In a red vertical dashed line (if any), the date in which satellite observations (Gray et al., 2019) suggest an eruption is depicted. Notorious glacier calving events at northeast (NE) and northwest (NW) azimuths from January to March, usually with ∼2-3 Hz. Candidate infrasound concentrates from May to November, with ∼1-2 Hz detections that are affected by seasonal deviations (see top pane).

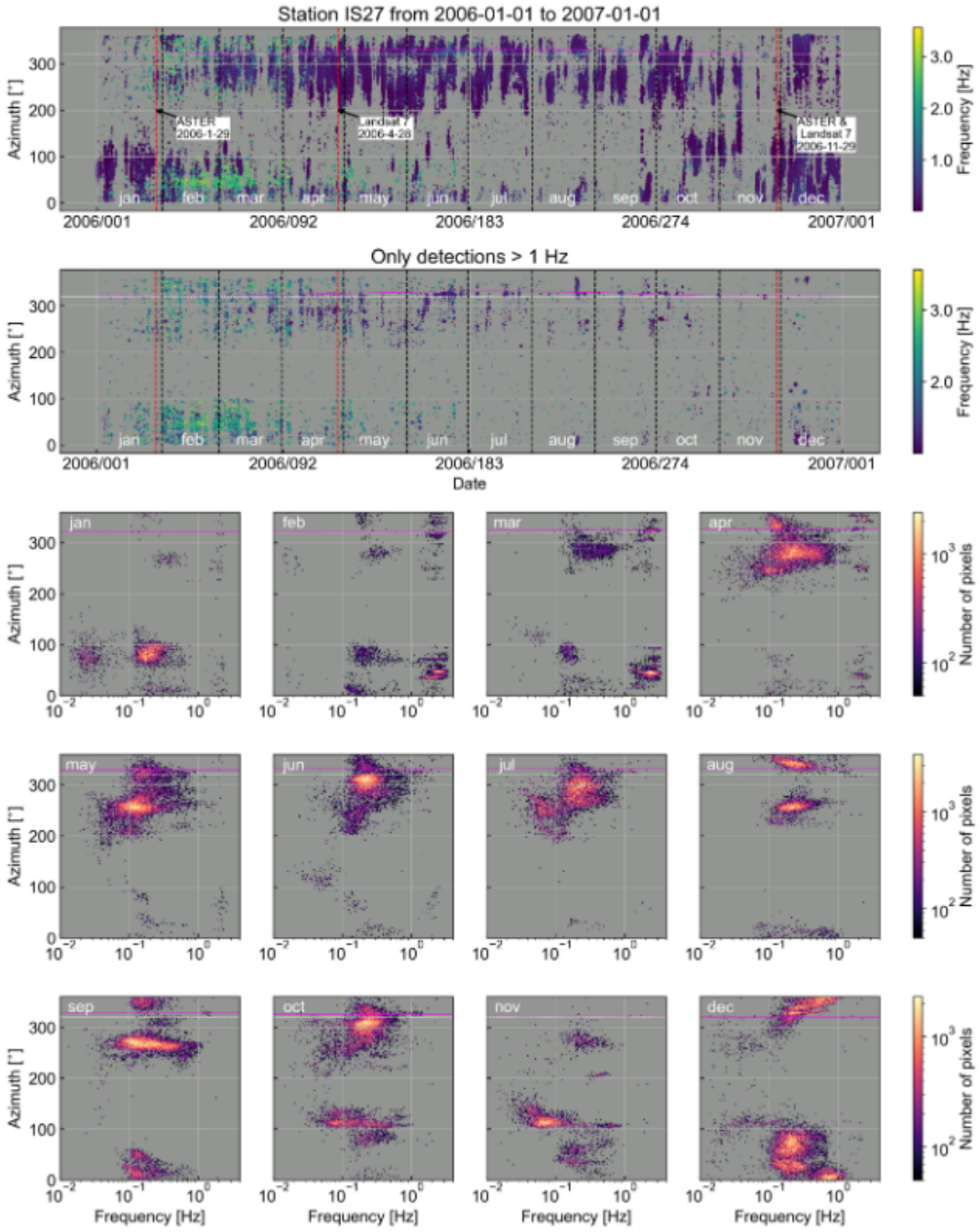

Figure C.11: 1-year PMCC dataset for 2006. Analogous to Figure S10. Notorious glacier calving events at NE/NW azimuths from February to April with similar characteristics from 2005 (Figure C.10). Smaller groups of candidate infrasound (∼1-2 Hz) appear from June to November. The satellite observations support the idea of mixing of sources from January to April, as they indicate possible eruptions on 29 January and 28 April, when there is no clear candidate infrasound.

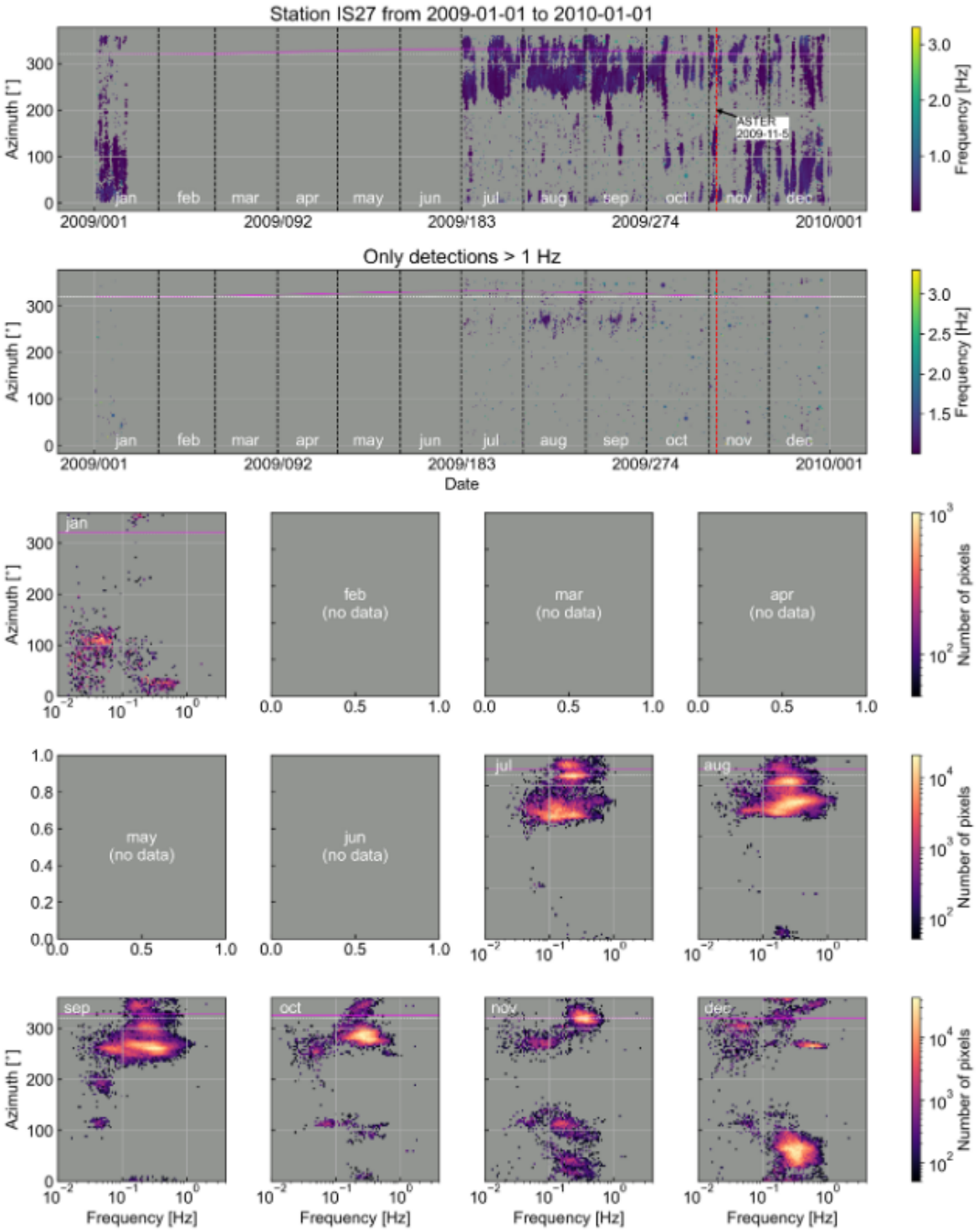

Figure C.12: 1-year PMCC dataset for 2009. Analogous to Figure C.10. The data gap due the IS27 relocation and revalidation is clearly visible from February to June. Satellite data indicates possible eruption on 5 November, but no clear infrasound records are available supporting this observation.

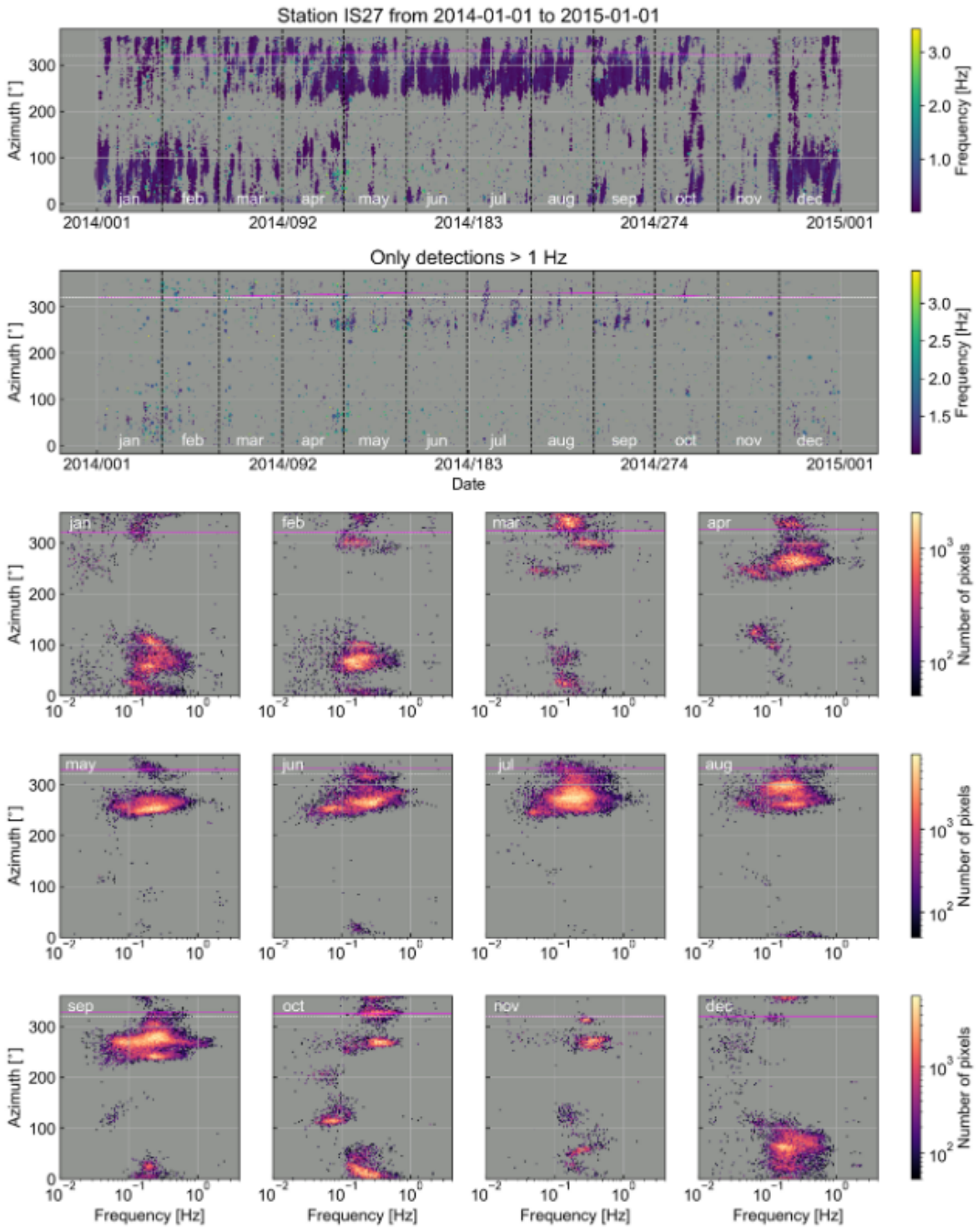

Figure C.13: 1-year PMCC dataset for 2014. Analogous to Figure C.10. This year did not have any noticeable volcanic or glacier infrasound (1-4 Hz band).

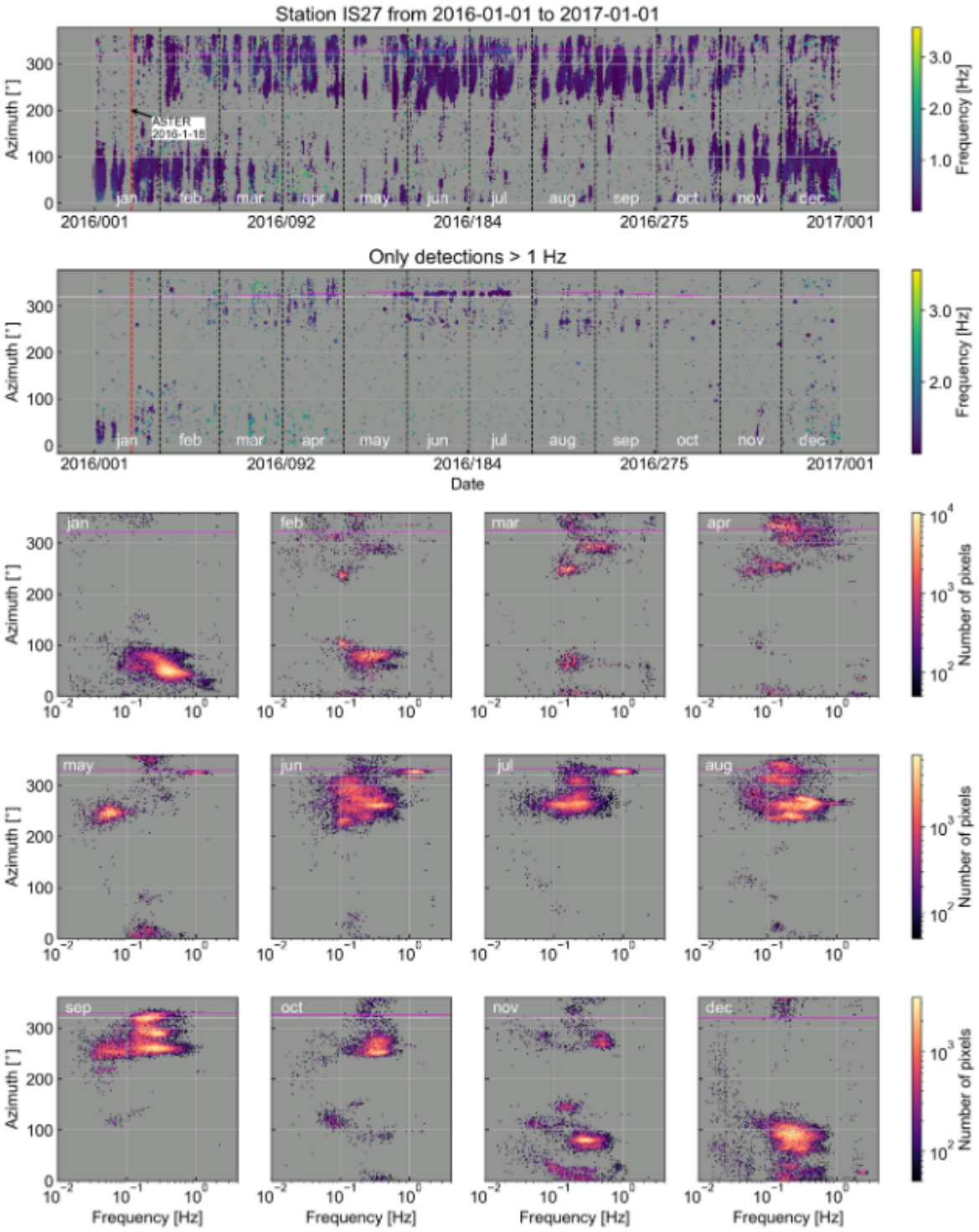

Figure C.14: 1-year PMCC dataset for 2016. Analogous to Figure C.10. Numerous detections on 0.6-2.5 Hz band at ∼320-330° appear from May to July, while there is no background glacier calving infrasound.

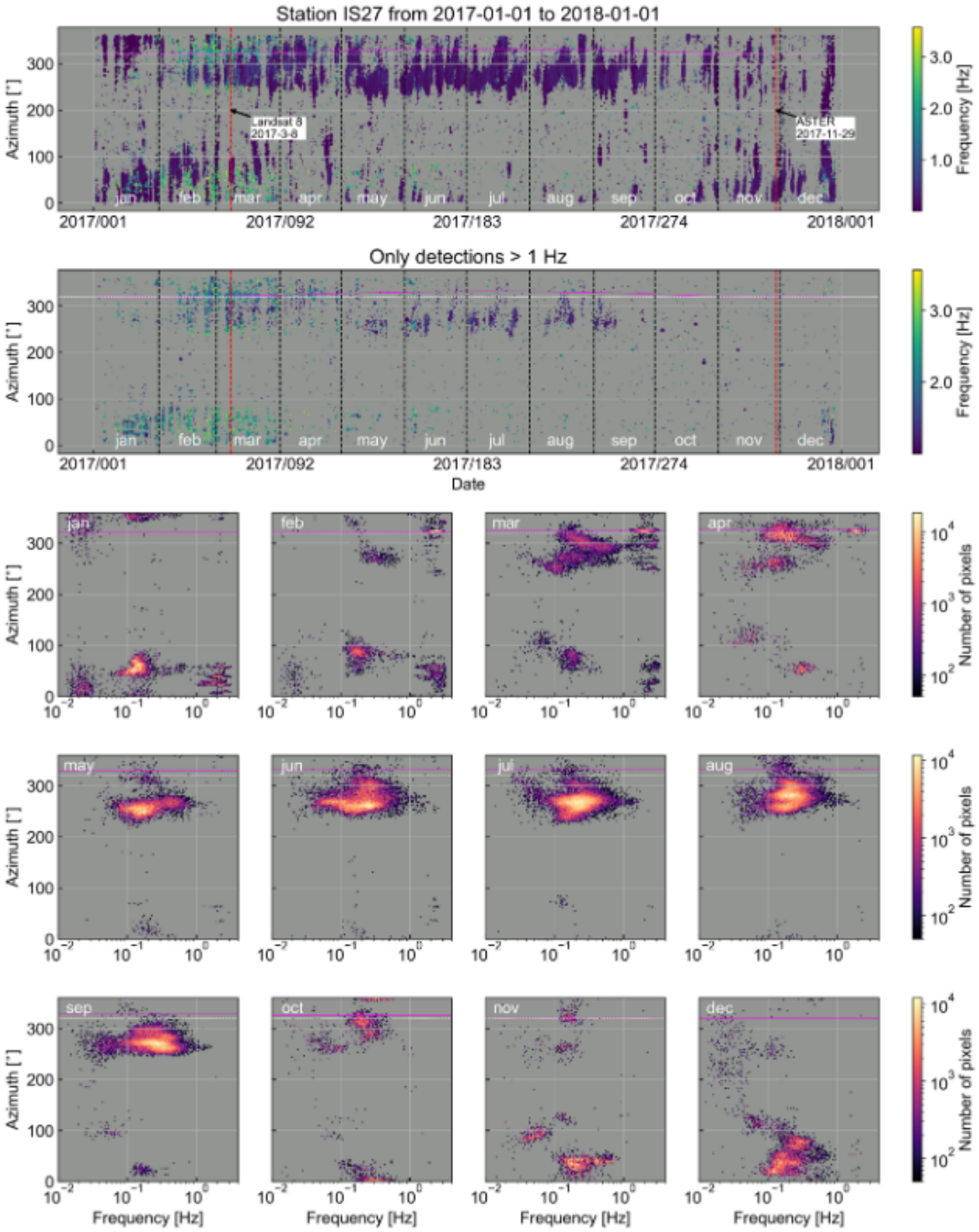

Figure C.15: 1-year PMCC dataset for 2017. Analogous to Figure C.10. Large amounts of glacier infrasound from January to March are present at NE/NW azimuths. A satellite observation on 8 March supports the idea of detections with possible mixture of infrasound sources at ∼320-330° from February to April. Candidate infrasound seems feasible especially March-April, when a group previously visible with ∼2-3 Hz at ∼320-330° migrates to ∼1-2 Hz.

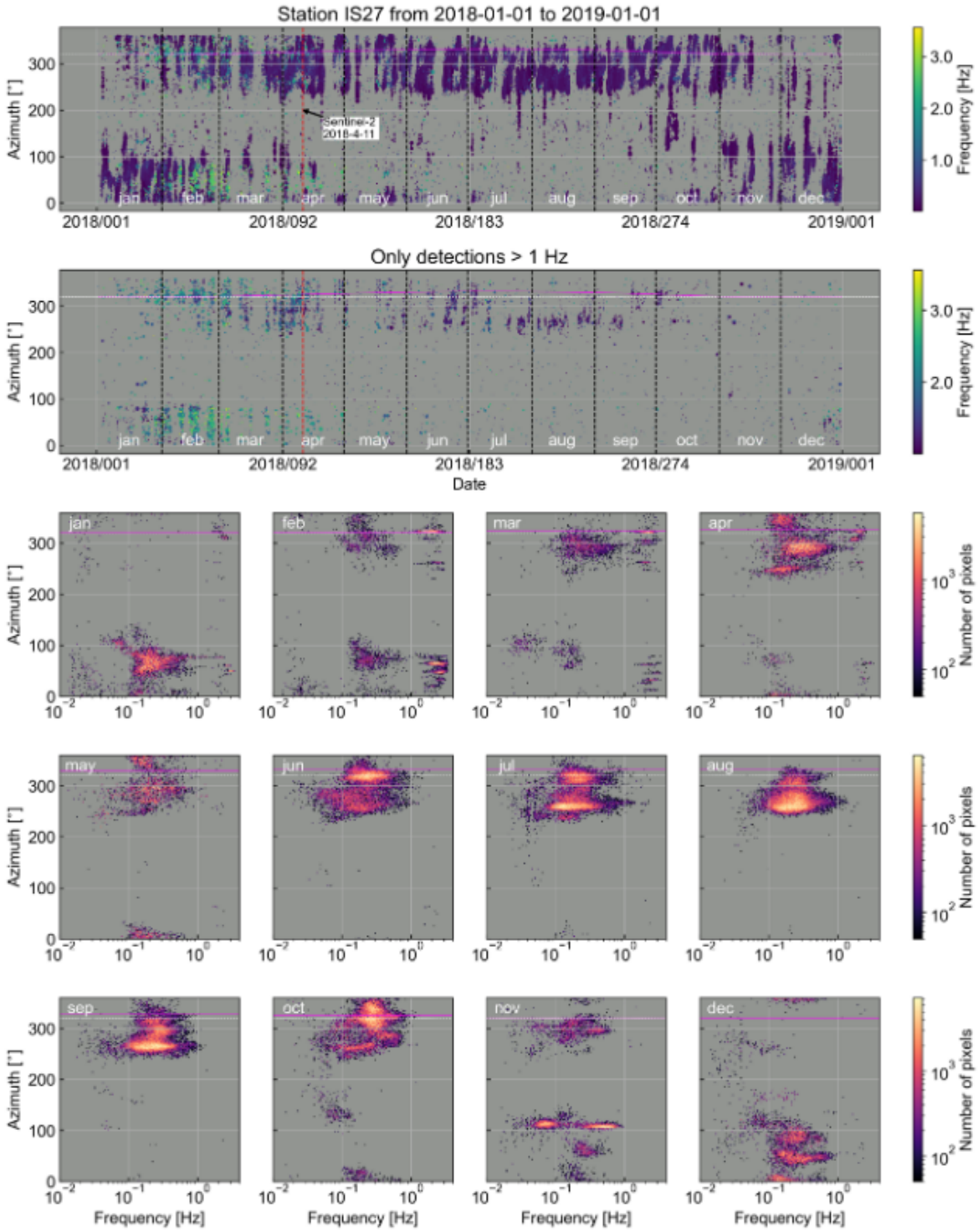

Figure C.16: 1-year PMCC dataset for 2018. Analogous to Figure C.10. Numerous detections appear from May to July, while there is no background glacier calving infrasound. Similar to 2017 (Figure S8 or S15), numerous detections on the frequency band 2-4 Hz appear from January to April on N-E and N-W azimuths (i.e., glacier calving), but concentrated on February and March. From February to April, a numerous group with 1-3 Hz appears at Mount Michael's azimuth (∼320°). A satellite observation of possible eruption on 11 April supports the idea of candidate infrasound in this time period.

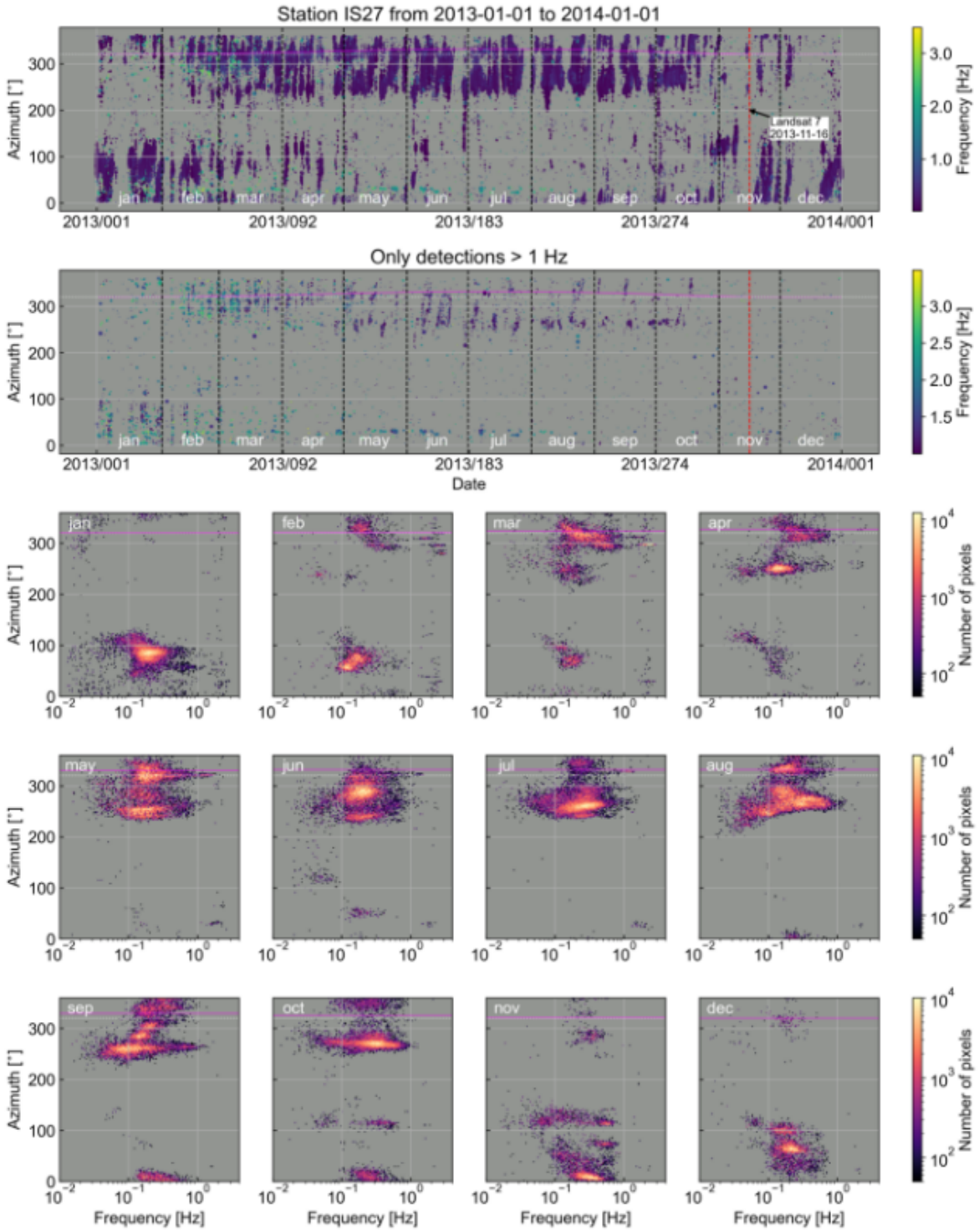

Figure C.17: 1-year PMCC dataset for 2013. Analogous to Figure C.10. Glacier calving concentrated on February and March mainly at NW azimuths, but not overlapping Mount Michael azimuth (∼320°). Sporadic candidate infrasound from May to August at ∼320°. The satellite observation on 16 November is not coincident with candidate infrasound suggesting low energy activity through the year.

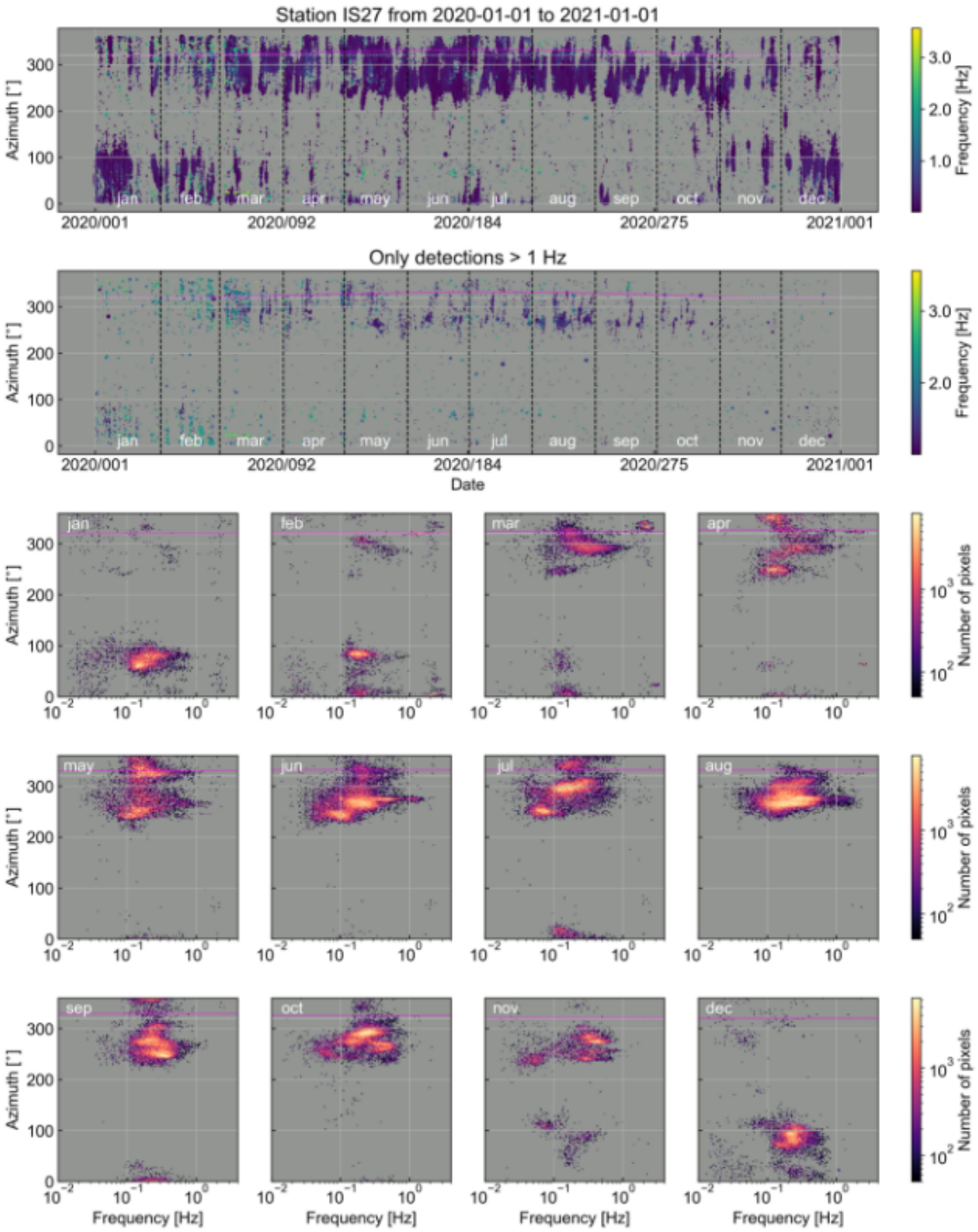

Figure C.18: 1-year PMCC dataset for 2020. Analogous to Figure C.10. From February to April sporadic clusters of candidate infrasound (1-2 Hz) at ∼320° accompanied with glacier infrasound at higher frequencies (2-4 Hz) at NW azimuths.

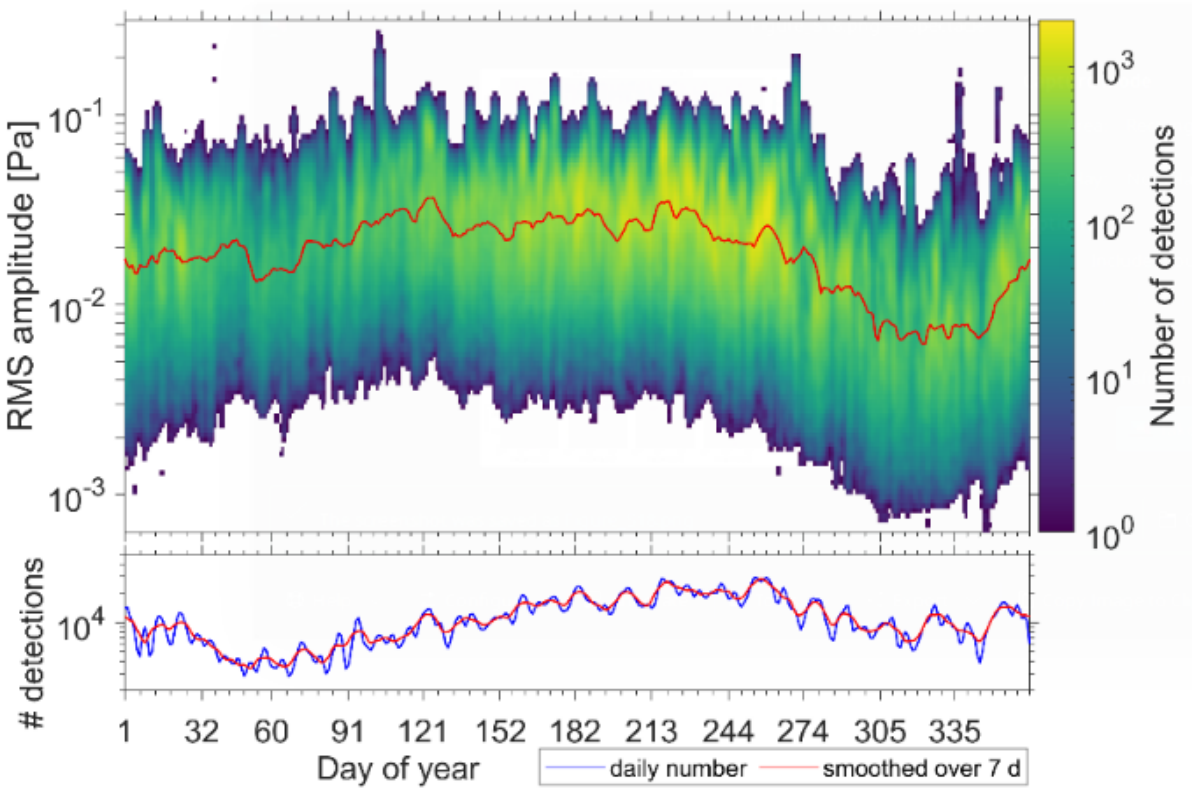

Figure C.19: 2-D histogram of PMCC detections with frequencies in the range of the quasi-continuously detected microbaroms (0.1-0.5 Hz) at IS27 from 2004 to 2020. Top: date vs. amplitude, colored by number of detections per amplitude bin (0.05 in base10 order scale) and Julian day (stacked over 17 years). Bottom: Total number of detections per Julian day within 17 years (blue line). The red lines show the 7-day running means of the amplitude and the daily number of detections, respectively. A lower number of detections from February to April and from October to mid-December happens around or after the equinox periods (around March 20 and September 23), when stratospheric winds change direction, weakening the ducts. Also, the snow coverage increasing at the end of the austral winter seems to dampen the amplitude values from October to December, while effectively increasing the signal-to-noise ratio.

Bibliography

Antier, K., Le Pichon, A., Vergniolle, S., Zielinski, C., and Lardy, M. (2007). Multi-year validation of the NRL-G2S wind fields using infrasound from Yasur. *Journal of Geophysical Research: Atmospheres*, 112(D23).

Arms Control Association (n.d.). *The Nuclear Testing Tally: Fact sheets & briefs*. `https://www.armscontrol.org/factsheets/nucleartesttally` [Accessed: 9-17-23].

Arrowsmith, S., Drob, D. P., Hedlin, M. A. H., and Edwards, W. (2007). A joint seismic and acoustic study of the Washington State bolide: Observations and modeling. *Journal of Geophysical Research*, 112(D9).

Arrowsmith, S., Euler, G., Marcillo, O., Blom, P., Whitaker, R., and Randall, G. (2015). Development of a robust and automated infrasound event catalogue using the International Monitoring System. *Geophysical Journal International*, 200(3):1411–1422.

Arrowsmith, S. and Whitaker, R. (2008). Inframonitor: A tool for regional infrasound monitoring. In *2008 Monitoring Research Review: Ground-Based Nuclear Explosion Monitoring Technologies*.

Arrowsmith, S. J., Whitaker, R., Taylor, S. R., Burlacu, R., Stump, B., Hedlin, M., Randall, G., Hayward, C., and Revelle, D. (2008). Regional monitoring of infrasound events using multiple arrays: application to Utah and Washington State. *Geophys. J. Int*, 175:291–300.

Assink, J., Smets, P., Marcillo, O., Weemstra, C., Lalande, J.-M., Waxler, R., and Evers, L. (2019). Advances in Infrasonic Remote Sensing Methods. In Le Pichon, A., Blanc, E., and Hauchecorne, A., editors, *Infrasound Monitoring for Atmospheric Studies: Challenges in Middle Atmosphere Dynamics and Societal Benefits*, pages 605–632. Springer International Publishing, Cham.

Assink, J. D., Pichon, A. L., Blanc, E., Kallel, M., and Khemiri, L. (2014). Evaluation of wind and temperature profiles from ECMWF analysis on two hemispheres using volcanic infrasound. *Journal of Geophysical Research: Atmospheres*, 119(14):8659–8683.

Assink, J. D., Waxler, R., and Drob, D. (2012). On the sensitivity of infrasonic traveltimes in the equatorial region to the atmospheric tides. *Journal of Geophysical Research: Atmospheres*, 117(D1).

Bani, P., Boudon, G., Balcone-Boissard, H., Delmelle, P., Quiniou, T., Lefèvre, J., Bule, E. G., Hiroshi, S., and Lardy, M. (2016). The 2009–2010 eruption of Gaua volcano (Vanuatu archipelago): Eruptive dynamics and unsuspected strong halogens source. *Journal of Volcanology and Geothermal Research*, 322:63–75.

Beaumais, A., Bertrand, H., Chazot, G., Dosso, L., and Robin, C. (2016). Temporal magma source changes at Gaua volcano, Vanuatu island arc. *Journal of Volcanology and Geothermal Research*, 322:30–47.

Bell, B., Hersbach, H., Simmons, A., Berrisford, P., Dahlgren, P., Horányi, A., Muñoz-Sabater, J., Nicolas, J., Radu, R., Schepers, D., Soci, C., Villaume, S., Bidlot, J., Haimberger, L., Woollen, J., Buontempo, C., and Thépaut, J. (2021). The ERA5 global reanalysis: Preliminary extension to 1950. *Quarterly Journal of the Royal Meteorological Society*, 147(741):4186–4227.

Blom, P. (2020). The influence of irregular terrain on infrasonic propagation in the troposphere. *The Journal of the Acoustical Society of America*, 148(4):1984–1997. Publisher: Acoustical Society of America.

Blom, P. and Waxler, R. (2012). Impulse propagation in the nocturnal boundary layer: Analysis of the geometric component. *The Journal of the Acoustical Society of America*, 131(5):3680–3690. Publisher: Acoustical Society of America.

Blom, P. and Waxler, R. (2017). Modeling and observations of an elevated, moving infrasonic source: Eigenray methods. *The Journal of the Acoustical Society of America*, 141(4):2681–2692.

Blom, P., Waxler, R., and Frazier, G. (2023). Quantification of spatial and seasonal trends in the atmosphere and construction of statistical models for infrasonic propagation. *Geophysical Journal International*, 235(2):1007–1020.

Brachet, N., Brown, D., Le Bras, R., Cansi, Y., Mialle, P., and Coyne, J. (2010). Monitoring the Earth's Atmosphere with the Global IMS Infrasound Network. In Le Pichon, A., Blanc, E., and Hauchecorne, A., editors, *Infrasound Monitoring for Atmospheric Studies*, pages 77–118. Springer Netherlands, Dordrecht.

Brown, D. J., Katz, C. N., Bras, R. L., Flanagan, M. P., Wang, J., and Gault, A. K. (2002). Infrasonic Signal Detection and Source Location at the Prototype International Data Centre. *Pure and Applied Geophysics*, 159(5):1081–1125.

Campus, P. and Christie, D. R. (2010). Worldwide Observations of Infrasonic Waves. In Le Pichon, A., Blanc, E., and Hauchecorne, A., editors, *Infrasound Monitoring for Atmospheric Studies*, pages 185–234. Springer Netherlands, Dordrecht.

Cansi, Y. (1995). An automatic seismic event processing for detection and location: The P.M.C.C. Method. *Geophysical Research Letters*, 22(9):1021–1024.

Cansi, Y. and Klinger, Y. (1997). An automated data processing method for mini-arrays. *Newsletter of the European-Mediterranean Seismological Center*, 11:2–4.

Cansi, Y. and Le Pichon, A. (2008). Infrasound Event Detection Using the Progressive Multi-Channel Correlation Algorithm. In Havelock, D., Kuwano, S., and Vorländer, M., editors, *Handbook of Signal Processing in Acoustics*, pages 1425–1435. Springer New York.

Cansi, Y., Vergoz, J., and Schissele-Rebel, E. (2005). A quantitative evaluation of P.M.C.C.'s detection capability. *Paper presented at the infrasound technology workshop, Tahiti, French Polynesia.*

Castruccio, A., Clavero, J., Segura, A., Samaniego, P., Roche, O., Pennec, J.-L. L., and Droguett, B. (2016). Eruptive parameters and dynamics of the April 2015 sub-Plinian eruptions of Calbuco volcano (southern Chile). *Bulletin of Volcanology*, 78(9).

Caudron, C., Taisne, B., Garcés, M., Le Pichon, A., and Mialle, P. (2015). On the use of remote infrasound and seismic stations to constrain the eruptive sequence and intensity for the 2014 Kelud eruption. *Geophysical Research Letters*, 42(16):6614–6621.

Ceranna, L., Le Pichon, A., Green, D. N., and Mialle, P. (2009). The Buncefield explosion: a benchmark for infrasound analysis across Central Europe. *Geophysical Journal International*, 177(2):491–508.

Ceranna, L., Matoza, R., Hupe, P., Le Pichon, A., and Landès, M. (2019). Systematic Array Processing of a Decade of Global IMS Infrasound Data. In Le Pichon, A., Blanc, E., and Hauchecorne, A., editors, *Infrasound Monitoring for Atmospheric Studies*, pages 471–482. Springer International Publishing.

Christie, D. R. and Campus, P. (2010). The IMS Infrasound Network: Design and Establishment of Infrasound Stations. In Le Pichon, A., Blanc, E., and Hauchecorne, A., editors, *Infrasound Monitoring for Atmospheric Studies*, pages 29–75. Springer Netherlands, Dordrecht.

Collini, E., Osores, M. S., Folch, A., Viramonte, J. G., Villarosa, G., and Salmuni, G. (2013). Volcanic ash forecast during the June 2011 Cordón Caulle eruption. *Natural Hazards*, 66(2):389–412.

Coppola, D., Laiolo, M., and Cigolini, C. (2016). Fifteen years of thermal activity at Vanuatu's volcanoes (2000-2015) revealed by MIROVA. *Journal of Volcanology and Geothermal Research*, 322:6–19.

CTBTO (n.d.a). *IMS Map*. `https://www.ctbto.org/our-work/ims-map` [Accessed: 2023-08-14].

CTBTO (n.d.b). *The Comprehensive Nuclear-Test-Ban Treaty (CTBT)*. `https://www.ctbto.org/our-mission/the-treaty` [Accessed: 2023-08-14].

Dabrowa, A., Green, D., Rust, A., and Phillips, J. (2011). A global study of volcanic infrasound characteristics and the potential for long-range monitoring. *Earth and Planetary Science Letters*, 310(3-4):369–379.

De Angelis, S., Fee, D., Haney, M., and Schneider, D. (2012). Detecting hidden volcanic explosions from Mt. Cleveland Volcano, Alaska with infrasound and ground-coupled airwaves. *Geophysical Research Letters*, 39(21). _eprint: https://onlinelibrary.wiley.com/doi/pdf/10.1029/2012GL053635.

de Groot-Hedlin, C. D., Hedlin, M. A. H., and Drob, D. P. (2010). Atmospheric Variability and Infrasound Monitoring. In Le Pichon, A., Blanc, E., and Hauchecorne, A., editors, *Infrasound Monitoring for Atmospheric Studies*, pages 475–507. Springer Netherlands, Dordrecht.

De Negri, R. and Matoza, R. S. (2023). Rapid Location of Remote Volcanic Infrasound Using 3D Ray Tracing and Empirical Climatologies: Application to the 2011 Cordón Caulle and 2015 Calbuco Eruptions, Chile. *Journal of Geophysical Research: Solid Earth*, 128(3):e2022JB025735. _eprint: https://onlinelibrary.wiley.com/doi/pdf/10.1029/2022JB025735.

De Negri, R. S., Rose, K. M., Matoza, R. S., Hupe, P., and Ceranna, L. (2022). Long-Range Multi-Year Infrasonic Detection of Eruptive Activity at Mount Michael Volcano, South Sandwich Islands. *Geophysical Research Letters*, 49(7).

Drob, D. (2019). Meteorology, Climatology, and Upper Atmospheric Composition for Infrasound Propagation Modeling. In Le Pichon, A., Blanc, E., and Hauchecorne, A., editors, *Infrasound Monitoring for Atmospheric Studies: Challenges in Middle Atmosphere Dynamics and Societal Benefits*, pages 485–508. Springer International Publishing, Cham.

Drob, D. P., Emmert, J. T., Meriwether, J. W., Makela, J. J., Doornbos, E., Conde, M., Hernandez, G., Noto, J., Zawdie, K. A., McDonald, S. E., Huba, J. D., and Klenzing, J. H. (2015). An update to the Horizontal Wind Model (HWM): The quiet time thermosphere. *Earth and Space Science*, 2(7):301–319.

Drob, D. P., Garcés, M., Hedlin, M., and Brachet, N. (2010a). The Temporal Morphology of Infrasound Propagation. *Pure and Applied Geophysics*, 167(4-5):437–453. Publisher: Birkhäuser-Verlag.

Drob, D. P., Meier, R. R., Picone, J. M., and Garcés, M. M. (2010b). Inversion of Infrasound Signals for Passive Atmospheric Remote Sensing. In *Infrasound Monitoring for Atmospheric Studies*, pages 701–731. Springer Netherlands.

Drob, D. P., Picone, J. M., Garcés, M., and Garce, M. (2003). Global morphology of infrasound propagation. *Journal of Geophysical Research*, 108(D21):1–12. Publisher: Wiley-Blackwell.

Eissen, J.-P., Lefèvre, C., Maillet, P., Morvan, G., and Nohara, M. (1991). Petrology and geochemistry of the central North Fiji Basin spreading centre (Southwest Pacific) between 16°S and 22°S. *Marine Geology*, 98(2):201–239.

Elissondo, M., Baumann, V., Bonadonna, C., Pistolesi, M., Cioni, R., Bertagnini, A., Biass, S., Herrero, J.-C., and Gonzalez, R. (2016). Chronology and impact of the 2011 Cordón Caulle eruption Chile. *Natural Hazards and Earth System Sciences*, 16(3):675–704.

Emmert, J. T., Drob, D. P., Picone, J. M., Siskind, D. E., Jones Jr., M., Mlynczak, M. G., Bernath, P. F., Chu, X., Doornbos, E., Funke, B., Goncharenko, L. P., Hervig, M. E., Schwartz, M. J., Sheese, P. E., Vargas, F., Williams, B. P., and Yuan, T. (2020). NRLMSIS 2.0: A Whole-Atmosphere Empirical Model of Temperature and Neutral Species Densities. *Earth and Space Science*, 8(3):e2020EA001321. _eprint: https://onlinelibrary.wiley.com/doi/pdf/10.1029/2020EA001321.

Engwell, S., Mastin, L., Tupper, A., Kibler, J., Acethorp, P., Lord, G., and Filgueira, R. (2021). Near-real-time volcanic cloud monitoring: insights into global explosive volcanic eruptive activity through analysis of Volcanic Ash Advisories. *Bulletin of Volcanology*, 83(2):9.

Evers, L. and Haak, H. (2005). The detectability of infrasound in The Netherlands from the Italian volcano Mt. Etna. *Journal of Atmospheric and Solar-Terrestrial Physics*, 67(3):259–268.

Evers, L. and Haak, H. (2007). Infrasonic forerunners: Exceptionally fast acoustic phases. *Geophysical Research Letters*, 34(10).

Fee, D., Bishop, J., Waxler, R., and Matoza, R. (2020). Infrasound propagation working group (IPWG) report.

Fee, D., Garces, M., and Steffke, A. (2010). Infrasound from Tungurahua Volcano 2006-2008: Strombolian to Plinian eruptive activity. *Journal of Volcanology and Geothermal Research*, 193(1-2):67–81.

Fee, D. and Matoza, R. S. (2013). An overview of volcano infrasound: From hawaiian to plinian, local to global. *Journal of Volcanology and Geothermal Research*, 249:123–139. Publisher: Elsevier B.V. ISBN: 03770273 (ISSN).

Fee, D., Matoza, R. S., Gee, K. L., Neilsen, T. B., and Ogden, D. E. (2013). Infrasonic crackle and supersonic jet noise from the eruption of Nabro Volcano, Eritrea. *Geophysical Research Letters*, 40(16):4199–4203.

Fee, D., Toney, L., Kim, K., Sanderson, R. W., Iezzi, A. M., Matoza, R. S., De Angelis, S., Jolly, A. D., Lyons, J. J., and Haney, M. M. (2021). Local Explosion Detection and Infrasound Localization by Reverse Time Migration Using 3-D Finite-Difference Wave Propagation. *Frontiers in Earth Science*, 9.

Garcés, M. (2004). On using ocean swells for continuous infrasonic measurements of winds and temperature in the lower middle, and upper atmosphere. *Geophysical Research Letters*, 31(19).

Garcés, M., Fee, D., Steffke, A., McCormack, D., Servranckx, R., Bass, H., Hetzer, C., Hedlin, M., Matoza, R., Yepes, H., and Ramon, P. (2008). Capturing the Acoustic Fingerprint of Stratospheric Ash Injection. *Eos Transactions American Geophysical Union*, 89(40):377–378.

Garcés, M., Hetzer, C., Merrifield, M., Willis, M., and Aucan, J. (2003). Observations of surf infrasound in Hawai'i. *Geophysical Research Letters*, 30(24). Publisher: Wiley-Blackwell.

Garcés, M. A., Hansen, R. A., and Lindquist, K. G. (1998). Traveltimes for infrasonic waves propagating in a stratified atmosphere. *Geophysical Journal International*, 135(1):255–263. Publisher: Oxford University Press.

Gheri, D., Marchetti, E., Belli, G., Pichon, A. L., Boulenger, V., Hupe, P., Ceranna, L., Mialle, P., and Hereil, P. (2023). Monitoring of Indonesian volcanoes with the IS06 infrasound array. *Journal of Volcanology and Geothermal Research*, 434:107753.

Gibson, R. G., Drob, D. P., and Norris, D. E. (2006). Advancement of infrasound propagation calculation techniques using synoptic and mesoscale atmospheric specifications. *Proceedings of the 28th Seismic Research Review: Ground-Based Nuclear Explosion Monitoring Technologies*, pages 900–909.

Global Volcanism Program (2013a). Global Volcanism Program — Volcanoes of the World v. 4.5.3. Accessed on June 2016.

Global Volcanism Program (2013b). Saunders (390090) in Volcanoes of the World, v. 4.10.0 (17 Sep 2023).

Goto, A. and Johnson, J. B. (2011). Monotonic infrasound and Helmholtz resonance at Volcan Villarrica (Chile). *Geophysical Research Letters*, 38(6):1–5. ISBN: 0094-8276.

Gray, D. M., Burton-Johnson, A., and Fretwell, P. T. (2019). Evidence for a lava lake on Mt. Michael volcano, Saunders Island (South Sandwich Islands) from Landsat, Sentinel-2 and ASTER satellite imagery. *Journal of Volcanology and Geothermal Research*, 379:60–71. Publisher: Elsevier B.V.

Green, D. N. and Bowers, D. (2010). Estimating the detection capability of the International Monitoring System infrasound network. *Journal of Geophysical Research*, 115(D18):D18116.

Green, D. N., Evers, L. G., Fee, D., Matoza, R. S., Snellen, M., Smets, P., and Simons, D. (2013). Hydroacoustic, infrasonic and seismic monitoring of the submarine eruptive activity and sub-aerial plume generation at South Sarigan, May 2010. *Journal of Volcanology and Geothermal Research*, 257:31–43.

Green, D. N., Matoza, R. S., Vergoz, J., and Le Pichon, A. (2012). Infrasonic propagation from the 2010 Eyjafjallajökull eruption: Investigating the influence of stratospheric solar tides. *Journal of Geophysical Research: Atmospheres*, 117(D21):D21202.

Green, D. N., Vergoz, J., Gibson, R., Le Pichon, A., and Ceranna, L. (2011). Infrasound radiated by the Gerdec and Chelopechene explosions: propagation along unexpected paths. *Geophysical Journal International*, 185(2):890–910.

Gutenberg, B. (1939). The Velocity of Sound Waves and the Temperature in the Stratosphere in Southern California. *Bulletin of the American Meteorological Society*, 20(5):192–201. Number: 5 Publisher: American Metereological Society.

Harkrider, D. and Press, F. (1967). The Krakatoa Air-Sea Waves: an Example of Pulse Propagation in Coupled Systems. *Geophysical Journal of the Royal Astronomical Society*, 13(1-3):149–159.

Hart, T. and Convey, P. (2018). The South Sandwich Islands - a community of metapopulations across all trophic levels. *Biodiversity*, 19(1-2):20–33. Publisher: Taylor & Francis _eprint: https://doi.org/10.1080/14888386.2018.1464952.

Headlin, M. A. H., Garces, M., Bass, H., Hayward, C., Herrin, G., Olson, J., and Wilson, C. (2002). Listening to the secret sounds of Earth's atmosphere. *Eos, Transactions American Geophysical Union*, 83(48):557–565. _eprint: https://onlinelibrary.wiley.com/doi/pdf/10.1029/2002EO000383.

Hupe, P., Ceranna, L., and Le Pichon, A. (2021a). The global and coherent infrasound wavefield: Recent advances in reprocessing the full International Monitoring System infrasound data.

Hupe, P., Ceranna, L., Le Pichon, A., Matoza, R. S., and Mialle, P. (2021b). Higher frequency data products of the International Monitoring System's infrasound stations [NetCDF].

Hupe, P., Ceranna, L., Le Pichon, A., Matoza, R. S., and Mialle, P. (2022). International Monitoring System infrasound data products for atmospheric studies and civilian applications. *Earth System Science Data Discussions*, 2022:1–40.

Johnson, J. (2019). Local Volcano Infrasound Monitoring. In Le Pichon, A., Blanc, E., and Hauchecorne, A., editors, *Infrasound Monitoring for Atmospheric Studies: Challenges in Middle Atmosphere Dynamics and Societal Benefits*, pages 989–1022. Springer International Publishing, Cham.

Johnson, J. B. (2003). Generation and propagation of infrasonic airwaves from volcanic explosions. *Journal of Volcanology and Geothermal Research*, 121(1-2):1–14. ISBN: 0377-0273.

Johnson, J. B. and Aster, R. C. (2005). Relative partitioning of acoustic and seismic energy during Strombolian eruptions. *Journal of Volcanology and Geothermal Research*, 148(3-4):334–354. ISBN: 0377-0273.

Johnson, J. B., Aster, R. C., Ruiz, M. C., Malone, S. D., McChesney, P. J., Lees, J. M., and Kyle, P. R. (2003). Interpretation and utility of infrasonic records from erupting volcanoes. *Journal of Volcanology and Geothermal Research*, 121(1):15–63.

Johnson, J. B. and Palma, J. L. (2015). Lahar infrasound associated with volcán villarrica's 3 march 2015 eruption. *Geophysical Research Letters*, 42(15):6324–6331.

Jones, K. R., Johnson, J. B., Aster, R., Kyle, P. R., and McIntosh, W. C. (2008). Infrasonic tracking of large bubble bursts and ash venting at Erebus Volcano, Antarctica. *Journal of Volcanology and Geothermal Research*, 177(3):661–672.

Jones, R. M. (1986). HARPA Manual.

Judd, J. W., Strachey, R., Wharton, W. J. L., Evans, F. J., Russell, F. A. R., Archibald, D., and Whipple, G. M. (1888). *The Eruption of Krakatoa: And Subsequent Phenomena*. Trübner & Company.

Kamo, K., Ishihara, K., and Tahira, M. (1994). Infrasonic and seismic detection of explosive eruption at Sakurajima Volcano, Japan, and the PEGASAS-VE early-warning system.

Kanamori, H., Mori, J., and Harkrider, D. G. (1994). Excitation of atmospheric oscillations by volcanic eruptions. *Journal of Geophysical Research*, 99(B11):21947–21961. ISBN: 0148-0227.

Kulichkov, S. N., Chunchuzov, I. P., and Popov, O. I. (2010). Simulating the influence of an atmospheric fine inhomogeneous structure on long-range propagation of pulsed acoustic signals. *Izvestiya Atmospheric and Oceanic Physics*, 46(1):60–68.

Lalande, J.-M. and Waxler, R. (2016). The interaction between infrasonic waves and gravity wave perturbations: Application to observations using UTTR Rocket Motor Fuel Elimination Events. *Journal of Geophysical Research: Atmospheres*, 121(10):5585–5600.

Le Pichon, A., Antier, K., and Drob, D. (2006). Multiyear validation of the NRL-G2S wind fields using infrasound from Yasur. *InfraMatics*, (16):1–9.

Le Pichon, A., Assink, J. D., Heinrich, P., Blanc, E., Charlton-Perez, A., Lee, C. F., Keckhut, P., Hauchecorne, A., Rüfenacht, R., Kämpfer, N., Drob, D. P., Smets, P. S. M., Evers, L., Ceranna, L., Pilger, C., Ross, O., and Claud, C. (2015). Comparison of co-located independent ground-based middle atmospheric wind and temperature measurements with numerical weather prediction models. *Journal of Geophysical Research: Atmospheres*, 120(16):8318–8331.

Le Pichon, A., Blanc, E., and Drob, D. (2005a). Probing high-altitude winds using infrasound. *Journal of Geophysical Research*, 110(D20).

Le Pichon, A., Blanc, E., Drob, D., Lambotte, S., Dessa, J. X., Lardy, M., Bani, P., and Vergniolle, S. (2005b). Infrasound monitoring of volcanoes to probe high-altitude winds. *Journal of Geophysical Research Atmospheres*, 110(13):1–12.

Le Pichon, A. and Cansi, Y. (2003). PMCC for infrasound data processing. *Inframatics*, 2:1–9.

Le Pichon, A., Ceranna, L., Garcés, M., Drob, D., and Millet, C. (2006). On using infrasound from interacting ocean swells for global continuous measurements of winds and temperature in the stratosphere. *Journal of Geophysical Research*, 111(D11).

Le Pichon, A., Ceranna, L., Vergoz, J., and Tailpied, D. (2019). Modeling the Detection Capability of the Global IMS Infrasound Network. In Le Pichon, A., Blanc, E., and Hauchecorne, A., editors, *Infrasound Monitoring for Atmospheric Studies*, pages 593–604. Springer International Publishing.

Le Pichon, A., Matoza, R. S., Brachet, N., and Cansi, Y. (2010). Recent Enhancements of the PMCC Infrasound Signal Detector. *InfraMatics*, (26):1–8.

Le Pichon, A., Vergoz, J., Blanc, E., Guilbert, J., Ceranna, L., Evers, L., and Brachet, N. (2009a). Assessing the performance of the International Monitoring System's infrasound network: Geographical coverage and temporal variabilities. *Journal of Geophysical Research*, 114(D8):D08112.

Le Pichon, A., Vergoz, J., Cansi, Y., Ceranna, L., and Drob, D. (2009b). Contribution of Infrasound Monitoring for Atmospheric Remote Sensing. In Le Pichon, A., Blanc, E., and Hauchecorne, A., editors, *Infrasound Monitoring for Atmospheric Studies*, pages 629–646. Springer Netherlands, Dordrecht.

Le Pichon, A., Vergoz, J., Herry, P., and Ceranna, L. (2008). Analyzing the detection capability of infrasound arrays in Central Europe. *Journal of Geophysical Research*, 113(D12).

Leat, P. T., Fretwell, P. T., Tate, A. J., Larter, R. D., Martin, T. J., Smellie, J. L., Jokat, W., and Bohrmann, G. (2016). Bathymetry and geological setting of the South Sandwich Islands volcanic arc. *Antartic Science*.

Lindemann, F. A. and Dobson, G. M. B. (1997). A theory of meteors, and the density and temperature of the outer atmosphere to which it leads. *Proceedings of the Royal Society of London. Series A, Containing Papers of a Mathematical and Physical Character*, 102(717):411–437. Publisher: Royal Society.

Liu, E. J., Wood, K., Aiuppa, A., Giudice, G., Bitetto, M., Fischer, T. P., McCormick Kilbride, B. T., Plank, T., and Hart, T. (2021). Volcanic activity and gas emissions along the South Sandwich Arc. *Bulletin of Volcanology*, 83(1). Publisher: Bulletin of Volcanology ISBN: 0044502001.

Lynch, H. J., White, R., Naveen, R., Black, A., Meixler, M. S., and Fagan, W. F. (2016). In stark contrast to widespread declines along the Scotia Arc, a survey of the South Sandwich Islands finds a robust seabird community. *Polar Biology*, 39(9):1615–1625.

Maher, S. P., Matoza, R. S., Jolly, A., de Groot-Hedlin, C., Gee, K. L., Fee, D., and Iezzi, A. M. (2022). Evidence for near-source nonlinear propagation of volcano infrasound from Strombolian explosions at Yasur Volcano, Vanuatu. *Bulletin of Volcanology*, 84(4):41.

Marchetti, E., Ripepe, M., Campus, P., Le Pichon, A., Vergoz, J., Lacanna, G., Mialle, P., Héreil, P., and Husson, P. (2019a). Long range infrasound monitoring of Etna volcano. *Scientific reports*, 9(1):18015.

Marchetti, E., Ripepe, M., Campus, P., Pichon, A. L., Brachet, N., Blanc, E., Gaillard, P., Mialle, P., Husson, P., and Arnal, T. (2019b). Infrasound Monitoring of Volcanic Eruptions and Contribution of ARISE to the Volcanic Ash Advisory Centers. In *Infrasound Monitoring for Atmospheric Studies*, pages 1141–1162. Springer International Publishing.

Marchetti, E., Ripepe, M., Delle Donne, D., Genco, R., Finizola, A., and Garaebiti, E. (2013). Blast waves from violent explosive activity at Yasur Volcano, Vanuatu. *Geophysical Research Letters*, 40(22):5838–5843. _eprint: https://onlinelibrary.wiley.com/doi/pdf/10.1002/2013GL057900.

Marcillo, O., Arrowsmith, S., Whitaker, R., Anderson, D., Nippress, A., Green, D. N., and Drob, D. (2014). Using physics-based priors in a Bayesian algorithm to enhance infrasound source location. *Geophysical Journal International*, 196(1):375–385.

Marcillo, O., Johnson, J. B., and Hart, D. (2012). Implementation, Characterization, and Evaluation of an Inexpensive Low-Power Low-Noise Infrasound Sensor Based on a Micromachined Differential Pressure Transducer and a Mechanical Filter. *Journal of Atmospheric and Oceanic Technology*, 29(9):1275–1284. Publisher: American Meteorological Society Section: Journal of Atmospheric and Oceanic Technology.

Marty, J. (2019). The IMS Infrasound Network: Current Status and Technological Developments. In Le Pichon, A., Blanc, E., and Hauchecorne, A., editors, *Infrasound Monitoring for Atmospheric Studies: Challenges in Middle Atmosphere Dynamics and Societal Benefits*, pages 3–62. Springer International Publishing.

Matoza, R., Fee, D., Green, D., and Mialle, P. (2019). Volcano Infrasound and the International Monitoring System. In Le Pichon, A., Blanc, E., and Hauchecorne, A., editors, *Infrasound Monitoring for Atmospheric Studies*, pages 1023–1077. Springer International Publishing.

Matoza, R. S. (2009). *Seismic and infrasonic source processes in volcanic fluid systems*. Doctoral dissertation, University of California.

Matoza, R. S., Chouet, B. A., Jolly, A. D., Dawson, P. B., Fitzgerald, R. H., Kennedy, B. M., Fee, D., Iezzi, A. M., Kilgour, G. N., Garaebiti, E., and Cevuard, S. (2022a). High-rate very-long-period seismicity at Yasur volcano, Vanuatu: source mechanism and decoupling from surficial explosions and infrasound. *Geophysical Journal International*, 230(1):392–426.

Matoza, R. S., Fee, D., Assink, J. D., Iezzi, A. M., Green, D. N., Kim, K., Toney, L., Lecocq, T., Krishnamoorthy, S., Lalande, J.-M., Nishida, K., Gee, K. L., Haney, M. M., Ortiz, H. D., Brissaud, Q., Martire, L., Rolland, L., Vergados, P., Nippress, A., Park, J., Shani-Kadmiel, S., Witsil, A., Arrowsmith, S., Caudron, C., Watada, S., Perttu, A. B., Taisne, B., Mialle, P., Le Pichon, A., Vergoz, J., Hupe, P., Blom, P. S., Waxler, R., De Angelis, S., Snively, J. B., Ringler, A. T., Anthony, R. E., Jolly, A. D., Kilgour, G., Averbuch, G., Ripepe, M., Ichihara, M., Arciniega-Ceballos, A., Astafyeva, E., Ceranna, L., Cevuard, S., Che, I.-Y., De Negri, R., Ebeling, C. W., Evers, L. G., Franco-Marin, L. E., Gabrielson, T. B., Hafner, K., Harrison, R. G., Komjathy, A., Lacanna, G., Lyons, J., Macpherson, K. A., Marchetti, E., McKee, K. F., Mellors, R. J., Mendo-Pérez, G., Mikesell, T. D., Munaibari, E., Oyola-Merced, M., Park, I., Pilger, C., Ramos, C., Ruiz, M. C., Sabatini, R., Schwaiger, H. F., Tailpied, D., Talmadge, C., Vidot, J., Webster, J., and Wilson, D. C. (2022b). Atmospheric waves and global seismoacoustic observations of the January 2022 Hunga eruption, Tonga. *Science*, 377(6601):95–100. Publisher: American Association for the Advancement of Science.

Matoza, R. S., Fee, D., Green, D. N., Le Pichon, A., Vergoz, J., Haney, M. M., Mikesell, T. D., Franco, L., Valderrama, O. A., Kelley, M. R., McKee, K., and Ceranna, L. (2018). Local, Regional, and Remote Seismo-acoustic Observations of the April 2015 VEI 4 Eruption of Calbuco Volcano, Chile. *Journal of Geophysical Research: Solid Earth*, 123(5):3814–3827. Publisher: Wiley-Blackwell.

Matoza, R. S., Garcés, M. A., Chouet, B. A., D'Auria, L., Hedlin, M. A. H., De Groot-Hedlin, C., and Waite, G. P. (2009). The source of infrasound associated with long-period events at Mount St. Helens. *Journal of Geophysical Research: Solid Earth*, 114(B4):B04305.

Matoza, R. S., Green, D. N., Le Pichon, A., Shearer, P. M., Fee, D., Mialle, P., and Ceranna, L. (2017). Automated detection and cataloging of global explosive volcanism using the International Monitoring System infrasound network. *Journal of Geophysical Research: Solid Earth*, 122(4):2946–2971.

Matoza, R. S., Hedlin, M. A. H., and Garcés, M. A. (2007). An infrasound array study of Mount St. Helens. *Journal of Volcanology and Geothermal Research*, 160(3-4):249–262. ISBN: 0377-0273.

Matoza, R. S., Landès, M., Le Pichon, A., Ceranna, L., and Brown, D. (2013). Coherent ambient infrasound recorded by the International Monitoring System. *Geophysical Research Letters*, 40(2):429–433.

Matoza, R. S., Le Pichon, A., Vergoz, J., Herry, P., Lalande, J.-M., Lee, H.-i., Che, I.-Y., and Rybin, A. (2011a). Infrasonic observations of the June 2009 Sarychev Peak eruption, Kuril Islands: Implications for infrasonic monitoring of remote explosive volcanism. *Journal of Volcanology and Geothermal Research*, 200(1):35–48.

Matoza, R. S., Vergoz, J., Le Pichon, A., Ceranna, L., Green, D. N., Evers, L. G., Ripepe, M., Campus, P., Liszka, L., Kvaerna, T., Kjartansson, E., and Höskuldsson, Á. (2011b). Long-range acoustic observations of the Eyjafjallajökull eruption, Iceland, April-May 2010. *Geophysical Research Letters*, 38(6):1–5. ISBN: 0094-8276.

McKee, K., Smith, C. M., Reath, K., Snee, E., Maher, S., Matoza, R. S., Carn, S., Mastin, L., Anderson, K., Damby, D., Roman, D. C., Degterev, A., Rybin, A., Chibisova, M., Assink, J. D., de Negri Leiva, R., and Perttu, A. (2021a). Evaluating the state-of-the-art in remote volcanic eruption characterization Part I: Raikoke volcano, Kuril Islands. *Journal of Volcanology and Geothermal Research*, 419:107354.

McKee, K., Smith, C. M., Reath, K., Snee, E., Maher, S., Matoza, R. S., Carn, S., Roman, D. C., Mastin, L., Anderson, K., Damby, D., Itikarai, I., Mulina, K., Saunders, S., Assink, J. D., de Negri Leiva, R., and Perttu, A. (2021b). Evaluating the state-of-the-art in remote volcanic eruption characterization Part II: Ulawun volcano, Papua New Guinea. *Journal of Volcanology and Geothermal Research*, 420:107381.

Meier, K., Hort, M., Wassermann, J., and Garaebiti, E. (2016). Strombolian surface activity regimes at Yasur volcano, Vanuatu, as observed by Doppler radar, infrared camera and infrasound. *Journal of Volcanology and Geothermal Research*, 322:184–195.

Mialle, P., Brachet, P., Gaillard, A., Le Pichon, A., Blanc, D., Tailpied, E., and Friha, N. (2015). Towards a volcanic notification system with infrasound data: Use of infrasound data in support of the VAACs in the framework of ARISE project. In *World meteorological organization 7th international workshop on volcanic ash (IWVA/7), Anchorage, Alaska*.

Mialle, P., Brown, D., Arora, N., and colleages from IDC (2019). Advances in Operational Processing at the International Data Centre. In *Infrasound Monitoring for Atmospheric Studies*, pages 209–248. Springer International Publishing.

Modified Copernicus Sentinel Data (2018). Processed by ESA.

Modrak, R. T., Arrowsmith, S., and Anderson, D. N. (2010). A Bayesian framework for infrasound location. *Geophysical Journal International*, 181(1):399–405.

Morelli, R. S., Gheri, D., Campus, P., Coppola, D., and Marchetti, E. (2022). Long range infrasound monitoring of Yasur volcano. *Journal of Volcanology and Geothermal Research*, 432:107707.

Morton, E. A. and Arrowsmith, S. (2014). The Development of Global Probabilistic Propagation Look-Up Tables for Infrasound Celerity and Back-Azimuth Deviation. *Seismological Research Letters*, 85(6):1223–1233.

NCAR High Altitude Observatory (n.d.). *Whole Atmosphere Community Climate Model with thermosphere and ionosphere extension (WACCM-X)*. `https://www2.hao.ucar.edu/modeling/waccm-x` [Accessed: 9-17-23].

Newhall, C. G. and Self, S. (1982). The volcanic explosivity index (VEI) an estimate of explosive magnitude for historical volcanism. *Journal of Geophysical Research*, 87(C2):1231.

Nippress, A. and Green, D. N. (2023). Global empirical models for infrasonic celerity and backazimuth. *Geophysical Journal International*, 235(2):1912–1925.

Nippress, A., Green, D. N., Marcillo, O. E., and Arrowsmith, S. (2014). Generating regional infrasound celerity-range models using ground-truth information and the implications for event location. *Geophysical Journal International*, 197(2):1154–1165.

Norris, D., Gibson, R., and Bongiovanni, K. (2009). Numerical Methods to Model Infrasonic Propagation Through Realistic Specifications of the Atmosphere. In *Infrasound Monitoring for Atmospheric Studies*, pages 541–573. Springer Netherlands.

Ortiz, H. D., Matoza, R. S., Garapaty, C., Rose, K., Ramón, P., and Ruiz, M. C. (2020). Multi-year regional infrasound detection of Tungurahua, El Reventador, and Sangay volcanoes in Ecuador from 2006 to 2013. *Proceedings of Meetings on Acoustics*, 41(1):022003.

Park, I., Jolly, A., Matoza, R. S., Kennedy, B., Kilgour, G., Johnson, R., Garaebiti, E., and Cevuard, S. (2021). Seismo-acoustic characterisation of the 2018 Ambae (Manaro Voui) eruption, Vanuatu. *Bulletin of Volcanology*, 83(9):60.

Park, J., Arrowsmith, S., Hayward, C., Stump, B. W., and Blom, P. (2014). Automatic infrasound detection and location of sources in the western United States. *Journal of Geophysical Research: Atmospheres*, 119(13):7773–7798.

Patrick, M. R. and Smellie, J. L. (2013). Synthesis a spaceborne inventory of volcanic activity in antarctica and southern oceans, 2000-10. *Antarctic Science*, 25(4):475–500. Publisher: Cambridge University Press.

Pekeris, C. L. and Taylor, G. I. (1997). The propagation of a pulse in the atmosphere. *Proceedings of the Royal Society of London. Series A. Mathematical and Physical Sciences*, 171(947):434–449. Publisher: Royal Society.

Perttu, A., Taisne, B., De Angelis, S., Assink, J. D., Tailpied, D., and Williams, R. A. (2020). Estimates of plume height from infrasound for regional volcano monitoring. *Journal of Volcanology and Geothermal Research*, 402:106997.

Picone, J. M., Hedin, A. E., Drob, D. P., and Aikin, A. C. (2002). NRLMSISE-00 empirical model of the atmosphere: Statistical comparisons and scientific issues. *Journal of Geophysical Research: Space Physics*, 107(A12):SIA 15–1–SIA 15–16. Publisher: Wiley-Blackwell.

Ripepe, M. and Marchetti, E. (2002). Array tracking of infrasonic sources at Stromboli volcano. *Geophysical Research Letters*, 29(22):2076.

Ripepe, M., Marchetti, E., Donne, D. D., Genco, R., Innocenti, L., Lacanna, G., and Valade, S. (2018). Infrasonic Early Warning System for Explosive Eruptions. *Journal of Geophysical Research: Solid Earth*, 123(11):9570–9585.

Sanderson, R. W., Matoza, R., Fee, D., Haney, M. M., and Lyons, J. J. (2020). Remote Detection and Location of Explosive Volcanism in Alaska With the EarthScope Transportable Array. *Journal of Geophysical Research: Solid Earth*, 125(4).

Sanderson, R. W., Matoza, R. S., Haymon, R. M., and Steidl, J. H. (2021). A Pilot Experiment on Infrasonic Lahar Detection at Mount Adams, Cascades: Ambient Infrasound and Wind-Noise Characterization at a Quiescent Stratovolcano. *Seismological Research Letters*, 92(5):3065–3086.

Schwaiger, H. F., Iezzi, A. M., and Fee, D. (2019). AVO-G2S: A modified open-source Ground-to-Space atmospheric specification for infrasound modeling. *Computers & Geosciences*, 125:90–97.

Self, S. (1992). Krakatau Revisited: The Course of Events and Interpretation of the 1883 Eruption. *GeoJournal*, 28(2):109–121. Publisher: Springer.

Shaw, W. and Dines, W. H. (1905). The study of the minor fluctuations of atmospheric pressure. *Quarterly Journal of the Royal Meteorological Society*, 31(133):39–52.

Simkin, T. and Siebert, L. (1994). *Volcanoes of the world: a regional directory, gazetteer, and chronology of volcanism during the last 10,000 years*. Geoscience Press, Tucson, Ariz, 2nd ed edition.

Smets, P. S. M., Assink, J. D., Pichon, A. L., and Evers, L. (2016). ECMWF SSW forecast evaluation using infrasound. *Journal of Geophysical Research: Atmospheres*, 121(9):4637–4650.

Smets, P. S. M., Evers, L., Näsholm, S. P., and Gibbons, S. J. (2015). Probabilistic infrasound propagation using realistic atmospheric perturbations. *Geophysical Research Letters*, 42(15):6510–6517.

Spina, L., Taddeucci, J., Cannata, A., Gresta, S., Lodato, L., Privitera, E., Scarlato, P., Gaeta, M., Gaudin, D., and Palladino, D. M. (2016). "Explosive volcanic activity at Mt. Yasur: A characterization of the acoustic events (9-12th July 2011)". *Journal of Volcanology and Geothermal Research*, 322:175–183.

Sutherland, L. C. and Bass, H. E. (2004). Atmospheric absorption in the atmosphere up to 160 km. *The Journal of the Acoustical Society of America*, 115(3):1012–1032.

Tailpied, D., Le Pichon, A., Marchetti, E., Assink, J., and Vergniolle, S. (2017). Assessing and optimizing the performance of infrasound networks to monitor volcanic eruptions. *Geophysical Journal International*, 208(1):437–448.

Taisne, B., Perttu, A., Tailpied, D., Caudron, C., and Simonini, L. (2019). Atmospheric Controls on Ground- and Space-Based Remote Detection of Volcanic Ash Injection into the Atmosphere, and Link to Early Warning Systems for Aviation Hazard Mitigation. In Le Pichon, A., Blanc, E., and Hauchecorne, A., editors, *Infrasound Monitoring for Atmospheric Studies*, pages 1079–1105. Springer International Publishing, Cham.

United Nations (n.d.). *Ending Nuclear Testing*. `https://www.un.org/en/observances/end-nuclear-tests-day/history` [Accessed: 9-17-23].

Van Eaton, A. R., Amigo, Á., Bertin, D., Mastin, L. G., Giacosa, R. E., González, J., Valderrama, O., Fontijn, K., and Behnke, S. A. (2016). Volcanic lightning and plume behavior reveal evolving hazards during the April 2015 eruption of Calbuco volcano Chile. *Geophysical Research Letters*, 43(7):3563–3571.

Verbeek, R. D. M. (1885). *Krakatau*. Uitgegeven op last van zijne excellentie den GouverneurGeneraal van Nederlandsch-Indië.

Vergniolle, S. and Métrich, N. (2016). A bird's eye view of "Understanding volcanoes in the Vanuatu arc". *Journal of Volcanology and Geothermal Research*, 322:1–5.

Vergoz, J., Hupe, P., Listowski, C., Le Pichon, A., Garcés, M., Marchetti, E., Labazuy, P., Ceranna, L., Pilger, C., Gaebler, P., Näsholm, S., Brissaud, Q., Poli, P., Shapiro, N., De Negri, R., and Mialle, P. (2022). IMS observations of infrasound and acoustic-gravity waves produced by the January 2022 volcanic eruption of Hunga, Tonga: A global analysis. *Earth and Planetary Science Letters*, 591:117639.

Virieux, J., Garnier, N., Blanc, E., and Dessa, J.-X. (2004). Paraxial ray tracing for atmospheric wave propagation. *Geophysical Research Letters*, 31(20). _eprint: https://onlinelibrary.wiley.com/doi/pdf/10.1029/2004GL020514.

Walker, K. T. and Hedlin, M. A. (2010). A Review of Wind-Noise Reduction Methodologies. In *Infrasound Monitoring for Atmospheric Studies*, pages 141–182. Springer Netherlands.

Waxler, R. and Assink, J. (2019). Propagation Modeling Through Realistic Atmosphere and Benchmarking. In Le Pichon, A., Blanc, E., and Hauchecorne, A., editors, *Infrasound Monitoring for Atmospheric Studies: Challenges in Middle Atmosphere Dynamics and Societal Benefits*, page 509–549. Springer International Publishing, Cham.

Waxler, R., Assink, J., and Velea, D. (2017). Modal expansions for infrasound propagation and their implications for ground-to-ground propagation. 141(2):1290–1307. Publisher: Acoustical Society of America.

Waxler, R., Hetzer, C., Assink, J., and Velea, D. (2023). *chetzer-ncpa/ncpaprop-release: NCPAprop v2.1.0*. urlhttps://zenodo.org/record/5562713/preview/chetzer-ncpa/ncpaprop-release-v2.1.0.zip.

Webley, P. and Mastin, L. (2009). Improved prediction and tracking of volcanic ash clouds. *Journal of Volcanology and Geothermal Research*, 186(1-2):1–9.

Whipple, F. J. W. (1923). The High Temperature of the Upper Atmosphere as an Explanation of Zones of Audibility. *Nature*, 111(2780):187–187. Number: 2780 Publisher: Nature Publishing Group.

Whipple, F. J. W. (1935). The propagation of sound to great distances. *Quarterly Journal of the Royal Meteorological Society*, 61(261):285–308. _eprint: https://onlinelibrary.wiley.com/doi/pdf/10.1002/qj.49706126102.